

# Investigating the impact of space weather on the polar atmosphere using rigorous statistical methods



Jone Øvretvedt Edvartsen

Thesis for the degree of Philosophiae Doctor (PhD)  
University of Bergen, Norway  
2023

UNIVERSITY OF BERGEN



# Investigating the impact of space weather on the polar atmosphere using rigorous statistical methods

Jone Øvretvedt Edvartsen



Thesis for the degree of Philosophiae Doctor (PhD)  
at the University of Bergen

Date of defense: 15.09.2023

© Copyright Jone Øvretvedt Edvartsen

The material in this publication is covered by the provisions of the Copyright Act.

Year: 2023

Title: Investigating the impact of space weather on the polar atmosphere using rigorous statistical methods

Name: Jone Øvretvedt Edvartsen

Print: Skipnes Kommunikasjon / University of Bergen

# Acknowledgements

I would like to thank my main supervisor Ville Maliniemi and my co-supervisor Hilde Nesse for their guidance and support throughout this research. While working with the thesis, I have been forced to acquire a multidisciplinary approach, resulting in a significant time spent studying. As my supervisors have readily provided their expertise in a wide range of topics, my learning process have been substantially amplified. Not to mention I have never felt a question ever being deemed to simple. Towards contributions to my research, I also want to thank Timo Asikainen, Spencer Hatch, Pavle Arsenovic and Timofei Sukhodolov for valuable assistance.

To my office mate and partner in PhD-crime, Eldho. Of all the possible office mates I could have been paired with, I am glad the universe chose us. Thanks for the laughs, the weird noises, the occasional mood swings, the real talks, and the additional memories outside of the office.

Having a Danish guy in the group is always fun, even though he is barely smarter than the Swedes, according to our generic Norwegian jokes. Always a pleasure talking to you, Michael. Never a dull moment, even though I never understand what you say.

Keeping a good work-life balance can be challenging during a PhD, but thanks to Andreas, I have always had a great companion for activities and adventures beyond the research.

Creating a positive and supportive work environment is crucial for a successful PhD journey, so a big thanks to Josephine, Simon, Ingrid, Margot, Sara, and Reham for enhancing our shared workspace. Honestly, you are definitely more fun than me.

A big shoutout to Jone and Jone for giving me the unique experience of encountering not one, but two other individuals with the same uncommon name. Triple the Jones, triple the fun!

Gratefulness is an understatement to my friends outside of work for making the PhD experience easier by providing essential breaks from mundanity.

Preceding my academic journey, I would like to express my gratitude to my family for providing support and being a constant safety net.

To my dear beloved girlfriend, Pernille, thank you for being you.



# Preface

This dissertation represents nearly three years of research, which was funded by the Research Council of Norway under contracts 223252/F50 (Birkeland Center for Space Science, BCSS) and 300724 (EPIC). The work was conducted from August 2020 to April 2023 at the University of Bergen, under the guidance of my supervisors Ville Maliniemi and Hilde Nesse, who provided invaluable insights and assistance. The dissertation is submitted as the main requirement for the degree of philosophiae doctor (PhD) in space physics/atmospheric dynamics at BCSS, Institute of Physics and Technology, University of Bergen. It consists of an introductory part that provides the necessary scientific background, and the three original research articles listed below:

**Paper I** Jone Øvretvedt Edvartsen, Ville Maliniemi, Hilde Nesse, Timo Asikainen & Spencer Hatch, (2022), "The Mansurov effect: Statistical Significance and the role of autocorrelation", *J. Space Weather Space Clim.*, **12**, 11. DOI: <https://doi.org/10.1051/swsc/2022008>

**Paper II** Jone Øvretvedt Edvartsen, Ville Maliniemi, Hilde Nesse & Spencer Hatch, (2023), "The Mansurov effect: Seasonal and solar wind sector structure dependence", *J. Space Weather Space Clim.*, **13**, 17. DOI: <https://doi.org/10.1051/swsc/2023013>

**Paper III** Jone Øvretvedt Edvartsen, Ville Maliniemi & Hilde Nesse (2023), "Effects of Energetic Particle Precipitation on stratospheric temperature during disturbed Stratospheric Polar Vortex conditions", *J. Geophys. Res. Atmos.*, **128**, 10. DOI: <https://doi.org/10.1029/2022JD038010>



# List of Abbreviations

<i>AO</i>	Arctic Oscillation
<i>BD</i>	Brewer-Dobson
<i>BCSS</i>	Birkeland Center for Space Science
<i>CAM</i>	Community Atmospheric Model
<i>CCM</i>	Chemistry-Climate Model
<i>CCN</i>	Cloud Condensation Nuclei
<i>CCSM</i>	Community Climate System Model
<i>CERN</i>	Conseil européen pour la recherche nucléaire (research organization)
<i>CIR</i>	Corotating Interaction Region
<i>CLOUD</i>	Cosmics Leaving Outdoor Droplets (Project at CERN)
<i>CMIP</i>	Coupled Model Intercomparison Project
<i>CME</i>	Coronal Mass Ejection
<i>ECHAM</i>	European Centre/Hamburg Atmospheric Model
<i>ENSO</i>	El Niño Southern Oscillation
<i>EPP</i>	Energetic Electron Precipitation
<i>ERA</i>	European Centre for Medium-Range Weather Forecasts Re-Analysis
<i>EXP</i>	Experiment
<i>FDR</i>	False Discovery Rate
<i>FT</i>	Fourier Transform
<i>GCR</i>	Galactic Cosmic Rays
<i>GEC</i>	Global Electric Circuit
<i>GSE</i>	Geocentric Solar Ecliptic (coordinate system)
<i>GW</i>	Gravity Waves
<i>HCS</i>	Heliospheric Current Sheet
<i>HO<sub>x</sub></i>	Hydrogen Oxides
<i>IMF</i>	Interplanetary Magnetic Field
<i>MEE</i>	Medium Energetic Electrons
<i>MEZON</i>	Model for Evaluation of oZONe trends
<i>MC</i>	Monte-Carlo
<i>MPIOM</i>	Max Planck Institute Ocean Model
<i>NCEP/NCAR</i>	National Centers for Environmental Prediction/National Center for Atmospheric Research
<i>NAO</i>	North Atlantic Oscillation



---

<i>NH</i>	Northern Hemisphere
<i>NLC</i>	Noctilucent Clouds
<i>NO<sub>x</sub></i>	Nitrogen Oxides
<i>NOAA</i>	National Oceanic and Atmospheric Administration
<i>PV</i>	Polar Vortex
<i>QBO</i>	Quasi-Biennial Oscillation
<i>REF</i>	Reference
<i>RRTMG</i>	Rapid Radiation Transfer suite of Models optimized for General circulation models
<i>SAM</i>	Southern Annular Mode
<i>SE</i>	Superimposed Epoch
<i>SH</i>	Southern Hemisphere
<i>SOCOL</i>	Solar Climate Ozone Links (model)
<i>SPE</i>	Solar Proton Events
<i>SSI</i>	Spectral Solar Irradiance
<i>SSW</i>	Sudden Stratospheric Warming
<i>TLCC</i>	Time Lagged Cross Correlation
<i>TSI</i>	Total Solar Irradiance
<i>ULF</i>	Ultra Low Frequency
<i>VLF</i>	Very Low Frequency
<i>WACCM</i>	Whole Atmosphere Community Climate Model
<i>WPI</i>	Wave-Particle Interaction
<i>WRS</i>	Wilcoxon Rank-Sum

# Abstract (English)

Recent years have seen a surge in observational, re-analysis, and model-based studies providing evidence of statistical correlations between day-to-day to interannual solar activity and climate/weather patterns. The overarching objective of this thesis is to delve into the theory of two solar-climate mechanisms, the Chemical-Dynamical coupling and the Mansurov effect. The Chemical-Dynamical coupling is linked to the ionization of the upper atmosphere ( $>50$  km) by energetic particle precipitation (EPP), resulting in the production of odd nitrogen and hydrogen oxides ( $\text{NO}_x$  and  $\text{HO}_x$ ). These compounds are effective ozone depleters, and can alter the radiative balance of the atmosphere, potentially leading to a cascading effect in dynamically induced atmospheric weather changes observable in the polar atmosphere. The Mansurov effect is related to the interplanetary magnetic field (IMF) and its ability to modulate the global electric circuit (GEC), which is further assumed to impact the polar troposphere through cloud generation processes. It is hypothesised to occur nearly instantaneously, providing a physical link between near-Earth-space and the lower atmosphere. These topics will be studied with sophisticated statistical analysis methods.

For the Chemical-Dynamical coupling, we use the SOCOL3-MPIOM model to compare the northern polar atmospheric temperature differences in ensemble members with and without EPP. The analyses builds on recent re-analysis evidence showing that EPP mostly impacts the northern polar atmospheric temperature right before and during disturbed Polar Vortex (PV) conditions. We find highly significant temperature responses during conditions set up by minor Sudden Stratospheric Warmings (SSW), associated with disturbed polar vortex and enhanced planetary wave activity. The largest anomalies are seen in February, and only for the latter half (1955–2008) of the simulation period (1900–2008). The findings suggest that during winter, the Chemical-Dynamical coupling could play a crucial role in stratospheric conditions and confirms the existence of the chemical-dynamical link in the model.

By using ERA5 atmospheric re-analysis data and OMNIweb IMF data spanning 1968–2020, the connection between the IMF  $B_y$  and polar surface pressure is investigated. Contrary to prior published studies on the Mansurov effect, no significant response is found after accounting for autocorrelation and multiple hypothesis testing. In addition, prior studies highlight a 27-day cyclic pressure response as indirect evidence of a physical link. However, we show that this periodic pressure behaviour occurs as a statistical artefact of the methods, and is not a reliable indicator of a causal connection. Furthermore, a new robust and statistically significant correlation is determined between the IMF  $B_y$  and polar surface pressure. It is found in the time-period March-

April-May for both hemispheres, but with an unphysical timing with respect to the Mansurov hypothesis. The analyses highlight the general need for rigorous statistical testing, as well as the need for caution when deploying certain methodologies with periodic and highly autocorrelated variables.

# Abstrakt (norsk)

I de senere år har det vært en økning i observasjonsbaserte, re-analytiske og modellbaserte studier som viser korrelasjoner mellom dag-til-dag og år-til-år solaktivitet og klima-/vær-mønstre. Det overordnede målet med avhandlingen er å undersøke to solklima-mekanismer, den Kjemisk-Dynamiske koblingen og Mansurov-effekten. Den Kjemisk-Dynamiske koblingen er knyttet til ioniseringen av den øvre atmosfæren (>50 km) som skjer ved energisk partikkelnedbør (EPP). Dette resulterer i produksjon av nitrogen- og hydrogenoksider ( $\text{NO}_x$  og  $\text{HO}_x$ ). Disse molekylene bryter effektivt ned ozon, og kan derfor endre strålingsbalansen i atmosfæren, noe som igjen potensielt kan føre til en kaskadeffekt av dynamisk induserte atmosfæriske værendringer i polaratmosfæren. Mansurov-effekten er knyttet til det interplanetariske magnetfeltet (IMF) og dets evne til å modulere den globale elektriske kretsen (GEC). Dette antas å videre påvirke den polare troposfæren gjennom å endre de fysiske prosessene bak dannelse og vekst av skyer. Effekten antas å være nesten umiddelbar, noe som gir en fysisk forbindelse mellom verdensrommet og den nedre del av Jordens atmosfære. Begge mekanismene har blitt studert ved hjelp av sofistikerte statistiske analysemetoder.

For den Kjemisk-Dynamiske koblingen, bruker vi SOCOL3-MPIOM-modellen for å sammenligne temperaturforskjeller i den nordlige atmosfæren i modellkjøringen med og uten EPP. Analysen bygger på en nylig studie som viser at EPP hovedsakelig påvirker den nordlige atmosfæriske temperaturen rett før og under forstyrrede forhold i den stratosfæriske polare jetstrøm. Vi finner svært signifikante temperaturresponser rett før hendelser karakterisert som små stratosfæriske oppvarminger, forhold assosiert med en svekket polar jetstrøm og økt bølgeaktivitet. De største temperaturforskjellene er synlig i februar, men bare for den siste halvdel (1955–2008) av simuleringsperioden (1900–2008). Funnene antyder at den Kjemisk-Dynamiske koblingen kan spille en avgjørende rolle i stratosfæriske forhold om vinteren og bekrefter eksistensen av den Kjemisk-Dynamiske koblingen i modellen.

Ved å bruke data fra OMNIweb og ERA5 re-analyse over tidsperioden 1968–2020, undersøkes forbindelsen mellom IMF  $B_y$  og polart atmosfærisk trykk på havnivå. I motsetning til tidligere publiserte studier om Mansurov-effekten, finner vi ingen signifikant respons etter å ha tatt hensyn til autokorrelasjon og kontrollert for falsk deteksjonsandel (*false discovery rate*). Tidligere studier har også fremhevet en 27-dagers syklisk trykkrespons i sine resultater som indirekte bevis for en fysisk forbindelse. Vi demonstrerer at denne periodiske trykkresponsen oppstår som et resultat av de statistiske metodene som er brukt, og kan derfor ikke brukes som en indikator på en fysisk sammenheng. Videre oppdages en hittil ukjent robust og statistisk signifikant korre-

lasjon mellom IMF  $B_y$  og polart atmosfærisk trykk ved havnivå. Korrelasjonen er tydelig i perioden mars-april-mai på begge halvkuler, men med en tilsynelatende ufy-sisk timing med hensyn til Mansurov-effekten. I alt fremhever resultatene det generelle behovet for grundig statistisk testing, samt behovet for varsomhet når man bruker spesi-fikke metoder sammen med periodiske og autokorrelerte variabler.

# Contents

<b>Acknowledgements</b>	<b>iii</b>
<b>Preface</b>	<b>v</b>
<b>List of Abbreviations</b>	<b>vii</b>
<b>Abstract (English)</b>	<b>ix</b>
<b>Abstrakt (norsk)</b>	<b>xi</b>
<b>1 Introduction</b>	<b>1</b>
<b>2 Theory</b>	<b>5</b>
2.1 The Chemical-Dynamical coupling . . . . .	5
2.1.1 Magnetic Reconnection and The Dungey Cycle . . . . .	6
2.1.2 Pitch angle and Loss cone . . . . .	7
2.1.3 Geomagnetic storms . . . . .	8
2.1.4 Particle acceleration and particle loss . . . . .	9
2.1.5 Effects of Ionization in the Polar Atmosphere and properties of Ozone . . . . .	10
2.1.6 General Atmospheric Circulation . . . . .	13
2.1.7 Atmospheric Waves . . . . .	15
2.1.8 The Polar Vortex and Sudden Stratospheric Warmings . . . . .	16
2.1.9 The Quasi-Biennial Oscillation . . . . .	19
2.1.10 Research on the Chemical-Dynamical Coupling . . . . .	19
2.2 The Mansurov effect . . . . .	25
2.2.1 Solar Wind (Interplanetary Magnetic Field) . . . . .	25
2.2.2 Global Electric Circuit . . . . .	26
2.2.3 External Influence on the Global Electric Circuit . . . . .	27
2.2.4 Global Electric Circuit: Fair Weather Current . . . . .	29
2.2.5 Influences on Microphysical Processes in Clouds . . . . .	29
2.2.6 Cloud opacity, radiation budget and surface pressure . . . . .	32
2.2.7 Research on the Mansurov Effect . . . . .	34
<b>3 Statistical Approaches</b>	<b>41</b>
3.1 Artificial periodicity produced by methods . . . . .	41
3.1.1 Derivation . . . . .	41

3.1.2	Simulation . . . . .	42
3.2	Monte Carlo approach . . . . .	43
3.2.1	Surrogate data . . . . .	44
3.2.2	Bootstrapping . . . . .	47
3.3	Multiple comparison problem . . . . .	48
3.3.1	False-Discovery Rate . . . . .	48
3.3.2	Optimizing $\alpha_{\text{FDR}}$ . . . . .	50
3.3.3	False-Discovery Rate combined with the Monte Carlo approach . . . . .	50
<b>4</b>	<b>Data</b>	<b>53</b>
4.1	Solar wind data . . . . .	53
4.2	Atmospheric data . . . . .	54
4.2.1	Re-analysis data . . . . .	54
4.2.2	Model data . . . . .	54
<b>5</b>	<b>Summary of Papers</b>	<b>57</b>
5.1	Paper I: The Mansurov effect: Statistical significance and the role of autocorrelation . . . . .	57
5.2	Paper II: The Mansurov effect: Seasonal and solar wind sector structure dependence . . . . .	58
5.3	Paper III: Effects of Energetic Particle Precipitation on stratospheric temperature during disturbed Stratospheric Polar Vortex conditions . . . . .	59
<b>6</b>	<b>Conclusion and Future Work</b>	<b>61</b>
6.1	Conclusion . . . . .	61
6.2	Future work . . . . .	62
<b>7</b>	<b>Scientific Results</b>	<b>83</b>
<b>A</b>	<b>Appendix</b>	<b>137</b>
A.1	Additional theory . . . . .	137
A.1.1	Three types of particle motion . . . . .	137
A.1.2	Adiabatic invariants . . . . .	139
A.2	Errata . . . . .	140
A.2.1	Paper I . . . . .	140
A.2.2	Paper III . . . . .	141
<b>B</b>	<b>Dictionary</b>	<b>143</b>

# Chapter 1

## Introduction

Since ancient times, the vast power of the Sun has been recognized by humankind. Its first scientific explanation was offered around the 5th century BC, proposed as a giant burning rock, rather than a mythical object. Today, it is common knowledge that the Sun regulates the climate and weather. However, details on whether and how day-to-day and year-to-year variability of the solar output can modulate everything from the chemical composition of our atmosphere to changed wind patterns at sea surface level are yet to be determined. Increased satellite coverage, extended atmospheric observational data record, and improved computational efficiency have aided recent scientific investigations suggesting that previously unknown mechanisms operating through the solar wind and its inherent magnetic field can also influence atmospheric weather patterns, along with solar radiation. The overarching goal of this thesis is to deepen our understanding of two such putative links with the use of rigorous statistical approaches.

### Hypothesis 1: The Chemical-Dynamical coupling

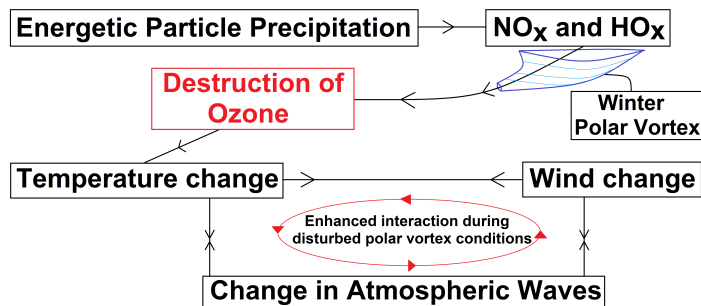


Figure 1.1: Diagram sketching the pathway of the mechanism.

Energetic particles precipitating (EPP) into our atmosphere are known to influence the formation of nitrogen ( $\text{NO}_x$ ) and hydrogen oxides ( $\text{HO}_x$ ) in the polar regions (Randall et al., 2005; Rozanov et al., 2005; Sinnhuber et al., 2012; Smith-Johnsen et al., 2017; Sætre et al., 2004; Turunen et al., 2009; Zawedde et al., 2016, 2018). Moreover, these molecules are well known catalytic ozone destroyers (Bates and Nicolet, 1950; Crutzen, 1970; Johnston, 1971). Ozone is important for the radiative balance in the



stratosphere and mesosphere. Hence, changing the ozone density will impact temperature, winds and wave propagation (Ward et al., 2021). This pathway received considerable attention after Seppälä et al. (2009) found a significant temperature change in polar surface air at winter time correlated with the geomagnetic index  $A_p$  (proxy for EPP). However, new evidence suggest that the mechanism may only operate right before and during certain atmospheric conditions, when the polar stratosphere is disturbed and planetary wave activity is high (Asikainen et al., 2020).

### Hypothesis 2: The Mansurov effect

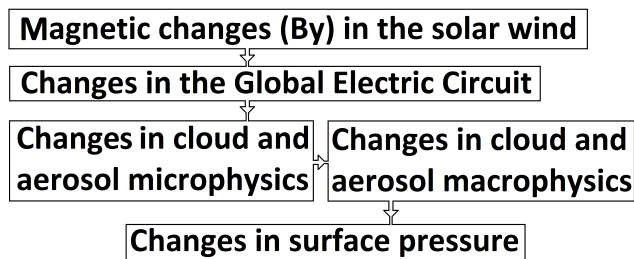


Figure 1.2: Diagram sketching the pathway of the mechanism.

In the 1970s, studies revealed a correlation between changes in the  $B_y$  component of the Interplanetary Magnetic Field (IMF) and changes in polar surface pressure. This correlation is now known in the literature as the Mansurov effect (Burns et al., 2007, 2008; Lam et al., 2013, 2014, 2018; Lam and Tinsley, 2016; Mansurov et al., 1974). IMF  $B_y$  is known to modulate the ionospheric polar cap potential, and therefore also the Global Electric Circuit (GEC) (Frank-Kamenetsky et al., 2001; Kabin et al., 2003; Lam et al., 2013; Pettigrew et al., 2010; Tinsley and Heelis, 1993). To explain the observed pressure anomalies, a potential mechanism is proposed where atmospheric electricity affects cloud generation processes (Lam and Tinsley, 2016; Tinsley, 2022; Tinsley and Heelis, 1993).

Evidence for the Mansurov effect is largely based on the limited time period of 1999–2002, and lacks rigorous statistical assessments. Similarly, for the Chemical-Dynamical coupling, studies have suggested that the statistical significance might be overstated (Meraner and Schmidt, 2018; Tartaglione et al., 2020). Wilks (2016) stated that only 3 of the 281 papers (1.1%) in the *Journal of Climate* during the first half of 2014 considered the effects of multiple hypothesis testing on their scientific conclusions, thereby overstating the significance of their results. Only by ensuring statistical rigor, can we build community-wide acceptance of new weather and climate phenomena.

With the use of appropriate data and statistical methods, the objective of this thesis is to further our understanding regarding **Hypothesis 1** and **Hypothesis 2** specifically by answering three key questions:

1. Is there a statistically sound relationship between space weather and atmospheric weather variations?
2. Are these relationships potentially important for the surface climate?
3. Are there any deviations between the hypotheses and the findings?



# Chapter 2

## Theory

This section presents relevant concepts and recent research needed to understand the physical reality underlying the hypotheses researched in paper I, II and III. It first introduces the Chemical-Dynamical coupling, before presenting the Mansurov effect.

### 2.1 The Chemical-Dynamical coupling

The Chemical-Dynamical coupling proposes a link between EPP induced chemistry changes in the Earth's upper atmosphere and large-scale dynamics affecting the lower atmosphere. Figure 1.1 illustrates the steps involved in the mechanism. Ionization of the atmosphere by EPP creates  $\text{NO}_x$  and  $\text{HO}_x$  radicals, which are known to be catalysts of ozone. In winter time, with little photolysis,  $\text{NO}_x$  species can have a long half-life (1–2 months). The polar vortex act as a boundary confining the molecules to polar latitudes, where the downward residual wind transport  $\text{NO}_x$  to the ozone rich stratosphere. Furthermore, ozone absorbs shortwave UV radiation and emits thermal longwave radiation. As the polar regions are subject to low UV exposure during winter, the longwave emittance dominates, and ozone acts as a local cooling agent. Therefore, by destroying ozone, the radiative balance changes, and the local area experiences a net warming effect. Due to the dynamical nature of the atmosphere, this change in temperature leads to changes in winds and atmospheric wave propagation, which creates a feedback loop between temperature, wind and wave propagation. Moreover, the feedback loop is hypothesized to strengthen during times of polar vortex disturbances and increased planetary wave activity. In the next subsections, the background theory and physical principles required to understand the Chemical-Dynamical coupling will be elaborated, followed by an update of recent research.

#### Solar Wind

Plasma in the outer solar corona is continuously heated to the point where gravitational forces can no longer retain its constituents. This results in charged particles (ions and electrons) propagating radially outwards, carrying the Sun's magnetic field with them. This combination of ejected mass and magnetic fields are known as the solar wind. The radially moving magnetic field embedded in the solar wind is referred to as the Interplanetary Magnetic Field (IMF). Further details about the solar winds inherent magnetic properties will be discussed in section 2.2.1 in regards to the Mansurov effect.

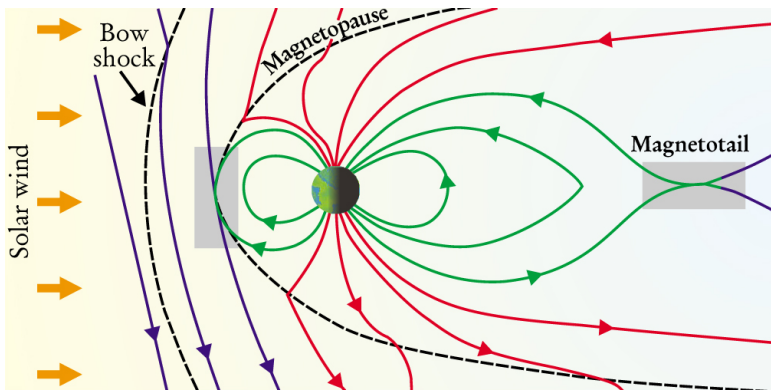


Figure 2.1: Illustration of the Dungey Cycle. Blue lines indicate the magnetic field lines of the IMF, green lines indicate Earth's magnetic field, and red lines indicate field lines connected to both the Earth and the IMF. The two grey boxes at day side and night side highlight the areas where anti-parallel magnetic field lines meet and reconnection occurs. [Figure obtained from *PhysicsToday* (2001).]

Here we will focus more on how the charged particles of the solar wind interact with Earth's geomagnetic field to create energetic particle precipitation.

### 2.1.1 Magnetic Reconnection and The Dungey Cycle

As the solar wind is continuously ejected radially outwards from the Sun, there is a continuous interaction between the IMF and the Earth's magnetic field. However, the interaction is highly variable in terms of energy input into the near Earth's space and atmosphere. It largely depends on the magnetic field geometry and solar wind speed which determines the magnetic reconnection rate. Magnetic reconnection implies that magnetic field lines of opposite polarities connect to each other. This process rearranges the magnetic topology and converts magnetic energy to kinetic and/or thermal energy (Dungey, 1961, 1963). Figure 2.1 illustrates the steps involved in this cycle. The IMF (blue lines), which points in the N-S directions, reconnects with Earth's magnetic field lines of opposite polarity (green lines which points in the S-N direction) at the day side. This results in magnetic field lines extending from Earth and into the solar wind, referred to as open field lines (red lines). As the solar wind flows past, the open field lines from both hemispheres are dragged past Earth, forming the magnetotail. Here on the nightside, due to the opposite polarity, the field lines can again reconnect. Furthermore, after reconnection at the nightside, the field lines convect back to the dayside and complete the cycle. A predominantly southward IMF orientation is favorable for increased reconnection rate. However, the geometry also allows reconnection when the IMF is directed in the northward direction (positive  $B_z$ ), though at a slower rate. Additionally, the rate of reconnection is also dependent on the radial bulk speed of the solar wind (e.g. Borovsky and Valdivia, 2018; Kabin et al., 2003; Kessel et al., 1996). Along with the conversion of magnetic energy, charged particles are also transferred from the solar wind to the magnetosphere, which is the region where the geomagnetic field dominates. Charged particles trapped inside the magnetosphere, can be accelerated by the new input of energy. Both the new influx of particles and the existing population can

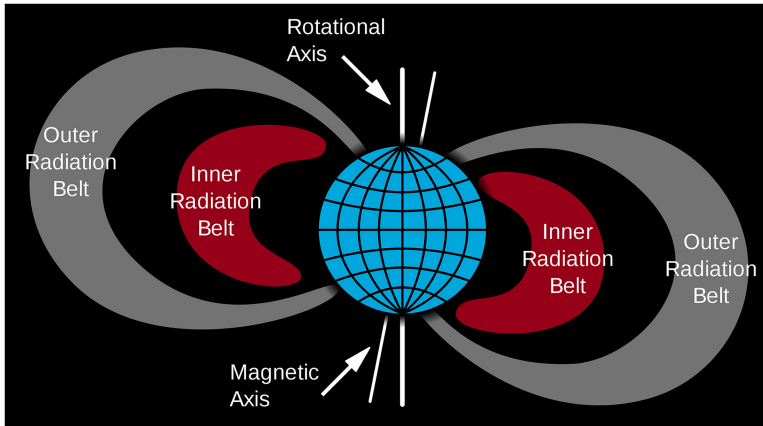


Figure 2.2: Illustration of the Van Allen belts [Figure obtained from Li and Hudson (2019)].

potentially end their journey into the atmosphere as particle precipitation.

### 2.1.2 Pitch angle and Loss cone

Inside the magnetosphere, large radiation belts were discovered in 1958 by James Van Allen. The inner and outer belts, which can be seen in Figure 2.2, are often termed the Van Allen belts. They are made up of ions and electrons that mainly originate from the solar wind. However, charged particles can also escape from Earth's ionosphere and end up trapped in the Van Allen belts. The trapping is caused by the electromagnetic forces acting on charged particles bound to magnetic field lines in a converging field. Charged particles both gyrate around magnetic field lines, as well as bounce between geomagnetic conjugate points known as mirror points. In addition, charged particles also evince a drift motion, with electrons drifting eastward and protons drifting westward. This is illustrated in Figure 2.3. A derivation of these forces and the resulting particle motion is found in Appendix A1. The angle between the particle's velocity vector and the magnetic field lines is termed the *pitch angle*. The *mirror points* are those locations where the pitch angle is  $90^\circ$ , implying zero velocity parallel to the magnetic field. The converging magnetic field exerts a force on a moving charge pointing away from the convergence. The relation between the pitch angle and magnetic field strength can be described (see Appendix A1) by the equation

$$\sin \alpha_0 = \sqrt{\frac{B_0}{B_1}}, \quad (2.1)$$

where  $B_0$  denotes the magnetic field strength at the location of the particle, and  $B_1$  denotes the magnetic field strength at the mirror point. Particles that reach about 100-km altitude will collide with the atmospheric gasses. Hence, by setting  $B_1$  equal to the magnetic field strength at 100-km altitude, the pitch angle range of the particles that are lost to the atmosphere can be calculated. This specific pitch angle is often referred to as the loss cone, as the angles trace out a cone around the magnetic field in three dimensions where all particles with smaller pitch angles will be lost to the atmosphere.

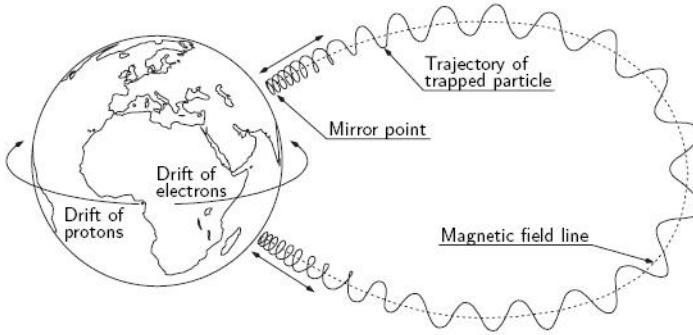


Figure 2.3: Illustration of the three main modes of particles motion. A derivation of the gyration and mirror-bouncing can be found in Appendix A [Figure obtained from ESA].

The loss cone will vary in size depending on the magnetic field strength ( $B_0$ ) at the location of the particles. Electromagnetic waves in the magnetosphere can interact with the trapped particles causing both acceleration and pitch angle diffusion.

### 2.1.3 Geomagnetic storms

Energy from the solar wind fuels the respective electromagnetic waves. As the magnetic field direction fluctuates continuously, reconnection can be said to occur quasi-continuously. The solar wind is often divided into three main categories; slow/ambient, High Speed Streams (HSS), and Coronal Mass Ejections (CMEs). The HSS and CMEs originate from magnetic phenomena at the Sun, and can lead to substantial changes in terms of solar wind speed, IMF magnetic field strength and/or density of charged particles in the solar wind. When the reconnection is efficient, magnetic field disturbances cause currents in the ionosphere and near-Earth, and can generate geomagnetic storms. A *geomagnetic storm* is a significant but temporary disturbance in Earth's geomagnetic field. Though not the subject of this thesis, these storms play a key role in the the Chemical-Dynamical coupling, as they generate energetic particle precipitation, and might play the key role for high energy precipitation. It is also worth mentioning the explosive magnetic forces involved with CMEs which can sometimes lead to unusual high acceleration of protons in the solar wind, called Solar Proton Events (SPEs). These high energy protons have sufficient rigidity and energy to penetrate the closed field lines and directly precipitate into the lower atmosphere (Belov, 2017; Cong et al., 2019; Torsti et al., 1999).

Particle precipitation correlates fairly well with geomagnetic activity (e.g. Mironova et al., 2015; Tyssøy et al., 2021). Therefore, it is common to use different indices as a proxy for EPP. One of these is the geomagnetic index  $A_p$ , which gives a daily scale measure of geomagnetic disturbances derived from ground-based measurements. This index has a long track record (since 1932), and is therefore suitable to e.g. climate analyses at decadal timescales. For the purpose of Paper III, which is a model study investigating the Chemical-Dynamical coupling, the EPP forcing input is taken from the

Coupled Model Intercomparison Project Phase 6 (CMIP6) recommendation (Matthes et al., 2017). Here, ionization rates are calculated based on geomagnetic index parameterized particle fluxes. These data will be described in further detail in Section 4.2.2.

### 2.1.4 Particle acceleration and particle loss

In the solar wind, the typical energies of electrons are relatively low, typically less than 50 eV (Pilipp et al., 1987). However, in the Van Allen belts, electrons can have relativistic energies of several MeVs. Also, particles escaping from the ionosphere have in general energies similar to those seen in the solar wind. The energy gap can be explained by magnetospheric large- and small-scale dynamics.

The different particle acceleration mechanisms are typically divided into radial acceleration and local acceleration (e.g. Hiraga and Omura, 2020; Li and Hudson, 2019; Reeves et al., 2003, 2013; Tu et al., 2014). Radial acceleration occurs through the process of inward diffusive radial transport. This mechanism might play an important role in providing seed electron populations (hundreds of keV) in the inner magnetosphere which can further be accelerated by local acceleration sources. The mechanism are driven by fluctuations in the magnetic field on time scales comparable to the drift period, which breaks the third adiabatic invariant (the adiabatic invariants are discussed in Appendix A2). These fluctuations can be caused by pressure instabilities, electromagnetic waves generated in the magnetosphere, or by changes in electromagnetic fields driven by geomagnetic storms. The main idea is that as particles are moved towards the Earth, the magnetic field strength increases, and charged particles gain energy as long as the first and second adiabatic invariants are conserved. Conversely, local acceleration happens in situ, and is thought to increase the lower energy electrons to relativistic energies via wave-particle-interactions (WPI). Both naturally occurring electromagnetic very low frequency (VLF, 3–30 kHz) waves and ultra low frequency (ULF, 0.3–3 kHz) waves are candidates for such interactions (Hiraga and Omura, 2020; Li and Hudson, 2019; Reeves et al., 2013). These waves can resonate with the electrons. If the temporal scale of the interactions is within a gyroperiod, it breaks the first adiabatic invariant and acceleration occur.

There are also mechanisms driving particle loss. Magnetopause shadowing can occur when the dynamic pressure of the solar wind moves the magnetosphere inward. This can result in opening of earlier closed drift paths leading to electrons lost to the outer magnetosphere (Turner et al., 2012). However, for Paper III which focuses on the Chemical-Dynamical coupling, particles lost to the atmosphere are of greatest importance. As discussed earlier, any perturbation that alters the pitch angles of particles such that they fall within the loss cone induces energetic particle precipitation. When reconnection between the IMF and Earth's magnetic field occur, fresh particles can be injected following magnetic field lines. Some of these particles have pitch angles falling into the loss cone, leading to direct energetic particle precipitation, presumably of low energies. Through radial diffusion and WPI, trapped particles may be accelerated to relativistic energies. During disturbed conditions, the trapped higher energy particles can further interact with waves and instabilities in the surrounding plasma, ul-



timately causing pitch angle scattering and loss to the atmosphere (Thorne et al., 2010; Turner et al., 2014; Zhu et al., 2020).

## 2.1.5 Effects of Ionization in the Polar Atmosphere and properties of Ozone

The atmosphere is often divided into layers based on physical properties such as the average temperature profile (specifically, the direction of the temperature gradient vs altitude). The region extending from the ground up to roughly  $\sim 10$  km is known as the troposphere, the region from  $\sim 10$  to  $\sim 50$  km is known as the stratosphere, and the region extending from  $\sim 50$  to  $\sim 85$  km is known as the mesosphere. Additionally, there is a region further extending from  $\sim 85$  to  $\sim 700$  km known as the thermosphere. The terms tropopause (10 km), stratopause (50 km) and mesopause (85 km) are also used to describe the top boundary region of each layer. Note that the altitudes given are approximate values and in general depend on season and latitude, as well as vary on relatively short timescales.

Figure 2.4 shows the ionization rates vs altitude for five different types of EPP as well as Solar EUV and X-rays. We will however only focus on the particles associated with geomagnetic disturbances. (Galactic Cosmic Rays (GCR) also consist of extremely energetic particles; however, their occurrence have an inverse relation to the strength of the solar wind and subsequently geomagnetic disturbances). Auroral electrons (red), originating from the plasma sheet and accelerated by WPI, have typical energies  $< 30$  keV, and deposit their energy mainly throughout the thermosphere with

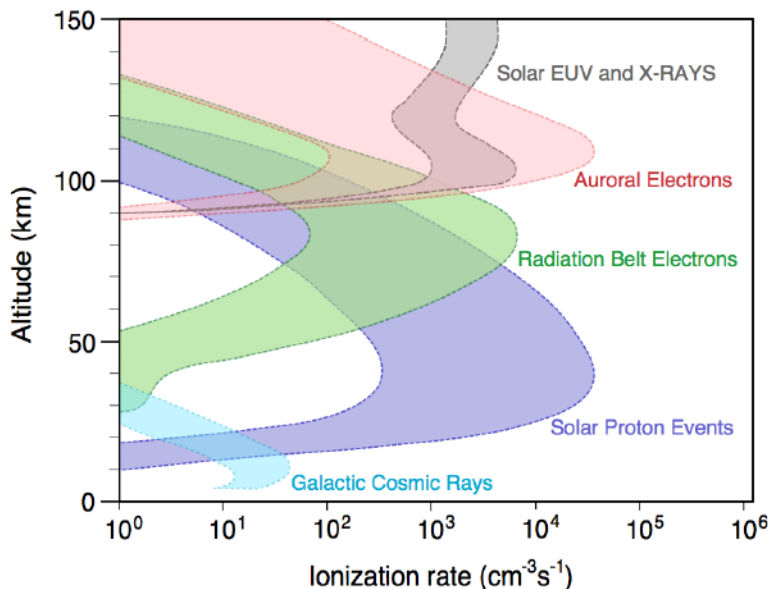


Figure 2.4: Illustration of different solar and intergalactic forcing that ionize the atmosphere [Figure obtained from Verronen (2021)]

the most energetic electrons depositing close to the mesopause. Radiation belt electrons at  $>30$  keV (green), which are trapped in the Van Allen belts and accelerated during geomagnetic disturbances, deposit their energy throughout the mesosphere, where relativistic electrons can reach as far down as the stratopause. SPEs (purple), precipitating directly from the solar wind ( $>1$  MeV protons) ionize as far down as the middle Stratosphere. These events are rare and sporadic compared to electron precipitation (Gerontidou et al., 2002). Thus, in recent years the electrons originating from the plasma sheet and radiation belts are considered to be the main driver of the Chemical-Dynamical coupling.

The increased ionization initiates a cascade of chemical reactions increasing the production of  $\text{NO}_x$  and  $\text{HO}_x$  gases that can reduce ozone in catalytic reactions. The vast majority of ozone molecules are found in the main ozone layer over altitudes of 15–30 km. However, as the density of the atmosphere itself decreases exponentially with altitude, ozone still plays an important role in the local radiative energy balance up to the mesopause. Figure 2.5 shows the primary ozone maximum around 30-km altitude, secondary maximum around 90-km and the tertiary ozone maximum around 70-km altitude. The latter is only found during winter.

Studies have shown that the ionization induced by EPP correlates well with the production of  $\text{NO}_x$  and  $\text{HO}_x$  (Randall et al., 2005; Rozanov et al., 2005; Smith-Johnsen et al., 2017; Sætre et al., 2004; Turunen et al., 2009; Zawedde et al., 2016, 2018). As  $\text{HO}_x$  particles have a lifetime of only hours in the mesosphere, they quickly dissociate

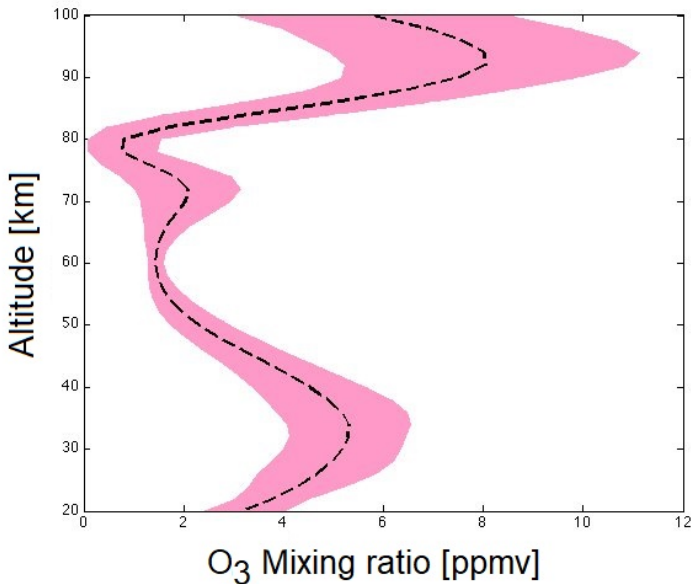


Figure 2.5: Nighttime ozone profile showing the three local ozone maxima occurring in mixing ratio [Figure obtained from Seppälä (2007)]

or react close to the area of production (Sinnhuber et al., 2012).  $\text{NO}_x$  particles have a lifetime of about 1 day in the upper mesosphere/lower thermosphere. However, the lifetime of  $\text{NO}_x$  is greatly increased (1–2 months) in the absence of sunlight, which is part of the reason why the Chemical-Dynamical coupling are most likely to occur during local polar winter (Sinnhuber et al., 2012; Ward et al., 2021). Moreover, the strong wintertime polar vortex confines the EPP-produced  $\text{NO}_x$  to high latitudes. The long-lived  $\text{NO}_x$  molecules are then able to participate in downward transport occurring inside of the boundaries of the polar vortex. In addition, both  $\text{NO}_x$  and  $\text{HO}_x$  have been shown to have a destructive influence on ozone (Bates and Nicolet, 1950; Crutzen, 1970; Johnston, 1971) via catalytic cycles of the form (Portmann et al., 2012):



with  $X = \{\text{NO}_x, \text{HO}_x\}$  giving a net total of:

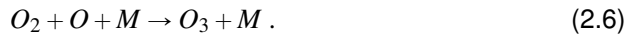


This recycling of the X-molecule increases the destructiveness of the  $\text{NO}_x$  and  $\text{HO}_x$  molecules, as one X-molecule can contribute to the destruction of many orders of magnitude of ozone molecules before it is converted to a less reactive agent (Lary, 1997). Randall et al. (2005) classifies this process into a direct and indirect impact. The direct effect implies that the production of  $\text{NO}_x$  and  $\text{HO}_x$  by EPP and the ozone reduction occur in the same region. The indirect effect implies that the long-lived EPP produced  $\text{NO}_x$  molecules are transported by the residual circulation from e.g. the thermosphere and/or mesosphere to the upper stratosphere where it efficiently can destroy ozone.

Due to ozone's radiative properties, these chemical changes couple with the atmospheric dynamics. Ozone absorbs shortwave UV radiation, and emits thermal long-wave radiation. The role of ozone was first theorized by Chapman (1930), and is found in textbooks covering the role of atmospheric ozone and oxygen (e.g. Neuman et al., 2000). The UV absorption process by ozone in the stratosphere occurs through the reaction:



which effectively destroy ozone at a fast rate. An important feature of this reaction is the creation of free oxygen atoms. These are highly reactive, and quickly combine with oxygen molecules to form ozone:



In this reaction, the atom/molecule M is needed for energy balance. M is usually  $\text{N}_2$  or  $\text{O}_2$ , as these comprise most of the atmosphere. When  $\text{O}_2$  and O react to form ozone, a significant amount of energy is released. This energy is carried away by molecule M through a collision with the newly formed ozone molecule. In essence, the fast cycle of ozone destruction and production involved in reactions (Eq. 2.5-2.6) ultimately converts incoming UV solar radiation into thermal energy, heating the stratosphere.

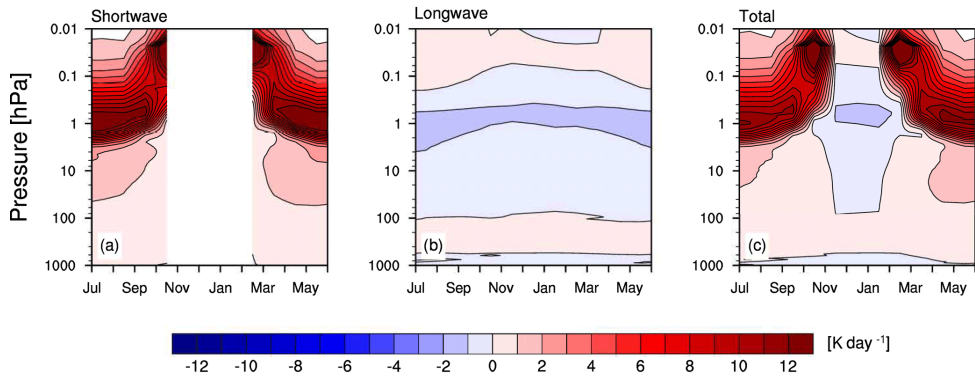


Figure 2.6: Monthly mean heating rates of ozone at  $75^{\circ}\text{N}$  calculated by the rapid radiation transfer suite of models optimized for general circulation models (RRTMG) for shortwave (left panel), longwave (middle panel) and the combination of both (right panel) [Figure obtained from Meraner and Schmidt (2018)].

As for thermal longwave radiation, ozone has specific vibrational-rotational transition bands corresponding to infrared wavelengths. In general, these states are induced by energy obtained through collisions with molecules in the surrounding atmosphere. During de-excitation, this excess energy is carried off as thermal longwave radiation, leading to local cooling (Petty, 2006). The relationship between ozone and temperature also involves various factors, such as altitude and presence of other molecules. However, these reactions provide a simplified conceptual framework to understand how a loss in ozone leads to temperature changes in the surrounding area.

Figure 2.6 illustrates the monthly mean radiative properties of ozone calculated by a radiative transfer model at  $75^{\circ}\text{N}$  for shortwave (left panel), longwave (middle panel), and the combination of both (right panel). During winter polar night with little UV, the ozone does not contribute to heating of the stratosphere and mesosphere. Therefore, thermal radiation loss dominates in these regions (0.1–100 hPa). This leads to the ozone population having a radiative cooling effect. Consequently, a reduction of the local ozone population induced by EPP will decrease the cooling effect, leading to a net stratospheric warming. However, in the late winter, when sunlight once again hit the polar atmosphere, the heating induced by the UV photolytic reactions starts to dominate. A reduction in the ozone population at this time will therefore lead to a local cooling of the surrounding. In addition, multiple other studies (e.g. Graf et al., 1998; Langematz et al., 2003; Randel and Wu, 1999) show similar evidence of stratospheric temperature dependence on ozone concentration.

### 2.1.6 General Atmospheric Circulation

The atmosphere is a rather complex system, where temperature, winds, and wave propagation and breaking are interdependent. Hence, the Chemical-Dynamical coupling is not confined to local perturbations, but is hypothesised to cause larger scale anomalies. To explore how the change of one atmospheric parameter feed into the next, we will

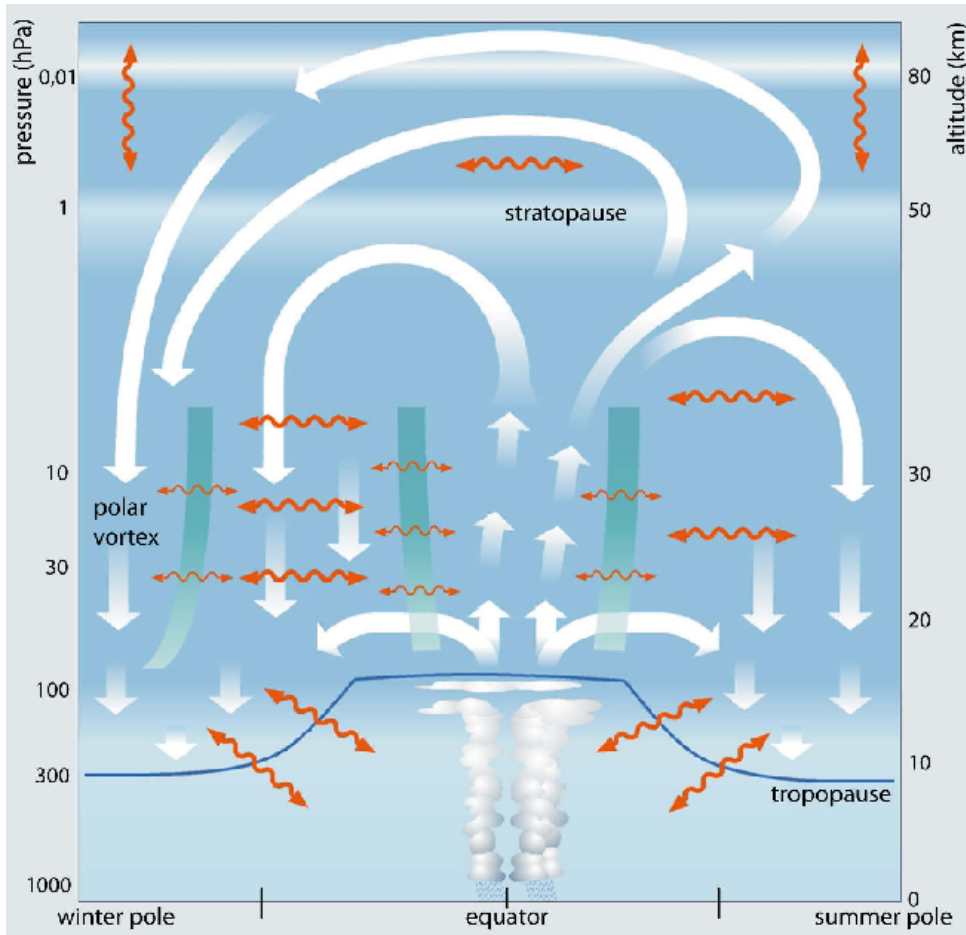


Figure 2.7: Schematic of the Brewer-Dobson Circulation. The white arrows depict the large-scale circulation, while the wavy orange arrows depict two-way mixing between regions. Both the circulation and mixing are mainly driven by atmospheric waves. The green lines represent stratospheric transport and mixing barriers [Figure obtained from Bönisch et al. (2011) and made by Dr. U. Schmidt]

first examine how the atmospheric circulation operates.

Figure 2.7 shows a schematic of the general circulation that occurs above the troposphere, known as the Brewer-Dobson circulation (BDC). In the stratosphere, winds primarily blow from the equator towards the poles, while the mesosphere exhibits a circulation pattern from the summer pole to the winter pole. This leads to a general pattern of flow from the equator towards the poles, which is enhanced in the direction of the winter pole. The enhancement is due both to a stronger temperature gradient in this direction and to gravity wave breaking and dissipation, which drives the summer to winter pole circulation in the mesosphere (Vincent, 2015). Ozone is mainly created around tropical latitudes due to the excess of UV. However, observations show that the largest concentrations are found located at polar latitudes. In the BDC, this can be ex-

plained by the transport of air masses directed from the stratospheric tropics toward the poles, with the strongest airflow toward the local winter pole Rosenlof (1995).

The main physical driving mechanism of the Brewer-Dobson circulation arises from the wave drag of dissipating, upward-propagating planetary waves originating from the troposphere. Without the Coriolis force, masses of air would move upwards in the tropics due to excessive heating. This heated air would then tend to move towards the poles, driven by the negative temperature gradient in this direction. As the air is transported polewards, it cools and becomes denser, ultimately leading to downwelling at higher latitudes. The cold air would then be transported along the surface towards the equator to fill the gap left by the ascending air, thus closing the loop. However, since the Earth is constantly rotating eastward, the air masses moving from the equator towards the poles in both hemispheres will experience a force in the direction of rotation, pushing them eastward. Nonetheless, large-scale circulation of air masses in the middle atmosphere still move towards the poles. This is because planetary waves induce a westward drag that counteracts the Coriolis force. The resulting force balance leads to the equator-to-pole stratospheric transport seen in the BDC (Butchart, 2014; Holton et al., 1995). The BDC effectively leads to adiabatic cooling in both the tropics and in the summer mesosphere as air ascends, and adiabatic heating in both polar stratospheres as air descends. This also helps to explain the feature of the mesospheric polar summer having the lowest temperature in our atmosphere (120 K) (Vincent, 2015).

This circulation scheme is responsible for the Chemical-Dynamical coupling, and the indirect NO impact on the stratospheric ozone. Understanding the coupling between temperature, wind and atmospheric waves is also essential to understanding how the stratospheric temperature perturbation due to EPP can be detected all the way down to the surface as atmospheric waves.

### 2.1.7 Atmospheric Waves

Gravity waves are driven by buoyancy forces, e.g., when parcels of air flow over mountains or moves upwards within thunderclouds to a region of less dense air buoyancy and gravity forces creates periodic waves. The scale sizes can vary from meters to hundreds of kilometers, and temporal scales from minutes to hours. Propagating upwards, the increasing amplitude due to the decrease in density ultimately renders the wave unstable, such that they break and deposit their energy and momentum. They are therefore a means for energy and momentum transport from the troposphere to the stratosphere and mesosphere (Sun et al., 2015). The point of absorption is known as a *critical level*. This can occur when the amplitude of the wave becomes sufficiently large, causing the wave to break as wave energy transforms into turbulent kinetic energy. A critical level can also occur when the component of background wind in the direction of wave propagation is equal to the wave's horizontal phase speed. However, for gravity waves generated entirely by topography (implies zero phase speed in the horizontal direction), a critical level will occur when the background wind is perpendicular to the wave's propagation direction (Whiteway and Duck, 1996).

Planetary waves, which are also known as Rossby waves, result from conservation of potential vorticity. In mechanics, this is analogous to conservation of angular momentum. Planetary waves are generated by pressure gradients displacing air parcels in the latitudinal direction, where Coriolis is the restoring force. As the Coriolis force also varies with latitude, it ultimately results in wave patterns as a mean of conserving the potential vorticity of the system (Rossby, 1939). These waves are larger than gravity waves in spatial extent, reaching thousands of kilometers which earns them the name planetary waves. They originate in the lower atmosphere (troposphere) and can be characterised by always having a westward phase velocity. These waves have a dominating role in the positioning of high and low pressure, and also significantly affect the distribution of atmospheric species (Homeyer and Bowman, 2013; Rodas and Pulido, 2017; Zhang et al., 2019). The waves themselves can be characterized by a *wavenumber*, a dimensionless quantity that describes the number of wavelengths that would fit within a full circle around the globe at a given latitude. The smaller the wavenumber, the larger the wavelength of the planetary wave. Wavenumbers of 1–3 are of this reason often referred to as long waves, while 4–10 are referred to as "synoptic" waves. Rossby waves are an important concept when it comes to the evolution of the Sudden Stratospheric Warmings (SSWs) events that are of importance in Paper III.

### 2.1.8 The Polar Vortex and Sudden Stratospheric Warmings

The BDC gives a crude understanding of the general circulation of air masses, while atmospheric waves defines the modes of momentum transfer. However, to understand how the Chemical-Dynamical coupling might lead to surface perturbations, the role of the winter polar vortex and the associated sudden stratospheric warmings needs to be explained.

The Polar Vortex (PV) is a large scale stratospheric polar circulatory wind system approximately centered over the geographic poles. The phenomenon exists in both hemispheres, and it also has a tropospheric counterpart known as the tropospheric polar jet. The system is mainly characterized by its predominately westerly wind direction during winter time, and is driven by temperature differences between high- and mid-latitudes. The strength of the PV increase during winter time (larger temperature gradients between local winter pole and mid latitudes) and decrease during local summer (Andrews, 2010). However, the strength of the PV also exhibit large interannual variability. During a strong PV, the westerly winds increase and low pressure zones joined by cooler temperatures occurs at polar latitudes relative to lower latitudes. A weak PV manifests as the opposite pattern, induced by increased drag and disturbances in the westward direction. Figure 2.8 illustrates the manifestation of a strong (left) and weak (right) polar vortex. To quantify this behaviour, the Arctic Oscillation (AO) and the North Atlantic Oscillation (NAO) index have been developed. Where the AO uses a signal analysis method (EOF) to qualitatively measure the strength of the pressure surrounding the polar region. The NAO measures the atmospheric sea level pressure between Iceland and the Azores (Hurrell, 1995). The NAO can be associated with more physically meaningful parameters, and may therefore carry more impact on measurable atmospheric changes (Ambaum et al., 2001).

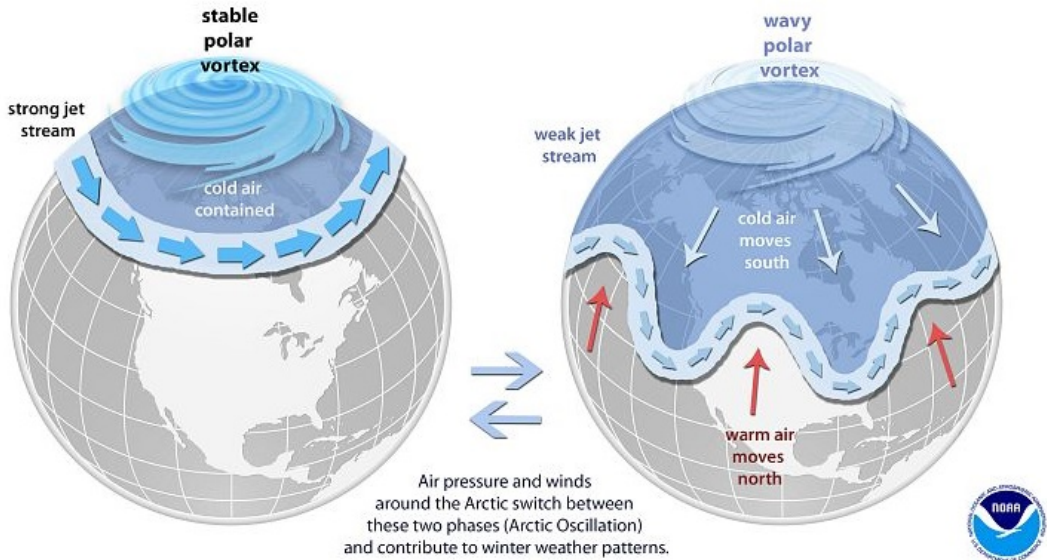


Figure 2.8: Illustration of the stable (left) and disturbed (right) phase of the PV. When disturbed, cold air is released from the PV to lower latitudes, which manifests as colder and drier winters in the NH [Figure obtained from National Oceanic and Atmospheric Administration (NOAA) website].

In the troposphere, synoptic planetary waves (wavenumbers 4–8) cannot in general propagate into the stratosphere (Charney and Drazin, 1961; Matsuno, 1970). However, multiple studies of wavenumber 1 and 2 have shown significant energy deposition and atmospheric perturbations in both the stratosphere and mesosphere (e.g. Cho et al., 2004; Cong et al., 2019; Eswaraiah et al., 2020; Kleinknecht et al., 2014; Walterscheid et al., 2000). If the convergence of waves becomes sufficiently strong, the increased drag can result in a temporarily splitting, displacement or complete breakdown of the polar vortex. If the disturbance is strong enough to completely reverse the stratospheric meridional winds, the event is termed a major Sudden stratospheric warming (SSW). This will also impact the downwelling of air masses inside of the vortex, which first halts before it strongly increases when the PV reforms. Thus, major SSWs lead to a significant increase of downward transport of air masses. Observational studies show these events to be happening roughly every 1.7 years in the NH (Baldwin et al., 2021; Schoeberl, 1978). However, they rarely happen in the SH. This is due to lower continent-ocean contrast making unfavorable conditions for the generation of planetary wavenumbers 1 and 2, and therefore results in less upward propagating disturbances and steadier polar vortex. SSWs can also cause wind reversal and subsequent cooling in the mesosphere, contrary to the warming observed in the stratosphere (Cho et al., 2004; Walterscheid et al., 2000). This pattern is likely to occur by a combination of planetary and gravity wave forcing (Liu and Roble, 2005; Shepherd et al., 2020). The temperature profile of an SSW occurring in late December 2018 is illustrated in Figure 2.9, where one can clearly see the dipole signature between the stratosphere and mesosphere.



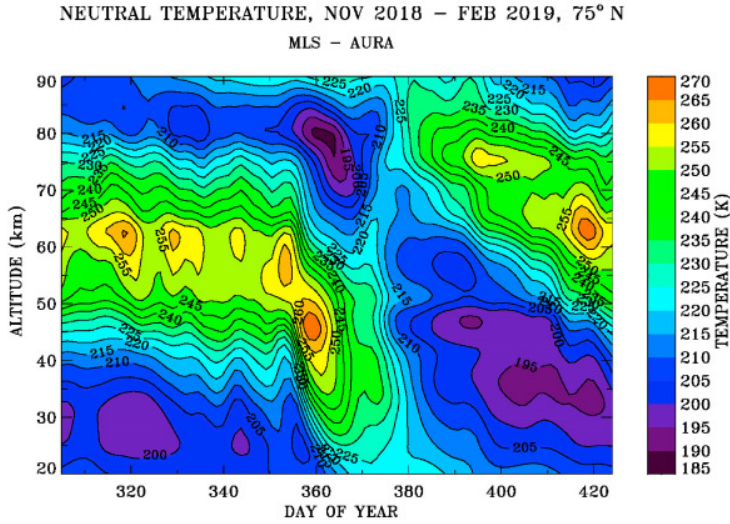


Figure 2.9: Temperature profile of an SSW occurring in late December 2018. [Taken from Shepherd et al. (2020)].

After the pioneering work by Matsuno (1971), theories regarding the generation of SSWs have generally suggested planetary waves as the driving mechanism. However, recent developments are now suggesting that gravity waves may play a larger role than previously thought (Shpynev et al., 2015; Song et al., 2020; Yasyukevich et al., 2022). Shpynev et al. (2015) proposes a physical mechanism using the analogy of a whirlpool for the PV. With little sunlight and thermal heating during winter time, there will be a significant source of kinetic energy inside the PV originating from the down welling of cooling stratospheric air masses. It is therefore proposed that pressure (baroclinical) instabilities can occur inside the PV at the boundaries between flows of different velocities. These instabilities are further proposed to act as a source of gravity waves. In this framework, the polar vortex itself can act a source of gravity waves. Though no conclusive studies exists, this internal source of gravity waves could make additional contributions when it comes to the formation and evolution of SSWs.

The disturbances leading to the high variability of the polar vortex and potential SSWs arise from waves dissipating their energy and momentum and acting as drag on the westerly flow. By disturbing the westerly circulation, one allows for increased air mixing between polar and lower latitudes, as well as a strengthening of polar stratospheric down-welling of air masses (Holton and Tan, 1980). This leads to increased polar temperatures, and cooler temperatures at lower latitudes. The changes in temperature, can then again change the behaviour of the atmospheric waves, as propagation and refraction of these waves are dependent on atmospheric properties. The system therefore creates a feedback loop which will further be referred to as wave-mean-flow interaction (Andrews, 1987; Matsuno, 1970, 1971).

### 2.1.9 The Quasi-Biennial Oscillation

Another internal mode is the Quasi-Biennial Oscillation (QBO), identified as a quasi-periodic variation in the equatorial stratosphere (16–40 km) between downward propagating east-ward and west-ward wind. It oscillates with a period of approximately 28 months, and the winds propagate downwards at a rate of 1 km per month (Baldwin et al., 2001). Work by Holton and Lindzen (1972); Lindzen and Holton (1968) showed that this periodic wind reversal were likely due to vertically traversing atmospheric waves originating from the tropical troposphere and dissipating in the stratosphere by radiative cooling. Further studies regarding the nature of the forcing waves have shown gravity waves to be an essential contributor to the QBO (Baldwin et al., 2001).

Even though the QBO is an equatorial phenomenon, it has been shown to significantly affect the strength of the PV; this is known as the Holton-Tan effect (Holton and Tan, 1980, 1982). It is therefore of particular interest for the results obtained in Paper III. In the QBO westward (QBO-W) phase the PV is typically stronger (lower pressure and cooler temperatures inside the polar vortex), while in the QBO eastward (QBO-E) phase the PV is typically weaker (opposite pattern). In consequence, a higher frequency of SSWs is observed during QBO-E. Different mechanisms have been proposed to explain this effect, however all with the common feature that the QBO modulates planetary wave activity. This modulation favours planetary wave activity converging in the polar region during QBO-E, and thereby decelerating the PV, with opposite modulation during QBO-W (Baldwin et al., 2001; Holton and Tan, 1980, 1982; Lu et al., 2014). To avoid systematic bias when studying the Chemical-Dynamical coupling, the QBO-phase as a potential precondition needs to be considered. Several studies in the EPP effect have found the most significant anomalies during the QBO-E phase, signalling that disturbed PV conditions might play an important role for the manifestation of the effect.

### 2.1.10 Research on the Chemical-Dynamical Coupling

The first steps of the mechanism explained above have reached scientific consensus, like the production of  $\text{NO}_x$  and  $\text{HO}_x$  correlating with EPP (e.g Marsh et al., 2004; Randall et al., 2005; Rozanov et al., 2005; Sinnhuber et al., 2011; Smith-Johnsen et al., 2017; Turunen et al., 2009),  $\text{NO}_x$  and  $\text{HO}_x$  having a destructive influence on ozone in the upper and middle atmosphere (e.g. Bates and Nicolet, 1950; Baumgaertner et al., 2011; Crutzen, 1970; Johnston, 1971; Lary, 1997; Portmann et al., 2012; Sinnhuber et al., 2018, 2012), and ozone's radiative properties (Graf et al., 1998; Langematz et al., 2003). The mentioned processes take place in both hemispheres (Damiani et al., 2016; Funke et al., 2005, 2014), however, due to increased planetary wave activity due to topography, the variability of the phenomenon is larger in the NH (Sinnhuber et al., 2012). Moreover, uncertainties also persist regarding the formation rate of  $\text{NO}_x$  and  $\text{HO}_x$ , downward transport of  $\text{NO}_x$ , and the complex coupling between atmospheric chemistry, heating and cooling rates and dynamics, as well as possibly necessary atmospheric preconditions (Asikainen et al., 2020; Sinnhuber et al., 2012). As this thesis (Paper III) focuses on the Chemical-Dynamical coupling and its impacts on atmo-

spheric dynamics in the NH, this section will specifically highlight research related to this connection.

As early as the 1980s, Solomon et al. (1982) proposed that auroral ionization producing NO<sub>x</sub> in the upper atmosphere could impact both stratospheric ozone levels and the overall circulation of the stratosphere. This hypothesis was based on the results of photochemical models that incorporated the mesosphere and lower thermosphere, with emphasis placed on the transportation and chemistry of NO<sub>x</sub>. A similar pathway was also suggested by Callis et al. (1998).

Later, statistical studies investigated the link between geomagnetic variability and atmospheric parameters during winter time in the NH. Geomagnetic activity was found to correlate well with perturbations in the PV, suggesting that downward winds produced in the polar thermosphere during geomagnetic storms were able to penetrate the troposphere (Arnold and Robinson, 2001; Bucha and Bucha, 1998). Rigorous statistical approaches confirmed the relationship (Thejll et al., 2003), and subsequent studies found the strongest relationship during the easterly QBO phase (Bochniek and Hejda, 2006; Palamara and Bryant, 2004). However, due to no consensus surrounding a viable mechanism, most early investigations did not consider a potential time-lag between the geomagnetic activity and the atmospheric state.

Nevertheless, studies conducted during mid-2000s started to point in the direction of a Chemical-Dynamical coupling induced by stratospheric ozone changes (Bochniek and Hejda, 2005). This theory gained traction with the work of Rozanov et al. (2005), which introduced EPP produced NO<sub>x</sub> into chemistry-climate model runs, and observed subsequent changes in stratospheric ozone levels and temperature. From there, multiple studies confirmed the role of downward descending NO<sub>x</sub> produced by EPP and stratospheric ozone destruction (Ciliverd et al., 2006; Hauchecorne et al., 2005; Randall et al., 2005; Seppälä et al., 2007). Based on the new evidence, Lu et al. (2008, 2007) conducted a statistical assessment trying to pinpoint the relationship between EPP-NO<sub>x</sub> and stratospheric dynamics during spring. The results showed a correlation between high geomagnetic activity and local stratospheric heating, opposite from an expected local cooling effect assumed to occur in spring time by *in situ* ozone destruction (See Figure 7). Additionally, the responses exhibited greater amplitude than what *in situ* chemical reactions would typically cause, suggesting the influence of indirect dynamical connections or wave-mean-flow interactions.

A famous study by Seppälä et al. (2009) showed NH polar surface air temperature correlating with geomagnetic activity measured by A<sub>p</sub> (proxy for EPP) during the last half of the 20th century. Winters were sorted according to high and low geomagnetic activity, with potential aliasing from solar radiation taken into account. Figure 2.10 shows the temperature difference when comparing the high and low geomagnetic winters for all available data (top panels), and when the F10.7cm index (proxy for solar radiation) was low (bottom panels). The results showed statistically significant temperature anomalies predominately during midwinter (DJF). This investigation excluded winters containing SSWs, as this enhanced the temperature anomalies. A similar exclusion of SSWs were also conducted by Lu et al. (2008), indicating that these events

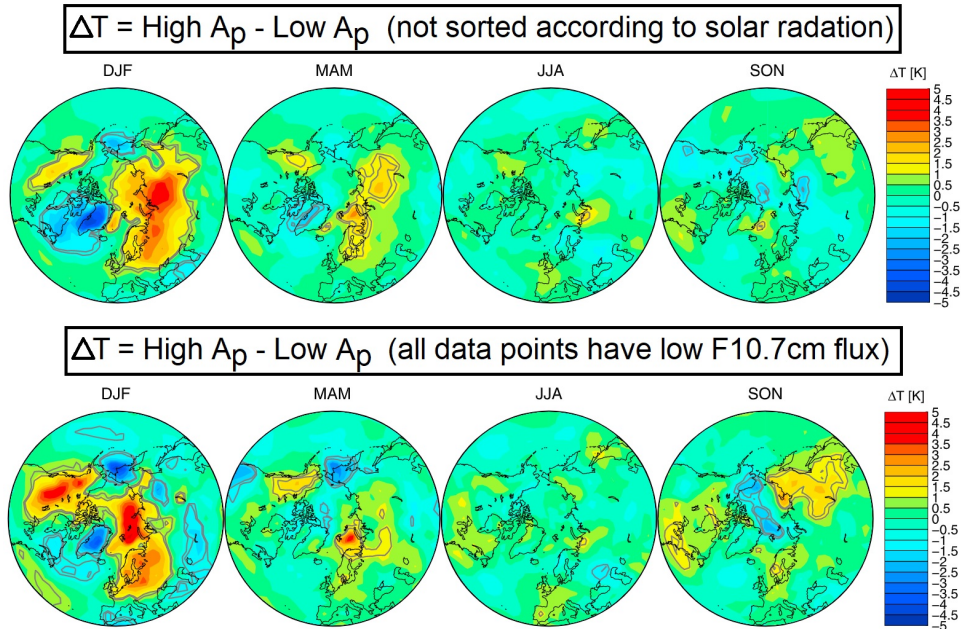


Figure 2.10: **Top panels:** Temperature anomalies at surface for all seasons calculated by  $\Delta T = \text{High } A_p - \text{Low } A_p$  for the time period 1957–2006 when SSWs are excluded. **Bottom panels:** Temperature anomalies at surface for all seasons calculated by  $\Delta T = \text{High } A_p - \text{Low } A_p$  when only low F10.7cm flux (65 – 120) data points are chosen for the time period 1957–2006. SSWs are also excluded in this case [Taken from Seppälä et al. (2009)].

where regarded as noise.

Model studies have further demonstrated the dynamical relationship between EPP related ozone loss and atmospheric changes. Baumgaertner et al. (2011) found geomagnetic activity causing local mesospheric heating and stratospheric cooling, coherent with results by Langematz et al. (2003), Rozanov et al. (2012) and Arsenovic et al. (2016). The local mesospheric heating is attributed to ozone’s radiative properties, while the stratospheric cooling and succeeding intensification of the PV is attributed to dynamical wave-mean-flow interactions.

Earlier studies also showed a discrepancy regarding the optimal atmospheric state for the Chemical-Dynamical coupling. While (Lu et al., 2008) and Seppälä et al. (2013) suggested stronger effects during the westerly QBO phase, Palamara and Bryant (2004) and Bochniek and Hejda (2006) reported stronger effects during the easterly QBO phase. Further investigations by Maliniemi et al. (2016, 2013) revealed that the discrepancy arose as different studies used QBO values at different altitudes. By showing that the Holton-Tan relation was systematically more valid for QBO at 30 hPa than QBO at 50 hPa, the QBO-E phase at 30 hPa was shown to favour the EPP impact. The studies proposed that the efficiency of planetary wave drag on the polar vortex is larger when the vortex is weaker (during QBO-E). Therefore, the changes in PV strength

related to ozone loss affect the deposition of planetary wave momentum more significantly in the QBO-E phase than in the QBO-W phase.

The direct effect was seriously considered as a potential climate influence after Andersson et al. (2014) found that local  $\text{HO}_x$  production due to EPP causes significant long term ozone variability (34%) in the mesosphere (70–80 km). Another study by Meraner and Schmidt (2018) used the coupled Max Planck Institute Earth System Model (MPI-ESM) to simulate and quantify the radiative forcing resulting from mesospheric ozone loss attributed to the direct effect, and stratospheric ozone loss attributed to the indirect effect. The direct effect resulted in mesospheric warming and stratospheric cooling during December, January and February, however, the results were not statistically significant. Rather, interesting results regarding the indirect effects emerged, as shown in Figure 2.11. Only December exhibited dynamically induced cooling (left panel) and strengthening of eastward zonal winds (right panel), similar to earlier findings (Baumgaertner et al., 2011; Langematz et al., 2003; Rozanov et al., 2012). The main response when averaged over the whole winter shows the opposite pattern, namely a net stratospheric warming, in line with the radiative transfer calculation model RRTMG (Figure 2.6). It is worth noting that the magnitude of the responses decreased after removal of SSWs, a divergence from prior studies reporting enhanced responses post-SSW exclusion.

An in-depth statistical study was further conducted by Tartaglione et al. (2020) to unravel the potential of falsely rejected null hypotheses being responsible for the surface impact of EPP found by Seppälä et al. (2009). The same data interval and sorting

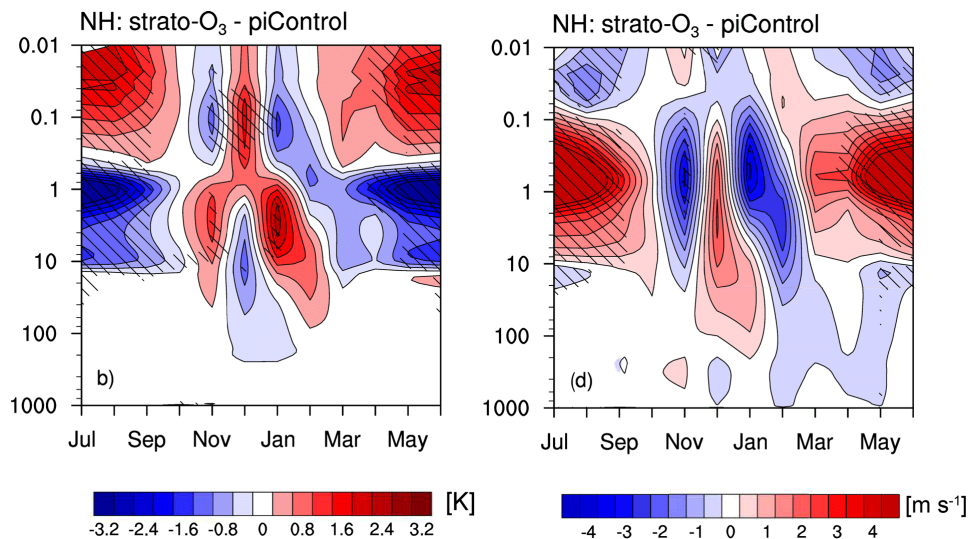


Figure 2.11: **Left panel:** Monthly mean temperature averaged between 60 and 90°N for the difference between simulation with stratospheric ozone reduction and control simulation. **Right panel:** Similar setup for zonal wind. Shaded areas show statistical significance at the 95% confidence level [Taken from Meraner and Schmidt (2018)].

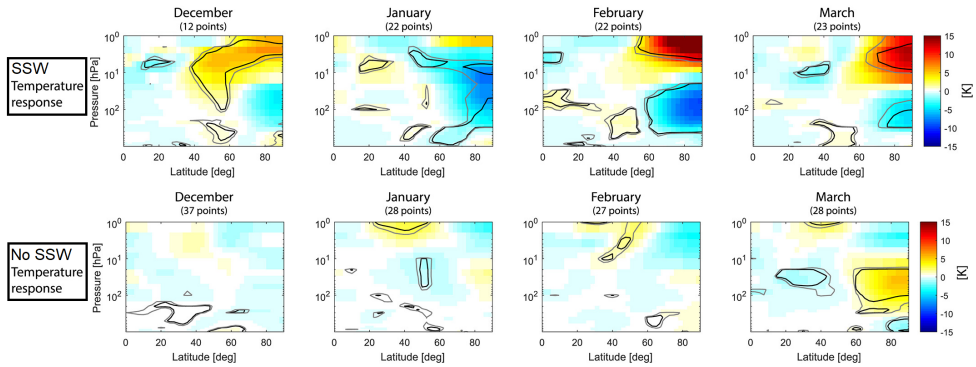


Figure 2.12: **Top panels:** Temperature response per standard deviation of  $A_p$  (through linear regression) for every December when an SSW occurs in either December or January, and for every January-March where an SSW occurs in either February or March. **Bottom panels:** The remaining winters where no SSW occurred. Statistical significance at the 95% confidence level is shown by black lines [Figure obtained from Asikainen et al. (2020)].

as Seppälä et al. (2009) was used focusing on the stratosphere (1–200 hPa). It was found that when accounting for temporal and spatial autocorrelation, no statistically significant results could be obtained at any stratospheric level. The study did not discourage future research on the mechanism, but suggested that it might be weak and consequently difficult to detect.

Using re-analysis data, Salminen et al. (2019) revealed that the zonal wind, temperature, and ozone were most significantly affected by geomagnetic activity when winters were sorted based on the  $QBO_{30\text{hPa}}$  value obtained 6 months in advance. The study found that the strength of the BDC reached a maximum for the same QBO sorting with similar time lag. It was suggested that the enhanced circulation leads to increased downward transport of  $\text{NO}_x$  and ozone, resulting in more ozone destruction and larger radiative and dynamical responses. In Salminen et al. (2020), during the easterly  $QBO_{30\text{hPa}}$  phase (measured in autumn), a significantly higher proportion of SSWs was found in winters with low geomagnetic activity, compared to winters with high geomagnetic activity. With previous analyses discarding SSWs as noise, a potential relationship was now suggested.

Using the combined re-analysis of ERA-40 and ERA-Interim spanning 1957-2017, and the geomagnetic index  $A_p$ , Asikainen et al. (2020) found a strong connection between NH atmospheric responses and EPP right before the initial onset of SSWs. Figure 2.12 shows the results with heat maps exhibiting the atmospheric temperature response to one standard deviation of  $A_p$ . In the top panels, all Decembers are selected where an SSW occurs in either December or January, while all January-March are selected where an SSW occur in either February or March. In the bottom panels, the remaining winters with no SSWs are chosen. Additionally, strongest anomalies were found with no lag for  $A_p$  in December and January, 1 month lag in February, and 3 months lag in March. The temperature responses are clearly magnified for winter months prior to SSWs, compared to winter months with no subsequent SSWs. Upper

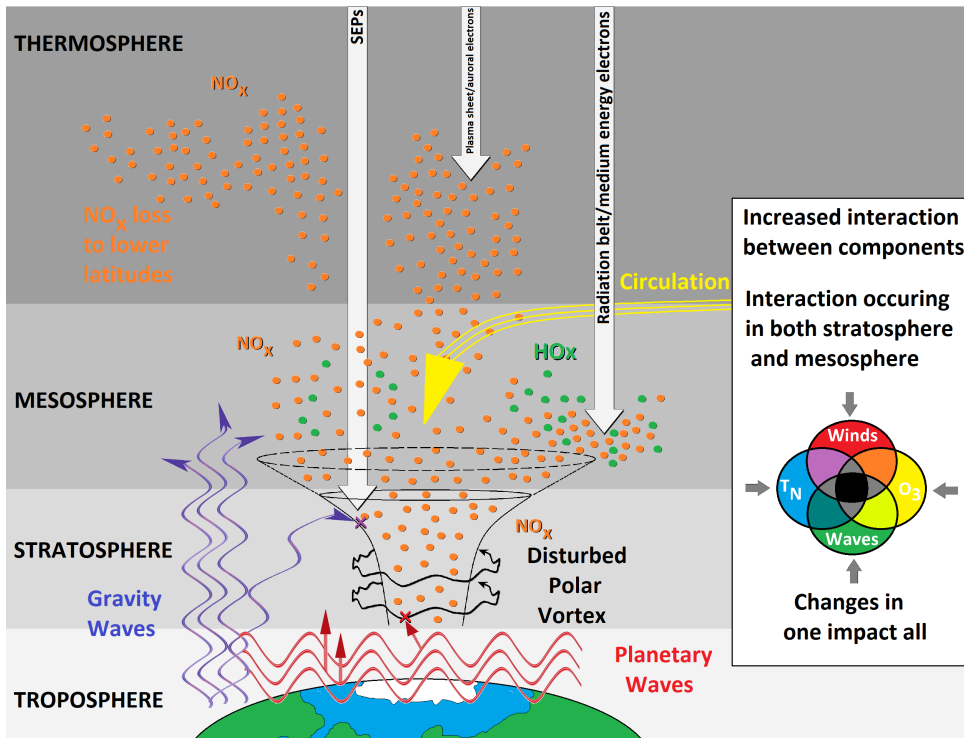


Figure 2.13: Updated hypothesis regarding the Chemical-Dynamical coupling. Here, the initial ozone loss related to EPP is hypothesised to have an increased dynamical impact when the PV is disturbed. Both direct and indirect effects are included.

stratospheric heating and lower stratospheric cooling is observed. Additionally, further investigations reported the maximum anomalies occurring 5–15 days prior to the initiation of SSWs.

Asikainen et al. (2020) suggested that increased planetary wave activity before the onset of SSWs favour enhanced wave-mean-flow interactions, which can dynamically amplify the initial strengthening of the polar vortex caused by ozone loss. This hypothesis was further complimented by a model study by Zúñiga López et al. (2022) which found that even weak ionization rates could modulate the mesospheric signal right before and during an SSW event. However, the study only had one ensemble member for the control and experiment run, and therefore cannot constitute reliable statistical evidence. Further, as SSWs are mainly hypothesised to be driven by planetary wave activity, Salminen et al. (2020) investigated the EPP influence on the northern polar atmosphere (zonal winds) during different latitudinal planetary wave propagation patterns. Responses comparable to Asikainen et al. (2020) were found when planetary waves propagated at mid-latitudes (50–52.5°) as opposed to polar latitudes (70.72°). It was suggested that planetary waves propagating at the southward flank of the PV either can be refracted away or toward the vortex, which can be controlled by small initial EPP-induced changes, while planetary waves propagating at polar latitudes are more

likely to get trapped and dissipate inside of the vortex.

Figure 2.13 summarizes the updated Chemical-Dynamical coupling based on the recent research. The key point, which also is the main investigative objective of Paper III, is the role of disturbed polar vortex conditions, and the possibility of disturbed conditions enhancing wave-mean-flow interactions leading to enhanced dynamical atmospheric impact.

## 2.2 The Mansurov effect

The Mansurov effect links the Interplanetary Magnetic Field (IMF)  $B_y$ -component to polar surface pressure anomalies in both hemispheres. The hypothesis is based on positive correlations observed between the IMF  $B_y$  and polar surface pressure in the SH, and negative correlations between the same variables in the NH (Mansurov et al., 1974). The steps involved in the mechanism are illustrated in Figure 1.2. Magnetic changes in the  $B_y$ -component of the solar wind induce an electric field which adds to the the polar ionospheric potential in each hemisphere and changes currents in the Global Electric Circuit (GEC). The  $B_y$ -induced currents, referred to as fair weather currents, are further hypothesised to change cloud formation processes by changing properties at the microscopic scales, which ultimately leads to macroscopic changes. Moreover, cloud properties changes are hypothesised to significantly affect the surface pressure in a predictable manner, yielding anti-symmetric surface pressure changes between the hemispheres. In the next sections, the background theory and physical principles of the Mansurov effect will be explained, followed by a literature review.

### 2.2.1 Solar Wind (Interplanetary Magnetic Field)

The Mansurov effect starts with the solar wind, and the magnetic changes of the  $y$ -component ( $B_y$ ) of the IMF. As described in section 2.1, the solar wind originates from the solar corona, the outermost layer of the Sun, and consists of ions and electrons continuously moving outwards in all radial directions. First described by Alfvén (1943),

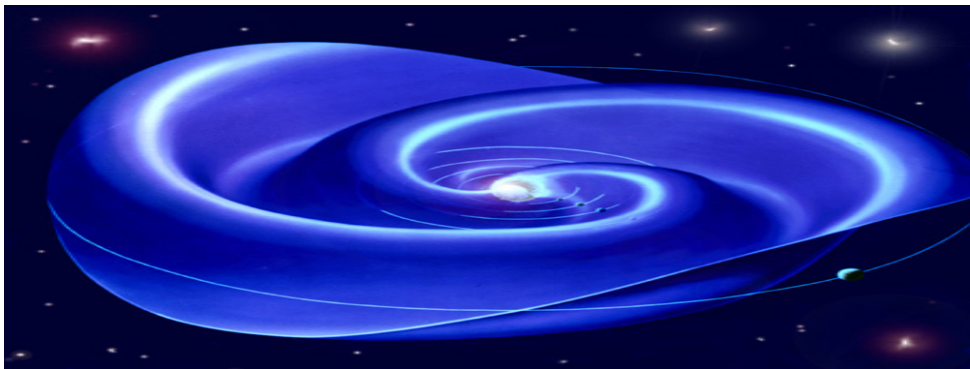


Figure 2.14: Artistic illustration of the HCS [Obtained from NASA: <https://www.nasa.gov/content/goddard/heliospheric-current-sheet>]



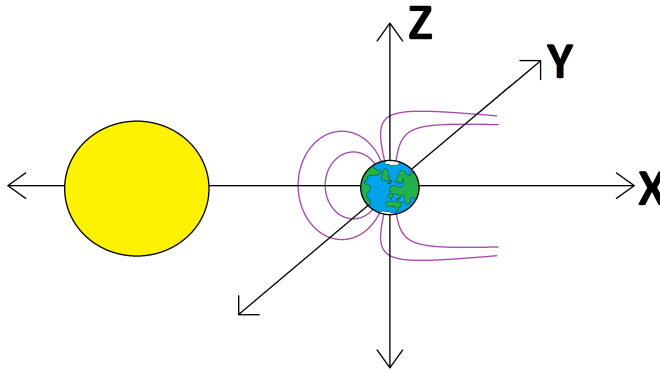


Figure 2.15: Illustration of the GSM coordinate system. The X-axis aligns with the Earth-Sun line, while the Z-axis aligns with the magnetic dipole axis. The Y-axis is perpendicular to both X and Z.

the solar wind has an inherent magnetic field, known as the IMF, which can be approximated to be frozen-in to and moving along with the plasma. The IMF is shaped as a spiral (known as the Parker spiral and first identified by Parker (1965)) due to the rotation of the Sun and the so-called "frozen-in" property of ideal MHD magnetic field lines. As such, the magnetic field lines connected to the Sun are dragged outwards in unison with the ejected plasma in a specific angular direction. The magnetic polarity of the source point on the Sun determines the magnetic polarity of the spiralling arms of the IMF.

The surface boundary encircling the Sun that separates the opposing magnetic polarities, is often called the heliospheric current sheet (HCS) (Hoeksema et al., 1983; Smith, 2001). An illustrative depiction of the HCS is given in Figure 2.14. By crossing the HCS, the magnetic polarity of the IMF changes. The shape of the current sheet is in constant dynamical evolution, however, the larger scale structures follow the solar rotational period of  $\sim 27$  days. Substantial structural changes are observed during the 11-year solar cycle (Hoeksema et al., 1983), as the Sun's magnetic field reverses during a cycle. The HCS represents the magnetic equator of the global heliosphere (Smith, 2001). Since HCS crossings are associated with changes in IMF polarity, these events should also have an associated connection to the Mansurov effect.

For the IMF observations, the standard Geocentric Solar Magnetospheric (GSM) coordinate will be used throughout the thesis. This convention is illustrated and described in Figure 2.15. It is the magnetic field strength along the y axis, denoted as  $B_y$ , that is hypothesised to be relevant for the Mansurov effect.

## 2.2.2 Global Electric Circuit

The GEC couples the electric fields and currents flowing in the magnetosphere, ionosphere and lower atmosphere (Siingh et al., 2007). As illustrated in Figure 2.16, thunderstorms and electrified clouds generate upward driven currents which help to main-

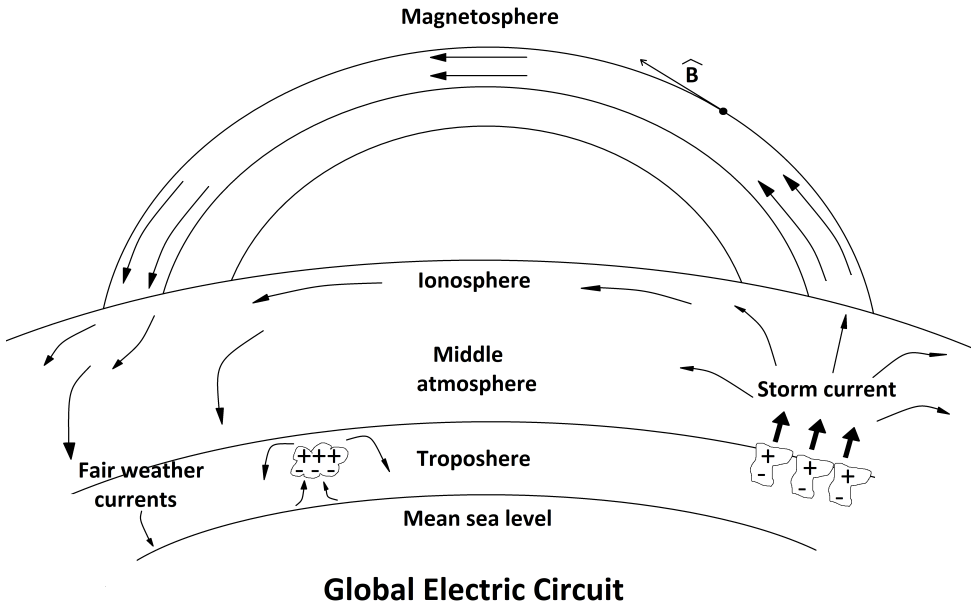


Figure 2.16: Illustration of the GEC. Arrows show direction of currents.

tain a potential difference of about 300 kV between the ground and ionosphere (ionosphere is at positive potential). Furthermore, these currents spread around the globe through the ionosphere and magnetosphere following geomagnetic field lines. In fair weather regions return currents flow, ultimately closing the circuit (Siingh et al., 2007). Due to the exponential increase of conductivity with altitude, most of this ionosphere-ground potential difference is found across the lowest 10 km of the atmosphere (Roble and Tzur, 1986).

### 2.2.3 External Influence on the Global Electric Circuit

During the Dungey cycle (the process for magnetic reconnection discussed in Section 2.1.1), field lines from Earth's geomagnetic field connects to the IMF. As the solar wind flows past the Earth, an observer stationed at Earth will observe an induced electrical field (Borovsky, 2016; Dungey, 1961). This is known as the motional electrical field, and can be expressed as

$$E = \frac{-[\mathbf{V} \times \mathbf{B}]}{c}. \quad (2.7)$$

Along the open magnetic field lines, where the IMF has reconnected with Earth's magnetic field, transmission of electric fields can occur via, e.g., propagation of Alfvén waves. Alfvén waves are plasma oscillations in response to a restoring force provided by tension of the magnetic field lines (Alfvén, 1942). Additionally, electric fields can be transmitted along conducting magnetic field lines as a result of potential differences established between two points, either in the ionosphere or the magnetosphere (Blanc, 1988). In simpler terms, assuming an IMF component along the  $y$  axis, and the velocity of the solar wind in the  $x$ -direction, the motional electric field (Equation 2.7)

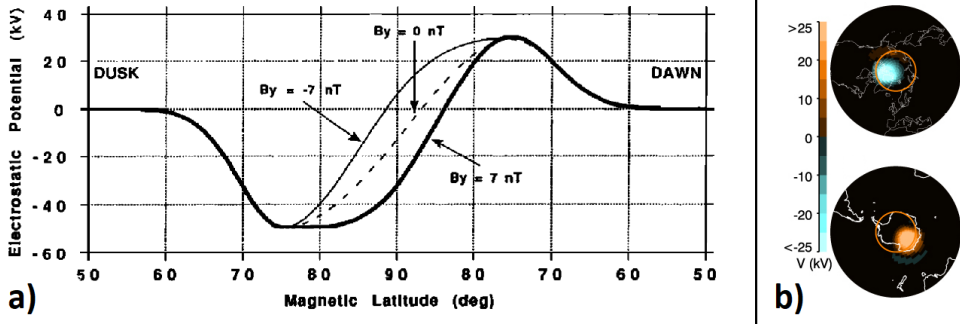


Figure 2.17: **a)** Average variations in the ionospheric polar cap potential measured along the dawn-dusk line in the NH with  $B_z$  negative. The electrostatic potential in respect to magnetic latitude for three different  $B_y$  values are shown [Taken from Tinsley and Heelis (1993)]. **b)** Map plot of the resulting electrostatic potential anomaly obtained from averaging days with  $B_y$  positive and subtracting the average of the days with  $B_y$  negative for both hemispheres. The result represents the signal seen when averaging all days in the time period 1999–2002 with  $B_y > 3$  nT and subtracting the average of all days with  $B_y < -3$  nT. The anomalies, which are centered around the geomagnetic poles, are in the range -30 kV to +30 kV [Taken from Lam et al. (2013)].

will point in the  $z$  direction. In an ideal scenario, with transmission occurring strictly along magnetic field lines, this  $z$  axis-aligned electric field will impose anti-symmetric perturbation on the ionospheric potential between the hemispheres. This occurs as the ionospheric potential points in the direction ionosphere-ground, leading to oppositely directed ionospheric potentials between the poles (oppositely signed  $z$  components with respect to the GSM coordinate system). With the superimposed motional electric field having a  $z$  component in the same direction for both poles, it then follows that the ionospheric potential will be perturbed in an anti-symmetric manner.

Illustrated in Figure 2.17 a) is a result of the electrostatic potential in the NH for a constant negative  $B_z$  and three different  $B_y$  components (-7, 0, 7 [nT]). The figure is from Tinsley and Heelis (1993) which uses an analytical model by Hairston and Heelis (1990) derived from an empirical fit to a large data base of satellite measurements to obtain the results. As can be seen from the figure, when integrating the electrostatic potential curve for the two oppositely signed  $B_y$  modulations (-7 and 7 [nT]) over all magnetic latitudes in the NH, there is a net positive (negative) perturbation for  $B_y$  negative (positive). In the SH, the same pattern occur, with opposite  $B_y$  values. The ionospheric potential perturbations for both hemispheres are shown in Figure 2.17 b).

The influence of IMF  $B_y$  on the ionospheric potential is in general well researched, including the observational studies and empirical models of Frank-Kamenetsky et al. (2001); Kabin et al. (2003); Pettigrew et al. (2010); Weimer (1996, 2001), and many others. Even though the transmissions of electrical fields is not a straightforward process, the simplistic conceptual view discussed above can be assumed in respect to the Mansurov hypothesis. Therefore,  $B_y$  will work as a proxy for perturbations in the ionospheric potential.

## 2.2.4 Global Electric Circuit: Fair Weather Current

Based on Ohms law ( $V = RI$ ), it is clear that changing either the earth-ionosphere conductivity ( $1/R$ ) or the earth-ionosphere electrical potential ( $V$ ) will change GEC and the fair weather currents ( $I$ ) in the system.

Both internal (thunderstorm generator) and external generators modulate the fair weather current on a day to day basis. External influence includes variations induced by e.g. IMF  $B_y$  as discussed above. In addition, external influences also includes variations in conductivity ( $1/R$ ) due to ionization of the atmosphere, which can originate from sources such as Galactic Cosmic Rays (GCR) or deeply penetrating solar particles. In fact, changes related to ionization are much larger than the changes related to IMF  $B_y$  (Slyunyaev et al., 2015; Tinsley, 2022). Therefore, investigating the connection between ionization rates and surface pressure could offer valuable insights into the impact of the GEC on the atmosphere. Furthermore, a more general understanding of the relationship can be achieved by analyzing the correlation between atmospheric effects and measurement of the Ionosphere-Earth vertical electric field (field set up by the ionospheric-ground potential). These measurements do actually exist, but are unfortunately quite uncertain. Due to local meteorological conditions associated with high wind speeds lifting snow and ice particles into the air, the measurements are significantly affected, ultimately making it hard to produce continuous reliable data series (Burns et al., 2017, 2012). Thus, the IMF  $B_y$  acts as a reasonable indicator/proxy for changes (about  $\pm 10\%$  in respect to the total) in the ionospheric potential in both hemispheres.

## 2.2.5 Influences on Microphysical Processes in Clouds

Space charge density can accumulate due to the non-uniformity of the electrical conductivity of the atmosphere. Here, space charge density,  $p$ , is defined as the net difference between positive and negative charge per unit volume. Calculations show that attachments of ions to droplets can decrease the conductivity inside clouds by a factor of 3 to 40 compared to the conductivity in clear air (Griffiths et al., 1974; Pruppacher and Klett, 1997, p. 802). Figure 2.18 illustrates the ideal case of space charge accumulation inside clouds. Assuming conductivity of air being larger than the conductivity of clouds ( $\sigma_a > \sigma_c$ ), and assuming that space charge density accumulates in horizontally stratified layers, the charge separation on a fundamental level occurs as a consequence of the continuity principle:

$$\nabla \cdot \mathbf{J} = \frac{\partial J_z}{\partial z} = -\frac{\partial p}{\partial t}$$

(2.8)

where  $J_z$  is the vertical current density directed downwards, and  $p$  represents space charge density. The conservation of charge state that the divergence of the current density is equal to the negative rate of change of the space charge density. As the

conductivity of the cloud is less than the conductivity of air, the current density  $J_z$  inside clouds will ultimately be less than the current density in the air according to Ohm's law for an applied electric field:

$$E = \frac{J}{\sigma}, \tag{2.9}$$

where  $\sigma$  represents the conductivity. From the continuity equation (Equation 2.2.5), this reduction in current density  $J_z$  at the boundary air-cloud leads to a negative term on the left hand side. This results in a positive rate of change of space charge density in this area. At the lower boundary (cloud-air), the same situation arises, only reversed, resulting in a negative rate of change of space charge density.

In turn, the accumulating space charges give rise to an additional electric field,  $E$ , directed downwards inside the cloud. This field superimposes on  $E_z$ , ultimately combating the decrease in conductivity inside the cloud, which leads to a steady current density  $J_z$  through the whole medium air-cloud-air. Thus, one can also relate the space charges to the Gauss's divergence theorem:

$$\nabla \cdot E = \frac{\rho}{\epsilon_0} \tag{2.10}$$

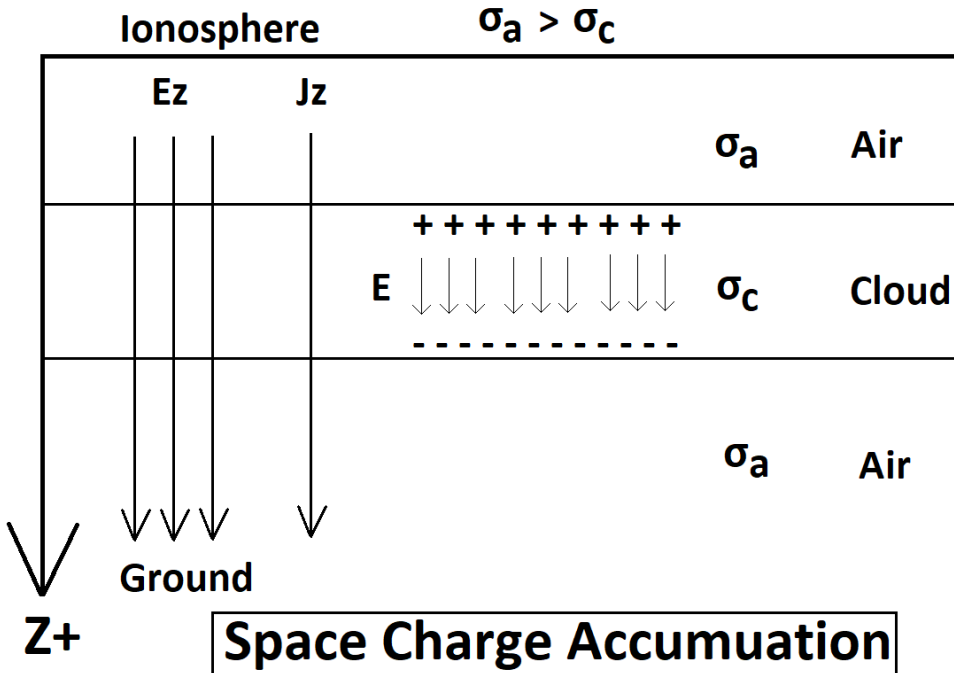


Figure 2.18: Illustration of space charge accumulation in an ideal case of clouds with lower conductivity than the air, where horizontal stratification is assumed. Accumulation of positive charge will occur near the top boundary of the cloud, while accumulation of negative charge will occur near the bottom boundary.

with  $\epsilon_0$  being the permittivity of free space, and  $E$  a three-dimensional vector. By substituting  $E$  through Ohm's law (Equation 2.9) and assuming that space charge accumulates along horizontally stratified layers, the space charge,  $p$ , can be written as:

$$p = \epsilon_0 J_z \frac{\partial}{\partial z} \left( \frac{1}{\sigma(z)} \right) \quad (2.11)$$

where  $z$  is the distance measured along the direction of the current density  $J_z$ . As  $J_z$  is assumed constant due to  $E$  superimposed on  $E_z$  inside the cloud, this term is placed outside the derivative. This function shows that at the boundary air-cloud, with  $\sigma(z)$  decreasing (conductivity is less inside clouds than air), the space charge  $p$  is positive, while in the boundary cloud-air, with  $\sigma(z)$  increasing, the space charge  $p$  is negative. Hence, the accumulation of space charge in this ideal case is directly proportional to the vertical current density  $J_z$ . It is worth noting that space charge density accumulation also occurs in cloud free regions, as conductivity gradients exist all the way through the atmosphere as a consequence of the exponentially increasing conductivity with altitude. However, the quantities are relatively small compared to areas of higher particle/droplet (clouds) concentration (Nicoll, 2012; Tinsley, 2022).

Several aircraft measurements confirm the accumulation of space charge near cloud boundaries. A multiple site comparison by Nicoll and Harrison (2016) has shown that cloud tops and cloud bases charge asymmetrically with net charge averages of  $+32 \text{ pC m}^{-3}$  and  $-24 \text{ pC m}^{-3}$ , respectively. In addition, observations have also shown that this space charge is reflected in the aerosol droplet distribution, with the average net charge on droplets forming near cloud tops reaching peaks of  $85e$ , and average net charge on droplets forming near cloud base being measured to  $-40e$  (Beard et al., 2004). It is noted that both of these investigations show some redistribution of charges compared to the ideal case of cloud top having the absolute highest peak, and cloud base having the absolute minimum. This is attributed to updrafts and downdrafts due to warming and cooling of air near cloud base and cloud top. More extensive review of measurements of droplet charge distribution and space charge in clouds are given by Nicoll (2012); Tinsley (2022).

Generally, the science of cloud nucleation, defined as the formation of water droplets and ice crystals, is not well understood. The process mainly occurs when tiny particles, known as cloud condensation nuclei (CCN), provide a surface for water vapor to condense around (e.g. Brock et al., 1995; Clarke, 1992; Kulmala et al., 2004a). However, it is uncertain if this process is mainly neutral, or dependent on atmospheric ions affected by atmospheric electricity. In an experiment using the CLOUD (Cosmics Leaving Outdoor Droplets) chamber at CERN, it was found that a considerable fraction of nucleation involves ions, nevertheless, only a weak dependence was found on the ion concentration (Dunne et al., 2016). In contrast, other experimental and theoretical investigations have suggested that increases in the ion concentration do in fact lead to significant increases in CCN (e.g. Kulmala et al., 2004b; Lee et al., 2003; Svensmark et al., 2017).

Tinsley (2022) lists electro-scavenging and electro-anti-scavenging as processes responsible for affecting cloud properties related to space charge accumulation. Electro-

scavenging is caused by the attractive Coulomb force. With large droplet/particles sizes, and also large electrical forces, this acts to attract droplets/particles of opposite charge, leading to increased rates of collision, and reduced droplet/particles concentration. If charged particles are captured by droplets, these can act as ice nucleating particles, ultimately changing opacity and thereby radiative properties of the clouds. Electro-anti-scavenging is the reversed action. Here, the repulsive force between droplets/particles of same charge acts to decrease the rate of collisions. This process is mainly dominant in areas of strong space charge separation, and with an excess of same sign droplet/particles. As there is more repulsive than attractive interactions in these regions, the collisional loss of smaller particles is reduced. This can allow small and ultrafine particles the time to grow by e.g. vapor deposition, which can ultimately increase cloud opacity. It is hypothesized that the microphysical changes begin in less than a day, while it is expected to take days for the accumulative effect to change cloud radiative forcing (Frederick et al., 2019; Tinsley et al., 2021).

Though large uncertainties prevail, models by Khain et al. (2004) and Tinsley et al. (2001, 2006), which consider the effects of charged droplets in weakly electrified clouds, indicate that electro-scavenging and electro-anti-scavenging may be of importance for the evolution of clouds. In addition, observations showing positive correlations for droplet size in the presence of electric fields exists (Mudiar et al., 2021). However, it should be noted that the latter mentioned study investigated strongly electrified clouds, with internal charging mechanisms related to other factors (storms and thunder clouds) than space charge accumulation due to the vertical current density only.

## 2.2.6 Cloud opacity, radiation budget and surface pressure

In general, when the opacity of clouds change the radiation budget also changes, which in turn affects the atmospheric system. However, the complexity of the climate system prevents straightforward deduction of how different regions are affected by localized changes in cloud properties. In addition, investigating cloud properties over extended time periods in polar regions is challenging due to the equipment involved in such measurements.

Regarding the hypothesised pathway of the Mansurov effect summarized above, studies have examined the relationship between both IMF  $B_y$  and  $E_z$  measurements, and longwave radiation (Frederick and Tinsley, 2018; Frederick et al., 2019). These studies used  $E_z$  measurements for the time periods 1998–2001 and 2006–2011 (these data are described by Burns et al. (2017)), as well as longwave radiation data acquired from a Precision Infrared Radiometer-Pyranometer operated by the NOAA Earth Systems Research Laboratory. Frederick and Tinsley (2018), focusing on Antarctica, found that increases in  $E_z$  leads to significant increases in longwave radiation at a lag of 1 days. This correlation is only found during the absence of sunlight (polar night). In Frederick et al. (2019), focusing on northern latitudes, a marginally significant negative correlation at the 95% level is found at Alert, Canada ( $3^\circ$  from the magnetic pole), between the IMF  $B_y$  and downward longwave irradiance with a three-day lag. This study also investigated the longwave irradiance at Barrow, Alaska ( $20^\circ$  from the magnetic pole),

where no connection to the IMF  $B_y$  was found. The study concludes that if IMF  $B_y$  changes are able to change cloud opacity (which leads to changes in irradiance), these changes are localised to areas close to the geomagnetic pole. Further investigations of the relation between IMF  $B_y$  and longwave irradiance were conducted by Tinsley et al. (2021). The study focused on Alert, Canada, as this was the area exhibiting the significant correlations found by Frederick et al. (2019). Using similar longwave irradiance data obtained by NOAA over 2004–2015, the strongest correlations between the IMF  $B_y$  and cloud properties were found during winter with irradiance changes lagging the IMF by 3–4 days. This study also found that correlation coefficients are largest when the IMF is emerged in a 2-sector structure, rather than a 4-sector structure. When the IMF exhibit a 2-sector structure, it fluctuates with a periodicity of roughly 27 days, while a 4-sector structure fluctuates with a 13.5-day periodicity. Nevertheless, there is no statistical assessment or uncertainty limits on the correlation coefficients. Tinsley (2022) further hypothesised that the effect might be dependent on extended periods of 2-sector structure IMF, as this might nudge uncorrelated pressure oscillations into partial synchronization (Tinsley (2022); Tinsley et al. (2021) also found correlations of nearly equal amplitude as those seen during winter, but with no clear relationship between the forcing and response.

More recently Zhang et al. (2022) have investigated the relationship between IMF  $B_y$  and noctilucent clouds (NLCs) in both hemispheres. They find that the mean ice particle radius inside these mesospheric clouds positively correlate with IMF  $B_y$  in the SH, with negative correlations found in the NH. The study is conducted for all summers in the time period 2007–2017, and the results are stated to be statistically significant. In addition, albedo, ice water content and frequency of occurrence of NCLs are also found to positively correlate with IMF  $B_y$  in the SH, while no significant correlations were found for these same parameters in the NH.

However, the mentioned studies have not examined the correlation between the observed anomalies in longwave radiation (and cloud properties) and surface pressure or temperature. Further research is needed here to develop a more complete understanding. More generally, Lubin et al. (1998) conducted a simulation study using different sizes of particles in clouds ( $10\mu\text{m}$  in control vs distribution of 10 and  $40\mu\text{m}$  in experiment) to investigate the relationship between cloud opacity and atmospheric temperature anomalies. The results show that cloud opacity can have a significant impact on tropospheric temperatures (changes of 1–2 K). In addition, the anomalies were stronger for longwave radiation, indicating that the effect is stronger during winter. As the results of Tinsley et al. (2021) also show the largest correlation values between IMF  $B_y$  and cloud opacity during winter time, these findings seem to line up in favour of the Mansurov effect. There has also been an extensive review of the current state of knowledge about tropospheric clouds in Antarctica, however, there is no research included analysing the relationship between cloud opacity and pressure anomalies (Bromwich et al., 2012).



## 2.2.7 Research on the Mansurov Effect

The main idea behind the Mansurov hypothesis is that the IMF  $B_y$  component superimposes an electric field in an anti-symmetric manner between the polar hemispheres. This leads to changes in the vertical current density  $J_z$  which again lead to changes in the accumulation of space charge in the atmosphere, particularly around the boundaries of clouds. This further affects different processes (electro-scavenging and electro-anti-scavenging) which are assumed to be important in determining cloud properties such as opacity. The change in cloud opacity in each hemisphere links to anti-symmetric pressure anomalies at the surface level. Evidence that might be found by measuring the changes in microphysical properties of clouds, and their relationship to localized surface pressure anomalies, remains elusive because of the difficulty of making relevant measurements. Nevertheless, this absence of evidence does not invalidate the hypothesis. This section covers the research specifically done for the Mansurov effect.

The Mansurov effect was first proposed in 1974, after Mansurov et al. (1974) found correlations between polar surface pressure and the IMF  $B_y$  component in both hemispheres for the year 1964. The effect manifested as a positive pressure anomaly occurring in the SH for days with positive  $B_y$ , and negative pressure anomalies occurring at days with negative  $B_y$ . The opposite pattern was seen in the NH, as illustrated in Figure 2.19. The whole period 1958–1964 displayed evidence of this IMF modulation of pressure in both hemispheres, with maximum pressure differences observed at the peak of the maximum phase of the solar cycle (1960). In addition, synchronous behaviour between the meridional wind direction and the IMF  $B_y$  component was also found.

Decades later, Tinsley and Heelis (1993) and Tinsley (2000) developed the theoretical framework (section 2.2.5) which connects the IMF  $B_y$  to microphysical cloud changes through the global electric circuit. Burns et al. (2007, 2008) studied the link of IMF  $B_y$  to polar surface pressure changes and showed that the Mansurov associated responses were present in surface pressure data obtained in Antarctica (Vostok) over the time period 1998–2002. In addition, measurements of the vertical electrical field  $E_z$  (which acts as a proxy for  $J_z$ ) were shown to also correlate with the surface pressure for the same time period. The  $E_z$  measurements excluded the IMF contribution by use of the Weimer (1996, 2001) models. Thus, the contribution to  $E_z$  by the internal thunderstorm generator was estimated. The correlations for  $E_z$  and pressure were larger than the correlations seen for IMF  $B_y$ , which is expected as the IMF  $B_y$  is only

	SH	NH
By+	P+	P-
By-	P-	P+

Figure 2.19: Illustration of the sign of polar surface pressure anomalies in each hemisphere in response to the  $B_y$  component.

one of many sources of variability of  $J_z$ . In addition, the sign of the pressure responses from estimates of  $E_z$  were also coherent with the  $J_z$  perturbations caused by IMF  $B_y$  in both hemispheres. However, some strange features emerged, as illustrated in Figure 2.20. The two right panels show the results of a lead-lag regression analysis between the measurements of the vertical electric field  $E_z$  and surface pressure at the Antarctic coast (top) and at Arctic (bottom) for the time period 1998–2001. In both hemispheres, the pressure response leads  $E_z$  by two days. In the right panel, the same analysis is performed, only with IMF  $B_y$  and surface pressure, and for the extended time period 1995–2005 at Antarctic above  $83^\circ$  mlat. The pressure peaks two days before the maximum peak in IMF  $B_y$  which occurs at day 0. Not shown are lead-lag regression results for  $E_z$  and surface pressure at the Antarctic plateau. Here, the surface pressure lags  $E_z$  by 3 days, which is more in line with the Mansurov hypothesis, as the micro-physical properties of clouds are hypothesised to take days to accumulate into macro-physical changes (Frederick et al., 2019; Tinsley et al., 2021).

Burns et al. (2007, 2008) justified the forcing lagging behind the response as being within the uncertainty limit of a day zero lag. Alternatively, a lag of -2 days could be reasonable if the mechanism is non-linear and have a maximum threshold of where it shuts of, or even reverses, even though additional forcing is experienced. In addition, the 27-day cycle evident in the pressure responses in both hemispheres after applying the lead-lag regression method was highlighted as additional evidence for a physical link between the IMF  $B_y$  and polar surface pressure. However, as will be discussed later (main results from Paper I), this 27-day cycle occurs as a statistical artefact. It should also be noted that these analyses did not have a thorough statistical testing regime, and relied on the  $t$ -test and standard deviation to the mean.

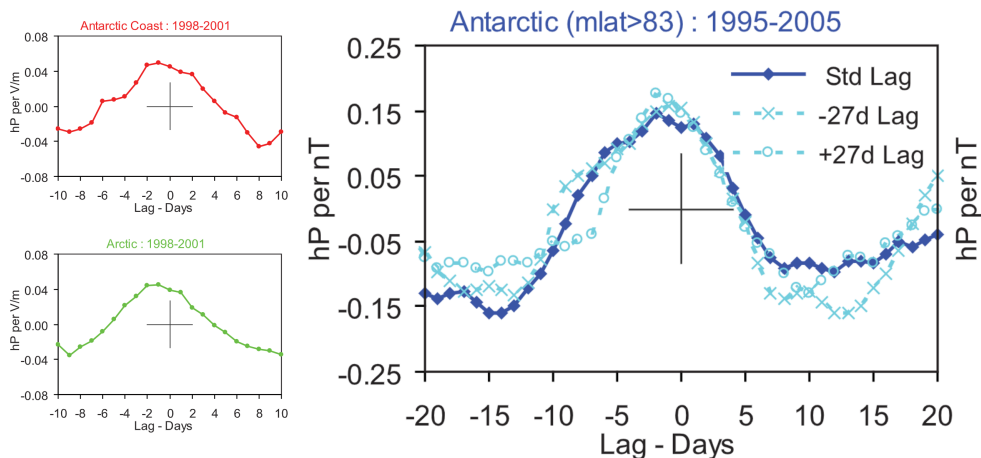


**Figure 2.20:** *Left panels:* Lead-lag linear regression analysis between measurements of  $E_z$  and surface pressure at the Antarctic coast (top) and at Arctic (bottom) for the period 1998–2001. **Right panel:** Same analysis, only for IMF  $B_y$  and surface pressure at Antarctic for the period 1995–2005. The dark blue line shows the responses in respect to day 0, while the light blue lines, marked with x and o, shows the response curve shifted -27 and +27 days, respectively [Taken from Burns et al. (2008)].

Lam et al. (2013, 2014, 2018) continued the investigation on the Mansurov effect. Lam et al. (2013) proposed that the Mansurov effect also has a mid-latitude influence, and is not confined to polar latitudes. In their work, NCEP/NCAR reanalysis data at 12 UT was used, and the study was conducted using the same time period (1999–2002) as the investigations by Burns et al. (2007, 2008). Figure 2.21 shows the zonal mean pressure as function of latitude averaged over days with  $B_y > 3$  nT (red line) and days with  $B_y < -3$  nT (blue line). The pressure anomalies were significant at the 1% level poleward of  $58^\circ\text{S}$  and  $50^\circ\text{N}$  by usage of Wilcoxon Rank-Sum (WRS) test. This is a non-parametric test of the null hypothesis assuming that the two populations of pressure measurements have the same mean of distribution, against the hypothesis that they differ. A field significance test was also applied according to a method by Wilks (2006), which is the precursor of the FDR-method developed for atmospheric applications by Wilks (2016) (this method will be discussed in detail in Section 3.3). Further, an investigation of the Rossby wave structures at mid latitudes was conducted, ultimately concluding that midlatitude atmospheric phenomena are also affected by the proposed IMF  $B_y$  mechanism. In Lam et al. (2014), the same methods were applied over the same time period (1999–2002). This study examined the altitude extent of the pressure anomalies, however, limited to Antarctica. It concluded that the pressure anomalies originate in the lower troposphere ( $\sim 1$  day) and propagated upwards reaching the tropopause in  $\sim 6$ – $8$  days. (The result leading to this conclusion is shown in the left panel of Figure 2.22.) Lam et al. (2018) investigated the same time period was once again investigated for Antarctica, with the study focusing on temperature anomalies. In agreement with Lam et al. (2014), the temperature anomalies were found to originate in the lower troposphere, and propagate upwards (right panel of Figure 2.22). All results were found to be significant at the 1% level. It should be noted that in Lam et al. (2018), a 27-day cyclic responses occurring in the results of Lam et al. (2014, 2018) is once again highlighted as additional evidence of a physical link. The results from Lam et al. (2014, 2018) exhibiting this cyclic response can also be seen in both pan-

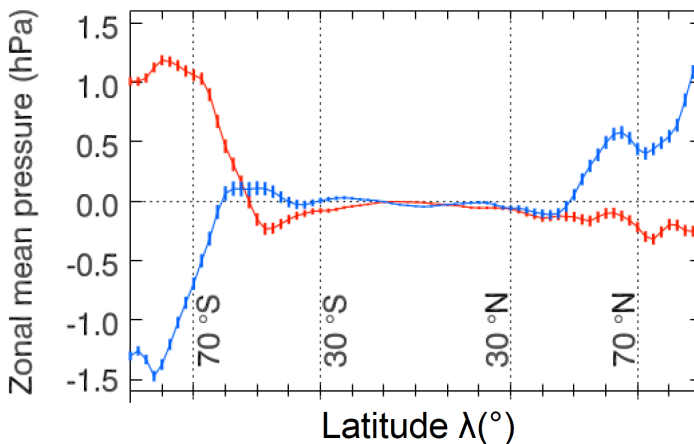


Figure 2.21: Red (blue) line represents the average over days with  $B_y > 3$  nT ( $B_y < -3$  nT). Data covers the time period 1999–2002 [Taken from Lam et al. (2013)].

els of Figure 2.22. Shortly after, the study of Freeman and Lam (2019) also focused on the temperature responses related to IMF  $B_y$  for the 1999–2002 period in Antarctica. Their investigation focused on interannual variations, and found the highest temperature anomalies to occur in autumn ( $3.2^\circ\text{C}$ ), followed by winter ( $2.4^\circ\text{C}$ ), spring ( $1.6^\circ\text{C}$ ) and summer ( $0.9^\circ\text{C}$ ).

Zhou et al. (2018) looked for the presence of the Mansurov effect during a new time period, 2005–2016. Their study used reanalysis data from the National Atmospheric and Oceanic Administration (NOAA), and analysed the zonal mean pressure by averaging all days with  $B_y > 3$  nT and subtracting from this the average of all days with  $B_y < -3$  nT. These results can be seen in the right panel of Figure 2.23. In the left panel, the more well researched period of 1995–2005 is shown for comparison. However, the dotted lines mark the uncertainty estimate, which only signifies one standard deviation including about 68% of all values. Two standard deviations would make the results statistically significant at the 95% level. Thus, it is questionable if the response seen for 2006–2015 is statistically significant. Further, by using the same  $E_z$  time series as Burns et al. (2008), which covers the time period 1998–2001, the latitudinal extent of the surface pressure response to the internally generated  $E_z$  were investigated. Similar to the double superimposed technique used when handling IMF  $B_y$ , the zonal surface pressure on days with high and low  $E_z$  were first averaged, before assessing their difference. The result, which can be seen in Figure 2.24, is also known as the Burns effect. Higher values of  $E_z$  represents an increased downward current density  $J_z$ , and lead to positive pressure anomalies in both hemispheres. In the Mansurov hypothesis, the IMF  $B_y$  component that leads to an increase in the ionospheric potential, and

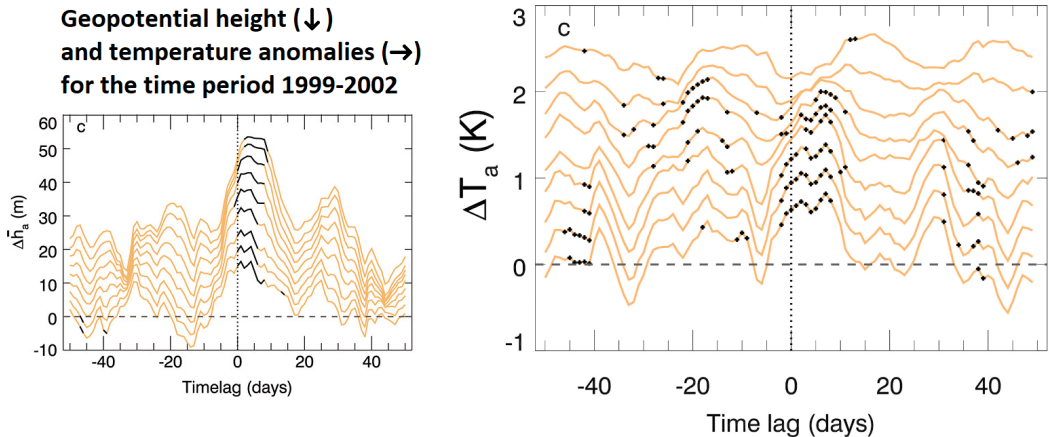


Figure 2.22: **Left panel:** Geopotential height for days with IMF  $B_y > 3\text{nT}$  subtracted days with IMF  $B_y < -3\text{nT}$  for multiple lead lags [Taken from Lam et al. (2014)]. **Right panel:** Same analysis as in the left panel, only with temperature as the response variable [Taken from Lam et al. (2018)]. In both figures, the different lines represent the hPa levels 1000, 925, 850, 700, 600, 500, 400, 300 and 250. The black lines and dots represent statistical significance at the 5% level. All curves can be seen to exhibit a clear 27-day cycle. The results also show that the anomalies originate in the lower troposphere and propagate upwards.

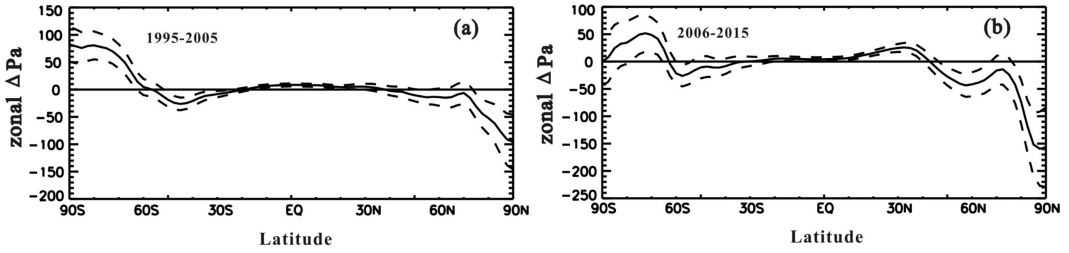


Figure 2.23: **Left panel:** Zonal mean surface pressure for days with IMF  $B_y > 3$  nT subtracted days with IMF  $B_y < -3$  nT for 1995–2005. **Right panel:** Same analysis, only for the time period 2006–2015. The dotted lines signify the uncertainty estimate given as one standard deviation of the mean [Taken from Zhou et al. (2018)].

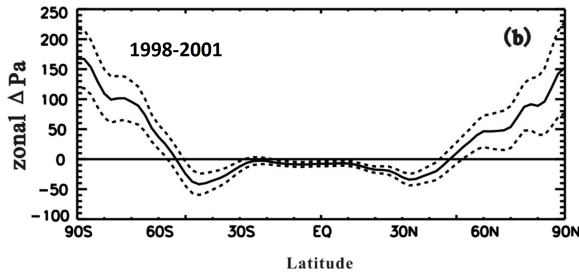


Figure 2.24: Latitudinal pressure response to the internally generated  $E_z$  for the time period 1998–2001. The dotted lines indicate the uncertainty estimate given as one standard deviation of the mean [Taken from Zhou et al. (2018)].

consequently  $J_z$ , is also the component that is related to a positive pressure anomaly. Though only one standard deviation from the mean was used as the uncertainty limit, it is still compelling evidence in favour of the Mansurov effect that the pressure have a consistent response to both the internally and externally driven changes in  $E_z$ . Furthermore, Zhou et al. (2018) also investigated seasonal variations of the Burns effect, with findings indicating the strongest response in local winter for both Arctic (DJF) and Antarctic (JJA). These results are in line with the findings of Freeman and Lam (2019), which found the Antarctic winter to exhibit the second strongest temperature anomalies ( $2.4^\circ$ ) after autumn ( $3.2^\circ$ ).

In Karagodin et al. (2022a), the Mansurov effect was investigated with the SOCOLv3 Chemistry-Climate Model. The analysis assumed a linear dependence of changes in  $J_z$  and changes in autoconversion rate. The autoconversion rate is the rate at which water mass in the form of cloud droplets forms raindrops. The study found that even small changes  $\pm 12\%$  lead to larger-scale pressure anomalies in good agreement with the observational results of the Mansurov effect at both high and mid latitudes. Reservations were, however, made as an unrealistic assumption of constant induced changes in the autoconversion rate was applied. The study also highlighted the need for more ensemble members to properly assess the statistical significance of the results. In a follow up study, Karagodin et al. (2022b) tested if the mechanism involved

in the Mansurov effect is dependent on the rate of droplet coalescence, meaning the process by which two or more droplets or particles merge during contact to form a single daughter droplet/particle. The SOCOLv3 Chemistry-Climate Model and real IMF  $B_y$  data for the period 1999-2002 was used. In the experiment runs, a linear dependence between the IMF  $B_y$  and coalescence rate was also assumed, while no IMF  $B_y$  was used in the control runs. The study found no robust or significant signal when comparing the experiments to the control runs. The standard deviation of anomalies in surface pressure and temperature between ensemble members were consistent with the magnitude of the effects seen in the control run, suggesting that the internal variability of the model is larger than the IMF  $B_y$  induced effect.



# Chapter 3

## Statistical Approaches

The level of statistical testing vary in scientific research. For instance, if an astronomer claims to have discovered a star, the statistical significance of the discovery is usually not important. However, when the reality of the phenomenon in question is less binary and dependent on multiple variables, the need to infer statistical significance increases. When studying how space weather impacts atmospheric dynamics, a system dominated by noise and spatial or temporal interdependence, the need for appropriate statistical inference is crucial. This section will first discuss a possible bias occurring when deploying specific analyses methods, which can in turn lead to erroneous conclusions. Secondly, the statistical methods used throughout the thesis to account for temporal and spatial autocorrelation will be elaborated upon. Finally, a discussion will be provided on how to handle the problem of multiple null hypotheses testing.

### 3.1 Artificial periodicity produced by methods

The main analysis tools used throughout this thesis are time-lagged cross-correlation (TLCC) and the superimposed epoch (SE) method. Both methods are used to identify relationships between two time-series variables as well as associated time lags. Additionally, both methods are also prone to the creation of artificial periodically biased results if either the forcing or response time-series is periodic. Here, this bias will be derived mathematically for TLCC and visualized using a simulation experiment for both TLCC and SE.

#### 3.1.1 Derivation

The Pearson linear correlation coefficient is defined as

$$r_{xy} = \frac{\sum_{i=1}^N (x_i - \bar{x})(y_i - \bar{y})}{\sqrt{\sum_{i=1}^N (x_i - \bar{x})^2 (y_i - \bar{y})^2}}. \quad (3.1)$$

When applying TLCC method, one data series is shifted in respect to another. If  $d$  represents the shift, the TLCC at any specific shift is represented by the equation

$$r_{xy}(d) = \frac{\sum_{i=1}^N (x_i - \bar{x})(y_{i-d} - \bar{y})}{\sqrt{\sum_{i=1}^N (x_i - \bar{x})^2 (y_{i-d} - \bar{y})^2}}. \quad (3.2)$$



Here,  $y$  is shifted relative to  $x$ . Assuming that time series  $y$  represents a pure sinusoidal curve with an amplitude of unity, and periodicity  $P$ , it can be written as

$$y = \sin\left(\frac{2\pi i}{P}\right), \quad (3.3)$$

where  $i = 1, \dots, N$  represents the number of data points. For a nonzero periodicity  $P$ , the periodic nature of a sinus function can be proven as long as the relation

$$\sin\left(\frac{2\pi i}{P}\right) = \sin\left(\frac{2\pi(i \pm P)}{P}\right) \quad (3.4)$$

is true for all  $i$  in the domain. Therefore, in a time-lagged cross correlation analysis, if one of the time series is a sinusoidal function with period  $P$ , the resulting correlation values will also exhibit a repeating pattern of period  $P$  as:

$$r_{xy}(d) = \frac{\sum_{i=1}^N (x_i - \bar{x})(\sin\left(\frac{2\pi(i-d)}{P}\right) - \bar{y})}{\sqrt{\sum_{i=1}^N (x_i - \bar{x})^2 (\sin\left(\frac{2\pi(i-d)}{P}\right) - \bar{y})^2}} = r_{xy}(d \pm P) = \frac{\sum_{i=1}^N (x_i - \bar{x})(\sin\left(\frac{2\pi(i-d \pm P)}{P}\right) - \bar{y})}{\sqrt{\sum_{i=1}^N (x_i - \bar{x})^2 (\sin\left(\frac{2\pi(i-d \pm P)}{P}\right) - \bar{y})^2}}. \quad (3.5)$$

Therefore, if the TLCC method is applied on a strongly periodic time-series and an arbitrary time series where no physical connection exists between the two, the results will still exhibit a periodicity, which can easily lead to erroneous conclusions.

### 3.1.2 Simulation

The problem of artificial periodic bias can also occur with the SE-method, and in quasi-periodic time-series. To illustrate, an idealized simulation experiments is shown in Figure 3.1. Here, the IMF  $B_y$  values at a daily scale is used as the forcing time series (quasi-periodic), while normally distributed randomly generated noise are used as the response variable (no physical connection between forcing and response). The top left panel show the IMF  $B_y$  values for the period  $\sim 1966-1980$ , while the bottom left panel show the randomly generated noise. Both plots respective power spectra are shown in the right panels. As can be seen, the forcing time-series have dominating frequencies around 27 days/cycle.

The result after applying the TLCC and SE method for -200 to 200 lead-lags is shown in the left panels of Figure 3.2. For the SE method, all days with IMF  $B_y > 0$  nT are chosen as key times. Frequency analysis of the results (of the left panels), show that both methods produce response curves exhibiting a clear 27-day periodicity. This artificial bias can be misinterpreted as evidence for a physical connection between time-series, when it is actually only a statistical artefact. Understanding this phenomenon is essential when interpreting the results of Paper I and Paper II.

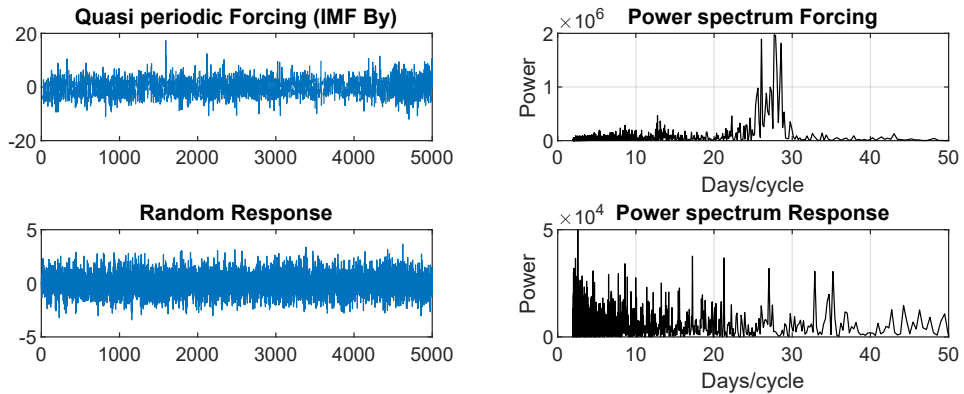


Figure 3.1: **Top panels:** IMF  $B_y$  daily values for the period  $\sim 1966$ –1980 (left) and frequency analysis of the time-series (right). **Bottom panels:** Normally distributed randomly generated noise with similar length as the IMF  $B_y$  (left) and a frequency analysis of the time-series (right).

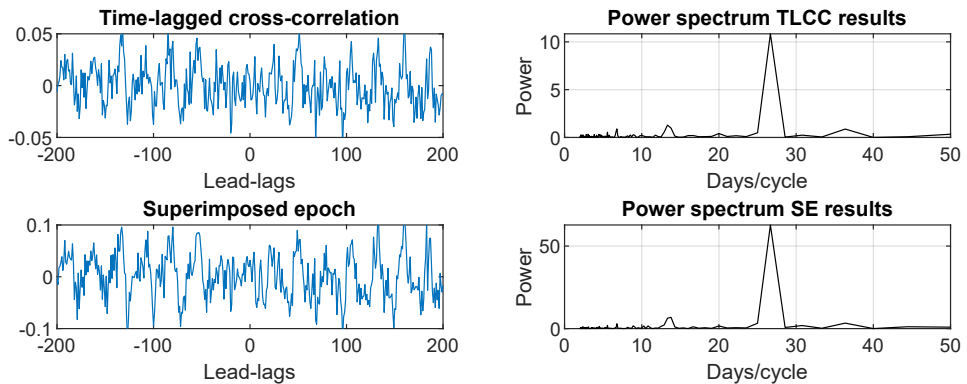


Figure 3.2: **Top panels:** TLCC between forcing (IMF  $B_y$ ) and response (normally distributed random numbers) (left) and a frequency analysis of the result between lead-lag -200 and 200 (right). **Bottom panels:** Similar as top panels, but for the SE method. Both methods exhibit a response with 27-day periodicity.

## 3.2 Monte Carlo approach

The Monte Carlo (MC) approach is applied in the thesis as a statistical significance testing tool. A key advantage of this method over the standard  $t$ -test is the ability to conduct significance estimation without requiring any underlying assumptions or knowledge about the data. This allows the method to account for spatial and temporal autocorrelation without the need for assumptions about the degrees of freedom in the data along any specific spatio-temporal direction. To achieve this, a repeated analysis is employed where the underlying statistical conditions must remain similar to the conditions found in the original analysis, while also introducing a random element. The MC approach produces a distribution of simulated results that assumes the null hypothesis while being representative of the original analysis's underlying statistics. By comparing the original result to the fraction of simulated results that are as extreme or more extreme, one obtains the p-value which represents the likelihood of obtaining

a similar result by chance when the null hypothesis is assumed correct. Two different Monte Carlo techniques are featured in the thesis. Paper I and II use the MC-approach with surrogate data, while Paper III uses bootstrapping. Details about both methods are provided in the following sections.

### 3.2.1 Surrogate data

Surrogate data is used in the thesis when applying the TLCC and SE analyses. The main objective is to replace one of the time series (response data-series in our cases) with surrogate data when conducting significance estimation, i.e., a statistically equivalent but random data series. Both Paper I and II generate surrogate data with the Fourier transform (FT) surrogate method by Lancaster et al. (2018) described in section 4.5. The procedure is computationally cheap and originally developed as a non-linearity testing tool. However, Theiler and Prichard (1996) has shown it to be a viable surrogate option when the distribution of targeted values (correlation values in our case) under the null hypothesis is unknown. The technique has also commonly been applied for statistical analyses regarding the Chemical-Dynamical coupling (e.g. Asikainen et al., 2020; Maliniemi et al., 2016, 2013; Thejll et al., 2003).

The method involves Fourier transforming ( $ft_x$ ) the original response data series ( $x_n$ ), and creating a random phase vector ( $\phi_r$ ) with half the length of  $x_n$ . Since Fourier transform is symmetrical, the first half of the new phase randomized vector ( $ft_r$ ) is obtained by multiplying the first half of  $ft_x$  by  $\exp(i\phi_r)$ . The remainder of  $ft_r$  is then the horizontally flipped complex conjugate of the first half. Finally, the FT surrogate data is computed by the inverse Fourier transform of  $ft_r$ . The method preserves mean, standard deviation, frequency spectrum and autocorrelation function (implied by preserved frequency spectrum) of the original response data series. However, the method does not preserve the amplitude spectrum.

A surrogate method which also preserves the amplitude spectrum is called time-shifted (TS) surrogates (Section 7.4 in Lancaster et al. (2018)). Given a response data-series ( $x_n$ ), the TS surrogate is simply computed by shifting the data series in the temporal direction by a random number between 0 and the length of  $x_n$ , and wrapping its end to the beginning. The TS surrogate will have the same state space trajectory, and therefore preserve all properties of the original response data-series. It is noted by Lancaster et al. (2018) that proper preprocessing is necessary when calculating TS surrogates to avoid nonlinearities in the end points of the data-series. However, when using long continuous noisy data series (geopotential height) without clear periodicities (when seasonality is removed at daily scale) this is not a major issue. A problem can also occur with TS surrogates if the original response data-series is short, as the number of different possible TS surrogate versions is exactly similar to the length of the original response data-series. Too short response data-series could therefore potentially lead to the distribution created by TS surrogates not fully describing the underlying statistics (distribution of correlation coefficients).

Figure 3.3 shows different statistical quantities for ERA5 re-analysis geopotential height data-series at the surface (1000 hPa) in the NH ( $90^\circ$ ) for the time period 1968–2020. The top panels illustrate the raw data, its autocorrelation function, its power spectrum and its amplitude distribution. The middle and bottom panels illustrate the same quantities for the FT- and TS-surrogates, respectively. As can be seen, the FT-surrogate method preserves all quantities except the amplitude spectrum, while the TS-surrogate method preserves all quantities.

Figure 3.4 shows the significance limits created by the FT-method (left panels) and TS-method (right panels) for TLCC between the geopotential height data series described above (Figure 3.3), and the IMF- $B_y$  for the corresponding period. The top and bottom panels show the appropriate significance limits when the data source is year 1999 (365 data points) and 1968–2018 (18615 data points), respectively. For every iteration, new FT- and TS-surrogate data series are created, and cross-correlated with IMF  $B_y$  for the lead-lags  $-23$  to  $+23$ . By iterating, a distribution of correlation coefficients for each lead-lag is created. As correlation values can be both positive and negative values, the distribution is two-tailed. The green shaded area (which covers 95% of the values) illustrates the range of correlation values regarded as non-significant, while the red shaded area (which covers only 5% of the values) illustrates the range of correlation coefficients regarded as statistically significant assuming a significance limit of 5%. The figure shows that when the response data series is small (top panels), the TS-surrogate method saturates for the most extreme cases. As discussed above, the number of random configurations is equal to the length of the original response data-series. With only 365 possible random configurations, the largest values have a high probability of occurring at all lead-lags, which explains why the upper limit of the red shaded area appears as a straight line. However, even with only 365 configurations, the area containing 95% of all values is nearly identical to the 95% area obtained by the FT-surrogate method, which in the-

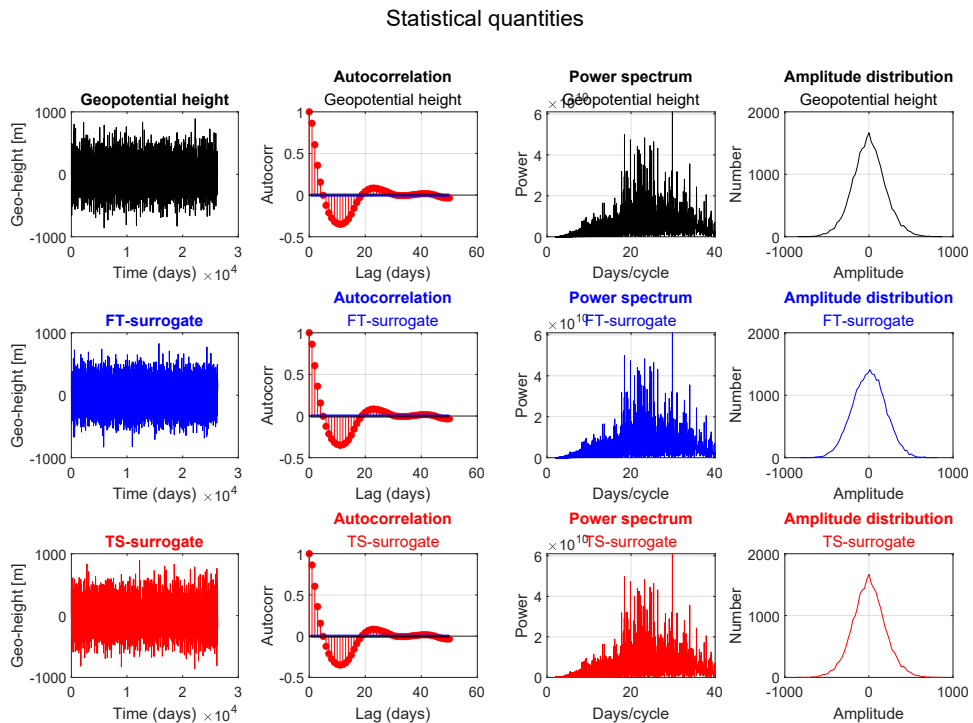


**Figure 3.3:** *Top panels:* The raw ERA5 re-analysis geopotential height data-series at the surface (1000 hPa) in the NH ( $90^\circ$ ) for the time period 1968–2020 (left), the data-series autocorrelation function (middle left), its power spectrum (middle right) and its amplitude spectrum (right). *Middle & bottom panels:* Same quantities for the FT- and TS- surrogates, respectively.

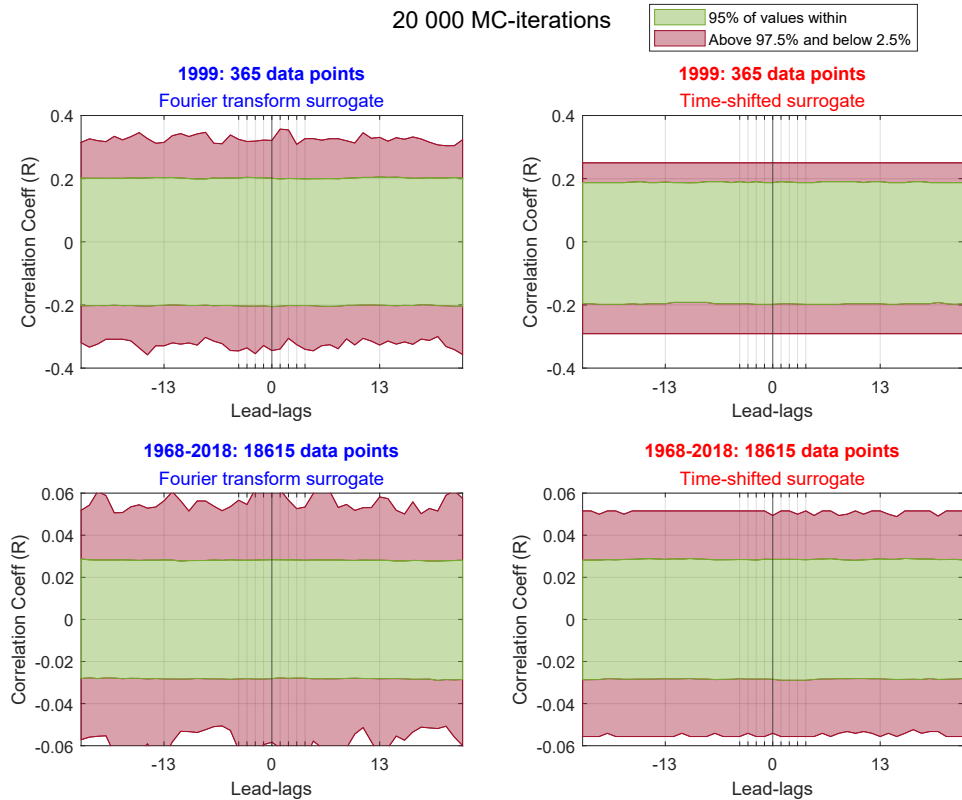


Figure 3.4: **Left panels:** Statistical significance limits obtained by the FT-method when TLCC is performed between the geopotential height (1000 hPa and  $90^\circ\text{N}$ ) and IMF  $B_y$  for the full year 1999 (top) and period 1968–2018 (bottom). **Right panels:** Same as top left panels, only with significance limits obtained by the TS-method. Both method calculates similar 95 percentiles (green shaded area) for both data-series lengths.

ory have infinite random configurations. Also, for the longer data-series (bottom panels), both methods produce similar results, with only small deviations seen at the extremes of the distributions. Thus, given sufficiently long time-series, both methods are equivalent in estimating significance limits when applied to geopotential height data. However, as some of the investigations conducted in the thesis focus on rather short time intervals, the FT-method is chosen as the preferred technique.

When using the MC-approach with surrogate data, it is important to note that continuous data are needed. Non-continuous data, such as data series containing NaN values or data series from specific seasons and stitched together, can introduce artificial frequencies in the surrogates. Therefore, a suitable interpolation technique is recommended when dealing with NaN's in the data series. However, when investigating the impact of a seasonal effect hypothesized to occur only in e.g. December, January, and February (DJF) over a five-year period, it is common practice to create a single data-series of the form  $|\text{DJF}|\text{DJF}|\text{DJF}|\text{DJF}|\text{DJF}|$ . To avoid nonlinearities and artificial frequencies originating from the stitching points, the surrogate method should always be applied first for each individual period, before the data series is

unified into the stitched surrogate form  $|DJF_{sur}|DJF_{sur}|DJF_{sur}|DJF_{sur}|DJF_{sur}|$ .

### 3.2.2 Bootstrapping

The MC-approach with bootstrapping is used in the thesis when analysing pair of opposing bins (e.g. high  $A_p$  and low  $A_p$ ). The main objective of the method is to generate multiple re-samples of the original data (bins in our case). These re-samples should be of a similar size as the original samples and be selected at random with replacement from all available samples. The original analysis (e.g. high  $A_p$  - low  $A_p$ ) is then applied to the re-sampled bins.

As an example, the temperature response from high  $A_p$  winters is subtracted by low  $A_p$  winters ( $\Delta T = \text{HIGH } A_p - \text{LOW } A_p$ ). The HIGH bin and LOW bins consist of 10 and 8 data points/winters, respectively. Thus, when bootstrapping each iteration, the  $\text{HIGH}_{boot}$  and  $\text{LOW}_{boot}$  bins are filled to the lengths 10 and 8, respectively, and at random from the pool of 18 available winters with replacement allowed (same winters can be chosen multiple times). Then, for each iteration, the difference of the random sampled HIGH and LOW bins will be calculated. This process results in a distribution of values. The original analysis is then compared to the distribution for a measure of significance.

In bootstrapping, it is important to use replacement. To accurately represent the underly-

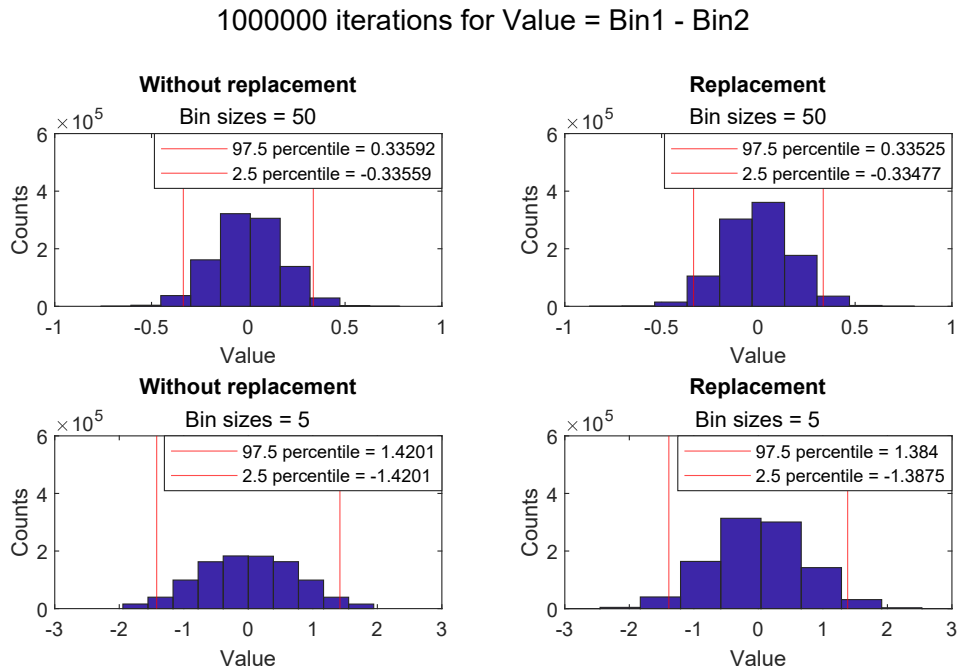


Figure 3.5: **Top panels:** Bootstrapping without replacement (left panel) and with replacement (right) for bin sizes of 50 taken through the analysis Value = Bin1 - Bin2 for 1 000 000 iterations. 100 normally distributed numbers are first generated, before they are picked at random and appointed to the bins. **Bottom panels:** Same as the top panels, only with bin sizes of 5.

ing statistics in the distribution, every valid representation should have the potential to occur multiple times. Figure 3.5 illustrates the effect of replacement. In the top panels, 100 normally distributed random numbers are generated and sorted 1 000 000 times into two bins of size 50 ( $\text{Value}=\text{Bin1}-\text{Bin2}$ ) without (left) and with replacement (right). The histogram shows the distribution of these values, along with the corresponding significance limits. The bottom panels show a similar setup, only with 10 random numbers generated and sorted into bins of size 5. With large bin sizes, with or without replacement yields very similar results. However, the effect of replacement becomes more prominent using small bin sizes. Without replacement, the number of configurations is heavily restricted, leading to the saturation observed in the bottom left panel. This widened distribution can lead to overly strict significance limits.

### 3.3 Multiple comparison problem

The Monte Carlo methods estimate the  $p$ -value. Threshold of, e.g.,  $p = 0.05$  implies that for an individual null hypothesis, a similar or more extreme result have a 5% probability of occurring when there is no actual relationship in the data. Inversely, this also means that every individual null hypothesis have a 5% probability of being a false rejection of the null hypothesis. Accordingly, when the number of individual null hypotheses increase (e.g. in map plots with multiple grids or TLCC analyses with multiple lead-lags), the probability of falsely rejecting at least one null hypothesis will also increase. Given 100 independent null hypothesis, the probability of at least one being falsely rejected is  $1 - P_{\text{No False Rejections}} = 1 - (1 - P_{\text{False Rejection}})^{\text{Number of Tests}} = 1 - (1 - 0.05)^{100} = 99,4\%$ . Without appropriate methods to address this issue, any space-climate scientist risks including the error.

The top panels of Figure 3.6 show TLCC for lead-lags -100 to +100 between two fully independent variables (left), and two weakly correlated variables (right). Significance limits are calculated by 20 000 iterations for the MC-approach with FT-surrogate data. The bottom panels show the distribution of  $p$ -values from the respective top panels. When no correlation in the data exists (left panels),  $p$ -values follow a uniform distribution (bottom left). When an actual relationship exists in the data (right panels), the distribution of  $p$ -values becomes skewed towards lower values (bottom right). It is evident that even when an actual connection exists, a large fraction of the 0-0.05 bin still consists of false rejections. Thus, a method that accounts for and removes the expected number of false rejections is needed.

#### 3.3.1 False-Discovery Rate

The False-Discovery Rate (FDR) method was originally developed by Benjamini and Hochberg (1995) and later adapted for atmospheric sciences by Wilks (2016). The method assumes statistically independent null hypotheses and identical distribution of observations. Statistically independent null hypotheses mean that the data points (e.g., specific grid points or lead-lags) are not correlated with each other. Identical distribution of observations means that the data characteristics, such as mean, median, variance, and standard deviation, are the same for every data point being compared. Applying the MC method, identical distribution of observations can be confirmed if the significance limits are identical for all data points (lead-lags or grid points). In Figure 3.4, displaying IMF  $B_y$  and geopotential height data, the distribution limits at each lead-lag are approximately identical. However, autocorrelation is often present in at-

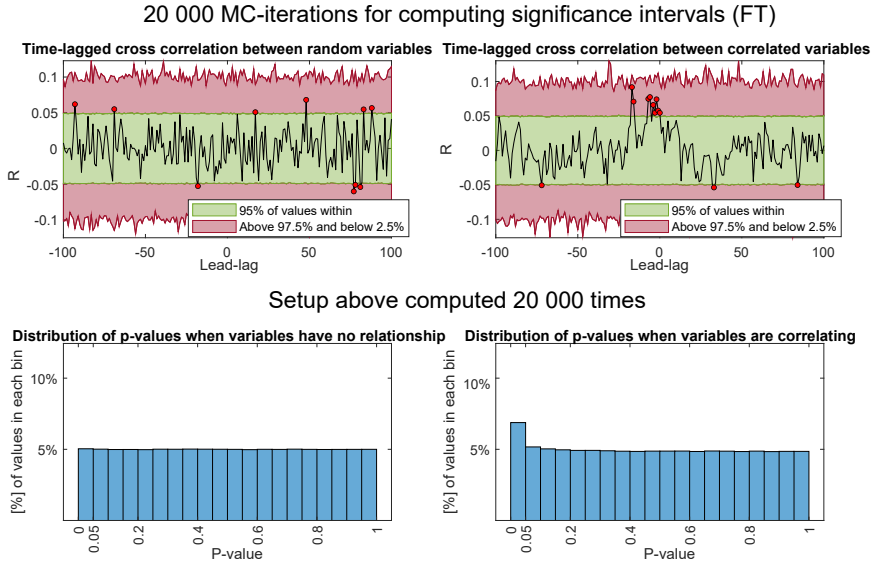


*Figure 3.6: **Top panels:** TLCC between two completely random variables (left) and two variables where some correlation is introduced between them (right). The significance limits are calculated by 20 000 iterations where one of the variables is replaced by FT-surrogates for each iteration. **Bottom panels:** Corresponding distribution of p-values between the uncorrelated variables (left) and correlated variables (right).*

mospheric data where e.g. lead-lags or grid points on a map are statistically interdependent. Therefore, Wilks (2016) introduced a factor accounting for autocorrelation in the approach by Benjamini and Hochberg (1995). It is both simplistic and computationally cheap. It requires all  $p$ -values to be sorted in ascending order forming the set  $i = 1, \dots, N$  where  $N$  represents the total number of null hypotheses to be tested. A new global  $p$ -value,  $p_{\text{FDR}}$ , is calculated by iterating through the individual  $p$ -values starting from the lowest and finding the last  $p$ -value satisfying the following equation:

$$p_{\text{FDR}} = \max[p(i) : p(i) \leq \left(\frac{i}{N}\right) \cdot \alpha_{\text{FDR}}], i = 1, \dots, N \quad (3.6)$$

If all  $p$ -values are independent (zero autocorrelation between grid points or lead-lags in a TLCC analysis), the global  $p$ -value ( $p_{\text{FDR}}$ ) can be interpreted at the 95% confidence level by setting  $\alpha_{\text{FDR}} = 0.05$ . To determine the statistical significance of individual data points, their original  $p$ -values are compared to the newly calculated global threshold value  $p_{\text{FDR}}$ . Only data points with  $p$ -values equal to or lower than  $p_{\text{FDR}}$  are considered statistically significant. Furthermore, Wilks (2016) demonstrates that by adjusting  $\alpha_{\text{FDR}}$  appropriately, autocorrelation can be taken into account while still ensuring the validity of the FDR-method. It is shown that for autocorrelation with an e-folding distance of  $1.54 \cdot 10^3$  km (common spatial autocorrelation found in atmospheric data), setting  $\alpha_{\text{FDR}} = 0.1$  ensures global statistical significance at the 95% level.



### 3.3.2 Optimizing $\alpha_{\text{FDR}}$

The correct  $\alpha_{\text{FDR}}$  should ideally be calculated for the specific data at hand as not all atmospheric data have the same e-folding distance in regards to autocorrelation. The FDR-method is designed such that if the null hypotheses are assumed to hold (i.e., no relationship exists in the data), there is a 5% probability that a collection of multiple comparable null hypothesis will pass the FDR criterion (Equation 3.6) with the appropriate  $\alpha_{\text{FDR}}$ . Therefore, the respective  $\alpha_{\text{FDR}}$  value can be calculated. This is demonstrated in Paper II by second-order MC simulation after initial individual  $p$ -value estimation. The process is repeated for different  $\alpha_{\text{FDR}}$  values to find the FDR threshold where only a desired percentage (e.g. 5%) of the iterations pass. However, it should be noted that this optimization process increases the computational costs of the otherwise inexpensive FDR-method. Wilks (2016) demonstrates that  $\alpha_{\text{FDR}}$  converges to approximately 0.1 (while keeping the global confidence level at 95%) as the degree of autocorrelation increases beyond the mentioned e-folding distance.

### 3.3.3 False-Discovery Rate combined with the Monte Carlo approach

Given 50 data points, and  $\alpha_{\text{FDR}} = 0.05$ , the first sorted  $p$ -value must be lower or equal to  $(1/50) \cdot 0.05 = 0.001$ . This implies that the  $p$ -values need a resolution of at least 0.001, or at least 1000 iterations when significance is calculated by the MC-approach. The required number of iterations at a given level of statistical accuracy can readily be calculated.

As shown in Figure 3.6, when the null hypothesis is true,  $p$ -values are distributed uniformly. Thus, obtaining an accurate  $p$ -value of 0.001 (accurate with respect to the realistic underlying statistical distribution) can be thought of as a 1/1000 event. The following assessment gives the probability that

$$\text{One MC iteration is not the 0.001 event} = 1 - \frac{1}{1000} \quad (3.7)$$

$$1000 \text{ MC iterations are not the 0.001 event} = \left(1 - \frac{1}{1000}\right)^{1000} \quad (3.8)$$

$$1000 \text{ MC iterations give at least one 0.001 event} = 1 - \left(1 - \frac{1}{1000}\right)^{1000}. \quad (3.9)$$

The latter equation shows there is only a 63.23% probability of obtaining a realistic  $p$ -value of 0.001 with 1000 iterations. A larger number of iterations is therefore needed to accurately represent the underlying distribution at the required resolution. By substituting the FDR formula for the resolution level (1/1000) in Equation 3.9, and setting the equation equal to 1, the formula represents the number of iterations needed (with constant  $N$  and  $\alpha_{\text{FDR}}$ ) for the desired level of resolution to be achieved with 100% accuracy:

$$1 - \left(1 - \left(\frac{1}{N} \cdot \alpha_{\text{FDR}}\right)\right)^{\text{Iterations}} \approx 1. \quad (3.10)$$

By subtracting 1 from each side of the equation, the resulting formula approaches zero as the number of iterations approaches infinity:

$$\lim_{\text{Iterations} \rightarrow \infty} \left(1 - \left(\frac{1}{N} \cdot \alpha_{\text{FDR}}\right)\right)^{\text{Iterations}} = 0. \quad (3.11)$$

Increasing the number of iterations, decreases the error in accuracy. By replacing the right side with  $E_A$ , symbolizing the error in accuracy, and applying the natural logarithm on both sides:

$$\text{Iterations} = \frac{\ln(E_A)}{\ln\left(1 - \left(\frac{1}{N} \cdot \alpha_{\text{FDR}}\right)\right)}. \quad (3.12)$$

The resulting equation describes the relationship between the number of iterations and the desired accuracy at a given level of resolution required by the FDR-method.



# Chapter 4

## Data

To study the impact of space weather on the polar atmosphere, we use observational data of the solar wind obtained from satellite measurements, and atmospheric data obtained from re-analyses and climate models. In this chapter, a detailed description of the data will be provided.

### 4.1 Solar wind data

OMNI space weather data<sup>1</sup> provides the IMF data. The data, compiled and deduced from various spacecraft missions in either geocentric or L1 (Lagrange point) orbits, offer continuous daily averages for various IMF components. This is achieved through cross-comparison and normalization of the data, spanning the period from 1963 to the present.

Vokhmyanin et al. (2019) evaluate the limitations of the OMNI IMF database. The distance between the Lagrange point L1 and the dayside magnetopause means that the IMF values measured at L1 may not accurately represent the values interacting with the magnetosphere. The study compared OMNI data to independent measurements near the bow shock and classified 42% of the data as very good, 33% as moderate, and 25% as poor quality. This suggests being cautious when interpreting results based on these measurements. However, it remains the best alternative for the topic of this thesis due to the long data interval.

The GSM coordinate system is used by both Tinsley and Heelis (1993) and Lam et al. (2013) to show that opposing IMF  $B_y$  directions on daily scales create asymmetric ionospheric perturbations between the hemispheres. As these are the perturbations hypothesised to change the fair weather current, using GSM for when looking at potential surface impact is justified. The results of Paper I and II have also been tested using the geocentric solar ecliptic (GSE) coordinate system, resulting in only negligible differences.

In Paper II, the surface pressure response to HCSC is also investigated. The data on sector boundary crossings are compiled by Leif Svalgaard and obtained from his personal research homepage (<https://www.leif.org/research/sblist.tx>). They are based on ground magnetometer data, and in situ interplanetary magnetic field observations. The author relies on a simple algorithm, involving a slight smoothing of the IMF data to avoid the inclusion of tiny sector crossings. A sector duration of about four days is needed to confirm a crossing. Since the data

---

<sup>1</sup><https://omniweb.gsfc.nasa.gov/>

partly relies on ground magnetometers, it has good temporal coverage dating from 1926 to the present.

## 4.2 Atmospheric data

### 4.2.1 Re-analysis data

To capture the impact of space weather on the atmosphere over large areas and long periods at high latitudes and altitudes, one must rely on re-analysis data. Re-analysis data is created by combining observations with numerical simulations to provide a modelled dataset with enhanced resolution. While aiming to be a realistic frame of reference, the data may include artificial trends originating from the numerical modelling. However, when used appropriately, re-analysis data has proven to be useful in research.

The thesis uses the European Center for Medium-Range Weather Forecast (ECMRWF) data set ERA5 Copernicus Climate Change Service (2017) which covers the period from 1940 to now. It has a  $30 \text{ km} \times 30 \text{ km}$  grid with a height resolution of 137 levels from the surface up to  $80 \text{ km}^2$ . Though validation experiments are somewhat limited in regards to location, ERA5 have been shown to simulate highly accurate atmospheric profiles in both Arctic and Antarctic (e.g. Graham et al., 2019; Tetzner et al., 2019; Zhu et al., 2021). The data is constructed using 4D-Var (four dimensional variational) data assimilation technique. The data are assimilated over a time period known as the assimilation window, which is then used to adjust the initial conditions of a numerical model of the atmosphere. In an iterative process the model is run multiple times until it best fits real world observations over the assimilation window (Rabier et al., 2000). After a best fit, the process can be repeated for the chronologically next assimilation window. Due to the dependence on observations, re-analysis data are generally more accurate for current times and lower altitudes compared to the pre-satellite era due to the increased availability and quality of observations during recent decades.

The data used in Paper I and Paper II of this thesis are mostly geopotential height values extracted from ERA5 at pressure levels near the surface (750 hPa and 1000 hPa) and near the poles (latitude  $>60^\circ\text{N/S}$ ). Geopotential height is a measure of the height (meters) of a given constant pressure level in the atmosphere. The height of a constant pressure level will be closely related to the distribution of air pressure and temperature in the atmosphere, as regions of high pressure generally corresponds to higher geopotential height, while regions of low pressure generally correspond to lower geopotential height. The geopotential height near the surface and near the poles are particularly relevant for investigating the Mansurov effect, as this phenomenon manifests itself in surface pressure data in polar regions.

### 4.2.2 Model data

#### Main internal components in SOCOL3-MPIOM

The atmospheric temperature data analyzed in Paper III are obtained from SOCOL3-MPIOM (Muthers et al., 2014; Stenke et al., 2013), which is a chemistry-climate model with an interactive ocean. In general, a chemistry-climate model (CCM) is a type of numerical model that

---

<sup>2</sup>ERA5 documentation: <https://confluence.ecmwf.int/display/CKB/ERA5%3A+data+documentation>

simulates interactions between the atmosphere/ocean and its chemical composition. This includes detailed representations of formation, transport, conversions and removal of greenhouse gases, aerosols, and other chemical species. It makes CCMs ideal for simulating atmospheric ozone depletion and corresponding atmospheric dynamical responses.

The atmospheric component of the coupled model is represented by the general atmospheric circulation model European Centre/Hamburg Atmospheric Model (ECHAM), version 5.4 (Roeckner et al., 2003). Simulation runs were performed using a spatial resolution (latitude) of  $3.75^\circ \times 3.75^\circ$  and 39 vertical pressure levels (post-processed to 30 pressure levels) from surface to the upper mesosphere (0.01 hPa,  $\sim 80$  km). ECHAM5.4 operates primarily in a free-running mode, generating its own internal dynamics. However, the model is unable to generate the quasi-biennial oscillation (QBO) with the applied vertical resolution, so QBO data from the long reconstruction by Brönnimann et al. (2007) are explicitly forced in the model. These data are shown to be reliable and capture the maximum phases of the QBO relatively well after 1910.

The oceanic component of SOCOL3-MPIOM is represented by the Max Planck Institute Ocean Model (MPIOM) (Marsland et al., 2003). The model uses a spatial resolution of  $3^\circ \times 3^\circ$  for latitude and longitude and includes 40 vertical levels from the ocean bottom to the surface. The model also incorporates a dynamic/thermodynamic representation of sea ice. Unlike traditional grid systems using rectangles and squares, MPIOM uses an orthogonal curvilinear coordinate system, allowing more complex shapes and movements to be represented in curved space. This unique feature improves the model's accuracy compared to its predecessors. However, the model still has certain inaccuracies, e.g., Marsland et al. (2003) pointed out that the model tends to underestimate the poleward heat transport in the North Atlantic region.

The chemistry component is called the Model for Evaluation of oZONe trends (MEZON) (Egorova et al., 2003). The model calculates the tendencies of 41 gas species, which has a total of 200 gas-phase reactions, 16 heterogeneous reactions and 35 photolytic reactions. Evidently, as MEZON is used in coupled climate models for assessment of ozone trends,  $\text{NO}_x$  and  $\text{HO}_x$  are represented amongst the gas species. In addition to the three main coupled components, the tropospheric aerosols are from the National Center for Atmospheric Research (NCAR) Community Atmospheric Model (CAM3.5) simulations with a bulk aerosol model. Furthermore, concentrations of greenhouse gases, ozone precursors, and depleting substances in the simulations follow historical values (Meinshausen et al., 2011).

### **Solar forcing components in SOCOL3-MPIOM**

The solar radiation is obtained from the long reconstruction by Shapiro et al. (2011), which is divided into two components: Total Solar Irradiance (TSI) and Spectral Solar Irradiance (SSI). While TSI variations during the 11-year solar cycle only affect the total radiative budget slightly ( $\sim 0.1\%$ ), SSI can vary significantly ( $\sim 10\%$ ) in the UV spectrum (Lean, 1997; Shapiro et al., 2011). These variations in UV radiation have been shown to have a significant impact on the radiative heating and ozone budget of the middle atmosphere (Haigh, 2017). Moreover, in addition to irradiance effects and pre-calculated photolytic reaction rates, some parameterization is used to account for missing solar heating variations in the stratosphere and the mesosphere (Sukhodolov et al., 2014).

For the EPP forcing, the Coupled Model Intercomparison Project Phase 6 (CMIP6) recommendation (Matthes et al., 2017) is used. The recommendation includes medium-energy electrons ( $>30\text{keV}$ ) forced as daily ionisation rates, with the routines developed to generate a specific quantity of  $\text{NO}_x$  and  $\text{HO}_x$  dependent on these rates. The recommendation also includes auroral electrons ( $<30\text{keV}$ ), which use a semi-empirical model of  $\text{NO}_x$  and  $\text{HO}_x$  input through the model top (Funke et al., 2016). The ionization rates and resulting  $\text{NO}_x$  and  $\text{HO}_x$  production is obtained through parameterization models of the  $A_p$  index. This index is used as a global measure of geomagnetic disturbances (obtained by a multitude of ground magnetometer measurements at specific locations), and is shown to have a near-linear relationship with ionization rates when accounting for the time-lag introduced by downward transport. Finally, daily ionization rates are also forced for SPEs and GCR.

In the simulations, the experiment included 11-member (EXP) ensemble runs and 11-member reference (REF) ensemble runs each spanning the time period 1850–2008. The EXP ensemble members included particle forcing, while the REF ensemble members excluded it. The ensembles were generated by varying the initial  $\text{CO}_2$  concentration with 0.1% among the different members, leading to different model trajectories in terms of the internal variability due to the nonlinear nature of interactions in the coupled model. However, during the download process, 4 of the original ensemble members were found to be corrupted. Therefore, Paper III utilized 10 EXP and 8 REF ensemble members. To obtain a realistic representation of dynamics, a 50-year spin-up period was required. As a result, the investigation focuses on the time period 1900–2008.

# Chapter 5

## Summary of Papers

Recent years have seen a surge in observational, re-analysis, and model studies providing evidence of statistical correlations between day-to-day to interannual solar activity and climate/weather patterns. The overarching objective and common denominator of the three papers constituting the thesis, is to examine the hypothesized physical links between near-Earth-space and the lower atmosphere applying sophisticated statistical analysis methods.

### **5.1 Paper I: The Mansurov effect: Statistical significance and the role of autocorrelation**

Paper I builds on the statistical evidence reported since the 70's suggesting an instantaneous correlation between the IMF  $B_y$  and polar surface pressure in both hemispheres, known as the Mansurov effect (Mansurov et al., 1974). The supporting evidence has, however, been relatively sparse and often limited to specific sub-periods, such as solar cycle 23 (1995–2005) Burns et al. (2008); Lam et al. (2014, 2018); Lam and Tinsley (2016); Zhou et al. (2018). In particular the period 1999–2002, which is centered around the solar maximum, has been regularly cited as a sub-period where the Mansurov effect operates based on both observational and re-analysis data.

For the investigation, ERA5 atmospheric re-analysis dataset at the 1000 hPa level is utilized in both hemispheres. During solar cycle 23, no statistically significant relationship between IMF  $B_y$  and polar surface pressure at the 95% level is found after accounting for the autocorrelation in the data by MC with surrogate data and the multiple comparison problem by the FDR approach. Nevertheless, when applying the time-lagged cross-correlation method, the pressure response during this sub-period exhibited a clear 27-day cycle. Since the IMF  $B_y$  has a 27-day periodicity originating from the solar rotational period, this 27-day pressure response has been cited in multiple studies as evidence of a physical relationship. Moreover, when investigating other sub-periods (other 11-year periods: 1984–1994, 2006–2016, and 4-year periods centered around solar maximums: 1980–1983, 1989–1992, 2012–2015), a similar 27-day cycle in the pressure response is observed in all of them, but with seemingly random offsets in respect to timing. By constructing an experiment where the real IMF  $B_y$  (for the time period 1995–2005) is cross-correlated with randomly generated uniformly distributed numbers with different levels of autocorrelation (to simulate the pressure), it is demonstrated that this 27-day periodic response is in fact a statistical artefact. The manifestation of the artefact increases as the autocorrelation in the data increases. By setting lag-1 autocorrelation in the randomly



generated numbers, corresponding to the real autocorrelation in surface pressure for the period 1995–2005, the periodic bias is of similar magnitude as the response associated with and cited as evidence for the Mansurov effect.

The absence of significant responses during the frequently cited solar cycle 23, in addition to the statistical artefact giving the impression of a physical link, leads to the conclusion that the Mansurov associated responses might just be chance events. The research presents a reminder that methodological artefacts and biases can easily be misinterpreted as physical signals if one does not tread cautiously.

## 5.2 Paper II: The Mansurov effect: Seasonal and solar wind sector structure dependence

Paper II is a follow-up to Paper I. In Paper I, only continuous time-periods were investigated. However, new evidence suggested that the Mansurov effect may be enhanced during local winter time and when the IMF  $B_y$  exhibits a 2-sector structure phase (a clear 27-day periodicity, as opposed to a 13.5-day periodicity) (Tinsley et al., 2021). To account for the new revised hypothesis, Paper II explores the seasonal and solar wind sector structure dependence of the Mansurov effect.

The study divides data from 1968–2020 into seasons, solar sector structures, and combinations of both. However, even when investigating the proposed optimal sub-periods (Tinsley et al., 2021) using the same rigorous statistical methods as in Paper I, no significant Mansurov-associated responses are found in either hemisphere. Moreover, the highly cited period of solar cycle 23 yielded similar non-significant results when focusing solely on the assumed optimal conditions.

Nonetheless, a previously undiscovered statistical relationship is found. During March–April–May and 2-sector solar wind structures, significant correlations between the IMF  $B_y$  and polar surface pressure in both hemispheres are found over the entire data period of 1968–2020. The relationship is remarkably robust, with  $p$ -values below 0.000001, though the correlation coefficient is small, 0.1, amounting to explaining about 1% of the pressure variations. The timing of the response is also not consistent with the Mansurov hypothesis. Based on the time-lagged cross-correlation analyses, the pressure response in both hemispheres peaks five days before the peak in IMF  $B_y$ . According to the Mansurov hypothesis, the pressure response should follow with a 1–2 day lag after the IMF  $B_y$  peak. To further investigate this unusual occurrence, a superposed epoch analysis of heliospheric current sheet crossings (HCSC) is conducted with respect to surface pressure. The timing of crossings is highly correlated with  $B_y$ , usually occurring a couple of days before the peak  $B_y$  amplitude. A slightly better fit is found for this in the NH, as the largest pressure anomaly occurs two days before the crossing event. However, a pressure lag of -2 days is still hard to justify. Additionally, the response is not significant in the SH.

To explain the lack of significant Mansurov effect and the newly discovered correlation, five possible hypotheses are proposed. Overall, the five explanations suggests that the Mansurov hypothesis needs to be revisited and revised. The impact on surface pressure is likely misunderstood, and it may be possible that the real phenomenon is connected to the

newly discovered correlation. The robust correlation might, however, still be a chance occurrence as long as no plausible explanation exists. Further research on links between the solar wind magnetic field and the neutral atmosphere, is as such highly encouraged.

### **5.3 Paper III: Effects of Energetic Particle Precipitation on stratospheric temperature during disturbed Stratospheric Polar Vortex conditions**

The topic of Paper III examines the potential EPP effect on stratospheric dynamics. Studies have shown how the QBO modulates the EPP response, with the largest atmospheric responses seen during the easterly QBO phase (Maliniemi et al., 2016, 2013; Salminen et al., 2019). This phase is highly correlated with disturbed polar vortex conditions associated with increased planetary wave activity. Recently, a re-analysis study showed how times preceding and during SSWs, which predominantly occur during QBOE, might play a crucial role for the mechanism to operate (Asikainen et al., 2020). Another recent re-analysis study has also shown a relationship between EPP and the occurrence rate of SSWs during QBOE (Salminen et al., 2020). Therefore, Paper III aimed at investigating these relationships using the SOCOL3-MPIOM model in combination with rigorous statistical tools.

For the investigation, atmospheric temperature measurements obtained from SOCOL3-MPIOM model runs for the period 1900–2008 and latitudes 60°–90°N are used. Ten experiment (EXP) ensemble members containing particle forcing and eight reference (REF) ensembles without particle forcing are analyzed to examine the relationship between EPP and the occurrence rate of minor SSWs during various QBO-phases, and the temperature impact during minor SSWs. Note that we focus on events defined as minor SSWs which may or may not contain major SSWs, which we term "disturbed events".

For the occurrence rate of "disturbed events", no statistically significant relationship related to EPP is found for either QBO phase. Both the EXP and REF runs have fairly equal number of "disturbed events". However, as (Salminen et al., 2020) showed this relationship only for major SSWs, our result is not directly comparable.

For the atmospheric temperature impact, highly significant results are found after accounting for autocorrelation and multiple null hypotheses. The most significant responses are evident in the stratosphere between 100 hPa and 10 hPa during the month of February. Upon closer inspection, the anomalies occur just prior and during the onset of minor SSWs, which is consistent with the re-analysis study by Asikainen et al. (2020). Moreover, the response pattern, which includes a middle stratospheric cooling and upper stratospheric heating, is also in line with the re-analysis study. However, contrary to Asikainen et al. (2020), our study does not find a significant surface impact. Still, this could be related to our smaller latitudinal and parameter range, as significant surface impact was found below 60°N and mostly for zonal winds in Asikainen et al. (2020). Moreover, our study only finds significant responses for the latter half of the data period, from 1955 to 2008. The time period 1900–1954 displays insignificant opposite responses.

Overall, the model runs show that disturbed conditions associated with minor SSWs might play an important role in how the Chemical-Dynamical coupling manifests. During highly

disturbed conditions, it is possible that small initial EPP temperature perturbations lead to enhanced wave-mean-flow interactions, compared to small initial perturbations occurring during relatively stable conditions. Additionally, if the phenomenon is only prominent during the latter half of the 1900s, it might indicate that the mechanism could become more influential in the future. We therefore recommend more studies using other general circulation models, as well as re-analyses studies focusing on the relation between EPP and disturbed polar vortex conditions.

# Chapter 6

## Conclusion and Future Work

### 6.1 Conclusion

The overarching goal of this thesis has been to investigate the impact of two distinct mechanisms connecting space weather and atmospheric weather phenomena: the Chemical-Dynamical coupling and the Mansurov effect. Because of increasing computing power and longer time-series of measurements, we are now able to detect and identify ever smaller signal-to-noise ratios in complex systems like our atmosphere. However, the smaller the signal-to-noise ratio, the greater the likelihood of drawing erroneous conclusions. Consequently, all three studies conducted place a strong emphasis on employing rigorous, up-to-date statistical assessment methods. Final remarks are now made regarding the three key questions of the thesis.

#### **1. Is there a statistically sound relationship between space weather and atmospheric weather variations?**

Both Paper I and II study the connection between the IMF  $B_y$  and polar surface air pressure. In Paper I, the importance of statistical rigor is strongly highlighted. By accounting for autocorrelation and the multiple comparison problem, the significance of the Mansurov associated responses during a highly cited period (1995–2005) is called into question. Additionally, an experiment shows that the methods applied to support the effect are highly susceptible to artificial periodic response patterns that can be easily misinterpreted as evidence for a physical link. Paper II further investigates the seasonal and solar sector structure dependence, but finds no statistically significant relationship supporting the Mansurov effect. Thus, the investigations conducted cannot find a statistically sound relationship for the hypothesized Mansurov effect. However, in Paper II, a statically significant relationship between IMF  $B_y$  and surface pressure do occur, though the timing is difficult to justify physically. Moreover, Paper III discovers a statistically sound relationship between particle forcing and atmospheric temperature anomalies in the SOCOL3-MPIOM model. In conclusion, the thesis supports that there are statistically significant relationships between space weather and atmospheric weather variations, both at interannual/monthly and daily scales.

#### **2. Are these relationships potentially important for the surface climate?**

Although the statistical evidence does not support the existence of the proposed physical link associated with the Mansurov effect, the statistically significant relationship between the

IMF  $B_y$  and surface pressure with the seemingly unphysical timing suggests that an instantaneous connection between the solar wind and surface polar climate may still exist, albeit operating differently than previously suggested. However, even if we assume that the connection found is of physical origin, its importance for surface climate might still be debatable. As the study in Paper II shows, the relationship only exists in certain months (mostly MAM), and the correlation coefficients are relatively small (about 0.1). Thus, the relationship can only explain ( $R^2$ ) up to 1% of the variations in surface geopotential height, in a fraction of all months.

For the Chemical-Dynamical coupling, the results of our model study in Paper III are consistent with a previous re-analysis study (Asikainen et al., 2020). This consistency further supports an actual physical relationship mediated by disturbed polar vortex conditions. However, there is no conclusive evidence regarding the mechanism's importance in terms of surface impact. Although highly significant temperature perturbations are visible in large parts of the stratosphere, no consistent statistically significant surface impact is detected. The re-analysis study, in comparison, showed statistically significant surface anomalies in zonal winds, as well as at latitudes below  $60^\circ$ , both parameters which were not included in Paper III.

### 3. Are there any deviations between the hypotheses and the findings?

The Mansurov hypothesis predicts a positive and negative relation between the IMF  $B_y$  and polar surface pressure in the NH and SH, respectively. The maximum  $B_y$  amplitude is theorized to affect the microphysical conditions in cloud generation processes, with a macro-scale cloud/pressure anomaly manifesting 1–3 days after the peak in  $B_y$ . The hypothesis also suggests that local winter time and the presence of a 2-sector solar wind structure will enhance the impact of the effect. However, in Papers I and II, we find that none of these relations hold. Even for the time period 1999–2002, from which these relations are mainly derived, the pressure responses themselves are not statistically significant. With the discovery of the -5 day lag anomaly, which appears more closely related to HSCS crossings, we suggest that the entire mechanism related to surface pressure impact needs revision due to the deviations between the hypothesis and findings.

Our findings in Paper III are generally consistent with the new Chemical-Dynamical coupling hypothesis, which posits that disturbed polar vortex conditions serve as an important mediator of the dynamically induced atmospheric EPP impact. In Asikainen et al. (2020), the atmospheric temperature perturbations related to EPP were found to be largest 5–15 days before the onset of major SSW events, while our study found the largest perturbations during the events. This deviation might occur as our events includes mostly minor SSWs, rather than only major ones, possibly allowing for different dynamics. Similarly, another re-analysis study found EPP to modulate the occurrence rate of major SSWs during QBOE Salminen et al. (2020), while our study showed no EPP modulation of the occurrence rate of minor SSWs in either QBO phase.

## 6.2 Future work

Regarding the seemingly unphysical -5 day lagged correlation between the IMF  $B_y$  and polar surface pressure found in Paper II, investigations focusing on higher altitudes would be a logical next step that could provide valuable information in respect to its origin. Additionally, studies should be conducted to examine the impact in the years following volcanic eruptions,

when sulfate aerosols are injected into the stratosphere. Some literature has suggested these conditions are ideal for the Mansurov effect to operate, but this was not investigated in the thesis. More generally, future studies exploring instantaneous relationships between the solar wind magnetic field and surface pressure mediated by the GEC would benefit greatly from reliable long-term vertical electric field measurements. Obtaining these measurements is generally difficult and often riddled with noise. Therefore, both experimental and theoretical studies focusing on reliable long-term setups for measuring the vertical electric field/polar cap ionospheric potential could help unravel the relationship between GEC and weather patterns. Furthermore, studies relating lightning activity and weather anomalies would also be useful for this purpose, as the thunder generator is the main driver of the ionosphere-Earth potential.

Regarding the Chemical-Dynamical coupling, a logical next step would be to examine the consistency of the results obtained using re-analysis data focusing on minor SSWs defined in a similar manner. Additionally, consistency should be explored using atmospheric models that also includes wind measurements in order to include a standard identification of major SSWs. By being able to separate between major and minor SSWs, greater nuances could be discovered, while also increasing the overall reliability and help confirm that the models represent the underlying atmospheric dynamics needed for the EPP mechanism to operate. Another interesting area for further investigation is the work by (Hauchecorne, 2022), which identifies two distinct types of stratospheric final warmings - dynamical and radiative. The type of warming notably determines the dynamical evolution of the polar vortex throughout the corresponding winter. Research focusing on the link between EPP and atmospheric perturbations for these two distinct categories could provide valuable insight into the operation of the dynamical impact. Additionally, our results show the largest atmospheric impact during the most recent time period, the mechanism could become more important in the future. This is also noted by the findings of Maliniemi et al. (2020, 2021), which suggest that an increasing Brewer-Dobson circulation leads to increased NO<sub>x</sub> downwelling, which, when combined with decreasing stratospheric chlorine species, results in enhanced ozone depletion from EPP-produced NO<sub>x</sub>, regardless of the level of EPP activity. More simulation studies focusing on future scenarios would therefore benefit our understanding of the mechanism and its impact in a changing climate.



# Bibliography

- Alfvén, H., 1942. Existence of Electromagnetic-Hydrodynamic Waves. *Nature*, (150), 405406. URL <https://doi.org/10.1038/150405d0>. 2.2.3
- Alfvén, H., 1943. On the existence of electromagnetic-hydromagnetic waves. *Arkiv. Mat. Astron. Fys.* URL <https://cir.nii.ac.jp/crid/1574231875408716416>. 2.2.1
- Ambaum, M. H. P., B. J. Hoskins, and D. B. Stephenson, 2001. Arctic Oscillation or North Atlantic Oscillation?. *Journal of Climate*, **14**(16), 3495–3507. URL [https://doi.org/10.1175/1520-0442\(2001\)014<3495:A00NA0>2.0.CO;2](https://doi.org/10.1175/1520-0442(2001)014<3495:A00NA0>2.0.CO;2). 2.1.8
- Andersson, M., P. Verronen, C. Rodger, M. Clilverd, and A. Seppälä, 2014. Missing driver in the Sun-Earth connection from energetic electron precipitation impacts mesospheric ozone. *Nat Commun*, **5**(5197). URL <https://doi.org/10.1038/ncomms6197>. 2.1.10
- Andrews, D., 1987. Chapter 5 - Extratropical Planetary-Scale Circulations. In D. Andrews, J. Holton, and C. Leovy, eds., *Middle Atmosphere Dynamics*, vol. 40 of *International Geophysics*, 220–258. Academic Press. URL <https://doi.org/10.1016/B978-0-12-058575-5.50010-4>. 2.1.8
- Andrews, D., 2010. Atmospheric thermodynamics. In *An introduction to atmospheric physics*. 1951. Cambridge University Press, 2nd edn. URL <https://doi.org/10.1017/CB09780511800788.003>. 2.1.8
- Arnold, N. F., and T. R. Robinson, 2001. Solar magnetic flux influences on the dynamics of the winter middle atmosphere. *Geophysical Research Letters*, **28**(12), 2381–2384. URL <https://doi.org/10.1029/2000GL012825>. 2.1.10
- Arsenovic, P., E. Rozanov, A. Stenke, B. Funke, J. Wissing, K. Mursula, F. Tummon, and T. Peter, 2016. The influence of Middle Range Energy Electrons on atmospheric chemistry and regional climate. *Journal of Atmospheric and Solar-Terrestrial Physics*, **149**, 180–190. URL <https://doi.org/10.1016/j.jastp.2016.04.008>. 2.1.10
- Asikainen, T., A. Salminen, V. Maliniemi, and K. Mursula, 2020. Influence of Enhanced Planetary Wave Activity on the Polar Vortex Enhancement Related to Energetic Electron Precipitation. *J. Geophys. Res. Atmos.*, **125**(9). URL <https://doi.org/10.1029/2019JD032137>. 1, 2.1.10, 2.12, 2.1.10, 3.2.1, 5.3, 6.1
- Baldwin, M. P., B. Ayarzagüena, T. Birner, N. Butchart, A. H. Butler, et al., 2021. Sudden Stratospheric Warmings. *Reviews of Geophysics*, **59**(1), e2020RG000,708. URL <https://doi.org/10.1029/2020RG000708>. 2.1.8



- Baldwin, M. P., L. J. Gray, T. J. Dunkerton, K. Hamilton, P. H. Haynes, et al., 2001. The quasi-biennial oscillation. *Reviews of Geophysics*, **39**(2), 179–229. URL <https://doi.org/10.1029/1999RG000073>. 2.1.9
- Bates, D. R., and M. Nicolet, 1950. ATMOSPHERIC HYDROGEN. *Publications of the Astronomical Society of the Pacific*, **62**(365), 106. URL <https://dx.doi.org/10.1086/126244>. 1, 2.1.5, 2.1.10
- Baumgaertner, A. J. G., A. Seppälä, P. Jöckel, and M. A. Clilverd, 2011. Geomagnetic activity related NO<sub>x</sub> enhancements and polar surface air temperature variability in a chemistry climate model: modulation of the NAM index. *Atmospheric Chemistry and Physics*, **11**(9), 4521–4531. URL <https://doi.org/10.5194/acp-11-4521-2011>. 2.1.10, 2.1.10, 2.1.10
- Beard, K. V., H. T. Ochs III, and C. H. Twohy, 2004. Aircraft measurements of high average charges on cloud drops in layer clouds. *Geophysical Research Letters*, **31**(14). URL <https://doi.org/10.1029/2004GL020465>. 2.2.5
- Belov, A., 2017. Flares, ejections, proton events. *Geomagn. Aeron*, **57**, 727–737. URL <https://doi.org/10.1134/S0016793217060020>. 2.1.3
- Benjamini, Y., and Y. Hochberg, 1995. Controlling the False Discovery Rate: A Practical and Powerful Approach to Multiple Testing. *Journal of the Royal Statistical Society: Series B (Methodological)*, **57**(1), 289–300. URL <https://doi.org/10.1111/j.2517-6161.1995.tb02031.x>. 3.3.1
- Blanc, M., 1988. Magnetosphere-ionosphere coupling. *Computer Physics Communications*, **49**(1), 103–118. URL [https://doi.org/10.1016/0010-4655\(88\)90219-6](https://doi.org/10.1016/0010-4655(88)90219-6). 2.2.3
- Bochniek, J., and P. Hejda, 2005. The winter NAO pattern changes in association with solar and geomagnetic activity. *Journal of Atmospheric and Solar-Terrestrial Physics*, **67**(1), 17–32. Solar Activity Forcing of the Middle Atmosphere, URL <https://doi.org/10.1016/j.jastp.2004.07.014>. 2.1.10
- Bochniek, J., and P. Hejda, 2006. Connections between the distribution of prevailing winds in the winter Northern Hemisphere, solar/geomagnetic activity and the QBO phase. *Studia Geophysica et Geodaetica*, **50**(3), 299–318. URL <https://doi.org/10.1007/s11200-006-0017-9>. 2.1.10, 2.1.10
- Bönisch, H., A. Engel, T. Birner, P. Hoor, D. W. Tarasick, and E. A. Ray, 2011. On the structural changes in the Brewer-Dobson circulation after 2000. *Atmospheric Chemistry and Physics*, **11**(8), 3937–3948. URL <https://doi.org/10.5194/acp-11-3937-2011>. 2.7
- Borovsky, J., 2016. Relativity and the Solar Wind: The Maxwell-Equation Origins of the Solar-Wind Motional Electric Field. *Journal of Electromagnetic Analysis and Applications*, **8**, 133–151. URL <https://doi.org/10.4236/jemaa.2016.88014>. 2.2.3
- Borovsky, J. E., and J. A. Valdivia, 2018. The Earths Magnetosphere: A Systems Science Overview and Assessment. *Surveys in Geophysics*, **39**(5), 817–859. URL <https://doi.org/10.1007/s10712-018-9487-x>. 2.1.1

- Brock, C. A., P. Hamill, J. C. Wilson, H. H. Jonsson, and K. R. Chan, 1995. Particle Formation in the Upper Tropical Troposphere: A Source of Nuclei for the Stratospheric Aerosol. *Science*, **270**(5242), 1650–1653. URL <https://doi.org/10.1126/science.270.5242.1650>. 2.2.5
- Bromwich, D., J. Nicolas, K. Hines, J. Kay, E. Key, et al., 2012. Tropospheric clouds in Antarctica. *Reviews of Geophysics*, **50**. URL <https://doi.org/10.1029/2011RG000363>. 2.2.6
- Brönnimann, S., J. L. Annis, C. Vogler, and P. D. Jones, 2007. Reconstructing the quasi-biennial oscillation back to the early 1900s. *Geophysical Research Letters*, **34**(22). URL <https://doi.org/10.1029/2007GL031354>. 4.2.2
- Bucha, V., and V. Bucha, 1998. Geomagnetic forcing of changes in climate and in the atmospheric circulation. *Journal of Atmospheric and Solar-Terrestrial Physics*, **60**(2), 145–169. URL [https://doi.org/10.1016/S1364-6826\(97\)00119-3](https://doi.org/10.1016/S1364-6826(97)00119-3). 2.1.10
- Burns, G. B., A. V. Frank-Kamenetsky, B. A. Tinsley, W. J. R. French, P. Grigioni, G. Camporeale, and E. A. Bering, 2017. Atmospheric Global Circuit Variations from Vostok and Concordia Electric Field Measurements. *Journal of the Atmospheric Sciences*, **74**(3), 783 – 800. URL <https://doi.org/10.1175/JAS-D-16-0159.1>. 2.2.4, 2.2.6
- Burns, G. B., B. A. Tinsley, A. V. Frank-Kamenetsky, and E. A. Bering, 2007. Interplanetary magnetic field and atmospheric electric circuit influences on ground-level pressure at Vostok. *Journal of Geophysical Research: Atmospheres*, **112**(D4). URL <https://doi.org/10.1029/2006JD007246>. 1, 2.2.7, 2.2.7
- Burns, G. B., B. A. Tinsley, A. V. Frank-Kamenetsky, O. A. Troshichev, W. J. R. French, and A. R. Klekociuk, 2012. Monthly Diurnal Global Atmospheric Circuit Estimates Derived from Vostok Electric Field Measurements Adjusted for Local Meteorological and Solar Wind Influences. *Journal of the Atmospheric Sciences*, **69**(6), 2061 – 2082. URL <https://doi.org/10.1175/JAS-D-11-0212.1>. 2.2.4
- Burns, G. B., B. A. Tinsley, W. J. R. French, O. A. Troshichev, and A. V. Frank-Kamenetsky, 2008. Atmospheric circuit influences on ground-level pressure in the Antarctic and Arctic. *Journal of Geophysical Research: Atmospheres*, **113**(D15). URL <https://agupubs.onlinelibrary.wiley.com/doi/abs/10.1029/2007JD009618>. 1, 2.2.7, 2.20, 2.2.7, 2.2.7, 5.1
- Butchart, N., 2014. The Brewer–Dobson circulation. *Reviews of Geophysics*, **52**(2), 157–184. URL <https://doi.org/10.1002/2013RG000448>. 2.1.6
- Callis, L. B., M. Natarajan, J. D. Lambeth, and D. N. Baker, 1998. Solar atmospheric coupling by electrons (SOLACE): 2. Calculated stratospheric effects of precipitating electrons, 1979–1988. *Journal of Geophysical Research: Atmospheres*, **103**(D21), 28,421–28,438. URL <https://doi.org/10.1029/98JD02407>. 2.1.10
- Chapman, S., 1930. XXXV. On ozone and atomic oxygen in the upper atmosphere. *The London, Edinburgh, and Dublin Philosophical Magazine and Journal of Science*, **10**(64), 369–383. URL <https://doi.org/10.1080/14786443009461588>. 2.1.5
- Charney, J. G., and P. G. Drazin, 1961. Propagation of planetary-scale disturbances from the lower into the upper atmosphere. *jgr*, **66**(1), 83–109. URL <https://doi.org/10.1029/JZ066i001p00083>. 2.1.8

- Cho, Y.-M., G. G. Shepherd, Y.-I. Won, S. Sargoytchev, S. Brown, and B. Solheim, 2004. MLT cooling during stratospheric warming events. *Geophysical Research Letters*, **31**(10). URL <https://doi.org/10.1029/2004GL019552>. 2.1.8
- Clarke, A. D., 1992. Atmospheric nuclei in the remote free-troposphere. *Journal of Atmospheric Chemistry*, **14**, 479–488. URL <https://doi.org/10.1007/BF00115252>. 2.2.5
- Clilverd, M. A., A. Seppälä, C. J. Rodger, P. T. Verronen, and N. R. Thomson, 2006. Ionospheric evidence of thermosphere-to-stratosphere descent of polar NO<sub>x</sub>. *Geophysical Research Letters*, **33**(19). URL <https://doi.org/10.1029/2006GL026727>. 2.1.10
- Cong, W., C. Yan-mei, A. Xian-zhi, L. Bing-xian, W. Jing-jing, and L. Si-qing, 2019. Relationship of Halo CMEs and Solar Proton Events. *Chinese Astronomy and Astrophysics*, **43**(1), 34–46. URL <https://doi.org/10.1016/j.chinastron.2019.02.006>. 2.1.3, 2.1.8
- Copernicus Climate Change Service, C., 2017. ERA5: Fifth generation of ECMWF atmospheric reanalyses of the global climate. Copernicus Climate Change Service Climate Data Store (CDS), date of access: 2020/11/12, <https://cds.climate.copernicus.eu/cdsapp#!/home>. 4.2.1
- Crutzen, P. J., 1970. The influence of nitrogen oxides on the atmospheric ozone content. *Quarterly Journal of the Royal Meteorological Society*, **96**(408), 320–325. URL <https://doi.org/10.1002/qj.49709640815>. 1, 2.1.5, 2.1.10
- Damiani, A., B. Funke, M. López Puertas, M. L. Santee, R. R. Cordero, and S. Watanabe, 2016. Energetic particle precipitation: A major driver of the ozone budget in the Antarctic upper stratosphere. *Geophysical Research Letters*, **43**(7), 3554–3562. URL <https://doi.org/10.1002/2016GL068279>. 2.1.10
- Dungey, J. W., 1961. Interplanetary Magnetic Field and the Auroral Zones. *Phys. Rev. Lett.*, **6**, 47–48. URL <https://link.aps.org/doi/10.1103/PhysRevLett.6.47>. 2.1.1, 2.2.3
- Dungey, J. W., 1963. The structure of the exosphere, or adventures in velocity space. *Geophysics: The Earths Environment*, 505–550. 2.1.1
- Dunne, E. M., H. Gordon, A. Kürten, J. Almeida, J. Duplissy, et al., 2016. Global atmospheric particle formation from CERN CLOUD measurements. *Science*, **354**(6316), 1119–1124. URL <https://doi.org/10.1126/science.aaf2649>. 2.2.5
- Egorova, T., E. Rozanov, V. Zubov, and I. Karol, 2003. Model for investigating ozone trends (MEZON). *IZVESTIYA ATMOSPHERIC AND OCEANIC PHYSICS*, **39**(3), 277–292. 4.2.2
- ESA, ????. Basic motion of trapped particles in the earth magnetic field. URL [https://www.esa.int/ESA\\_Multimedia/Images/2007/03/Basic\\_motion\\_of\\_trapped\\_particles\\_in\\_the\\_earth\\_magnetic\\_field](https://www.esa.int/ESA_Multimedia/Images/2007/03/Basic_motion_of_trapped_particles_in_the_earth_magnetic_field). 2.3
- Eswaraiah, S., J.-H. Kim, W. Lee, J. Hwang, K. N. Kumar, and Y. H. Kim, 2020. Unusual Changes in the Antarctic Middle Atmosphere During the 2019 Warming in the Southern Hemisphere. *Geophysical Research Letters*, **47**(19), e2020GL089199. URL <https://doi.org/10.1029/2020GL089199>. 2.1.8

- Frank-Kamenetsky, A. V., O. A. Troshichev, G. B. Burns, and V. O. Papitashvili, 2001. Variations of the atmospheric electric field in the near-pole region related to the interplanetary magnetic field. *Journal of Geophysical Research: Space Physics*, **106**(A1), 179–190. URL <https://doi.org/10.1029/2000JA900058>. 1, 2.2.3
- Frederick, J. E., and B. A. Tinsley, 2018. The response of longwave radiation at the South Pole to electrical and magnetic variations: Links to meteorological generators and the solar wind. *Journal of Atmospheric and Solar-Terrestrial Physics*, **179**, 214–224. URL <https://doi.org/10.1016/j.jastp.2018.08.003>. 2.2.6
- Frederick, J. E., B. A. Tinsley, and L. Zhou, 2019. Relationships between the solar wind magnetic field and ground-level longwave irradiance at high northern latitudes. *Journal of Atmospheric and Solar-Terrestrial Physics*, **193**, 105,063. URL <https://doi.org/10.1016/j.jastp.2019.105063>. 2.2.5, 2.2.6, 2.2.7
- Freeman, M. P., and M. M. Lam, 2019. Regional, seasonal, and inter-annual variations of Antarctic and sub-Antarctic temperature anomalies related to the Mansurov effect. *Environmental Research Communications*, **1**(11), 111,007. URL <https://dx.doi.org/10.1088/2515-7620/ab4a84>. 2.2.7, 2.2.7
- Funke, B., M. López-Puertas, G. P. Stiller, S. Versick, and T. von Clarmann, 2016. A semi-empirical model for mesospheric and stratospheric NO<sub>y</sub> produced by energetic particle precipitation. *Atmospheric Chemistry and Physics*, **16**(13), 8667–8693. URL <https://doi.org/10.5194/acp-16-8667-2016>. 4.2.2
- Funke, B., M. López-Puertas, S. Gil-López, T. von Clarmann, G. P. Stiller, H. Fischer, and S. Kellmann, 2005. Downward transport of upper atmospheric NO<sub>x</sub> into the polar stratosphere and lower mesosphere during the Antarctic 2003 and Arctic 2002/2003 winters. *Journal of Geophysical Research: Atmospheres*, **110**(D24). URL <https://doi.org/10.1029/2005JD006463>. 2.1.10
- Funke, B., M. López-Puertas, G. P. Stiller, and T. von Clarmann, 2014. Mesospheric and stratospheric NO<sub>y</sub> produced by energetic particle precipitation during 20022012. *Journal of Geophysical Research: Atmospheres*, **119**(7), 4429–4446. URL <https://doi.org/10.1002/2013JD021404>. 2.1.10
- Gerontidou, M., A. Vassilaki, H. Mavromichalaki, and V. Kurt, 2002. Frequency distributions of solar proton events. *Journal of Atmospheric and Solar-Terrestrial Physics*, **64**(5), 489–496. Space Storms and Space Weather, URL [https://doi.org/10.1016/S1364-6826\(02\)00004-4](https://doi.org/10.1016/S1364-6826(02)00004-4). 2.1.5
- Graf, H.-F., I. Kirchner, and J. Perlwitz, 1998. Changing lower stratospheric circulation: The role of ozone and greenhouse gases. *Journal of Geophysical Research: Atmospheres*, **103**(D10), 11,251–11,261. URL <https://doi.org/10.1029/98JD00341>. 2.1.5, 2.1.10
- Graham, R. M., S. R. Hudson, and M. Maturilli, 2019. Improved Performance of ERA5 in Arctic Gateway Relative to Four Global Atmospheric Reanalyses. *Geophysical Research Letters*, **46**(11), 6138–6147. URL <https://doi.org/10.1029/2019GL082781>. 4.2.1
- Griffiths, R. F., J. Latham, and V. Myers, 1974. The ionic conductivity of electrified clouds. *Quarterly Journal of the Royal Meteorological Society*, **100**(424), 181–190. URL <https://doi.org/10.1002/qj.49710042405>. 2.2.5

- Haigh, J., 2017. The role of stratospheric ozone in modulating the solar radiative forcing of climate. *Nature*, **370**, 544–546. URL <https://doi.org/10.1038/370544a0>. 4.2.2
- Hairston, M. R., and R. A. Heelis, 1990. Model of the high-latitude ionospheric convection pattern during southward interplanetary magnetic field using DE 2 data. *Journal of Geophysical Research: Space Physics*, **95**(A3), 2333–2343. URL <https://doi.org/10.1029/JA095iA03p02333>. 2.2.3
- Hauchecorne, A., J.-L. Bertaux, F. Dalaudier, C. Cot, J.-C. Lebrun, et al., 2005. First simultaneous global measurements of nighttime stratospheric NO<sub>2</sub> and NO<sub>3</sub> observed by Global Ozone Monitoring by Occultation of Stars (GOMOS)/Envisat in 2003. *Journal of Geophysical Research: Atmospheres*, **110**(D18). <https://doi.org/10.1029/2004JD005711>. 2.1.10
- Hauchecorne, C. C. K. P. M. A., A., 2022. Stratospheric Final Warmings fall into two categories with different evolution over the course of the year. *Communications Earth Environment*, **3**(4). URL <https://doi.org/10.1038/s43247-021-00335-z>. 6.2
- Hiraga, R., and Y. Omura, 2020. Acceleration mechanism of radiation belt electrons through interaction with multi-subpacket chorus waves. *Earth Planets Space*, **72**(21). URL <https://doi.org/10.1186/s40623-020-1134-3>. 2.1.4
- Hoeksema, J. T., J. M. Wilcox, and P. H. Scherrer, 1983. The structure of the heliospheric current sheet: 1978–1982. , **88**(A12), 9910–9918. URL <https://doi.org/10.1029/JA088iA12p09910>. 2.2.1
- Holton, J. R., P. H. Haynes, M. E. McIntyre, A. R. Douglass, R. B. Rood, and L. Pfister, 1995. Stratosphere-troposphere exchange. *Reviews of Geophysics*, **33**(4), 403–439. URL <https://doi.org/10.1029/95RG02097>. 2.1.6
- Holton, J. R., and R. S. Lindzen, 1972. An Updated Theory for the Quasi-Biennial Cycle of the Tropical Stratosphere. *Journal of Atmospheric Sciences*, **29**(6), 1076 – 1080. URL [https://doi.org/10.1175/1520-0469\(1972\)029<1076:AUTFTQ>2.0.CO;2](https://doi.org/10.1175/1520-0469(1972)029<1076:AUTFTQ>2.0.CO;2). 2.1.9
- Holton, J. R., and H.-C. Tan, 1980. The Influence of the Equatorial Quasi-Biennial Oscillation on the Global Circulation at 50 mb. *Journal of Atmospheric Sciences*, **37**(10), 2200 – 2208. URL [https://doi.org/10.1175/1520-0469\(1980\)037<2200:TIOTEQ>2.0.CO;2](https://doi.org/10.1175/1520-0469(1980)037<2200:TIOTEQ>2.0.CO;2). 2.1.8, 2.1.9
- Holton, J. R., and H.-C. Tan, 1982. The Quasi-Biennial Oscillation in the Northern Hemisphere Lower Stratosphere. *Journal of the Meteorological Society of Japan. Ser. II*, **60**(1), 140–148. URL [https://doi.org/10.2151/jmsj1965.60.1\\_140](https://doi.org/10.2151/jmsj1965.60.1_140). 2.1.9
- Homeyer, C. R., and K. P. Bowman, 2013. Rossby Wave Breaking and Transport between the Tropics and Extratropics above the Subtropical Jet. *Journal of the Atmospheric Sciences*, **70**(2), 607 – 626. URL <https://doi.org/10.1175/JAS-D-12-0198.1>. 2.1.7
- Hurrell, J. W., 1995. Decadal Trends in the North Atlantic Oscillation: Regional Temperatures and Precipitation. *Science*, **269**(5224), 676–679. URL <https://doi.org/10.1126/science.269.5224.676>. 2.1.8
- Johnston, H., 1971. Reduction of stratospheric ozone by nitrogen oxide catalysts from supersonic transport exhaust. *Science*, **173**(3996), 517–522. URL <https://doi.org/10.1126/science.173.3996.517>. 1, 2.1.5, 2.1.10

- Kabin, K., R. Rankin, R. Marchand, T. I. Gombosi, C. R. Clauer, A. J. Ridley, V. O. Pavitashvili, and D. L. DeZeeuw, 2003. Dynamic response of Earth's magnetosphere to By reversals. *Journal of Geophysical Research: Space Physics*, **108**(A3). URL <https://doi.org/10.1029/2002JA009480>. 1, 2.1.1, 2.2.3
- Karagodin, A., I. Mironova, and E. Rozanov, 2022a. Sensitivity of Surface Meteorology to Changes in Cloud Microphysics Associated with IMF B<sub>y</sub>. In A. Kostrov, N. Bobrov, E. Gordeev, E. Kulakov, E. Lyskova, and I. Mironova, eds., *Problems of Geocosmos–2020*, 413–420. Springer International Publishing, Cham. URL [https://doi.org/10.1007/978-3-030-91467-7\\_30](https://doi.org/10.1007/978-3-030-91467-7_30). 2.2.7
- Karagodin, A., E. Rozanov, and I. Mironova, 2022b. On the Possibility of Modeling the IMF By-Weather Coupling through GEC-Related Effects on Cloud Droplet Coalescence Rate. *Atmosphere*, **13**(6). URL <https://doi.org/10.3390/atmos13060881>. 2.2.7
- Kessel, R. L., S.-H. Chen, J. L. Green, S. F. Fung, S. A. Boardsen, L. C. Tan, T. E. Eastman, J. D. Craven, and L. A. Frank, 1996. Evidence of high-latitude reconnecting during northward IMF: Hawkeye observations. *Geophysical Research Letters*, **23**(5), 583–586. URL <https://doi.org/10.1029/95GL03083>. 2.1.1
- Khain, A., V. Arkhipov, M. Pinsky, Y. Feldman, and Y. Ryabov, 2004. Rain Enhancement and Fog Elimination by Seeding with Charged Droplets. Part I: Theory and Numerical Simulations. *Journal of Applied Meteorology*, **43**(10), 1513 – 1529. URL <https://journals.ametsoc.org/view/journals/apme/43/10/jam2131.1.xml>. 2.2.5
- Kleinknecht, N. H., P. J. Espy, and R. E. Hibbins, 2014. The climatology of zonal wave numbers 1 and 2 planetary wave structure in the MLT using a chain of Northern Hemisphere SuperDARN radars. *Journal of Geophysical Research: Atmospheres*, **119**(3), 1292–1307. URL <https://doi.org/10.1002/2013JD019850>. 2.1.8
- Kulmala, M., L. Laakso, K. E. J. Lehtinen, I. Riipinen, M. Dal Maso, T. Anttila, V.-M. Kerminen, U. Hörrak, M. Vana, and H. Tammet, 2004a. Initial steps of aerosol growth. *Atmospheric Chemistry and Physics*, **4**(11/12), 2553–2560. URL <https://doi.org/10.5194/acp-4-2553-2004>. 2.2.5
- Kulmala, M., H. Vehkamäki, T. Petäjä, M. Dal Maso, A. Lauri, V.-M. Kerminen, W. Birmili, and P. McMurry, 2004b. Formation and growth rates of ultrafine atmospheric particles: a review of observations. *Journal of Aerosol Science*, **35**(2), 143–176. URL <https://doi.org/10.1016/j.jaerosci.2003.10.003>. 2.2.5
- Lam, M. M., G. Chisham, and M. P. Freeman, 2013. The interplanetary magnetic field influences mid-latitude surface atmospheric pressure. *Environmental Research Letters*, **8**(4), 045,001. URL <https://dx.doi.org/10.1088/1748-9326/8/4/045001>. 1, 2.17, 2.2.7, 2.21, 4.1
- Lam, M. M., G. Chisham, and M. P. Freeman, 2014. Solar wind-driven geopotential height anomalies originate in the Antarctic lower troposphere. *Geophysical Research Letters*, **41**(18), 6509–6514. URL <https://doi.org/10.1002/2014GL061421>. 1, 2.2.7, 2.2.7, 2.22, 5.1

- Lam, M. M., M. P. Freeman, and G. Chisham, 2018. IMF-driven change to the Antarctic tropospheric temperature due to the global atmospheric electric circuit. *Journal of Atmospheric and Solar-Terrestrial Physics*, **180**, 148–152. Variability of the Sun and Its Terrestrial Impacts, URL <https://doi.org/10.1016/j.jastp.2017.08.027>. 1, 2.2.7, 2.2.7, 2.22, 5.1
- Lam, M. M., and B. A. Tinsley, 2016. Solar wind-atmospheric electricity-cloud microphysics connections to weather and climate. *Journal of Atmospheric and Solar-Terrestrial Physics*, **149**, 277–290. URL <https://doi.org/10.1016/j.jastp.2015.10.019>. 1, 5.1
- Lancaster, G., D. Iatsenko, A. Pidde, V. Ticcinelli, and A. Stefanovska, 2018. Surrogate data for hypothesis testing of physical systems. *Physics Reports*, **748**, 1–60. Surrogate data for hypothesis testing of physical systems, URL <https://doi.org/10.1016/j.physrep.2018.06.001>. 3.2.1
- Langematz, U., M. Kunze, K. Krüger, K. Labitzke, and G. L. Roff, 2003. Thermal and dynamical changes of the stratosphere since 1979 and their link to ozone and CO<sub>2</sub> changes. *Journal of Geophysical Research: Atmospheres*, **108**(D1), ACL 9–1–ACL 9–13. URL <https://doi.org/10.1029/2002JD002069>. 2.1.5, 2.1.10, 2.1.10, 2.1.10
- Lary, D. J., 1997. Catalytic destruction of stratospheric ozone. *Journal of Geophysical Research: Atmospheres*, **102**(D17), 21,515–21,526. URL <https://doi.org/10.1029/97JD00912>. 2.1.5, 2.1.10
- Lean, J., 1997. THE SUN'S VARIABLE RADIATION AND ITS RELEVANCE FOR EARTH. *Annual Review of Astronomy and Astrophysics*, **35**(1), 33–67. URL <https://doi.org/10.1146/annurev.astro.35.1.33>. 4.2.2
- Lee, S.-H., J. M. Reeves, J. C. Wilson, D. E. Hunton, A. A. Viggiano, T. M. Miller, J. O. Ballenthin, and L. R. Lait, 2003. Particle Formation by Ion Nucleation in the Upper Troposphere and Lower Stratosphere. *Science*, **301**(5641), 1886–1889. URL <https://doi.org/10.1126/science.1087236>. 2.2.5
- Li, W., and M. Hudson, 2019. Earth's Van Allen Radiation Belts: From Discovery to the Van Allen Probes Era. *Journal of Geophysical Research: Space Physics*, **124**(11), 8319–8351. URL <https://doi.org/10.1029/2018JA025940>. 2.2, 2.1.4
- Lindzen, R. S., and J. R. Holton, 1968. A Theory of the Quasi-Biennial Oscillation. *Journal of Atmospheric Sciences*, **25**(6), 1095 – 1107. URL [https://doi.org/10.1175/1520-0469\(1968\)025<1095:ATOTQB>2.0.CO;2](https://doi.org/10.1175/1520-0469(1968)025<1095:ATOTQB>2.0.CO;2). 2.1.9
- Liu, H.-L., and R. G. Roble, 2005. Dynamical coupling of the stratosphere and mesosphere in the 2002 Southern Hemisphere major stratospheric sudden warming. *Geophysical Research Letters*, **32**(13). URL <https://doi.org/10.1029/2005GL022939>. 2.1.8
- Lu, H., T. J. Bracegirdle, T. Phillips, A. Bushell, and L. Gray, 2014. Mechanisms for the Holton-Tan relationship and its decadal variation. *Journal of Geophysical Research: Atmospheres*, **119**(6), 2811–2830. URL <https://doi.org/10.1002/2013JD021352>. 2.1.9
- Lu, H., M. A. Clilverd, A. Seppälä, and L. L. Hood, 2008. Geomagnetic perturbations on stratospheric circulation in late winter and spring. *Journal of Geophysical Research: Atmospheres*, **113**(D16). URL <https://doi.org/10.1029/2007JD008915>. 2.1.10, 2.1.10

- Lu, H., M. J. Jarvis, H.-F. Graf, P. C. Young, and R. B. Horne, 2007. Atmospheric temperature responses to solar irradiance and geomagnetic activity. *Journal of Geophysical Research: Atmospheres*, **112**(D11). URL <https://doi.org/10.1029/2006JD007864>. 2.1.10
- Lubin, D., B. Chen, D. H. Bromwich, R. C. J. Somerville, W.-H. Lee, and K. M. Hines, 1998. The Impact of Antarctic Cloud Radiative Properties on a GCM Climate Simulation. *Journal of Climate*, **11**(3), 447 – 462. URL [https://doi.org/10.1175/1520-0442\(1998\)011<0447:TIOACR>2.0.CO;2](https://doi.org/10.1175/1520-0442(1998)011<0447:TIOACR>2.0.CO;2). 2.2.6
- Maliniemi, V., T. Asikainen, and K. Mursula, 2016. Effect of geomagnetic activity on the northern annular mode: QBO dependence and the Holton-Tan relationship. *Journal of Geophysical Research: Atmospheres*, **121**(17), 10,043–10,055. URL <https://doi.org/10.1002/2015JD024460>. 2.1.10, 3.2.1, 5.3
- Maliniemi, V., T. Asikainen, K. Mursula, and A. Seppälä, 2013. QBO-dependent relation between electron precipitation and wintertime surface temperature. *Journal of Geophysical Research: Atmospheres*, **118**(12), 6302–6310. URL <https://doi.org/10.1002/jgrd.50518>. 2.1.10, 3.2.1, 5.3
- Maliniemi, V., R. Marsh, Daniel, H. N. Tyssøy, and C. Smith-Johnsen, 2020. Will Climate Change Impact Polar NO<sub>x</sub> Produced by Energetic Particle Precipitation? *Geophysical Research Letters*, **47**(9), e2020GL087,041. URL <https://doi.org/10.1029/2020GL087041>. 6.2
- Maliniemi, V., H. Nesse Tyssøy, C. Smith-Johnsen, P. Arsenovic, and D. R. Marsh, 2021. Effects of enhanced downwelling of NO<sub>x</sub> on Antarctic upper-stratospheric ozone in the 21st century. *Atmospheric Chemistry and Physics*, **21**(14), 11,041–11,052. URL <https://doi.org/10.5194/acp-21-11041-2021>. 6.2
- Mansurov, S., L. Mansurova, G. Mansurov, V. Mikhnevich, and A. Visotsky, 1974. North-south asymmetry of geomagnetic and tropospheric events. *Journal of Atmospheric and Terrestrial Physics*, **36**(11), 1957–1962. URL [https://doi.org/10.1016/0021-9169\(74\)90182-2](https://doi.org/10.1016/0021-9169(74)90182-2). 1, 2.2, 2.2.7, 5.1
- Marsh, D. R., S. C. Solomon, and A. E. Reynolds, 2004. Empirical model of nitric oxide in the lower thermosphere. *Journal of Geophysical Research: Space Physics*, **109**(A7). URL <https://doi.org/10.1029/2003JA010199>. 2.1.10
- Marsland, S., H. Haak, J. Jungclaus, M. Latif, and F. Röske, 2003. The Max-Planck-Institute global ocean/sea ice model with orthogonal curvilinear coordinates. *Ocean Modelling*, **5**(2), 91–127. URL [https://doi.org/10.1016/S1463-5003\(02\)00015-X](https://doi.org/10.1016/S1463-5003(02)00015-X). 4.2.2
- Matsuno, T., 1970. Vertical Propagation of Stationary Planetary Waves in the Winter Northern Hemisphere. *Journal of Atmospheric Sciences*, **27**(6), 871 – 883. URL [https://doi.org/10.1175/1520-0469\(1970\)027<0871:VPOSPW>2.0.CO;2](https://doi.org/10.1175/1520-0469(1970)027<0871:VPOSPW>2.0.CO;2). 2.1.8, 2.1.8
- Matsuno, T., 1971. A Dynamical Model of the Stratospheric Sudden Warming. *Journal of Atmospheric Sciences*, **28**(8), 1479 – 1494. URL [https://doi.org/10.1175/1520-0469\(1971\)028<1479:ADMOTS>2.0.CO;2](https://doi.org/10.1175/1520-0469(1971)028<1479:ADMOTS>2.0.CO;2). 2.1.8
- Matthes, K., B. Funke, M. E. Andersson, L. Barnard, J. Beer, et al., 2017. Solar forcing for CMIP6 (v3.2). *Geoscientific Model Development*, **10**(6), 2247–2302. URL <https://doi.org/10.5194/gmd-10-2247-2017>. 2.1.3, 4.2.2



- Meinshausen, M., S. J. Smith, K. Calvin, J. S. Daniel, M. L. T. Kainuma, et al., 2011. The RCP greenhouse gas concentrations and their extensions from 1765 to 2300. *Clim. Change*, **109**, 213241. URL <https://doi.org/10.1007/s10584-011-0156-z>. 4.2.2
- Meraner, K., and H. Schmidt, 2018. Climate impact of idealized winter polar mesospheric and stratospheric ozone losses as caused by energetic particle precipitation. *Atmospheric Chemistry and Physics*, **18**(2), 1079–1089. 10.5194/acp-18-1079-2018, URL <https://acp.copernicus.org/articles/18/1079/2018/>. 1, 2.6, 2.1.10, 2.11
- Mironova, I. A., K. L. Aplin, F. Arnold, G. A. Bazilevskaya, R. G. Harrison, A. A. Krivolutsky, K. A. Nicoll, E. V. Rozanov, E. Turunen, and I. G. Usoskin, 2015. Energetic Particle Influence on the Earths Atmosphere. *Space Sci Rev*, **194**, 1–96. URL <https://doi.org/10.1007/s11214-015-0185-4>. 2.1.3
- Mudiar, D., S. D. Pawar, V. Gopalakrishnan, and E. Williams, 2021. Electric Field Enlarges Raindrops Beneath Electrified Clouds: Observational Evidence. *Geophysical Research Letters*, **48**(14), e2021GL093577. URL <https://doi.org/10.1029/2021GL093577>. 2.2.5
- Muthers, S., J. G. Anet, A. Stenke, C. C. Raible, E. Rozanov, et al., 2014. The coupled atmospherechemistryocean model SOCOL-MPIOM. *Geoscientific Model Development*, **7**(5), 2157–2179. URL <https://doi.org/10.5194/gmd-7-2157-2014>. 4.2.2
- Neuman, P., B. Meeson, E. Smith, C. Evans, M. Alfultis, R. Bell, and C. Rice. The Stratospheric Ozone: Electronic Textbook, chap. 3: Morphology of Ozone. NASA, 2000. URL [http://www.ccpo.odu.edu/SEES/ozone/oz\\_class.htm](http://www.ccpo.odu.edu/SEES/ozone/oz_class.htm). 2.1.5
- Nicoll, K. A., 2012. Measurements of Atmospheric Electricity Aloft. *Surveys in Geophysics*, **33**, 9911057. URL <https://doi.org/10.1007/s10712-012-9188-9>. 2.2.5
- Nicoll, K. A., and R. G. Harrison, 2016. Stratiform cloud electrification: comparison of theory with multiple in-cloud measurements. *Quarterly Journal of the Royal Meteorological Society*, **142**(700), 2679–2691. URL <https://doi.org/10.1002/qj.2858>. 2.2.5
- Palamara, D. R., and E. A. Bryant, 2004. Geomagnetic activity forcing of the Northern Annular Mode via the stratosphere. *Annales Geophysicae*, **22**(3), 725–731. URL <https://doi.org/10.5194/angeo-22-725-2004>. 2.1.10, 2.1.10
- Parker, E. N., 1965. Dynamical Theory of the Solar Wind. , **4**(5-6), 666–708. URL <https://doi.org/10.1007/BF00216273>. 2.2.1
- Pettigrew, E. D., S. G. Shepherd, and J. M. Ruohoniemi, 2010. Climatological patterns of high-latitude convection in the Northern and Southern hemispheres: Dipole tilt dependencies and interhemispheric comparisons. *Journal of Geophysical Research: Space Physics*, **115**(A7). URL <https://doi.org/10.1029/2009JA014956>. 1, 2.2.3
- Petty, G. A First Course in Atmospheric Radiation, chap. A First Course in Atmospheric Radiation. Sundog Publishing, 2006. URL [http://www.ccpo.odu.edu/SEES/ozone/oz\\_class.htm](http://www.ccpo.odu.edu/SEES/ozone/oz_class.htm). 2.1.5
- PhysicsToday, 2001. Spacecraft Probes the Site of Magnetic Reconnection in Earths Magnetotail. URL <https://doi.org/10.1063/1.1420541>. 2.1

- Pilipp, W. G., H. Miggenrieder, M. D. Montgomery, K. H. Mühlhäuser, H. Rosenbauer, and R. Schwenn, 1987. Characteristics of electron velocity distribution functions in the solar wind derived from the Helios Plasma Experiment. *Journal of Geophysical Research: Space Physics*, **92**(A2), 1075–1092. URL <https://doi.org/10.1029/JA092iA02p01075>. 2.1.4
- Portmann, R., J. Daniel, and A. Ravishankara, 2012. Stratospheric ozone depletion due to nitrous oxide: influences of other gases. *Philos Trans R Soc Lond B Biol Sci*, **367**(1593), 1256–64. URL <https://doi.org/10.1098/rstb.2011.0377>. 2.1.5, 2.1.10
- Pruppacher, H. R., and J. D. Klett. Microphysics of clouds and precipitation. Kluwer Academic Publishers, 2nd ed. edn., 1997. 2.2.5
- Rabier, F., H. Järvinen, E. Klinker, J.-F. Mahfouf, and A. Simmons, 2000. The ECMWF operational implementation of four-dimensional variational assimilation. I: Experimental results with simplified physics. *Quarterly Journal of the Royal Meteorological Society*, **126**(564), 1143–1170. URL <https://doi.org/10.1002/qj.49712656415>. 4.2.1
- Randall, C. E., V. L. Harvey, G. L. Manney, Y. Orsolini, M. Codrescu, et al., 2005. Stratospheric effects of energetic particle precipitation in 20032004. *Geophysical Research Letters*, **32**(5). URL <https://doi.org/10.1029/2004GL022003>. 1, 2.1.5, 2.1.5, 2.1.10
- Randel, W. J., and F. Wu, 1999. Cooling of the Arctic and Antarctic Polar Stratospheres due to Ozone Depletion. *Journal of Climate*, **12**(5), 1467 – 1479. URL [https://doi.org/10.1175/1520-0442\(1999\)012<1467:COTAAA>2.0.CO;2](https://doi.org/10.1175/1520-0442(1999)012<1467:COTAAA>2.0.CO;2). 2.1.5
- Reeves, G. D., K. L. McAdams, R. H. W. Friedel, and T. P. O'Brien, 2003. Acceleration and loss of relativistic electrons during geomagnetic storms. *Geophysical Research Letters*, **30**(10). URL <https://doi.org/10.1029/2002GL016513>. 2.1.4
- Reeves, G. D., H. E. Spence, M. G. Henderson, S. K. Morley, R. H. W. Friedel, et al., 2013. Electron Acceleration in the Heart of the Van Allen Radiation Belts. *Science*, **341**(6149), 991–994. URL <https://doi.org/10.1126/science.1237743>. 2.1.4
- Roble, R. G., and I. Tzur, 1986. The global atmospheric-electrical circuit. *The Earth's Electrical Environment*, **69**(6), 206–231. URL <https://cir.nii.ac.jp/crid/1572261548986890112>. 2.2.2
- Rodas, C., and M. Pulido, 2017. A climatology of Rossby wave generation in the middle atmosphere of the Southern Hemisphere from MERRA reanalysis. *Journal of Geophysical Research: Atmospheres*, **122**(17), 8982–8997. URL <https://doi.org/10.1002/2017JD026597>. 2.1.7
- Roeckner, E., G. Bäuml, L. Bonaventura, R. Brokopf, M. Esch, M. Giorgetta, and et al., 2003. The atmospheric general circulation model ECHAM 5. PART I: Model description. *Max-Planck-Institut für Meteorologie*, (349). URL <https://hdl.handle.net/11858/00-001M-0000-0012-0144-5>. 4.2.2
- Rosenlof, K. H., 1995. Seasonal cycle of the residual mean meridional circulation in the stratosphere. *Journal of Geophysical Research: Atmospheres*, **100**(D3), 5173–5191. URL <https://doi.org/10.1029/94JD03122>. 2.1.6

- Rosby, C.-G., 1939. Relation between variations in the intensity of the zonal circulation of the atmosphere and the displacements of the semipermanent centers of action. *J. Marine Res.*, **2**, 38–54. 2.1.7
- Roazanov, E., M. Calisto, T. Egorova, T. Peter, and W. Schmutz, 2012. Influence of the Precipitating Energetic Particles on Atmospheric Chemistry and Climate. *Surv Geophys*, **33**, 483–501. URL <https://doi.org/10.1007/s10712-012-9192-0>. 2.1.10, 2.1.10
- Roazanov, E., L. Callis, M. Schlesinger, F. Yang, N. Andronova, and V. Zubov, 2005. Atmospheric response to NO<sub>y</sub> source due to energetic electron precipitation. *Geophysical Research Letters*, **32**(14). URL <https://doi.org/10.1029/2005GL023041>. 1, 2.1.5, 2.1.10
- Salminen, A., T. Asikainen, V. Maliniemi, and K. Mursula, 2019. Effect of Energetic Electron Precipitation on the Northern Polar Vortex: Explaining the QBO Modulation via Control of Meridional Circulation. *Journal of Geophysical Research: Atmospheres*, **124**(11), 5807–5821. URL <https://doi.org/10.1029/2018JD029296>. 2.1.10, 5.3
- Salminen, A., T. Asikainen, V. Maliniemi, and K. Mursula, 2020. Dependence of Sudden Stratospheric Warmings on Internal and External Drivers. *Geophysical Research Letters*, **47**(5), e2019GL086444. URL <https://doi.org/10.1029/2019GL086444>. 2.1.10, 2.1.10, 5.3, 6.1
- Schoeberl, M. R., 1978. Stratospheric warmings: Observations and theory. *Reviews of Geophysics*, **16**(4), 521–538. URL <https://doi.org/10.1029/RG016i004p00521>. 2.1.8
- Seppälä, A., 2007. Observations of production and transport of NO<sub>x</sub> formed by energetic particle precipitation in the polar night atmosphere. Ph.D. thesis. 2.5
- Seppälä, A., H. Lu, M. A. Clilverd, and C. J. Rodger, 2013. Geomagnetic activity signatures in wintertime stratosphere wind, temperature, and wave response. *Journal of Geophysical Research: Atmospheres*, **118**(5), 2169–2183. URL <https://doi.org/10.1002/jgrd.50236>. 2.1.10
- Seppälä, A., C. E. Randall, M. A. Clilverd, E. Roazanov, and C. J. Rodger, 2009. Geomagnetic activity and polar surface air temperature variability. *Journal of Geophysical Research: Space Physics*, **114**(A10). URL <https://doi.org/10.1029/2008JA014029>. 1, 2.1.10, 2.10, 2.1.10
- Seppälä, A., P. T. Verronen, M. A. Clilverd, C. E. Randall, J. Tamminen, V. Sofieva, L. Backman, and E. Kyrölä, 2007. Arctic and Antarctic polar winter NO<sub>x</sub> and energetic particle precipitation in 20022006. *Geophysical Research Letters*, **34**(12). URL <https://doi.org/10.1029/2007GL029733>. 2.1.10
- Shapiro, A., W. Schmutz, E. Roazanov, M. Schoell, M. Haberreiter, A. Shapiro, and S. Nyeki, 2011. A new approach to the long-term reconstruction of the solar irradiance leads to large historical solar forcing. *A&A*, **529**, A67. URL <https://doi.org/10.1051/0004-6361/201016173>. 4.2.2
- Shepherd, M. G., C. Meek, W. Hocking, C. Hall, N. Partamies, F. Sigernes, A. H. Manson, and W. Ward, 2020. Multi-instrument study of the mesosphere-lower thermosphere dynamics at 80°N during the major SSW in January 2019. *Journal of Atmospheric and Solar-Terrestrial*

- Physics*, **210**, 105,427. URL <https://doi.org/10.1016/j.jastp.2020.105427>. 2.1.8, 2.9
- Shpynev, B., S. Churilov, and M. Chernigovskaya, 2015. Generation of waves by jet-stream instabilities in winter polar stratosphere/mesosphere. *Journal of Atmospheric and Solar-Terrestrial Physics*, **136**, 201–215. SI:Vertical Coupling, URL <https://doi.org/10.1016/j.jastp.2015.07.005>. 2.1.8
- Siingh, D., V. Gopalakrishnan, R. Singh, A. Kamra, S. Singh, V. Pant, R. Singh, and A. Singh, 2007. The atmospheric global electric circuit: An overview. *Atmospheric Research*, **84**(2), 91–110. URL <https://doi.org/10.1016/j.atmosres.2006.05.005>. 2.2.2
- Sinnhuber, M., U. Berger, B. Funke, H. Nieder, T. Reddmann, G. Stiller, S. Versick, T. von Clarmann, and J. M. Wissing, 2018. NO<sub>y</sub> production, ozone loss and changes in net radiative heating due to energetic particle precipitation in 2002–2010. *Atmospheric Chemistry and Physics*, **18**(2), 1115–1147. URL <https://doi.org/10.5194/acp-18-1115-2018>. 2.1.10
- Sinnhuber, M., S. Kazeminejad, and J. M. Wissing, 2011. Interannual variation of NO<sub>x</sub> from the lower thermosphere to the upper stratosphere in the years 19912005. *Journal of Geophysical Research: Space Physics*, **116**(A2). URL <https://doi.org/10.1029/2010JA015825>. 2.1.10
- Sinnhuber, M., H. Nieder, and N. Wieters, 2012. Energetic Particle Precipitation and the Chemistry of the Mesosphere/Lower Thermosphere. *Surveys in Geophysics*, **33**, 1281–1334. URL <https://doi.org/10.1007/s10712-012-9201-3>. 1, 2.1.5, 2.1.10
- Slyunyaev, N. N., E. A. Mareev, and A. A. Zhidkov, 2015. On the variation of the ionospheric potential due to large-scale radioactivity enhancement and solar activity. *Journal of Geophysical Research: Space Physics*, **120**(8), 7060–7082. URL <https://doi.org/10.1002/2015JA021039>. 2.2.4
- Smith, E. J., 2001. The heliospheric current sheet. *Journal of Geophysical Research: Space Physics*, **106**(A8), 15,819–15,831. URL <https://doi.org/10.1029/2000JA000120>. 2.2.1
- Smith-Johnsen, C., H. Nesse Tyssøy, K. Hendrickx, Y. Orsolini, G. Kishore Kumar, L.-K. G. Ødegaard, M. I. Sandanger, F. Stordal, and L. Megner, 2017. Direct and indirect electron precipitation effect on nitric oxide in the polar middle atmosphere, using a full-range energy spectrum. *Journal of Geophysical Research: Space Physics*, **122**(8), 8679–8693. URL <https://doi.org/10.1002/2017JA024364>. 1, 2.1.5, 2.1.10
- Solomon, S., P. J. Crutzen, and R. G. Roble, 1982. Photochemical coupling between the thermosphere and the lower atmosphere: 1. Odd nitrogen from 50 to 120 km. *Journal of Geophysical Research: Oceans*, **87**(C9), 7206–7220. URL <https://doi.org/10.1029/JC087iC09p07206>. 2.1.10
- Song, B.-G., H.-Y. Chun, and I.-S. Song, 2020. Role of Gravity Waves in a Vortex-Split Sudden Stratospheric Warming in January 2009. *Journal of the Atmospheric Sciences*, **77**(10), 3321–3342. URL <https://doi.org/10.1175/JAS-D-20-0039.1>. 2.1.8

- Stenke, A., M. Schraner, E. Rozanov, T. Egorova, B. Luo, and T. Peter, 2013. The SOCOL version 3.0 chemistryclimate model: description, evaluation, and implications from an advanced transport algorithm. *Geoscientific Model Development*, **6**(5), 1407–1427. URL <https://doi.org/10.5194/gmd-6-1407-2013>. 4.2.2
- Sukhodolov, T., E. Rozanov, A. I. Shapiro, J. Anet, C. Cagnazzo, T. Peter, and W. Schmutz, 2014. Evaluation of the ECHAM family radiation codes performance in the representation of the solar signal. *Geoscientific Model Development*, **7**(6), 2859–2866. URL <https://doi.org/10.5194/gmd-7-2859-2014>. 4.2.2
- Sun, J., C. J. Nappo, L. Mahrt, D. Belui, B. Grisogono, et al., 2015. Review of wave-turbulence interactions in the stable atmospheric boundary layer. *Reviews of Geophysics*, **53**(3), 956–993. URL <https://doi.org/10.1002/2015RG000487>. 2.1.7
- Svensmark, H., M. Enghoff, N. Shaviv, and J. Svensmark, 2017. Increased ionization supports growth of aerosols into cloud condensation nuclei. *Nature Communications*, **8**. URL <https://doi.org/10.1038/s41467-017-02082-2>. 2.2.5
- Sætre, C., J. Stadsnes, H. Nesse, A. Aksnes, S. M. Petrinec, C. A. Barth, D. N. Baker, R. R. Vondrak, and N. Østgaard, 2004. Energetic electron precipitation and the NO abundance in the upper atmosphere: A direct comparison during a geomagnetic storm. *Journal of Geophysical Research: Space Physics*, **109**(A9). URL <https://doi.org/10.1029/2004JA010485>. 1, 2.1.5
- Tartaglione, N., T. Toniazzo, Y. Orsolini, and O. H. Otterå, 2020. A note on the statistical evidence for an influence of geomagnetic activity on Northern Hemisphere seasonal-mean stratospheric temperatures using the Japanese 55-year Reanalysis. *Annales Geophysicae*, **38**(2), 545–555. URL <https://doi.org/10.5194/angeo-38-545-2020>. 1, 2.1.10
- Tetzner, D., E. Thomas, and C. Allen, 2019. A Validation of ERA5 Reanalysis Data in the Southern Antarctic Peninsula/Ellsworth Land Region, and Its Implications for Ice Core Studies. *Geosciences*, **9**(7). URL <https://doi.org/10.3390/geosciences9070289>. 4.2.1
- Theiler, J., and D. Prichard, 1996. Constrained-realization Monte-Carlo method for hypothesis testing. *Physica D: Nonlinear Phenomena*, **94**(4), 221–235. URL [https://doi.org/10.1016/0167-2789\(96\)00050-4](https://doi.org/10.1016/0167-2789(96)00050-4). 3.2.1
- Thejll, P., B. Christiansen, and H. Gleisner, 2003. On correlations between the North Atlantic Oscillation, geopotential heights, and geomagnetic activity. *Geophysical Research Letters*, **30**(6). URL <https://doi.org/10.1029/2002GL016598>. 2.1.10, 3.2.1
- Thorne, R. M., B. Ni, X. Tao, R. B. Horne, and N. P. Meredith, 2010. Scattering by chorus waves as the dominant cause of diffuse auroral precipitation. *Nature*, **467**, 943–946. URL <https://doi.org/10.1038/nature09467>. 2.1.4
- Tinsley, B., 2000. Influence of Solar Wind on the Global Electric Circuit, and Inferred Effects on Cloud Microphysics, Temperature, and Dynamics in the Troposphere. *Space Science Reviews*, **94**, 231–258. URL <https://doi.org/10.1023/A:1026775408875>. 2.2.7
- Tinsley, B., R. Rohrbaugh, and M. Hei, 2001. Electroscavenging in clouds with broad droplet size distributions and weak electrification. *Atmospheric Research*, **59–60**, 115–135. 13th International Conference on Clouds and Precipitation, URL [https://doi.org/10.1016/S0169-8095\(01\)00112-0](https://doi.org/10.1016/S0169-8095(01)00112-0). 2.2.5

- Tinsley, B. A., 2022. Uncertainties in Evaluating Global Electric Circuit Interactions With Atmospheric Clouds and Aerosols, and Consequences for Radiation and Dynamics. *Journal of Geophysical Research: Atmospheres*, **127**(5), e2021JD035,954. URL <https://doi.org/10.1029/2021JD035954>. 1, 2.2.4, 2.2.5, 2.2.6
- Tinsley, B. A., and R. A. Heelis, 1993. Correlations of atmospheric dynamics with solar activity evidence for a connection via the solar wind, atmospheric electricity, and cloud microphysics. *Journal of Geophysical Research: Atmospheres*, **98**(D6), 10,375–10,384. URL <https://doi.org/10.1029/93JD00627>. 1, 2.17, 2.2.3, 2.2.7, 4.1
- Tinsley, B. A., L. Zhou, and A. Plemmons, 2006. Changes in scavenging of particles by droplets due to weak electrification in clouds. *Atmospheric Research*, **79**(3), 266–295. URL <https://doi.org/10.1016/j.atmosres.2005.06.004>. 2.2.5
- Tinsley, B. A., L. Zhou, L. Wang, and L. Zhang, 2021. Seasonal and Solar Wind Sector Duration Influences on the Correlation of High Latitude Clouds With Ionospheric Potential. *Journal of Geophysical Research: Atmospheres*, **126**(4), e2020JD034,201. URL <https://doi.org/10.1029/2020JD034201>. 2.2.5, 2.2.6, 2.2.7, 5.2
- Torsti, J., L. G. Kocharov, M. Teittinen, and B. J. Thompson, 1999. Injection of 10 MeV Protons in Association with a Coronal Moreton Wave. *The Astrophysical Journal*, **510**(1), 460. URL <https://dx.doi.org/10.1086/306581>. 2.1.3
- Tu, W., G. S. Cunningham, Y. Chen, S. K. Morley, G. D. Reeves, J. B. Blake, D. N. Baker, and H. Spence, 2014. Event-specific chorus wave and electron seed population models in DREAM3D using the Van Allen Probes. *Geophysical Research Letters*, **41**(5), 1359–1366. URL <https://doi.org/10.1002/2013GL058819>. 2.1.4
- Turner, D. L., V. Angelopoulos, W. Li, J. Bortnik, B. Ni, et al., 2014. Competing source and loss mechanisms due to wave-particle interactions in Earth's outer radiation belt during the 30 September to 3 October 2012 geomagnetic storm. *Journal of Geophysical Research: Space Physics*, **119**(3), 1960–1979. URL <https://doi.org/10.1002/2014JA019770>. 2.1.4
- Turner, D. L., Y. Shprits, M. Hartinger, and V. Angelopoulos, 2012. Explaining sudden losses of outer radiation belt electrons during geomagnetic storms. *Nature Physics*, **8**(3), 208–212. URL <https://doi.org/10.1038/nphys2185>. 2.1.4
- Turunen, E., P. T. Verronen, A. Seppälä, C. J. Rodger, M. A. Clilverd, J. Tamminen, C.-F. Enell, and T. Ulich, 2009. Impact of different energies of precipitating particles on NO<sub>x</sub> generation in the middle and upper atmosphere during geomagnetic storms. *Journal of Atmospheric and Solar-Terrestrial Physics*, **71**(10), 1176–1189. High Speed Solar Wind Streams and Geospace Interactions, URL <https://doi.org/10.1016/j.jastp.2008.07.005>. 1, 2.1.5, 2.1.10
- Tyssøy, H. N., N. Partamies, E. M. Babu, C. Smith-Johnsen, and J. A. Salice, 2021. The Predictive Capabilities of the Auroral Electrojet Index for Medium Energy Electron Precipitation. *Frontiers in Astronomy and Space Sciences*, **8**. URL <https://doi.org/10.3389/fspas.2021.714146>. 2.1.3

- Verronen, P. T., 2021. Response of the Earth's middle atmosphere to solar particle forcing. URL [https://mycourses.aalto.fi/pluginfile.php/1499547/mod\\_resource/content/1/Verronen\\_Space\\_Climate\\_lecture\\_2021.pdf](https://mycourses.aalto.fi/pluginfile.php/1499547/mod_resource/content/1/Verronen_Space_Climate_lecture_2021.pdf). 2.4
- Vincent, R., 2015. The dynamics of the mesosphere and lower thermosphere: a brief review. *Prog. in Earth and Planet. Sci.*, **2**(4). URL <https://doi.org/10.1186/s40645-015-0035-8>. 2.1.6
- Vokhmyanin, M. V., N. A. Stepanov, and V. A. Sergeev, 2019. On the Evaluation of Data Quality in the OMNI Interplanetary Magnetic Field Database. *Space Weather*, **17**(3), 476–486. URL <https://doi.org/10.1029/2018SW002113>. 4.1
- Walterscheid, R. L., G. G. Sivjee, and R. G. Roble, 2000. Mesospheric and lower thermospheric manifestations of a stratospheric warming event over Eureka, Canada (80°N). *Geophysical Research Letters*, **27**(18), 2897–2900. URL <https://doi.org/10.1029/2000GL003768>. 2.1.8
- Ward, W., A. Seppälä, E. Yiğit, T. Nakamura, C. Stolle, et al., 2021. Role Of the Sun and the Middle atmosphere/thermosphere/ionosphere In Climate (ROSMIC): a retrospective and prospective view. *Progress in Earth and Planetary Science*, **8**(1), 47. URL <https://doi.org/10.1186/s40645-021-00433-8>. 1, 2.1.5
- Weimer, D. R., 1996. A flexible, IMF dependent model of high-latitude electric potentials having Space Weather applications. *Geophysical Research Letters*, **23**(18), 2549–2552. URL <https://doi.org/10.1029/96GL02255>. 2.2.3, 2.2.7
- Weimer, D. R., 2001. An improved model of ionospheric electric potentials including substorm perturbations and application to the Geospace Environment Modeling November 24, 1996, event. *Journal of Geophysical Research: Space Physics*, **106**(A1), 407–416. URL <https://doi.org/10.1029/2000JA000604>. 2.2.3, 2.2.7
- Whiteway, J. A., and T. J. Duck, 1996. Evidence for critical level filtering of atmospheric gravity waves. *Geophysical Research Letters*, **23**(2), 145–148. URL <https://doi.org/10.1029/95GL03784>. 2.1.7
- Wilks, D. S., 2006. On Field Significance and the False Discovery Rate. *Journal of Applied Meteorology and Climatology*, **45**(9), 1181 – 1189. URL <https://doi.org/10.1175/JAM2404.1>. 2.2.7
- Wilks, D. S., 2016. The Stippling Shows Statistically Significant Grid Points: How Research Results are Routinely Overstated and Overinterpreted, and What to Do about It. *Bulletin of the American Meteorological Society*, **97**(12), 2263 – 2273. URL <https://journals.ametsoc.org/view/journals/bams/97/12/bams-d-15-00267.1.xml>. 1, 2.2.7, 3.3.1, 3.3.1, 3.3.2
- Yasyukevich, A. S., M. A. Chernigovskaya, B. G. Shpynev, D. S. Khabituev, and Y. V. Yasyukevich, 2022. Features of Winter Stratosphere Small-Scale Disturbance during Sudden Stratospheric Warmings. *Remote Sensing*, **14**(12). URL <https://www.mdpi.com/2072-4292/14/12/2798>. 2.1.8

- Zawedde, A. E., H. Nesse Tyssøy, R. Hibbins, P. J. Espy, L.-K. G. Ødegaard, M. I. Sandanger, and J. Stadsnes, 2016. The impact of energetic electron precipitation on mesospheric hydroxyl during a year of solar minimum. *Journal of Geophysical Research: Space Physics*, **121**(6), 5914–5929. URL <https://doi.org/10.1002/2016JA022371>. 1, 2.1.5
- Zawedde, A. E., H. Nesse Tyssøy, J. Stadsnes, and M. I. Sandanger, 2018. The Impact of Energetic Particle Precipitation on Mesospheric OH Variability of the Sources and the Background Atmosphere. *Journal of Geophysical Research: Space Physics*, **123**(7), 5764–5789. URL <https://doi.org/10.1029/2017JA025038>. 1, 2.1.5
- Zhang, L., B. Tinsley, and L. Zhou, 2022. Responses of CIPS/AIM noctilucent clouds to the interplanetary magnetic field. *Atmospheric Chemistry and Physics*, **22**(20), 13,355–13,370. URL <https://doi.org/10.5194/acp-22-13355-2022>. 2.2.6
- Zhang, Y., J. Fan, X. Chen, Y. Ashkenazy, and S. Havlin, 2019. Significant Impact of Rossby Waves on Air Pollution Detected by Network Analysis. *Geophysical Research Letters*, **46**(21), 12,476–12,485. URL <https://doi.org/10.1029/2019GL084649>. 2.1.7
- Zhou, L., B. Tinsley, L. Wang, and G. Burns, 2018. The zonal-mean and regional tropospheric pressure responses to changes in ionospheric potential. *Journal of Atmospheric and Solar-Terrestrial Physics*, **171**, 111–118. Vertical Coupling in the Atmosphere-Ionosphere System: Recent Progress, URL <https://doi.org/10.1016/j.jastp.2017.07.010>. 2.2.7, 2.23, 2.24, 2.2.7, 5.1
- Zhu, H., L. Chen, S. G. Claudepierre, and L. Zheng, 2020. Direct Evidence of the Pitch Angle Scattering of Relativistic Electrons Induced by EMIC Waves. *Geophysical Research Letters*, **47**(4), e2019GL085,637. URL <https://doi.org/10.1029/2019GL085637>. 2.1.4
- Zhu, J., A. Xie, X. Qin, Y. Wang, B. Xu, and Y. Wang, 2021. An Assessment of ERA5 Reanalysis for Antarctic Near-Surface Air Temperature. *Atmosphere*, **12**(2). URL <https://doi.org/10.3390/atmos12020217>. 4.2.1
- Zúñiga López, H. D., H. N. Tyssøy, C. Smith-Johnsen, and V. Maliniemi, 2022. The Direct Effect of Medium Energy Electron Precipitation on Mesospheric Dynamics During a Sudden Stratospheric Warming Event in 2010. *Geophysical Research Letters*, **49**(13). URL <https://doi.org/10.1029/2022GL097812>. 2.1.10





# **Chapter 7**

## **Scientific Results**



# Paper I

## **The Mansurov effect: Statistical Significance and the role of autocorrelation**

J.Ø. Edvartsen, V. Maliniemi, H. Nesse, T. Asikainen and S. Hatch.

*Journal of Space Weather and Space Climate*, **12**, 11. doi:10.1051/swsc/2022008 (2022)



# The Mansurov effect: Statistical significance and the role of autocorrelation

Jone Edvartsen<sup>1,\*</sup>, Ville Maliniemi<sup>1</sup>, Hilde Nesse Tyssøy<sup>1</sup>, Timo Asikainen<sup>2</sup>, and Spencer Hatch<sup>1</sup>

<sup>1</sup> Birkeland Center for Space Science, Department of Physics and Technology, University of Bergen, 5007 Bergen, Norway  
<sup>2</sup> Space Physics and Astronomy Research Unit, University of Oulu, 90570 Oulu, Finland

Received 22 November 2021 / Accepted 17 March 2022

**Abstract**—The Mansurov effect is related to the interplanetary magnetic field (IMF) and its ability to modulate the global electric circuit, which is further hypothesized to impact the polar troposphere through cloud generation processes. We investigate the connection between IMF  $B_y$ -component and polar surface pressure by using daily ERA5 reanalysis for geopotential height since 1980. Previous studies produce a 27-day cyclic response during solar cycle 23 which appears to be significant according to conventional statistical tests. However, we show here that when statistical tests appropriate for strongly autocorrelated variables are applied, there is a fairly high probability of obtaining the cyclic response and associated correlation merely by chance. Our results also show that data from three other solar cycles produce similar cyclic responses as during solar cycle 23, but with seemingly random offset in respect to the timing of the signal. By generating random normally distributed noise with different levels of temporal autocorrelation and using the real IMF  $B_y$ -time series as forcing, we show that the methods applied to support the Mansurov hypothesis up to now are highly susceptible to random chance as cyclic patterns always arise as artifacts of the methods. The potential non-stationary behavior of the Mansurov effect makes it difficult to achieve solid statistical significance on decadal time scales. We suggest more research on, e.g., seasonal dependence of the Mansurov effect to understand better potential IMF effects in the atmosphere.

**Keywords:** solar-climate link / significance testing / Monte-Carlo / false-detection-rate / periodic forcing

## 1 Introduction

First proposed in 1974, the Mansurov effect is based on the correlation between daily polar surface pressure and the  $B_y$ -component of the interplanetary magnetic field (IMF). A significant correlation has been shown in multiple studies (Mansurov et al., 1974; Burns et al., 2008; Lam et al., 2013, 2014). Evidence of significant ionospheric perturbations related to the same change in  $B_y$  also exists (Tinsley, 2000, 2008; Frank-Kamenetsky et al., 2001; Kabin et al., 2003; Pettigrew et al., 2010; Lam et al., 2013). A physical mechanism involving the Global Electric Circuit (GEC) modulating cloud generation processes has been suggested to link IMF  $B_y$  to the polar surface pressure (Lam & Tinsley, 2016). Studies have also focused on the internally generated vertical current density ( $J_z$ ). The internally driven changes in  $J_z$  have been linked to changes in the polar pressure (Tinsley, 2008; Lam & Tinsley, 2016; Zhou et al., 2018), indicating that the IMF  $B_y$ , which also induces changes in  $J_z$ , could play an important role.

For the Mansurov effect, the theory predicts a positive and negative relation between the IMF  $B_y$ -component and the polar surface pressure/geopotential height in the southern and northern hemispheres, respectively (Burns et al., 2008). The impact on the microphysics of clouds is predicted to begin in less than a day. As this effect is small, it is expected to take days for the accumulative effect to change cloud radiative forcing, leading to pressure changes related to the Mansurov effect (Frederick et al., 2019; Tinsley et al., 2020). The effect has been found to be first detectable in the lower troposphere (Lam et al., 2014). Mansurov et al. (1974) found correlations between IMF  $B_y$  and surface pressure in the time period around 1956–1964 (approximately solar cycle 19). Three individual periods (1964–1974, 1995–2005, and 2006–2015) have been found to show the associated pressure anomalies in both hemispheres (Mansurov et al., 1974; Page, 1989; Zhou et al., 2018). However, the statistical significance is only calculated through  $t$ -test or as one standard deviation of the mean. Most other publications on the effect focus on the period of solar cycle 23 (Burns et al., 2008; Lam et al., 2013, 2014, 2018; Zhou et al., 2018). This time interval produces statistical significance in both hemispheres when assessed by

\*Corresponding author: [jone.edvartsen@uib.no](mailto:jone.edvartsen@uib.no)

the  $t$ -test. Burns et al. (2008) (hereafter B2008) thoroughly investigate the 1995–2005 period.

The IMF  $B_y$  has a 27-day periodicity associated with the solar rotation period (e.g., Gonzalez & Gonzalez, 1987). B2008 found a 27-day periodic pressure response in both hemispheres when regressing polar pressure to the IMF  $B_y$  for the period 1995–2005. This periodic response was attributed as evidence for a physical link between the IMF  $B_y$  and the polar pressure. In the southern hemisphere (SH), statistical significance calculated through the  $t$ -test showed this periodic response to be significant for the given period, while no significance was found for the northern hemisphere (NH). However, it was noted that while statistical significance was not achieved in the NH, the appearance of a 27-day periodic pressure response serves as evidence of the Mansurov effect. Tinsley et al. (2020) found a 27-day periodic response when correlating the IMF  $B_y$  to optical thickness of the overhead stratus-type clouds, which was put forward as evidence of the pathway of the Mansurov effect. In addition, Lam et al. (2018) correlated the IMF  $B_y$  with atmospheric temperature for 1999–2002. The significance is calculated without taking into account the temporal autocorrelation but nonetheless shows a significant temperature perturbation at near-surface atmospheric levels. In the paper, it is also noted that the troposphere shows no significant temperature perturbation. However, a 27-day cycle in the temperature response at this level (and all lower atmospheric levels) is used as evidence for a physical link to the IMF  $B_y$ .

Two different analysis methods are typically used to demonstrate this effect. The first is the superposed epoch method (Mansurov et al., 1974; Lam et al., 2013, 2014). The pressure/geopotential height on days with strong positive  $B_y$  deflections are binned, where the pressure/geopotential height on the days with strong negative  $B_y$  deflections are binned and subtracted from the first bin. This can be represented by the formula  $\Delta p = B_y(+)-B_y(-)$ . The day of the largest deflections is marked as the key date, while different lead–lags are calculated with respect to the key date (similar to time-lagged cross-correlation). The second method is lead–lag regression plots (B2008). Here, the average pressure/geopotential height is calculated in five  $B_y$  bins ( $<-3$ ,  $-3$  to  $-1$ ,  $-1$  to  $1$ ,  $1$  to  $3$ ,  $>3$  (nT)), and the slope of the regression line between the averaged  $B_y$  bins and the corresponding average pressure/geopotential height (regressing 5 data points) is calculated and plotted for chosen daily leads and lags (also similar to time-lagged cross-correlation). We emphasize that both methods yield approximately the same results, as the slope of the regression line strongly depends on the pressure/geopotential height in the lowest and highest  $B_y$  bins.

This paper revisits the Mansurov hypothesis and previously applied methods with a more rigorous estimate of the statistical significance. Emphasis is also put on time periods other than solar cycle 23 (1995–2005). In addition, we examine the lead–lag regression method with the help of Monte Carlo simulations and randomly generated normally distributed temporally uncorrelated (white) noise and autocorrelated (red) noise. The aim is to demonstrate the need for appropriate significance tests, as well as the risk of misinterpreting a response from strongly periodic forcing. The implication of these findings goes beyond the current study as it will apply to all periodic forcing with an autocorrelated response variable.

## 2 Data and method

### 2.1 Solar wind ( $B_y$ ) data

We use hourly averaged IMF  $B_y$  (GSM) values obtained from the National Space Science Data Center (NSSDC) OMNI-Web database (<http://omniweb.gsfc.nasa.gov>) for the interval 1980–2016. IMF  $B_y$  daily averages are calculated when at least 1 hourly value is available.

### 2.2 Pressure/geopotential height data

For the atmospheric data, we use the European Center for Medium-Range Weather Forecast Re-Analysis (ERA5) (<https://cds.climate.copernicus.eu>). As well as being constructed by numerical simulations and models, ERA-5, and all other reanalysis data, uses large amounts of observational values to set the frame. Effectively, the numerical simulations and models work to interpolate the gaps between these observations. Thus, reanalysis data does not have the same accuracy as purely observational data at every grid point. However, it provides a physically justified estimate in these grid points where observations are not available. It is noted that reanalysis data have previously been applied to support the Mansurov effect, particularly ERA5 (Zhou et al., 2018) and NCEP/NCAR (Lam et al., 2013, 2014, 2018; Freeman & Lam, 2019). Mooney et al. (2011) have compared NCEP/NCAR reanalysis data with earlier ERA reanalysis versions, as well as observational data, finding good agreements between all.

We obtain the daily averaged geopotential heights at the 700 hPa (SH) and 1000 hPa (NH) level poleward of  $70^\circ$  in geomagnetic coordinates (mlat), covering the time period 1980–2016. The 700 hPa level is chosen for the SH as it represents the surface level in the Antarctic, while 1000 hPa represents the surface level in the NH. Geomagnetic coordinates are used as the perturbation of IMF  $B_y$  in the ionosphere is centered around the geomagnetic pole. For comparison, B2008 used surface pressure measurements obtained for 11 Antarctic sites from the NNDC (NOAA [National Oceanic and Atmospheric Administration] National Data Centers), selecting values within 90 min of 12 UT. An analog to the quantity  $\Delta p$  (pressure anomalies) that B2008 calculated, a variation value  $\Delta Z_g$  (geopotential height anomalies) is obtained for the geopotential height by subtracting a running mean of  $\pm 15$  days from the daily value in order to remove seasonal variability. It is noted that  $\Delta Z_g$  is averaged over  $70$ – $90^\circ$  mlat.

Figure 1 shows the temporal autocorrelation in  $\Delta Z_g$  (geopotential height anomalies) for the period 1980–2016 in the SH. Positive auto-correlation occurs until day 5. A similar autocorrelation is also found for the period 1995–2005, as well as for  $\Delta Z_g$  in the NH.

### 2.3 False detection rate method

For rigorous statistical testing of our results, we use the False Detection Rate (FDR) method. It was developed by Benjamini & Hochberg (1995) and later applied to atmospheric data by Wilks (2016). The main goal of the method is to account for the expected proportion of falsely rejected hypotheses when dealing with multiple null hypotheses scenarios. Statistically speaking, a result obtaining a  $p$ -value of 0.05

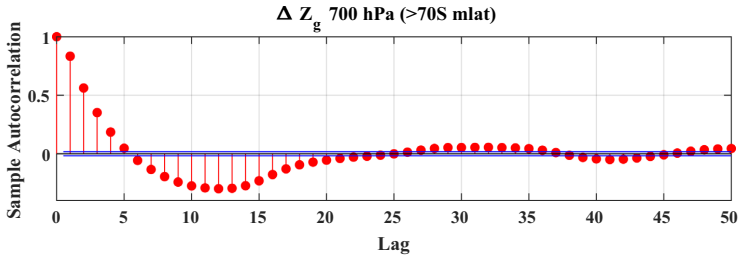


**Fig. 1.** Temporal autocorrelation of  $\Delta Z_g$  over the period 1980–2016. Positive auto-correlation occurs until day 5. The blue lines show the 95% confidence bounds of the autocorrelation function.

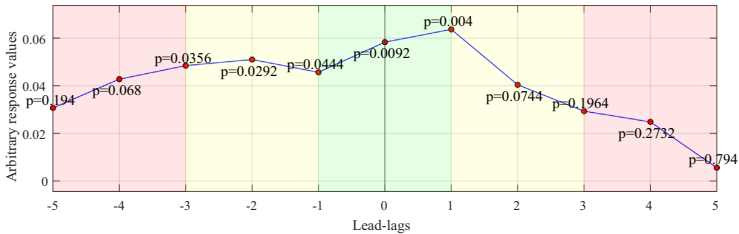


**Fig. 2.** Arbitrary response values on a temporal lead-lag  $x$ -axis (e.g. days). Every data point has also appointed a  $p$ -value. Different lead-lag intervals are shaded in different colors.

**Table 1.** FDR based sorting of  $p$ -values for the whole interval in ascending order.

$n$	1	2	3	4	5	6	7	8	9	10	11 = $N$
$p$ -values	0.004	0.009	0.029	0.035	0.044	0.068	0.074	0.194	0.196	0.273	0.794

implies a 5% probability of that specific result being caused by chance. With an increasing number of null hypotheses (e.g., map plot with multiple grids or a temporal plot showing consecutive days after the onset of a forcing), this 5% probability ultimately leads to an increasing number of falsely rejected null hypotheses.

In FDR, it is stated that if the global null hypothesis cannot be rejected, one cannot conclude that any of the individual tests constitute rejection of the null hypothesis. The method is applied by calculating the  $p$ -values for each individual data point. These  $p$ -values are then sorted in ascending order, matching the set  $i = 1, \dots, N$ , where  $N$  represents the total number of individual tests. The new global  $p$ -value,  $p_{FDR}$ :

$$p_{FDR} = \max[p(i) : p(i) \leq (i/N)\alpha_{FDR}], \quad i = 1, \dots, N \quad (1)$$

is then calculated with  $\alpha_{FDR} = 0.05$ , corresponding to significance at the 95% level (Wilks, 2016).

Figure 2 illustrates how FDR is used and calculated for a superposed epoch analysis on a daily scale represented by lead-lags. Also included are  $p$ -values obtained for each lead-lag. In this example, there is an arbitrary forcing that is nonzero and starts to increase at day  $-5$ , reaching a maximum at day 0, before it slowly decreases to zero at day  $+5$ . We also assume that the arbitrary forcing has an impact on the arbitrary response as long as it is nonzero. As the forcing is nonzero through the whole interval, we can also assume that every individual lead-lag has the same null hypothesis and that we are dealing

with a multiple hypotheses situation for lead-lags  $-5$  to  $+5$ . According to FDR, we first have to sort the  $p$ -values for the whole interval in ascending order (see Table 1).

Then, we have to apply Equation (1) iteratively until we reach the maximum  $p$ -value satisfying the criteria:

$$P(n)_{\text{ascending}} \leq n \times \frac{0.05}{N}, \quad (2)$$

$$0.004 \leq 1 \times \frac{0.05}{11} = \text{True} \quad (3)$$

$$0.009 \leq 2 \times \frac{0.05}{11} = \text{True} \quad (4)$$

$$0.029 \leq 3 \times \frac{0.05}{11} = \text{False} \quad (5)$$

⋮

Everyother is also False.

As the  $p = 0.009$  is the maximum value satisfying the criteria, this becomes the global  $p$ -value ( $p_{FDR}$ ) and defines the limit for the individual  $p$ -values to be regarded as significant at the 0.05 level after one has accounted for the false detection rate. In our example, this means that when the signal is looked at as a set of multiple equivalent null hypotheses, statistical



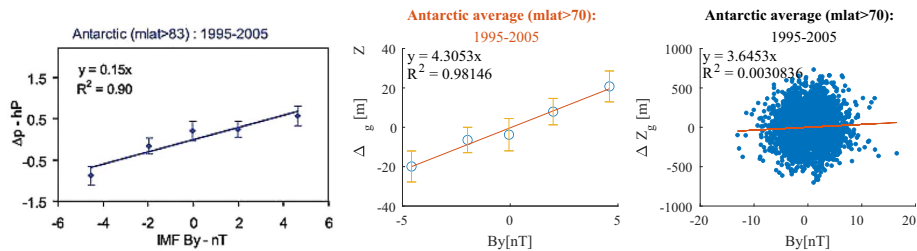


**Fig. 3.** *Left panel:* A copy of the upper panel of Figure 1 in B2008. It represents linear regression of  $\Delta p$  after the original measurement from three Antarctic stations at  $mLat > 83^\circ S$  was grouped according to the IMF  $B_y$ . *Middle panel:* Reproduction of the linear regression method using  $\Delta Z_g$  at  $\sim mLat > 70^\circ S$ . Error bars are plus/minus one standard-error-in-the-mean. *Right panel:* Scatter plot and linear regression for the  $\Delta Z_g$  data without the initial five-bin grouping. The upper panel of Figure 1 in B2008 is reproduced with permission from John Wiley and Sons.

significance is found at lead-lag 0 and +1. As we know the onset and offset of the forcing, this could be interpreted as lead-lag 0 and +1 being the only days where it is possible to distinguish a signal from the background noise in the data.

For this method to be correctly applied, it is important that the definition of equivalent null hypotheses is correct. For instance, assuming only three consecutive days around day zero (-1 to +1) to have equivalent null hypotheses, and performing the FDR method, would result in all of them satisfying the criteria ( $p_{FDR} = 0.044$ ). This would yield one more significant data point than what was acquired when the full interval -5 to +5 was grouped as a whole through the FDR method. Because of this, we will be testing different intervals when estimating the significance using the FDR method in lead-lag correlation plots in the following section. Multiple hypothesis testing situations can also be dealt with other methods than FDR, e.g., calculating a field significance or effective spatial degrees of freedom (Bretherton et al., 1999). While the FDR method is not yet well known in the atmospheric or space science communities, it offers a simple but superb way to deal with multiple hypothesis testing scenarios (Wilks, 2016).

### 3 Analyses and results

#### 3.1 Regression results for the time period 1995–2005

Based on observations from the 11 Antarctic stations, B2008 calculated the average  $\Delta p$  (surface pressure) values at each site within five separate IMF  $B_y$  bins:  $< -3$ ,  $-3$  to  $-1$ ,  $-1$  to  $1$ ,  $1$  to  $3$ , and  $> 3$  nT. Linear regression was then applied to the average value of  $\Delta p$  within these five intervals. The result for  $> 83^\circ S$   $mLat$ , corresponding to the upper panel of Figure 1 in B2008, is shown in the left panel in Figure 3. The same procedure is done for  $\Delta Z_g$  (equivalent to surface pressure), seen in the middle panel in Figure 3. Also included is a linear regression without the initial binning and averaging, as seen in the right panel in Figure 3. Note that the regression coefficients are similar with or without performing the initial binning, while the correlation coefficient ( $R^2$ ) differs substantially.

From the regression coefficient produced by these five data bins, lead-lag variations are calculated by B2008, as seen in the left panel of Figure 4. A clear 27-day cycle is seen for both data

sets, with the peak pressure value lagging the driver by -2 days. The significance has been estimated by Student's  $t$ -test, with the uncertainty illustrated by the cross at the keydate. Figures 3 and 4 indicate that  $\Delta Z_g$  yields a similar response as  $\Delta p$  in B2008. Furthermore, note that the normal regression without the initial grouping gives similar lead-lag regression coefficients.

When applying the  $t$ -test, a highly significant pattern is observed, as shown in the right panel of Figure 4. However, the lead-lag analysis is strongly affected by the temporal autocorrelation in the  $\Delta Z_g$  time series (Fig. 1). Instead of a  $t$ -test, we perform a Monte Carlo (MC) simulation to estimate the significance of the regression coefficients. For every iteration of the MC-simulation, phase randomization is applied to the  $\Delta Z_g$  data series. In essence, phase randomization scrambles the harmonic phases of the series. This results in a physically unrelated data series but preserves the autocorrelation function of  $\Delta Z_g$ , which gives the phase randomized series the same number of independent data points as  $\Delta Z_g$ . This process ensures that the MC simulation can perform the null hypothesis test on statistically suitable material (Theiler & Prichard, 1996; Thejll et al., 2003). Before the  $B_y$  series is regressed onto the phase randomized  $\Delta Z_g$  for every lead-lag, both data sets are standardized by subtracting their means and dividing by their standard deviations. This will ensure that the regression slope equals the linear correlation coefficient (Rodgers & Nicewander, 1988). The same standardization is also performed on the actual response ( $\Delta Z_g$ ) (transforming the regression slopes to correlation coefficients) before the actual result is compared to the distribution of correlation coefficients obtained from the MC simulation in each lead-lag. The fraction of correlation coefficients from the MC simulation with higher values than the actual response will represent the  $p$ -value.

Figure 5 shows the results after 3000 iterations of the MC simulation. The green shaded area shows the interval corresponding to 95% of the values from all iterations. The red shaded area shows above(below) the 97.5% (2.5%) percentile, corresponding to a  $p$ -value smaller or equal to 0.05 (both tails of the distribution). As can be seen, the significance is reduced compared to what is obtained by the  $t$ -test. Also, the peak around day 0 is only found significant at the 95% level for two data points, occurring at day -2 and -1. However, multiple points with 95% significance are obtained at the peaks around -27 and +27 days, along with the minimum around

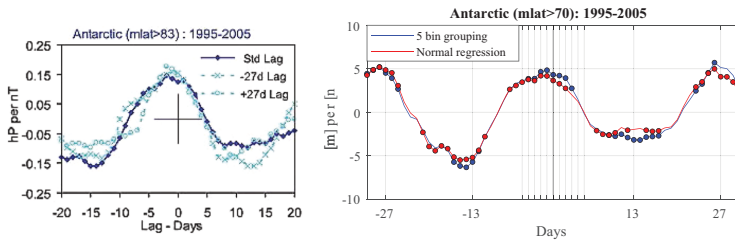


**Fig. 4.** *Left panel:* A copy of the upper panel of Figure 2 in B2008. The figure illustrates calculated regression coefficients showing lead–lag variations of  $\Delta p$  at  $\text{mlat} > 83^\circ \text{S}$ . It shows three cycles of IMF  $B_y$ , where the dark blue line represents the regression coefficients without any lag, while  $x$  and  $o$  cyan lines represent a  $-27$  and  $+27$  day lag between IMF  $B_y$  and  $\Delta p$  data series. All maxima in  $\Delta p$  are seen to occur  $-2$  days before the peak in the IMF driver, which occurs at day 0. *Right panel:* Lead–lag variations of  $\Delta Z_g$  at  $\text{mlat} > 70^\circ \text{S}$ . The blue line is the calculated regression coefficients showing lead–lags when the five bin method by B2008 is used. The red line is the regression coefficients showing lead–lag variations when regression is done without the initial grouping. Negative days (leads) represent  $\Delta Z_g$  occurring before the  $B_y$  component, and positive days  $B_y$  occurring before  $\Delta Z_g$ . Dots indicate significance at the 95% level for the regression coefficients calculated by Student’s  $t$ -test. The upper panel of Figure 2 in B2008 is reproduced with permission from John Wiley and Sons.

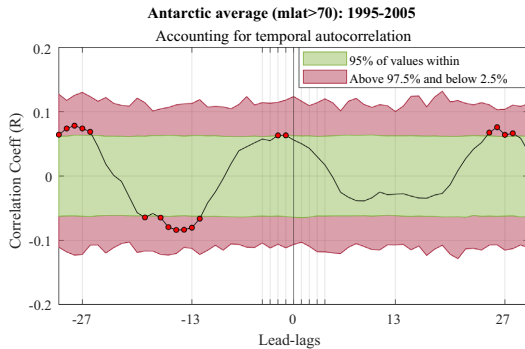


**Fig. 5.** The significance level for the lead–lag correlation coefficients after 3000 MC-iterations for the period 1995–2005. The red area equates to a  $p$ -value of 0.05. The green region shows where 95% of all values land for every lead–lag after 3000 iterations. Note that the significant data points (dark red circles) represent individual hypothesis tests before false detection rate method is applied.

$-13$  days. For day  $-2$  the correlation coefficient is equal to 0.064; for days  $-15$ ,  $-27$ , and  $+27$ , it is approximately 0.08. This implies that  $B_y$  can explain less than one percent of the pressure variability ( $R^2 < 0.01$ ).

B2008 refers to the apparent periodic response in Figure 5 as support for  $B_y$  forcing. Furthermore, B2008 results, shown in Figure 3, include 95 tests of individual null hypotheses (one for each lead–lag regression), while 55 are included in our replication given in Figure 4. In both our and B2008 results, we have the strange phenomena of the peak pressure response occurring before the peak forcing. We also obtained higher correlation coefficients at day  $-27$  and  $+27$ , which are days where the forcing is actually weaker than at day 0. Together with the  $B_y$  being continuous, a reasonable assumption is that the forcing always has an impact through this period and would render all null hypotheses in the interval  $-27$  to  $+27$  ( $N = 55$ ) equivalent. Another assumption can be derived from the fact that as the

IMF  $B_y$  has a 27-day periodicity, one can assume that the forcing is mostly positive for the interval  $-13$  to  $+13$  ( $N = 27$ ); this also takes into account a longer time delay for the response to occur. The last suggestion would be to only look at the interval  $-2$  to  $+2$  ( $N = 5$ ), as this is when the proposed forcing peaks. Here we also capture the two significant data points after the MC-simulation at lead–lag  $-2$  and  $-1$ . According to theory, it takes days before the accumulative effect on cloud properties leads to pressure changes (Frederick et al., 2019; Tinsley et al., 2020). Hence, a reasonable window would also be from day 0 and some days onwards. However, no significant (after MC) pressure peak occurs from day 0 and onwards. As of this, doing the FDR for lead–lag 0 and some days onward makes no sense.

When the FDR method is applied, no significance is obtained at the 95% level for any lead–lag in the period 1995–2005 for any of the suggested intervals. This means that the response as a whole cannot be assumed to be statistically significant. However, one must note that if only a single lead or lag (e.g., leads  $-2$  or  $-1$ ) is presented, the significance at the 95% level is justified (see Eq. (1)). However, from a physical perspective, it is hard to justify the response occurring 1 or 2 days (or more than 12 days) before the forcing instead of at day 0 or after.

Figure 6 shows the same procedure for the period 1999–2002 previously investigated by e.g., Burns et al. (2008) and Lam et al. (2013, 2014). After 3000 MC iterations, only 1 significant data point remains close to day 0 in the SH (top left panel), and 2 remain in the NH (top right panel). However, the application of FDR shows that no leads or lags that by themselves are above the 95% significance level constitute evidence in favor of rejecting the global null hypothesis in any of the hemispheres (bottom panels). This is true whether we calculate  $p_{\text{FDR}}$  for lead–lag intervals  $-27$  to  $+27$  ( $N = 55$ ),  $-13$  to  $+13$  ( $N = 27$ ) or even for  $-2$  to  $+2$  ( $N = 5$ ) ( $+2$  to  $+6$  ( $N = 5$ ) for the SH). Although the correlation coefficients for this period are not inconsistent with a physical effect, as the peak  $\Delta Z_g$  anomaly occurs after day 0 in both hemispheres, they are not significant in regards to the rejection of the global null hypothesis.

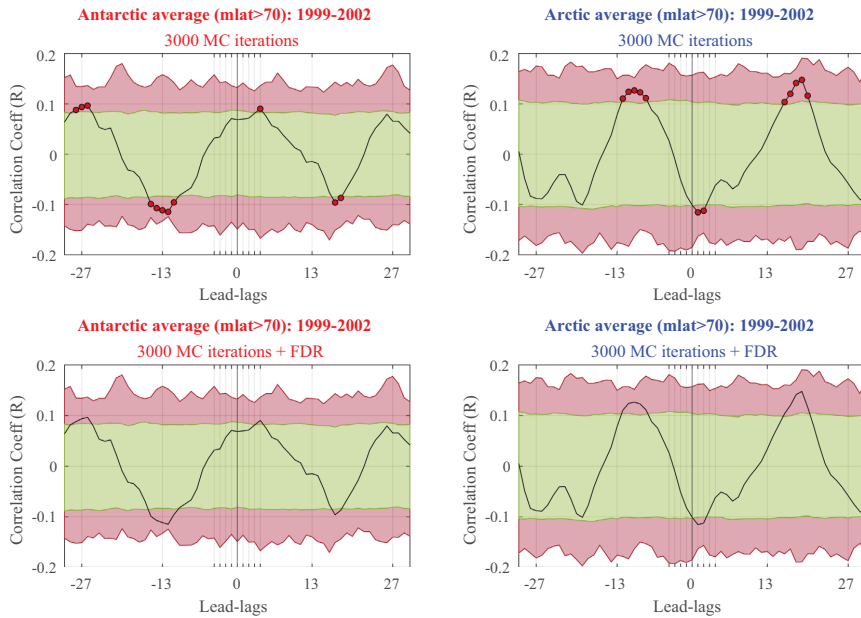


**Fig. 6.** *Left panels:* The significance level for the lead–lag correlation coefficients after 3000 MC-iterations for the period 1999–2002 in the SH. Dark red circles indicate 95% significance of the individual hypothesis tests (*top panel*). No significance is obtained after FDR. This is the case whether FDR is computed for the interval  $-27$  to  $+27$  ( $N = 55$ ),  $-13$  to  $+13$  ( $N = 27$ ) or  $+2$  to  $+6$  ( $N = 5$ ) lead-lags (*bottom panel*). *Right panels:* Same procedure, only for the NH (*top panel*). No significance is obtained after FDR. This is the case whether FDR is computed for the interval  $-27$  to  $+27$  ( $N = 55$ ),  $-13$  to  $+13$  ( $N = 27$ ) or  $-2$  to  $+2$  ( $N = 5$ ) lead-lags (*bottom panel*).

### 3.2 Other time periods

Figure 7 shows the correlation between  $\Delta Z_g$  and  $B_y$  for the periods 1984–1994, 1995–2005, and 2006–2016 in both hemispheres (top panels). The bottom panels show the same, only for 4-year periods centered around four different solar maxima. Nearly all of the time periods in both hemispheres show cyclic responses exhibiting a periodicity of  $\sim 27$  days. However, none of the time periods outside of solar cycle 23 (1995–2005 or 1999–2002) show responses supported by the theory (positive response in the SH and negative response in the NH at day zero or shortly after). Instead, the peaks occur seemingly at random but with an apparent periodicity of approximately 27 days.

### 3.3 Monte Carlo simulations with different levels of temporal autocorrelation

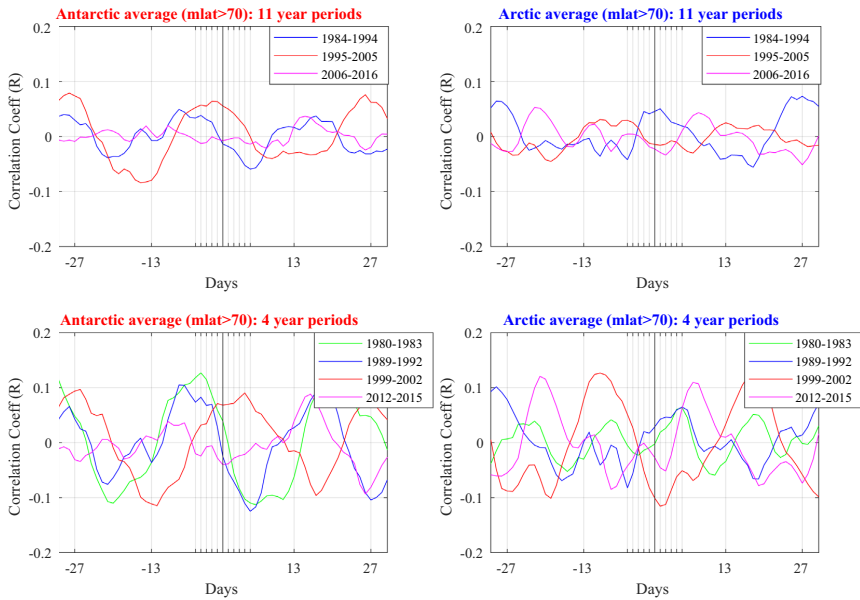
Figure 7 demonstrates that the periodic response in  $\Delta Z_g$  of  $\sim 27$  days is not unique to the 1995–2005 period, as it occurs in other time periods as well. Since the responses do not seem to have any relation to the forcing (day 0), the resulting cyclic response could be an artifact of the method itself, enhanced by the high temporal autocorrelation of the explanatory variable.

Figure 8 shows the power spectrum (left panel) and the autocorrelation function (right panel) of the IMF  $B_y$  over the time period 1995–2005. A strong 27-day solar rotation periodicity can be observed in both. When the regression coefficients

for lead–lag variations are calculated, one data set is moved with respect to the other, where the regression coefficient is calculated for each lag between the data sets. In essence, this can lead to the responses seen at day  $\pm 27$  days, being partially replications of the response seen at day 0, occurring as a consequence of the periodicity of the forcing. This is especially relevant if the response variable has a strong temporal autocorrelation.

To demonstrate this, we calculate three Monte Carlo simulations with varying levels of autocorrelation of the response variable. For all cases, the geopotential height data ( $\Delta Z_g$ ) is replaced by randomly generated normally distributed noise with the same length as the 1995–2005 period. For the first, second, and third cases, lag-1 autocorrelation is set to 0, 0.5, and 0.94, respectively. An autocorrelation of 0 represents a data set of normally distributed white noise, while the autocorrelation of 0.94 reflects the autocorrelation seen in the original geopotential height data series (not shown). The  $\pm 15$ -day moving average is further subtracted from the three random data series, analog to the calculation of  $\Delta Z_g$ .

For all three cases, 1000 independent Monte Carlo iterations are run. For each run, we calculate the lead–lag correlation coefficients between the real  $B_y$  forcing in the period 1995–2005 and the randomly generated data series. Figure 9 summarizes the results. The first column represents the lead–lag correlation coefficients for all runs in the three cases. The lead–lag curves appear to be random. However, if each curve is shifted such that the maximum value occurring inside the range



**Fig. 7.** Lead-lag correlation coefficients between  $\Delta Z_g$  and  $B_y$  in both hemispheres for three 11-year periods spanning 1984–2016 (top panels) and four 4-year periods centered around solar maximum (bottom panels).

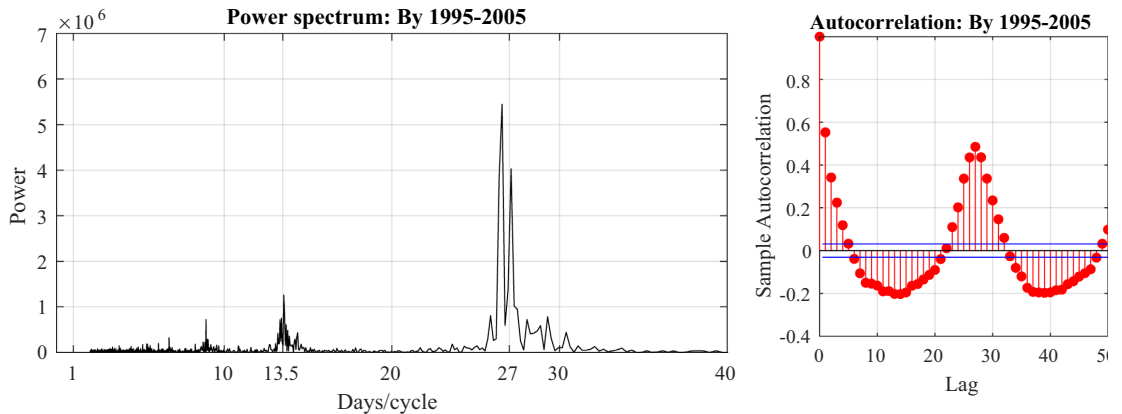


**Fig. 8.** Left panel: Power spectrum of the IMF  $B_y$ -index in the time period 1995–2005. Right panel: Autocorrelation function of the IMF  $B_y$ -index in the time period 1995–2005. The blue lines show the 95% confidence bounds of the autocorrelation function.

(−13, 13) days from day 0 is shifted to day 0, a pattern emerges. This is illustrated in the middle row of panels. When the responses are averaged over all independent simulations, as shown on the right, the resulting average lead-lag curve exhibits a periodicity equal to the periodicity of  $B_y$ . Furthermore, it is apparent that the higher the autocorrelation of the random data series at lag-1, the larger the amplitudes of the artificially created response. It is particularly interesting that the correlation

coefficients in Figure 7 are comparable to the correlation coefficients resulting from the third artificial case (lag-1 autocorrelation = 0.94) in Figure 9.

Figure 9 clearly shows that the 27-day cyclic response in surface pressure to the  $B_y$ -component cannot be used as a strong argument supporting the Mansurov effect. Furthermore, it clearly demonstrates the necessity of using FDR or a similar method when estimating the significance of the response.

4013 data points (By data from the period 1995-2005)

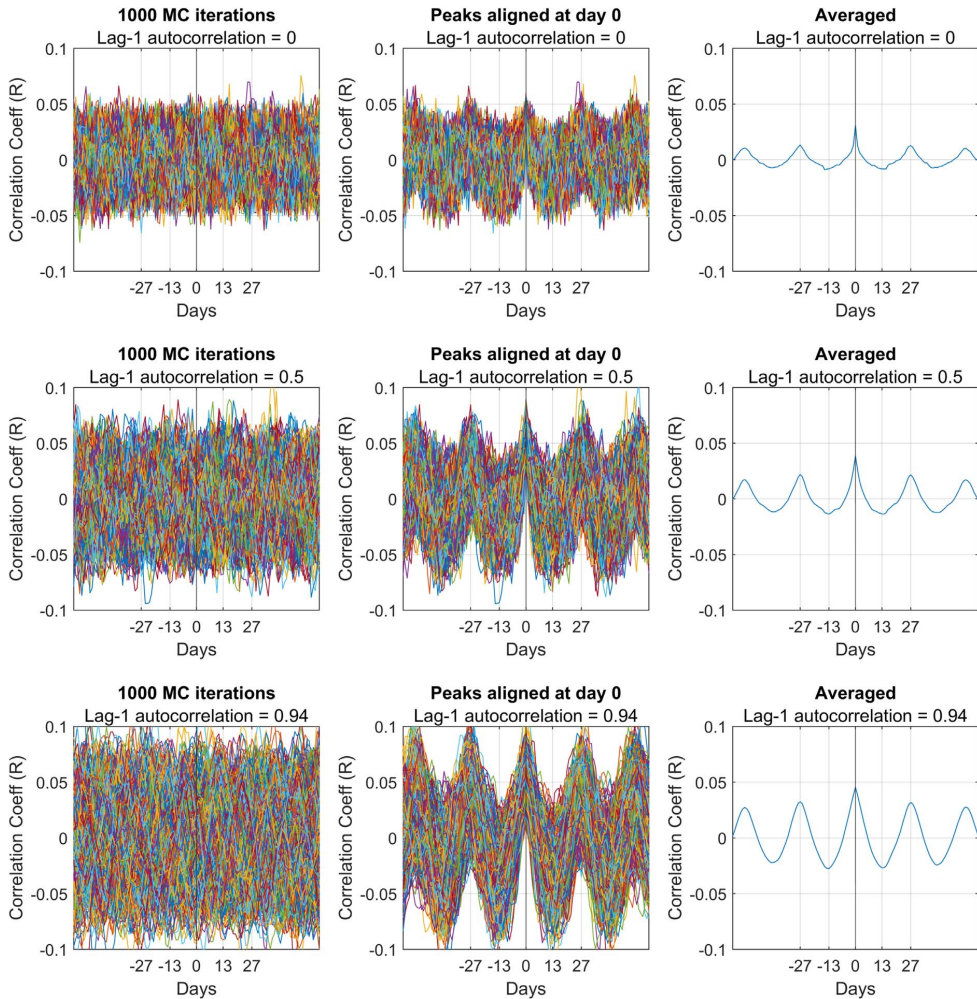


**Fig. 9.** *Left panels:* 1000 MC iterations where the correlation coefficients are calculated between the  $B_y$  data in the period 1995–2005 and normally distributed noise with three different lag-1 autocorrelation values (0, 0.5, 0.94) for every lead–lag between  $-60$  and  $+60$ . *Middle panels:* All 1000 individual lead–lag plots aligned such that the maximum value within  $-13$  to  $+13$  is projected to day 0. *Right panels:* Averaged response of the middle panels.

#### 4 Discussion

The aim of this paper is to demonstrate the need for appropriate significance tests, as well as the risk of misinterpreting a response from a strongly periodic forcing when studying the Mansurov effect (and also, more generally, any phenomena in cases of strong temporal autocorrelation). Figure 3 shows that similar values for the regression slopes are obtained with the five-bin grouping used by B2008 and the normal regression.

However, the explanatory power of the two models largely depends on whether or not the measurements are binned (with binning  $R^2 = 0.99$ , without binning  $R^2 = 0.0033$ ). Further, both the five-bin grouping and the normal regression produce similar lead–lag plots, as illustrated by Figure 4. Therefore, it is clear that the five-bin grouping gives the impression of a significantly better fit than it is found in the original data.

The majority of the research articles on the Mansurov effect focus on solar cycle 23 (B2008; Lam et al., 2013, 2014, 2018;

Zhou et al., 2018). We showed, however, that simple  $t$ -tests are not sufficient to establish significance for the link between the IMF  $B_y$  and the geopotential height variability at the polar surface. By applying MC simulations to validate the null hypotheses in addition to the false detection rate method, we showed that neither the period 1995–2005 nor the solar maximum period 1999–2002 indicate a statistically significant response. This remains true as long as the response is analyzed with multiple leads and lags greater or equal to 5 days, as the individual  $p$ -values exceed the global  $p$ -value (Eq. (1)) even for  $-2$  to  $+2$  lead-lags in all cases for solar cycle 23. Nonetheless, if only a single lead or lag is presented, the significance at the 95% level obtained by the MC simulation alone would be justified. During the period 1995–2005, the points with high statistical significance at leads  $-2$  or  $-1$  are hard to justify on physical grounds, as the surface pressure effect occurs before the forcing. However, individual significant data points obtained in the SH (day +4) and NH (day +1 and +2) for the period 1999–2002 cannot be completely discarded from the viewpoint of a single null hypothesis, as the effect occurs after the forcing.

By similar methodology, we observe periodic geopotential height responses in both hemispheres in other time periods, but with varying offset in respect to the forcing, as illustrated by Figure 7. The geopotential height deflections are also fairly equal to the amplitudes seen for solar cycle 23. Hence, the cyclic responses seen in solar cycle 23 are not unique to this period.

B2008, Lam et al. (2018) and Tinsley et al. (2020) all use this 27-day periodicity in the results as evidence in favor of the Mansurov effect. By using MC simulations of randomly generated data series with different levels of lag-1 autocorrelation, we showed that plotting lead-lag regression coefficients for a highly periodic forcing produces periodic responses, even when no physical relationship is present (Fig. 9). The periodic response always mimics the periodicity of the variable used as the forcing. One can also observe how this cyclic response is enhanced by a higher autocorrelation of the response variable. From this perspective, the alignment of the period 1999–2002 with the theory could, in fact, be a coincidence (1995–2005 is also approximately aligned with the theory in the SH). This result extends beyond the Mansurov effect itself and is applicable in any case where the relationship between a periodic explaining variable and an autocorrelated response variable is examined on a temporal scale.

However, the effect could be nonstationary in relation to atmospheric variability and the solar phases. If so, time periods restricted by similar atmospheric and solar conditions would be expected to respond in a similar manner, while averages of large continuous time periods would smoothen out the effect, making it much harder to detect. Tinsley et al. (2020) found a higher correlation between cloud irradiance and changes in the vertical electric field related to  $B_y$  during local northern winter (Oct–Apr 2004–2015), then local summer months. However, no statistical assessment of the correlation coefficients in respect to the empirical autocorrelation was made. An equal probable explanation for the larger coefficients could be the higher atmospheric variability in winter compared to summer. This could lead to higher levels of noise in the results, which are artificially replicated into a periodic response via the method used, as our results show. In agreement with Tinsley et al. (2020) and Zhou

et al. (2018) also found results with local winter in both hemispheres producing the largest response between the vertical electric field and surface pressure. However, only the period 1998–2001 is analyzed, and the results lack proper statistical testing. Sorting according to non-stationary behavior is beyond the scope of this article but is a recommended pathway for further research on the Mansurov effect, as the articles discussed here are pointing to a potential seasonal variability. However, future studies need to take into account the autocorrelation of variables and multiple hypothesis testing scenarios when assessing the statistical significance of their results.

## 5 Conclusion

We revisited the previous evidence suggesting a significant link between the IMF  $B_y$  and the surface pressure/geopotential height variability. We showed that after the pressure/geopotential height and IMF  $B_y$  data were subjected to rigorous estimation of statistical significance, evidence for the Mansurov effect during solar cycle 23 was not found when considering the whole year without individual seasons/months. In addition, our analyses showed that other time periods (before and after solar cycle 23) produced cyclic responses with a similar magnitude but with random offset with respect to the IMF  $B_y$  forcing. We also provided evidence showing that high temporal autocorrelation of variables can explain the cyclic responses without the need for a physical connection between the variables. These results underline the importance of robust statistical methods, especially when analyzing periodic variables or data with high temporal autocorrelation.

For the Mansurov effect, our applied methods indicate that even if a connection between IMF  $B_y$  changes and cloud microphysics exists, this effect is not strong enough to produce significant correlations for a stationary signal in surface polar geopotential height/pressure over interannual to decadal time-scales. We encourage more research on the topic to assess the potential cause of non-stationary behavior and seasonal variability.

*Acknowledgements.* We thank the ECMWF (European Center for Medium Weather Forecast) for ERA5 data (<https://www.ecmwf.int/en/forecasts/datasets/reanalysis-datasets/era5>) and the NASA Goddard Space Center for OMNIWeb database (<https://omniweb.gsfc.nasa.gov/>). All data used in this study are openly available. All codes and data required to reproduce the results of this study can be downloaded from Zenodo (<https://doi.org/10.5281/zenodo.5996692>). The research was funded by the Norwegian Research Council under contracts 223252/F50 (BCSS) and 300724 (EPIC). The editor thanks two anonymous reviewers for their assistance in evaluating this paper.

## References

- Benjamini Y, Hochberg Y. 1995. Controlling the false discovery rate: A practical and powerful approach to multiple testing. *J Roy Statist Soc: Ser B (Methodol)* 57: 289–300. <https://doi.org/10.1111/j.2517-6161.1995.tb02031.x>.

- Bretherton CS, Widmann M, Dymnikov VP, Wallace JM, Bladé I. 1999. The effective number of spatial degrees of freedom of a time-varying field. *J Climate* **12**(7): 1990–2009. [https://doi.org/10.1175/1520-0442\(1999\)012<1990:TENOSD>2.0.CO;2](https://doi.org/10.1175/1520-0442(1999)012<1990:TENOSD>2.0.CO;2).
- Burns GB, Tinsley BA, French WJR, Troshichev OA, Frank-Kamenetsky AV. 2008. Atmospheric circuit influences on ground-level pressure in the Antarctic and Arctic. *J Geophys Res* **113**: D15112. <https://doi.org/10.1029/2007JD009618>.
- Frank-Kamenetsky AV, Troshichev OA, Burns GB, Papitashvili VO. 2001. Variations of the atmospheric electric field in the near-pole region related to the interplanetary magnetic field. *J Geophys Res* **106**: 179–190. <https://doi.org/10.1029/2000JA900058>.
- Frederick JE, Tinsley BA, Zhou L. 2019. Relationships between the solar wind magnetic field and ground-level longwave irradiance at high northern latitudes. *J Atmos Sol-Terr Phys* **193**: 105063. <https://doi.org/10.1016/j.jastp.2019.105063>.
- Freeman MP, Lam MM. 2019. Regional, seasonal, and inter-annual variations of Antarctic and sub-Antarctic temperature anomalies related to the Mansurov effect. *Environ Res Commun* **1**: 111007. <https://doi.org/10.1088/2515-7620/ab4a84>.
- Gonzalez ALC, Gonzalez WD. 1987. Periodicities in the interplanetary magnetic field polarity. *J Geophys Res* **92**(A5): 4357–4375. <https://doi.org/10.1029/JA092iA05p04357>.
- Kabin K, Rankin R, Marchand R, Gombosi TI, Clauer CR, Ridley AJ, Papitashvili VO, DeZeeuw DL. 2003. Dynamic response of Earth's magnetosphere to  $B_z$  reversals. *J Geophys Res* **108**: 1–13. <https://doi.org/10.1029/2002JA009480>.
- Lam MM, Tinsley BA. 2016. Solar wind-atmospheric electricity cloud microphysics connections to weather and climate. *J Atmos Sol-Terr Phys* **149**: 277–290. ISSN: 1364-6826. <https://doi.org/10.1016/j.jastp.2015.10.019>.
- Lam MM, Chisham G, Freeman MP. 2013. The interplanetary magnetic field influences mid-latitude surface atmospheric pressure. *Environ Res Lett* **8**: 045001. <https://doi.org/10.1088/1748-9326/8/4/045001>.
- Lam MM, Chisham G, Freeman MP. 2014. Solar-wind-driven geopotential height anomalies originate in the Antarctic lower troposphere. *Geophys Res Lett* **41**: 6509–6514. <https://doi.org/10.1002/2014GL061421>.
- Lam MM, Freeman M, Chisham G. 2018. IMF-driven change to the Antarctic tropospheric temperature due to the global atmospheric electric circuit. *J Atmos Sol-Terr Phys* **180**: 148–152. <https://doi.org/10.1016/j.jastp.2017.08.027>.
- Mansurov SM, Mansurova LG, Mansurov GS, Mikhnevich VV, Visotsky AM. 1974. North-south asymmetry of geomagnetic and tropospheric events. *J Atmos Terr Phys* **36**(11): 1957–1962. [https://doi.org/10.1016/0021-9169\(74\)90182-2](https://doi.org/10.1016/0021-9169(74)90182-2).
- Mooney P, Mulligan F, Fealy R. 2011. Comparison of ERA-40, ERA-Interim and NCEP/NCAR reanalysis data with observed surface air temperatures over Ireland. *Int J Climatol* **31**: 545–557. <https://doi.org/10.1002/joc.2098>.
- Page DE. 1989. The interplanetary magnetic field and sea level polar atmospheric pressure. In: *Workshop on mechanisms for tropospheric effects of solar variability and the quasi-Biennial oscillation*, Avery SK, Tinsley BA (Eds.), University of Colorado, Boulder, CO, USA, 22 p.
- Pettigrew ED, Shepherd SG, Ruohoniemi JM. 2010. Climatological patterns of high-latitude convection in the Northern and Southern hemispheres: Dipole tilt dependencies and interhemispheric comparisons. *J Geophys Res* **115**: A07305. <https://doi.org/10.1029/2009JA014956>.
- Rodgers JL, Nicewander AW. 1988. Thirteen ways to look at the correlation coefficient. *Am Statist* **42**: 59–66. <https://doi.org/10.1080/00031305.1988.10475524>.
- Theiler J, Prichard D. 1996. Constrained-realization Monte-Carlo method for hypothesis testing. *Phys D* **94**: 221–235. [https://doi.org/10.1016/0167-2789\(96\)00050-4](https://doi.org/10.1016/0167-2789(96)00050-4).
- Thejll P, Christiansen B, Gleisner H. 2003. On correlations between the North Atlantic Oscillation, geopotential heights, and geomagnetic activity. *Geophys Res Lett* **30**: 1347. <https://doi.org/10.1029/2002GL016598>.
- Tinsley BA. 2000. Influence of solar wind on the global electric circuit, and inferred effects on cloud microphysics, temperature, and dynamics in the troposphere. *Space Sci Rev* **94**: 231–258. <https://doi.org/10.1023/A:1026775408875>.
- Tinsley BA. 2008. The global atmospheric electric circuit and its effect on cloud microphysics. *Rep Prog Phys* **71**: 66801–66831. <https://doi.org/10.1088/0034-4885/71/6/066801>.
- Tinsley BA, Zhou L, Wang L, Zhang L. 2020. Seasonal and solar wind sector duration influences on the correlation of high latitude clouds with ionospheric potential. *J Geophys Res: Atmos* **126**: e2020JD034201. <https://doi.org/10.1029/2020JD034201>.
- Wilks DS. 2016. “The stippling shows statistically significant grid points”: How research results are routinely overstated and over interpreted, and what to do about it. *Bull Am Meteorol Soc* **97**: 2263–2273. <https://doi.org/10.1175/BAMS-D-15-00267.1>.
- Zhou L, Tinsley BA, Wang L, Burns GB. 2018. The zonal mean and regional tropospheric pressure responses to changes in ionospheric potential. *J Atmos Sol-Terr Phys* **171**: 111–118. <https://doi.org/10.1016/j.jastp.2017.07.010>.

**Cite this article as:** Edvartsen J, Maliniemi V, Nesse Tyssøy H, Asikainen T & Hatch S 2022. The Mansurov effect: Statistical significance and the role of autocorrelation. *J. Space Weather Space Clim.* **12**, 11. <https://doi.org/10.1051/swsc/2022008>.

# Paper II


## **The Mansurov effect: Seasonal and solar wind sector structure dependence**

J.Ø. Edvartsen, V. Maliniemi, H. Nesse and S. Hatch. *Journal of Space Weather and Space Climate*, **13**, 17. doi:10.1051/swsc/2023013 (2023)





# The Mansurov effect: Seasonal and solar wind sector structure dependence

Jone Øvretvedt Edvartsen , Ville Maliniemi, Hilde Nesse, and Spencer Hatch

Birkeland Center for Space Science, Department of Physics and Technology, University of Bergen, 5007 Bergen, Norway

Received 10 July 2022 / Accepted 5 May 2023

**Abstract** – We investigate the connection between the interplanetary magnetic field (IMF)  $B_y$ -component and polar surface pressure, also known as the Mansurov effect. The aim of the investigation is to unravel potential dependencies on specific seasons and/or solar wind sector structures, and it serves as a sequel to Edvartsen et al. (2022) [*J Space Weather Space Clim* 12: 11]. The mechanism for the effect includes the ability of the IMF to modulate the global electric circuit (GEC), which is theorized to impact and modulate cloud generation processes. By usage of daily ERA5 reanalysis data for geopotential height since 1968, we find no significant response confirming the current Mansurov hypothesis. However, we do find statistically significant correlations on decadal timescales in the time period March–May (MAM) in the northern hemisphere, but with an unusual timing. Similar phased anomalies are also found in the southern hemisphere for MAM, but not at a significant level. In an attempt to explain the unusual timing, heliospheric current sheet crossing events, which are highly correlated with the  $B_y$ -index, are used. These events result in higher statistical significance in the NH for the MAM period, but cannot fully explain the timing of the response. In general, these statistically significant correlations differ from previously reported evidence on the Mansurov effect, and suggest a revision of the Mansurov hypothesis. Our results also highlight a general feature of time-lagged cross-correlation with autocorrelated variables, where the correlation value itself is shown to be a fragile indicator of the robustness of a signal. For future studies, we suggest that the  $p$ -values obtained by modern statistical methods are considered, and not the correlation values alone.

**Keywords:** Solar-climate link / Significance testing / Monte-Carlo / False-detection-rate / Periodic forcing

## 1 Introduction

The hypothesis on the Mansurov effect, which assumes a relation between daily polar surface pressure and the  $B_y$ -component of the interplanetary magnetic field (IMF), was first proposed by Mansurov et al. (1974). Multiple studies have found a correlation supporting this hypothesis in more recent times (Burns et al., 2008; Lam et al., 2013, Lam & Tinsley, 2016; Zhou et al., 2018; Tinsley et al., 2021; 2018). However, Edvartsen et al. (2022) found the previous correlations to be below the 95% statistical significance limit. Moreover, the 27-day cyclic response, which has previously been used as evidence for the effect (Burns et al., 2008; Lam et al., 2018; Tinsley et al., 2021), was shown to occur as a statistical artifact due to the periodic  $B_y$ -forcing and high autocorrelation in the surface pressure. This work aims at investigating the open ends not addressed by Edvartsen et al. (2022), mainly, the potential

for a seasonal and/or solar structure dependency for the link between  $B_y$ -forcing and polar surface pressure response.

The Mansurov hypothesis assumes a positive (negative) correlation between  $B_y$  and surface pressure anomalies in the Southern (Northern) Hemisphere. The effect is thought to arise in connection with the Global Electric Circuit (GEC). The GEC links the electric fields and currents flowing in the lower atmosphere, ionosphere, and magnetosphere to form a global spherical conductor (Siingh et al., 2007). Global thunderstorms act as batteries charging the GEC by generating upward-driven currents  $J_z$ . In addition to electrified clouds, this maintains an average potential difference ( $V_i$ ) between the ionosphere and the Earth's surface at about 250 kV (Tinsley, 2000; Williams, 2005). In fair weather regions, a return current ( $J_z$ ) flows in the direction ionosphere–surface, thereby completing the GEC. When the velocity of the solar wind ( $\mathbf{V}$ ) flows radially outwards from the sun with its frozen in the magnetic field ( $\mathbf{B}$ ), relative to the Earth, this gives rise to a  $\mathbf{V} \times \mathbf{B}$  motional electric field as seen by an observer stationed at Earth. Through the conducting magnetic field lines, the potential of the electric

\*Corresponding author: [jone.edvartsen@uib.no](mailto:jone.edvartsen@uib.no)

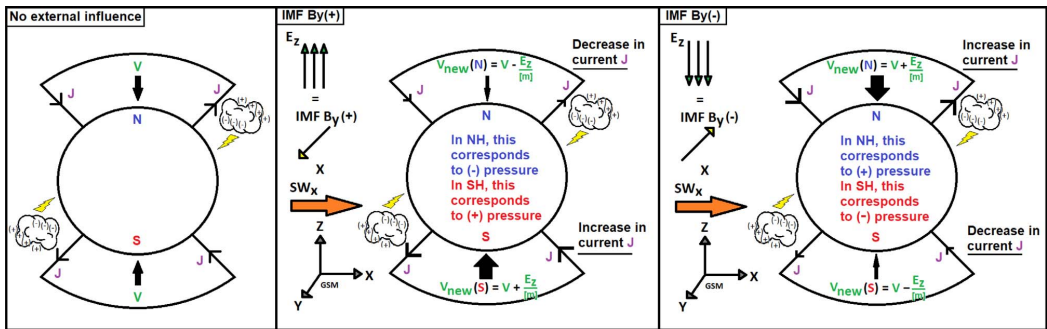


**Fig. 1.** IMF  $B_y(+)$  leads to a decrease in  $V$  and  $J$  in the NH and an increase in  $V$  and  $J$  in the SH. IMF  $B_y(-)$  leads to an increase in  $V$  and  $J$  in the NH, and a decrease in  $V$  and  $J$  in the SH. Relating this to the Mansurov-associated pressure changes means that an increase in the ionospheric potential and fair weather current leads to an increase in pressure.

field is superimposed on the global ionospheric potential  $V_i$  (Tinsley, 2008). In Geocentric Solar Magnetospheric (GSM) coordinates a magnetic field in the  $y$ -direction ( $B_y$ ) gives rise to a potential difference between the northern polar cap ionosphere and the southern polar cap ionosphere of typically a few tens of kV (Tinsley & Heelis, 1993). As the ionospheric potential  $V_i$  changes, so does the fair weather current  $J_z$ . Figure 1 shows an illustration of the components involved in the mechanism, mainly the perturbation of the ionospheric potential and the effect on  $J_z$ .

Tinsley (2008) also discusses other sources able to modulate  $J_z$  and then links to atmospheric changes. Studies have found a relation between Galactic Cosmic Rays (GCR) and cloud cover over decadal timescales (Tinsley, 2008; Veretenenko & Ogurtsov, 2012; Veretenenko et al., 2018). Correlations have also been found between internally driven modulations of  $J_z$  (thunderstorm generator) and atmospheric pressure changes, which are together known as the Burns effect (Burns et al., 2007, 2008; Zhou et al., 2018). It is suggested that all these mechanisms, through the modulation of the ionospheric fair weather current  $J_z$ , affect microphysical processes in clouds (Tinsley, 2022). As the currents flow through high gradients of conductivity across cloud boundaries they add to the separation of positive and negative ions. These ions can attach to aerosols and droplets, where they influence microphysical processes due to the Coulomb interaction (Tinsley & Deen, 1991; Tinsley, 2000, 2008). The influence on the microphysics of clouds should occur nearly instantaneously. However, this effect is relatively small, and it is predicted that the microscale changes take days before materializing as macro-physical changes in cloud radiative properties. Furthermore, after manifesting, these radiative changes might lead to pressure responses observed at the surface level (Frederick et al., 2019; Tinsley et al., 2021).

Both the atmosphere and the solar wind are highly variable in nature, potentially leading to different surface responses during different conditions. Tinsley et al. (2021) show an intensified relation between  $B_y$  and the surface pressure anomaly during local northern winter. However, no significance estimation is assessed. Zhou et al. (2018) found that during four years from 1998 to 2001, the correlation between the vertical electrical field and surface pressure is larger during local winter in both hemispheres. For the variability in the solar wind,

Tinsley et al. (2021) found that cloud irradiance over Alert, Canada was larger when the solar wind structure was two-sector (IMF  $B_y$  oscillating at a 27-day period), compared to four-sector (IMF  $B_y$  oscillating at a 13.5-day period). It is also highlighted that the most cited period in favor of the Mansurov effect, 1999–2002, is dominated by two-sector structures. In our work, we will focus exclusively on the Mansurov effect. We seek to determine whether there is statistically significant evidence in favor of its existence, and therefore confine attention in this study to the correlation between IMF  $B_y$  and surface pressure. We do not attempt to comment on the viability of any particular mechanism. In contrast to our previous work (Edvartsen et al., 2022), where we questioned the statistical significance of the effect on the basis of analysis of continuous decadal timescales, we now address the potential seasonal and solar wind sector structure dependence.

## 2 Data and method

### 2.1 Solar wind ( $B_y$ ) data

We use daily averaged IMF  $B_y$  (Geocentric Solar Magnetospheric, GSM, coordinates) values obtained from the National Space Science Data Center (NSSDC) OMNIWeb database (<http://omniweb.gsfc.nasa.gov>) for the interval 1968–2020. In this coordinate system,  $X$  points along the Sun–Earth line,  $Z$  points along Earth’s magnetic dipole axis, with  $Y$  perpendicular to both  $X$  and  $Z$ .

### 2.2 Pressure/geopotential height data

For the atmospheric data, we use the European Center for Medium-Range Weather Forecast Re-Analysis (ERA5) (<https://cds.climate.copernicus.eu>). These data are constructed by interpolating observations with numerical simulations and models, effectively constructing a high-resolution atmospheric database. It is noted that reanalysis data does not have the accuracy as pure observational data at every grid point. Nevertheless, it still allows for a physically justified approximation in the grids where observations are not accessible. Multiple studies have used reanalysis data in the examination of the Mansurov effect (Lam et al., 2013, 2018; Zhou et al., 2018; Freeman & Lam,

2019; Edvartsen et al., 2022), justifying its usage for the purpose of this study.

We focus on the geopotential height of the 700 hPa level in both hemispheres. In the SH this represents the surface, while in the NH this represents a few kilometers above surface level. The geomagnetic perturbations of IMF  $B_z$  in the ionosphere are centered around the geomagnetic pole. Therefore, the geopotential height will be averaged to one value for each hemisphere from 70° poleward in geomagnetic coordinates (mlat). The full data period covers the time period 1968–2020. To account for seasonal variability, a perturbation value is obtained for each hemisphere ( $Z_g(\text{NH})$  and  $Z_g(\text{SH})$ ). These are obtained by subtracting a running mean of  $\pm 15$  days from the daily value of the geopotential height data series.

### 2.3 Modern statistical methods

Analogous to Edvartsen et al. (2022), we use Monte Carlo (MC) simulation together with the false discovery rate (FDR) method to estimate the statistical significance. The MC approach handles the uncertainty introduced by temporal autocorrelation. The FDR method tests multiple null hypotheses simultaneously, namely the expected increase in falsely rejected null hypotheses at the 5% level as the number of hypotheses itself increases. The following sections provide details on how the MC and FDR methods are implemented in this study.

#### 2.3.1 Monte Carlo approach

The main goal of the MC approach is to construct a repeated analysis with similar statistical conditions as found in the original data series, however, with an introduced element of randomness for each iteration. The process results in a distribution of simulated results where the null hypothesis is assumed to hold. As such, original findings can be compared to the fraction of as extreme or more extreme simulated results to obtain the  $p$ -value, which then becomes the likelihood of obtaining a similar result by chance.

The main investigative tool used in our study is the time-lagged cross-correlation method (Pearson linear correlation coefficient). It correlates two different data series (forcing and response), with an introduced shift with respect to each other in the temporal direction. The method can therefore identify directionality (forcing  $\rightarrow$  response) between the data series, as well as the associated time lag. The MC significance test can be implemented by replacing the response data series with surrogate data while keeping the forcing data identical. The surrogate data have to be statistically equivalent in terms of statistical features (e.g. autocorrelation, standard deviation, mean, etc.). Lancaster et al. (2018) provide a technical overview of different ways to create simulated data. We use the Fourier transform (FT) method, which is computationally cheap and easy to implement, and proceeds as follows: First the FT ( $ft_x$ ) of the original response data series, the geopotential height, is calculated. Then, a random phase vector ( $\phi_r$ ) is generated. As the FT is symmetrical, the new phase randomized vector ( $ft_r$ ) can be obtained by multiplying the first half of  $ft_x$  with  $\exp(i\phi_r)$  (this corresponds to the positive frequencies). The second half of  $ft_r$  is then computed by horizontally flipping the complex conjugate of the first half. Finally, the inverse Fourier transform of  $ft_r$  gives the FT surrogate data. This method was initially

introduced to test for non-linearity in data. It has, however, been shown by e.g. Theiler & Prichard (1996) that the FT-based method provides a good surrogate technique alternative when the statistics of interest are not pivotal, meaning that the distribution of targeted values (correlation value in our case) under the null hypothesis is unknown.

Figure 2 displays the results of the FT-method performed for the geopotential height data series at the 700 hPa level averaged over 70°–90° S for the period 1968–2020. The top left panel shows the raw geopotential height data plotted against time, while the bottom left panel shows the surrogate data after the FT-procedure. In the middle panels, the autocorrelation function for the raw (top) and surrogate data (bottom) are shown, while the right panel shows the power spectrum of the raw (blue) and surrogate data (red). As expected, the FT-method produces a physically unrelated surrogate data series, however, it retains the necessary statistical conditions like autocorrelation (which implies the same number of independent data points), power spectrum, and other features such as standard deviation, variance, and mean (not shown).

This procedure requires continuous data. However, investigating the seasonal dependence of the response in December, January, and February (DJF), requires that these portions of the full continuous data period be extracted. To produce the surrogate data representing the geopotential height for every DJF, we perform the FT-procedure on every individual DJF period before finally stitching the surrogate data together to form a single data series (|DJF|DJF|DJF|...). This is computationally expensive, but necessary to avoid introducing artificial frequencies not found in the original data.

#### 2.3.2 False-discovery rate

The FDR is an appropriate tool when testing multiple null hypotheses simultaneously. When testing a null hypothesis in isolation, the  $p$ -value obtained by our MC approach defines the probability of obtaining a result at least as extreme as the observed result, under the assumption that the null hypothesis holds. For example, the common  $p = 0.05$  threshold implies that there is a 5% probability of obtaining a given result under the assumption that the null hypothesis is correct. When  $N$  null hypotheses are tested (e.g., map plot with multiple grids or time-lagged cross-correlation with multiple lead-lags), the probability of falsely rejecting at least one null hypothesis increases as  $pN$  increases. The FDR method, developed by Benjamini & Hochberg (1995) and later applied to atmospheric sciences by Wilks (2016), aims to account for the increase in the expected rate of falsely rejected null hypotheses as  $N$  increases.

In its simplest form, the FDR method assumes statistically independent null hypotheses and an identical distribution of observations (i.e., the data characteristics, such as the mean, median, and standard deviation, are the same for every group or sample being compared). When dealing with atmospheric data such as geopotential height, high autocorrelation exists, both temporally (Fig. 2 middle panels) and spatially. In a time-lagged cross correlation plot or map plot with multiple grids, each data point will therefore not be statistically independent. To address this issue, Wilks (2016) improved on the approach developed by Benjamini & Hochberg (1995), by introducing a factor that accounts for the autocorrelation in the data. The full process involves the computation of  $p$ -values

### Fourier transform surrogate

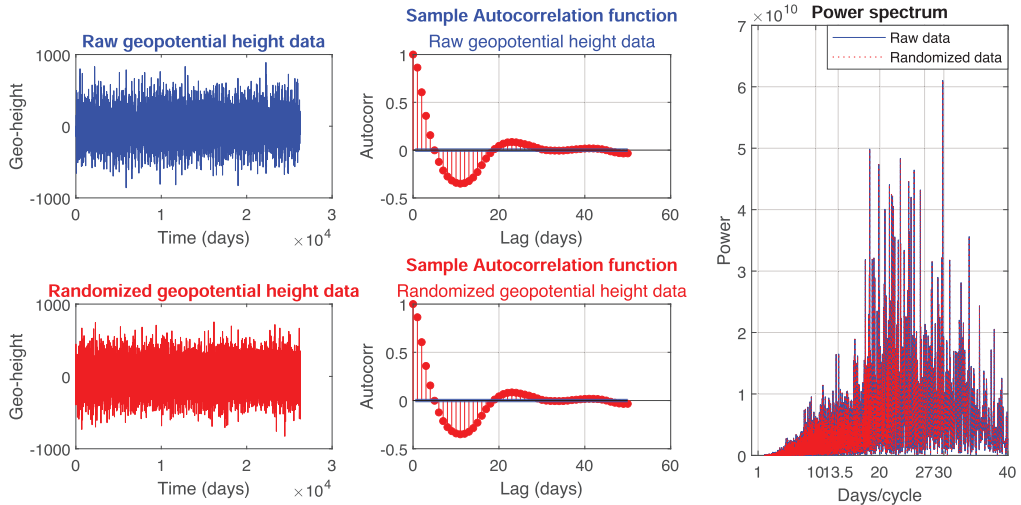


**Fig. 2.** Left panels: Raw geopotential height data series at the 700 hPa level averaged over 70°–90° S for the period 1968–2020 (top panel), and the FT surrogate (bottom panel). Middle panels: Autocorrelation function of the raw (top) and FT surrogate (bottom) geopotential height data. Right panel: Power spectrum of the raw data (blue) and the FT surrogate (red). As can be seen, there is an identical match for the autocorrelation and the power spectrum.

for each data point (MC-approach), before sorting them in ascending order. The sorting forms the set  $i = 1, \dots, N$  where  $N$  represents the total number of individual null hypotheses to be tested. A new global  $p$ -value,  $p_{\text{FDR}}$ , is then calculated by iterating through the individual  $p$ -values starting at the lowest, and looking for the last  $p$ -value fulfilling the equation:

$$p_{\text{FDR}} = \max[p(i) : p(i) \leq (i/N)\alpha_{\text{FDR}}], \quad i = 1, \dots, N. \quad (1)$$

In case of independent individual null hypotheses,  $\alpha_{\text{FDR}} = 0.05$  ensures that the global  $p$ -value ( $p_{\text{FDR}}$ ) is correctly interpreted at the 95% confidence level. The statistical significance of individual tests is determined by comparing their original  $p$ -values against the threshold value  $p_{\text{FDR}}$ . Only those tests with  $p$ -values equal to or lower than  $p_{\text{FDR}}$  are considered statistically significant. However, as discussed, individual data points in a time-lagged cross-correlation plot or map grid plot are not independent. Wilks (2016) demonstrates that for autocorrelation commonly found in atmospheric data, an  $e$ -folding distance of  $1.54 \cdot 10^3$  km, setting  $\alpha_{\text{FDR}} = 0.1$  corrects for dependence between data points and ensures that the  $p_{\text{FDR}}$  threshold is exceeded in only 5% of the cases globally.

We can calculate which  $\alpha_{\text{FDR}}$  value is appropriate for our specific data. This analysis will also give insight into how the FDR approach (Wilks, 2016) works at a global scale. The left panel of Figure 3 shows the distribution of correlation values constructed based on an MC-simulation with 20,000 iterations. The distribution of correlation values is made by cross-correlating the real IMF  $B_y$  for the period 1968–2020 with surrogate data made from the geopotential height (700 hPa level averaged over 70°–90° S for the same time period) with the FT method

for lead-lags  $-20$  to  $20$ . Then, we perform another 20,000 iterations of the same setup. In the right panel, the results from the new iterations are compared against the distribution to the left to calculate the  $p$ -value at each specific lead lag for each individual iteration. Simultaneously, the FDR approach is applied to the  $p$ -values for each iteration, where five different values for  $\alpha_{\text{FDR}}$  are tested. When  $\alpha_{\text{FDR}} = 0.09$ , only 5% of the iterations obtains  $p$ -values passing the global FDR threshold. In other words, for our specific data, when  $\alpha_{\text{FDR}}$  is set to 0.09, 5% of global responses will pass the FDR test when the null hypothesis is assumed correct. Therefore,  $\alpha_{\text{FDR}} = 0.09$  will be used in analyses conducted in this study. The requirement of identical distribution of the observations will also be valid in our case. The left panel of Figure 3 shows that all lead-lags have near identical distribution of correlation values after the MC simulation. They have also similar statistical features, such as standard deviation, mean, and median, in the geopotential height data series for two consecutive days. They only diverge slightly with increasing intervals between the days being compared (e.g., winter months tend to exhibit greater variance than summer months). However, since the lead-lag plots in our study are limited to a maximum of 41 days, the distribution of observations can be considered approximately identical.

#### 2.3.3 False-discovery rate in combination with Monte Carlo approach

The FDR method (Eq. (1)), requires a minimum  $p$ -value to reject the global null test. For example, if 50 data points are analyzed with  $\alpha_{\text{FDR}} = 0.05$ , the first sorted  $p$ -value must be lower than or equal to  $(1/50) \cdot 0.05 = 0.001$ . Assuming the null

20000 MC-iterations

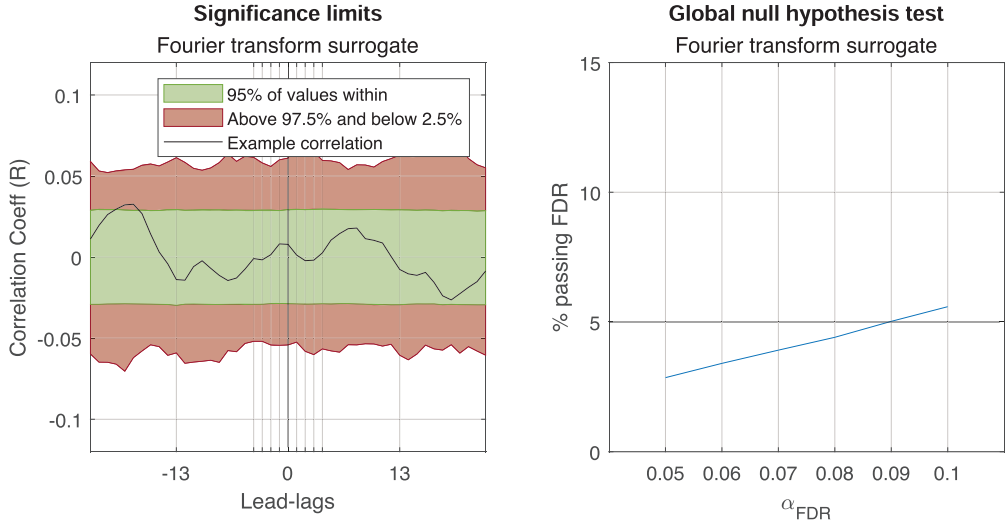


**Fig. 3.** *Left panel:* Surrogate data (FT-method) made from the raw geopotential height data series at the 700 hPa level averaged over 70°–90° S cross-correlated with the real IMF  $B_y$  index over the time period 1968–2020 for 20,000 iterations. The result of these iterations makes up a distribution of correlation values for every lead lag. The red area illustrates where only 5% of correlation values land, while the green shaded area illustrates where the remaining 95% of correlation values land. The black line is added as an example and shows a typical iteration when the surrogate data and  $B_y$  are cross-correlated. *Right panel:* After constructing the distribution of correlation values shown in the left panel, the surrogate data and  $B_y$  are again cross-correlated 20,000 times. Then, all data points at specific lead lags are measured against the distribution (in left panel) at the specific lead lag to obtain the  $p$ -values. To accurately estimate the appropriate  $\alpha_{FDR}$  in a way that takes into account the autocorrelation present in our data, all  $p$ -values generated from each iteration of the simulation are processed through the FDR method, where 5 different values for  $\alpha_{FDR}$  are tested. By doing so, we can obtain the specific  $\alpha_{FDR}$  value which ensures that any signal determined to be statistically significant occurs globally in only 5% of cases when the null hypothesis is assumed to be true for our data. As can be seen, when  $\alpha_{FDR}$  is set to 0.09, only 5% of the 20,000 iterations produce a response that passes the global FDR limit.

hypothesis holds, the distribution of  $p$ -values will be uniform. Therefore, obtaining a  $p$ -value of 0.001 is a 1/1000 event. If one has exactly 1000 tries, the probability of obtaining the 1/1000 event can be calculated as follows:

Probability that one MC iteration will not be the 0.001 event

$$= 1 - \frac{1}{1000}, \tag{2}$$

Probability that 1000 MC iterations will not be the 0.001 event

$$= \left(1 - \frac{1}{1000}\right)^{1000}, \tag{3}$$

Probability that 1000 MC iterations give atleast one 0.001 event

$$= 1 - \left(1 - \frac{1}{1000}\right)^{1000} = 0.6323 = 63.23\%. \tag{4}$$

For 1000 MC iterations, the probability that at least one 1/1000 event occurs is only 63.23%. Hence, applying 1000 iterations will not give an accurate estimate of the underlying statistics

of the distribution at a 0.001 resolution. We therefore propose a formula that gives the lowest possible number of iterations to perform for an accurate representation of the underlying statistics at the required resolution when combining the MC approach with FDR. It is analogous to probability with replacement, with the FDR equation for the first sorted  $p$ -value substituted for the 1/1000 chance event (the FDR equation gives the desired resolution level for accurate statistics). The new equation is also set equal to 1 to indicate that the statistics at the desired level of resolution should be achieved 100% of the time when the number of iterations is optimized:

$$1 - \left(1 - \left(\frac{1}{N} \cdot \alpha_{FDR}\right)\right)^{\text{Iterations}} \approx 1. \tag{5}$$

Evidently, the equation above can only be approximately fulfilled, as it converges as number of iterations goes to infinity:

$$\lim_{\text{Iterations} \rightarrow \infty} \left(1 - \left(\frac{1}{N} \cdot \alpha_{FDR}\right)\right)^{\text{Iterations}} = 0. \tag{6}$$

The right side of the equation can be replaced by  $E_A$ , symbolizing an error in accuracy. Then applying the natural logarithm

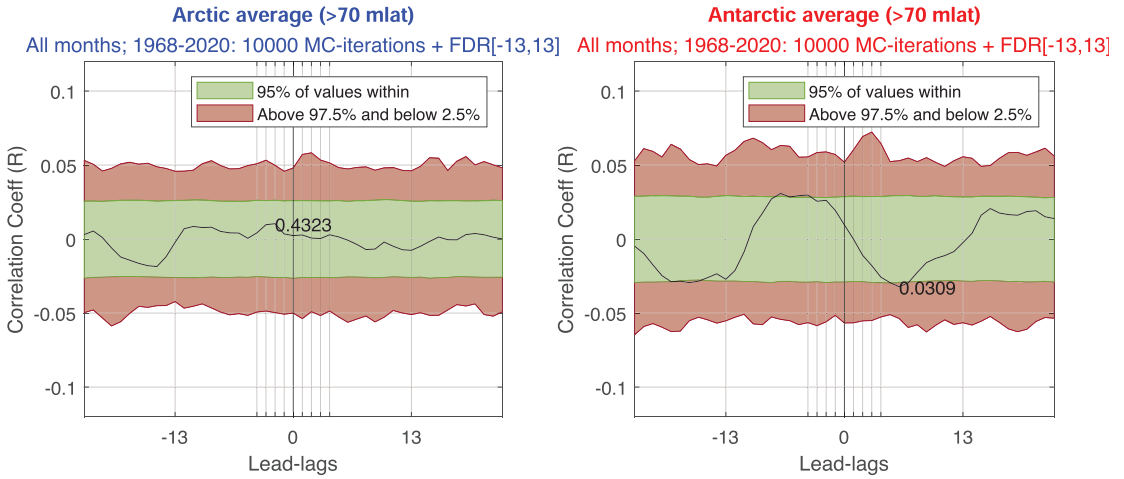


**Fig. 4.** *Left panel:* The significance level for the time-lagged cross-correlation after 10,000 MC-iterations for the period 1968–2020 in the NH. FDR interval is set between lead and lag  $-13$  to  $+13$ . *Right panel:* Same procedure, only for the SH. No significance is obtained in either hemisphere. The smallest  $p$ -value obtained from the MC simulation is highlighted at the point of occurrence. This routine will be done for every figure for comparison.

on both sides, the equation gives the number of iterations required to achieve the desired error in accuracy when representing the underlying statistics at a given resolution:

$$\text{Iterations} = \frac{\ln(E_A)}{\ln\left(1 - \left(\frac{1}{N} \cdot \alpha_{\text{FDR}}\right)\right)} \quad (7)$$

For our cases, where most time-lagged cross correlation plots consist of 41 lead-lags,  $\alpha_{\text{FDR}} = 0.09$ , and by setting  $E_A = 10^{-9}$  ( $E_A = 10^{-9}$  indicates there is a 1 in a billion chance of not obtaining an accurate representation of the underlying statistics at the desired resolution), the equation yields:

$$\text{Iterations} = \frac{\ln(10^{-9})}{\ln\left(1 - \left(\frac{1}{41} \cdot 0.09\right)\right)} = 9430. \quad (8)$$

This implies that  $>9430$  iterations will ensure that our specified resolution of  $(1/41) \cdot 0.09 = 0.0022$  will be fulfilled with a 99.9999999% accuracy. The following analyses apply significance assessments based on 10,000 MC iterations.

### 3 Analyses and results

#### 3.1 Full data period 1968–2020

The time-lagged cross correlation between the IMF  $B_y$  and the geopotential height  $Z_{g(\text{NH})}$  and  $Z_{g(\text{SH})}$  is calculated from 1968 to 2020. As seen in Figure 4, no significance is obtained in either hemisphere by applying MC simulation and FDR significance tests for the interval  $-13$  to  $+13$ . However, the SH exhibits a peak in the correlation values from lead-lag  $-8$  to  $-2$ .

#### 3.2 Seasonality analysis

The next step is to look for potential seasonal dependency. The atmosphere exhibits large variability depending on the seasons, which again could lead to different pathways and strengths of the coupling between IMF  $B_y$  and the polar surface pressure. The full data period is therefore sorted into the seasons grouped as December, January, February (DJF), March, April, May (MAM), June, July, August (JJA), and September, October, November (SON). The time-lagged cross-correlation analysis is then performed for each season individually, with the results shown in Figure 5. In the NH, a significant positive anomaly occurs around lead-lag  $-4$  for the MAM period (which is significant even after the FDR method). The same positive anomaly, shown in Figure 4, still occurs in the SH for both MAM and JJA but is not significant with FDR interval  $-13$  to  $+13$  lead-lags. The Mansurov effect should impose opposite responses in the ionospheric polar cap for the two hemispheres. Positive anomalies are expected in the SH and negative anomalies in the NH at lead-lag 0 and beyond. A general overview of the responses seems more in-phase than out-of-phase for our results. In line with previous studies the seasonal analysis in this section, as well as a sector structure analysis (Sect. 3.5) and combined seasons and sector structure analysis (Sect. 3.6) are also performed for the most cited period of 1999–2002. In summary, there is no season or sector structure rendering statistical significance for the 1999–2002 period after the FDR method is applied. Plots for this sub-period can be found in the Appendix.

#### 3.3 Sector structures

Structures in the solar wind originate from two mechanism. Structures are either imposed from the Sun directly, or, structures form as the solar wind propagates outwards and fills the

Seasons; 1968-2020: 10000 MC-iterations + FDR[-13,13]

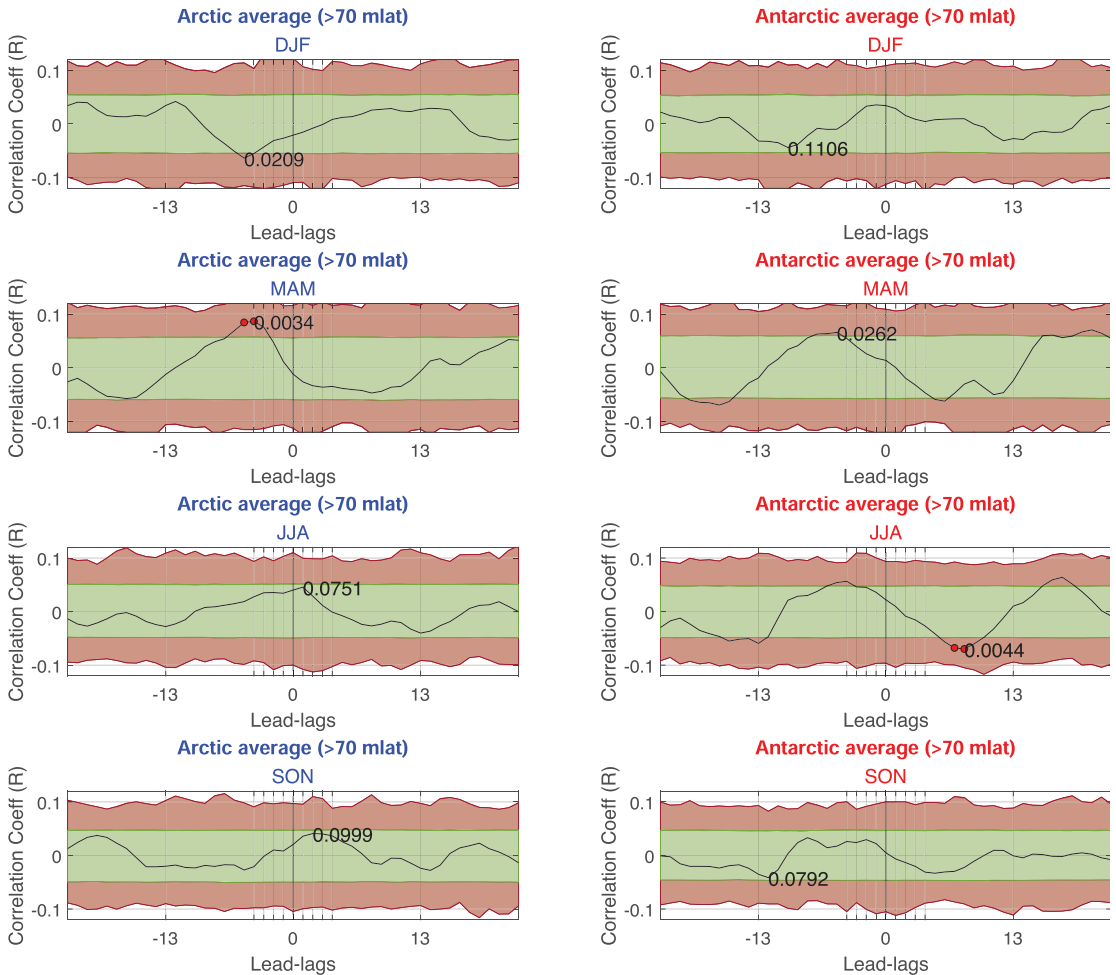


**Fig. 5.** *Left panels:* The significance level for the time-lagged cross-correlation after 10,000 MC-iterations for the period 1968–2020 in the NH for the months DJF (top panel), MAM (middle top panel), JJA (middle bottom panel) and SON (bottom panel). FDR interval is set between lead and lag –13 to +13. Statistical significance after the FDR method is observed in MAM at lead-lag –4 in the NH and in JJA at lead-lag 7 in the SH. *Right panels:* Same procedure, only for the SH. No significance is observed after the FDR method.

heliosphere (Viall et al., 2021). The global solar magnetic field itself is composed by a superposition of the dipole, quadrupole and octupole harmonics, which can lead to imposed 2-, 4- and higher order harmonic sector structures. Tinsley (2022) specifically highlights the importance of the 2-sector solar wind structures in regards to the Mansurov effect, and hypothesise that this sector structure favors the Mansurov effect compared to 4-sector or irregular sector structures. The distinction of the two solar wind sector structures are illustrated in Figure 6. In the left

panel, the dipole harmonics of the global solar magnetic field dominates, and the away and toward sectors experienced on Earth will oscillate with a periodicity of approximately 27-days. Tinsley (2022) hypothesises that longer duration of 2-sector structures nudges uncorrelated pressure oscillations into partial synchronization with the solar wind, while due to the more irregular nature, this is not accomplished for the 4- or irregular sector structures illustrated in the right panel. The frequently cited period 1999–2002 has a 68% occurrence rate of



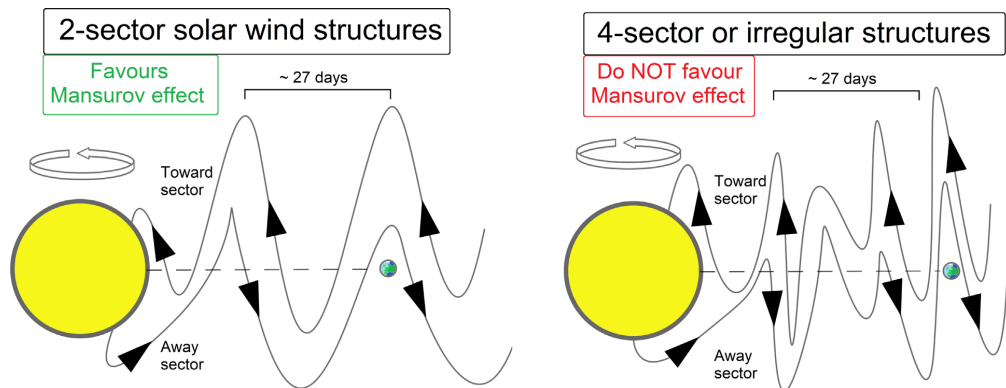


**Fig. 6.** *Left panel:* Illustration of 2-sector solar wind structures. The sector structures oscillate with a periodicity of approximately 27 days. *Right panel:* 4- or irregular sector structures. The sector structures oscillate with either a ~13.5 day periodicity, or irregular periodicity.

the 2-sector structure pattern (Tinsley, 2022). These numbers were manually identified by Tinsley (2022), which recommends a wavelet analysis for more accurate and objective identification.

The middle panel of Figure 7 shows the scalogram obtained by wavelet analysis of the  $B_y$ -index, while the top panel shows the raw  $B_y$ -index with red lines indicating a 2-sector structure, and blue lines indicating 4 or irregular sector structures.

The analysis itself is done by binning all days with the largest intensity in the scalogram of a period occurring in the interval between 22 and 32 days as a 2-sector structure, while the remaining days are binned as 4 or irregular sector structures. From the wavelet analysis, we find a 73% occurrence rate of 2-sector structures and a 27% occurrence rate for 4 or irregular sector structures in the 1999–2002 period. Tinsley (2022) state that the period 2007–2010 yields a less impactful Mansurov effect as the occurrence rate of 2-sector structures is only 40%. However, the wavelet analysis suggests a 65% occurrence rate of the 2-sector structure for this period. Figure 7 also provides the yearly occurrence rate for the period 1968–2020 of 2-sector structures obtained from the scalogram (bottom panel).

### 3.4 Time-lagged cross-correlation and the dependence on the autocorrelation function of both the forcing and responding variable

Before dividing the IMF  $B_y$  data into the two different sector structures, a clear understanding of the inner workings of the time-lagged cross-correlation method is needed.

Figure 8 shows a power spectrum analysis (left panels) of the IMF  $B_y$ , the autocorrelation function for  $Z_{g(\text{NH})}$  (middle panels) and the autocorrelation for  $Z_{g(\text{SH})}$  (right panels). The analysis is also divided into 2-sector structures (top panels) and 4- or irregular sector structures (bottom panel). The top left panel shows that there is a clear peak in power surrounding 27 days/cycle, which is expected as the 2-sector structures exhibit a 27-day periodicity on average. In the bottom left panel, a clear peak in power is seen around 13.5 day/cycle, which is also expected as the 13.5 periodicity is the second most dominant sector structure. For the autocorrelation functions of the

geopotential height, not much variance is seen by the sector division. The NH and SH exhibit similar autocorrelation functions.

Edvartsen et al. (2022) shows how a periodic forcing variable together with an autocorrelated response variable is susceptible to producing artificial periodic responses when a time-lagged cross-correlation method is used. Here, we demonstrate further implications of this artificial anomaly which is particularly relevant in the investigation of the Mansurov effect, but also generally in any other phenomenon with a periodic forcing and autocorrelated response variable.

The left column of Figure 9 shows 1000 iterations where the IMF  $B_y$  is firstly divided into 2- and 4- or irregular sector structures before it is cross-correlated with the geopotential height data series  $Z_{g(\text{NH})}$ . (Due to the roughly similar autocorrelation functions for the hemispheres, it is only necessary to show this experiment for one hemisphere, where the choice of NH is arbitrary.) For every iteration, the geopotential height data series are phase-randomized. In essence, this is the same process that defines the significance limits in the figures above (Figs. 4 and 5). In the middle column, the largest positive peaks occurring between day -13 and +13 for every iteration are shifted and placed at day 0. At last, the right column shows the averaged response of the shifted peaks shown in the middle panels. It is evident that the 2-sector structure in both hemispheres (1. and 3. row) produces a larger artificial periodicity than the 4- or irregular sector structure (2. and 4. row). Simply put, this means that any time-lagged cross correlation between the IMF  $B_y$  and the geopotential height in 2-sector structure periods will have higher values in general, as compared to the 4- or irregular sectors structures. These higher values are then only a result of the autocorrelation function of the forcing and responding variable. The same experiment is performed on the raw geopotential height data in both hemispheres for the period 1968–2020 with similar results.

In addition to being dependent on the autocorrelation function of the forcing and response variables, the value of the correlation coefficient will also depend on the amount of data points used. This highlights the need for modern statistical methods such as MC simulation. MC-simulations applied on suitable statistical material (phase-randomization of original

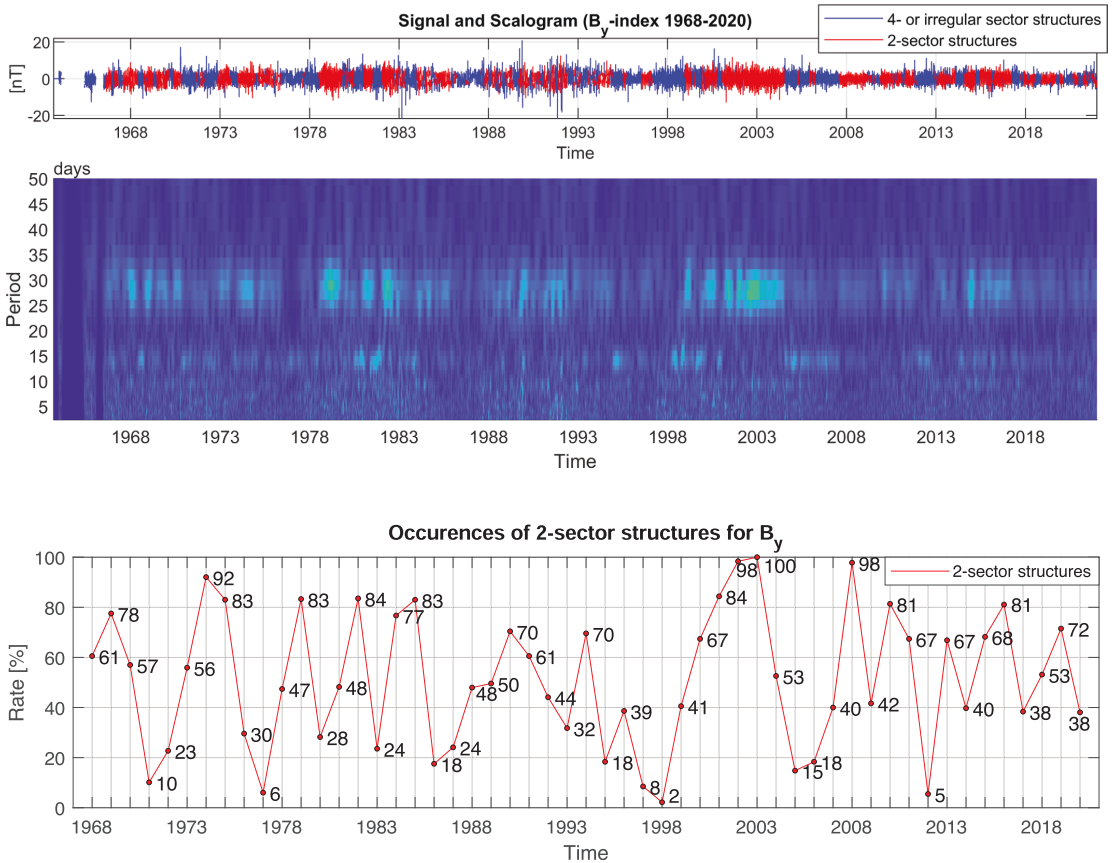


**Fig. 7.** Top panel: The  $B_y$ -index over the time period 1968–2020. Red mark periods of 2-sector structures, while blue mark periods of 4- or irregular sector structures. Middle panel: Scalogram obtained by a wavelet analysis of the  $B_y$ -index over the same time period. The dominating frequencies can be seen by the lighter color bands around 13.5 and 27 days per period. Bottom panel: Yearly occurrence rate of 2-sector structures for the  $B_y$ -index over the same period.

response data series) will take all the relevant information affecting the correlation analysis (autocorrelation of forcing and response variable, and amount of data points) into account. This will result in a realistic  $p$ -value that is of higher relevance than the correlation values itself.

### 3.5 Sector structures analysis

The time-lagged correlation analysis sorted by solar wind sector structures for the full-time period 1968–2020 is performed. Figure 10 shows the time-lagged cross correlation between the IMF  $B_y$  and the variation values  $Z_{g(NH)}$  and  $Z_{g(SH)}$  for periods of 2-sector structures (top panels) and periods of 4- or irregular sector structures (bottom panels). No clear response is seen in the NH for any of the sector structures over the whole data period. However, for the SH, the 2-sector structures seem to enhance the peak in pressure around day  $-6$  compared to Figure 4 where sector structures are not taken into account. It is noted that the positive anomaly is still not

statistically significant after applying the MC simulation together with the FDR method for the interval  $-13$  to  $13$ . The timing of the positive response on day  $-6$  is not in line with the current Mansurov hypothesis, where the pressure anomaly should lag the IMF  $B_y$  driver by a few days (Frederick et al., 2019; Tinsley et al., 2021). We also note that different magnitudes are seen for the significance intervals (green and red shaded area) between the results from the 2-sector structures and 4- or irregular structure analysis even though the two-sector structures have approximately the same number of data points. This is a consequence of the effect described in Section 3.4, demonstrating the importance of MC simulation when assessing the statistical significance.

### 3.6 Seasons and sector structure analysis

The final step investigates the combination of both seasonal and sector structure dependence. The results are shown in Figure 11. In the first column, the time-lagged cross-correlation

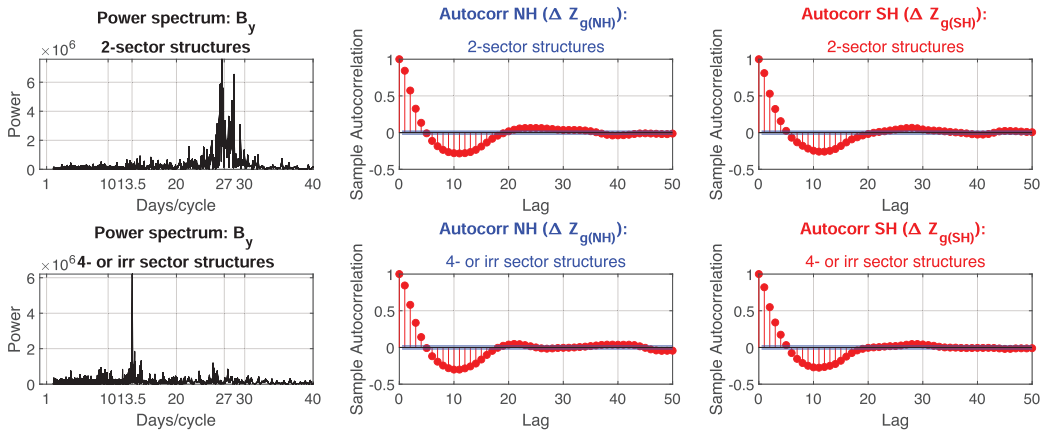


**Fig. 8.** Left panels: Power spectrum of the  $B_y$ -index over the time period 1968–2020 for 2-sector structures (top panel)/4- or irregular sector structures (bottom panel). Middle panels: Autocorrelation function of the geopotential height ( $Z_{g(NH)}$ ) over the same period in the NH for the 2-sector structures (top panel)/4- or irregular sector structures (bottom panel). Right panels: Autocorrelation function of the geopotential height ( $Z_{g(SH)}$ ) over the same period in the SH for the 2-sector structures (top panel)/4- or irregular sector structures (bottom panel).

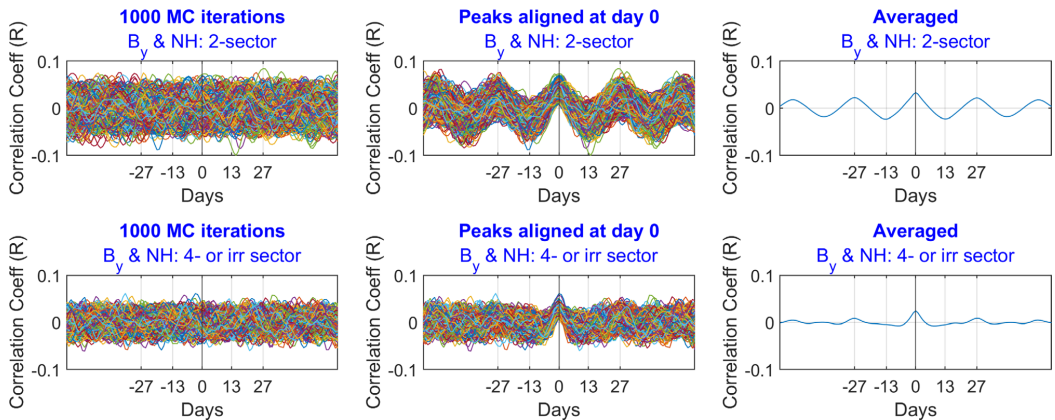


**Fig. 9.** Full data period 1968–2020 divided into the different sector structures Left panels: 1000 MC iterations where the correlation coefficients are calculated between the  $B_y$ -index and the phase randomized  $Z_{g(NH)}$  data series for the 2-sector structures (top panel)/4- or irregular sector structures (bottom panel). Middle panels: All 1000 individual results of the MC-iterations from the left panels aligned such that the maximum value within  $-13$  to  $+13$  is projected to day 0. Right panels: Averaged response of the middle panel. Note the large difference between the 2- and 4-sector structure periods.

for the four different seasons in the NH for 2-sector structures is shown, and 4- or irregular sector structures are shown in the second column. The third and fourth columns follow the same logic for the SH. In all plots, the FDR interval is set from lead  $-13$  to lag  $+13$ . The highest obtained significant data point is also marked with its corresponding  $p$ -value.

As a general overview, there exists no combination of sector structure and season obtaining significant data points in line with the current Mansurov theory (a positive significant anomaly around day 0 in the SH, and a negative significant anomaly

around day 0 in the NH). In DJF, the responses in both hemispheres do follow this pattern. For the NH, this fits the correlations found by Zhou et al. (2018) and Tinsley et al. (2021) predicting a local winter effect, but does not fit with the theory in the SH. It is noted that these correlations are still not statistically significant. However, the same reoccurring pattern of a positive pressure anomaly in both NH and SH around lead-lag  $-5$  appears in March, April and May (MAM) for the 2-structure periods, and renders statistically significant in the SH. It also appears in JJA (mostly in the SH).

All months; 1968–2020: 10000 MC-iterations + FDR[-13,13]

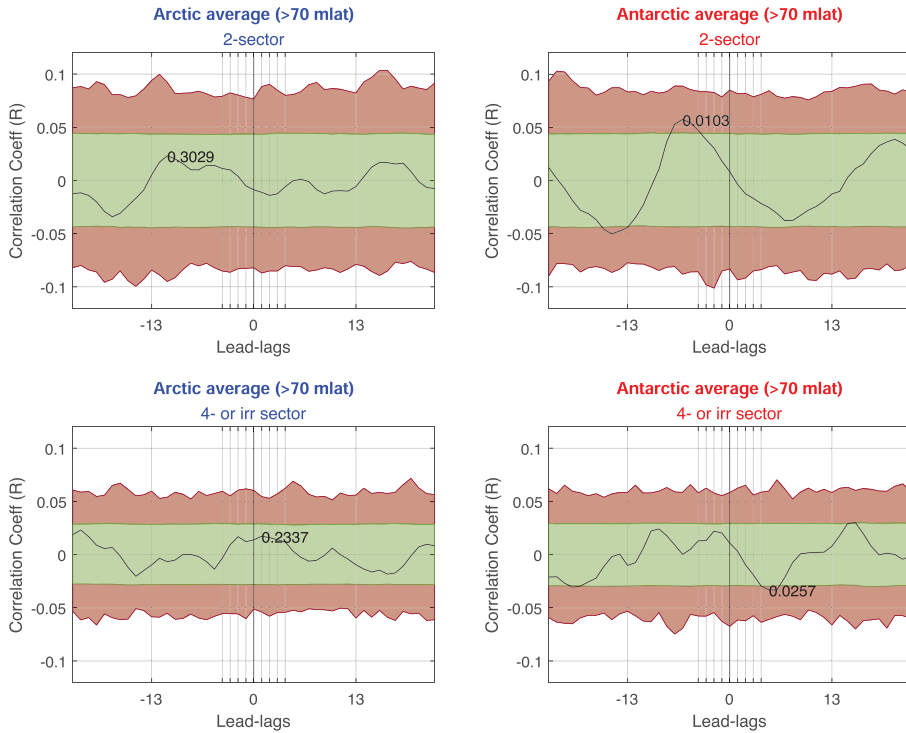


**Fig. 10.** *Left panels:* The significance level for the time-lagged cross correlation after 10,000 MC-iterations for the period 1968–2020 in the NH for 2-sector structures (top panel)/4- or irregular sector structures (bottom panel). FDR interval is set between lead and lag  $-13$  to  $+13$ . *Right panels:* Same procedure, only for the SH. No significance is obtained in either hemisphere.

### 3.7 Day $-5$ anomaly

From all the analyses no indication of the Mansurov effect is found. However, the work has unraveled a rather strange occurrence. In Figure 11, where atmospheric seasons and solar sector structures are combined, a positive anomaly around day  $-5$  is seen concentrated around MAM in both hemispheres for the 2-sector structure periods. This same anomaly is also present in the SH in Figure 10 when divided according to the 2-sector structures for all months. In Figure 5, the anomaly is even statistically significant in the NH for MAM after the FDR method is applied, and it is present in Figure 4 in the SH for the full data period with no sorting requirements. Summarized, our analyses have unveiled a reoccurring positive pressure anomaly happening on average 5 days before the peak  $B_y$  anomaly in both hemispheres. The anomaly obtains the highest statistical significance in MAM but is also visible in JJA in both hemispheres. For division into sector structures, the anomaly favors the 2-sector structure in both hemispheres.

As the anomaly is most persistent in both hemispheres in the 2-sector structure in MAM, the latitudinal extension at this specific lead lag is explored. Figure 12 shows the zonal mean pressure differences ( $Z_{g(SH)}$  and  $Z_{g(NH)}$ ) on lead  $-5$  for days with  $B_y > 3$  nT averaged and subtracted the average of days with

$B_y < -3$  nT (note that correlation is not used, but rather a double superposed epoch analysis. This is done for coherence with earlier analyses on the Mansurov effect (see Zhou et al., 2018, Figs. 1–3). As an extra fail-proof for the significance assessment, we have run the MC simulation for 1,000,000 iterations, including the FDR method over all latitudes giving a total of 72 data points. We note that the FDR over all latitudes may not be physically justified, as the Mansurov effect is only expected to occur at high latitudes. However, since day  $-5$  is a rather unknown anomaly, the latitude-wise extension is also unknown. With all latitudes included, one will therefore expect less significance at the 95% level than if the FDR method only covered the poles. Nevertheless, the figure still demonstrates a remarkable statistical result. The pressure response is significant from  $85$  to  $90^\circ$  S and  $70$  to  $90^\circ$  N, where the latitudes  $75$  to  $80^\circ$  N have a positive response outside of both tails of the probability distribution. In reality, this means that these data points have a  $p$ -value less than 0.000001.

### 3.8 Heliospheric current sheet crossings

To further investigate the reality of the day  $-5$  anomaly, a final analysis focusing on heliospheric current sheet crossing events (HCSC) is performed. HCSC marks the intersection

Seasons & Sectors; 1968-2020: 10000 MC-iterations + FDR[-13,13]

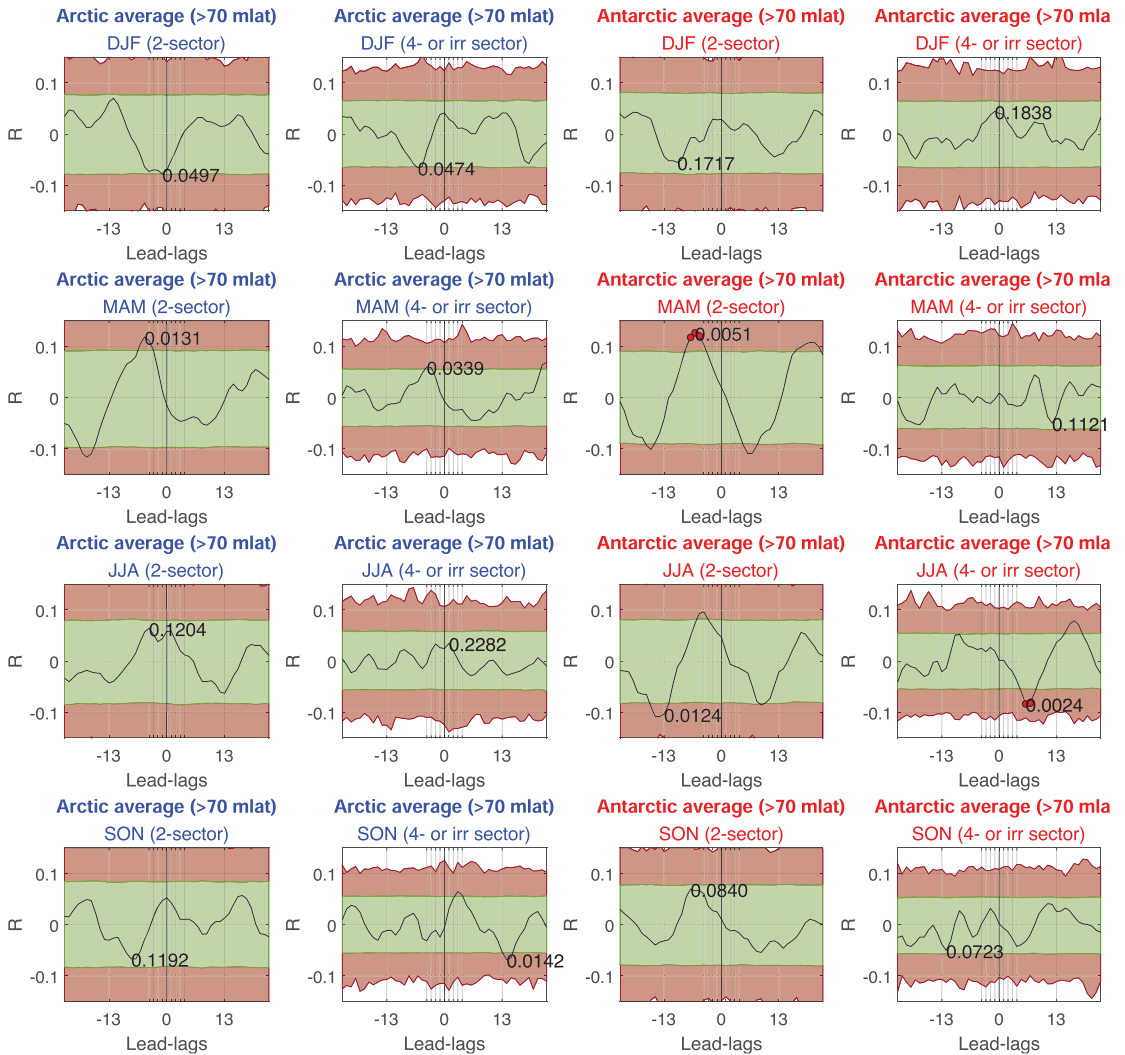


**Fig. 11.** *Left panels:* The significance level for the time-lagged cross-correlation after 10,000 MC-iterations for 2-sector structures in the period 1968–2020 in the NH for the months DJF (top panel), MAM (middle top panel), JJA (middle bottom panel), and SON (bottom panel). FDR interval is set between lead and lag  $-13$  to  $+13$ . *Left middle panels:* Same procedure for the 4- or irregular sector structures in the NH. *Right middle panels:* Same procedure for the 2-sector structures in the SH. *Right middle panels:* Same procedure for the 4- or irregular sector structures in the SH.

between the toward sector ( $B_x < 0, B_y > 0$ ) (T) and the away sector (A) ( $B_x > 0, B_y < 0$ ) of the IMF. As the magnetic field flips, there is an increase in proton density, proton dynamic pressure, magnetic field intensity, and a decrease in solar wind speed (Kan & Wu, 2021). Crossing events happen in between the

maximum  $B_y$  events, which could mean that the day  $-5$  anomalously observed fits with the time of the crossing. A list of crossing events derived by Prof. Leif Svalgaard<sup>1</sup> spanning the data

<sup>1</sup> <https://svalgaard.leif.org/research/sblist.txt>

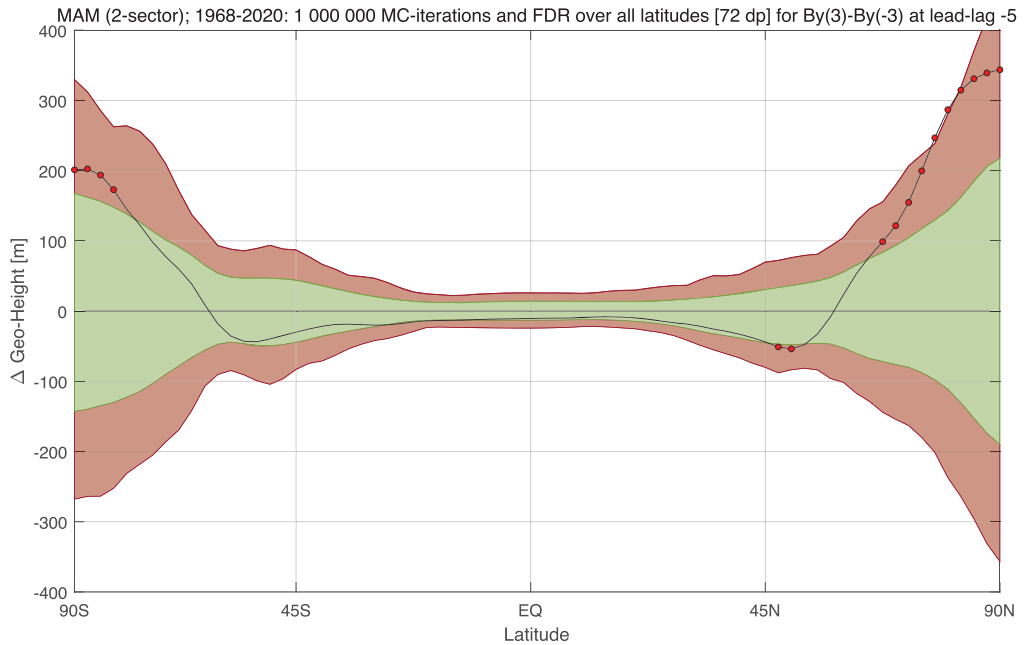


**Fig. 12.** The significance level for the superposed epoch analyses of zonal means after 1,00,000 MC-iterations for 2-sector structures in MAM for the period 1968–2020. Latitudes 75–80° N renders a  $p$ -value less than 0.000001 as the positive anomaly has an absolute value outside both tails of the distribution

interval 1968–2020 is applied. Since MAM without the sector structure sorting is the result with the highest significance for the lead-lag plots, we will focus on this period. Sector structure sorting for the HCSC will be considered in the discussion.

Figure 13 shows superposed epoch analyses of the HCSC for MAM over the whole data period 1968–2020. Similar significance assessment as other lead-lag plots apply. The top row shows the results when the pressure on days with “A T” sector crossings are averaged, and subtracted the average pressure on days with “T A” sector crossings. The middle row shows the superposed epoch for only days where an A sector crossing occurs, while the bottom row shows a superposed epoch for only days where a T sector crossing occurs. As seen in the figure, when the two different crossings are combined as seen in the top row, we get a statistically significant positive anomaly in the NH peaking at day  $-2$ . Comparing it to Figure 5, the significance is increased for the crossings compared to the correlation with  $B_y$ . For the SH, no significance is obtained. In the middle and bottom rows, where the different crossings are treated separately, significance is obtained in the NH for A  $\rightarrow$  T crossings.

Not shown is the same seasonal analysis for HCSC, also including the separation of sector structures, equivalent to Figure 11. The most significant response for the NH is seen in the 4- or irregular sector structures, and not the 2-sector structures which show the most significant response when  $B_y$  is correlated to the pressure. In the correlation analysis, (ex. Fig. 11), emphasis is put on the highs and lows of  $B_y$ . In the superposed epoch analysis of crossings, every event is treated equally, and

the average response of all events is shown. As any mechanism for the HCSC affecting the polar surface pressure is yet to be determined, we can not know if the most impactful HCSC is related to times with the largest variations of  $B_y$ . If we assume that the significant correlations seen for the  $B_y$  and pressure (Figs. 5 and 11) are in reality anomalies resulting from HCSC (Fig. 13), a non-linear relationship between the strength of the  $B_y$  and the surface effect of a HCSC could result in differing signal strengths between the two modes of analysis. We also note that analyzing the zonal mean differences of the HCSC (equivalent to Fig. 12) results in the 4-sector structure showing anomalies outside of the probability distribution in the NH at day  $-2$ .

In general, the HCSC superposed epoch analysis has shortcomings in terms of the timing of the response. The peak anomaly in the NH occurs 2 days before the actual event happens, and no significant response is seen in the SH. However, the responses seen are statistically significant, and one can argue that the pressure response is closer to a physically justified response.

#### 4 Discussion and possible hypotheses

In previous work, the Mansurov effect is shown to not be statistically significant on the decadal timescale (Edvartsen et al., 2022). The same study also shows how previous evidence for the Mansurov effect (27-day cyclic pressure response) is due to a statistical bias created by a periodic forcing and a temporally autocorrelated response variable, and cannot be treated

Edvartsen, Maliniemi, Nesse, and Hatch: Mansurov: SSWSSD

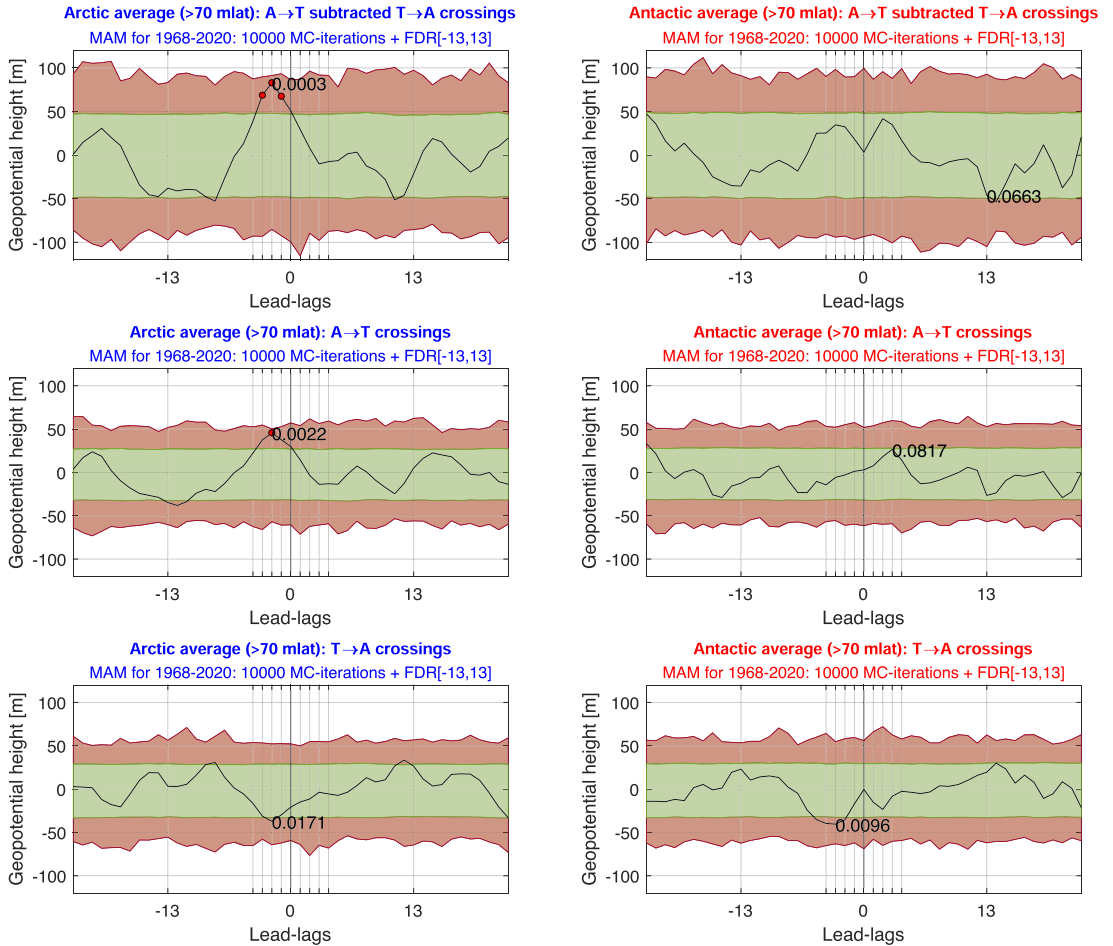


**Fig. 13.** *Left panels:* The significance level for the superposed epoch analyses of HCSC in MAM for the period 1968–2020 in the NH. The top panel show “A T” events subtracted “T A” events. The middle panel shows only “A T” events, while the bottom panel shows only “T A”. *Right panels:* Same procedure, only for the SH. Statistical significance after FDR is found in the NH when looking at the difference between the asymmetric events (top left panel) and for only the A→T events (middle left panel).

as evidence for a physical link. This evidence weakens the overall case for the Mansurov effect, as the hypothesis itself is built from pure correlation analyses (Mansurov et al., 1974; Burns et al., 2008; Lam et al., 2013, 2018; Zhou et al., 2018; Tinsley et al., 2021). However, Edvartsen et al. (2022) did not consider in depth the possibility of seasonal and solar wind structure dependence, which is the aim of the current study.

This study includes a seasonal analysis of decadal time-scales. When analyzing seasonal variations, this considers both the atmospheric state and the Earth’s dipole tilt relative to the IMF, which affects geomagnetic activity. Local winter months

lead to stronger polar vortices, and higher atmospheric variability, while less variability and weaker vortices are seen in local summer. In the solar wind, different seasons mean different geometric conditions impacting the connection between the IMF and Earth’s magnetic field. This manifests itself as the Russell McPherron effect, which is the increased probability of a negative  $B_z$ -component leading to increased geomagnetic activity occurring around early April and early October (Russell & McPherron, 1973). By dividing the time period 1968–2020 into DJF, MAM, JJA, and SON we show (Fig. 5) that none of the specific seasons produce a significant response in line with

1968-2020

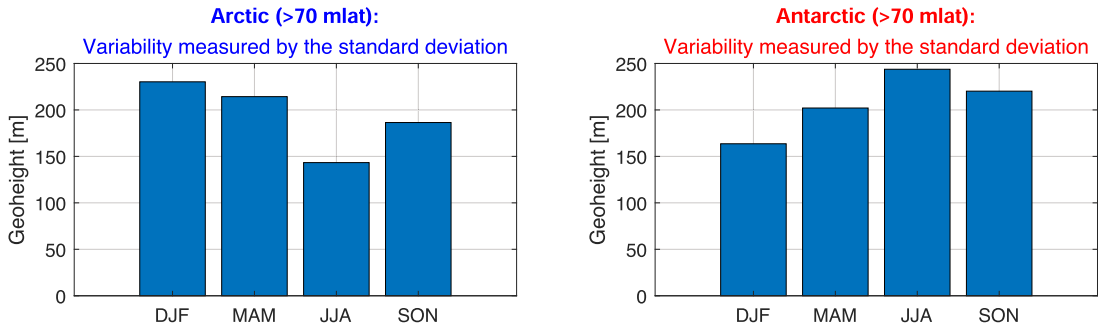


**Fig. 14.** Variability in  $Z_{g(NH)}$  and  $Z_{g(SH)}$  measured by the standard deviation of the different seasons. Largest variability is seen in the local winter.

the Mansurov hypothesis. However, a significant positive pressure anomaly occurs around lead-lag  $-5$  in the NH for MAM, with 3 data points rendered statistically significant after MC-simulations and FDR-method over the interval  $-13$  to 13 lead-lags. Though not significant according to the FDR method, the SH does show phase coherence with the NH for the MAM period. From the perspective of the Mansurov hypothesis, the peak pressure perturbation is expected to happen days after the forcing. This is due to the microphysical changes being small and acquiring time to materialize as macro-physical changes in cloud radiative properties (Frederick et al. 2019; Tinsley et al., 2021). In conclusion, an effect occurring 5 days before the forcing is unphysical given the Mansurov hypothesis. Considering the significant period of MAM, this might be linked to the Russel–McPherron effect, which states that in these months, the connectivity between the IMF and Earth’s geomagnetic field increases. This could be hypothesized to lead to the enhanced surface impact of any mechanism propagating from the solar wind to the surface. However, it would then also be reasonable to expect a pressure response around late September/early October, which is not observed in our results. Another way the atmospheric variability could play a role is if the effect is very small, and risks being disguised by background noise. Figure 14 shows the standard deviation of  $Z_{g(NH)}$  and  $Z_{g(SH)}$  as bars, for the specific seasons analyzed in this study. The local summer in both hemispheres has the least variability. However, the lowest  $p$ -values are obtained in MAM. In NH, this is the month with the second-largest pressure variability. On this basis, it is not likely that the atmospheric variability acts as an obscurer for an effect that is always occurring. Earth’s dipoles’ geometrical positioning or specific reoccurring atmospheric seasonal conditions increasing the coupling between IMF and the polar atmosphere might rather be at play. There have been studies showing that winters following volcanic eruptions, which inject large quantities of sulfate aerosols into the stratosphere, increase the correlation between solar wind parameters and atmospheric effects (Tinsley et al., 2012; Zhou et al., 2014). This effect is not taken into account in this study and remains an open pathway for further research.

Moreover, our study includes the division of the IMF into either 2-sector or 4- or irregular sector structures. These sectors are defined according to the periodicity of the fluctuating  $B_y$ ,

with 2-sector structures defined as a 27-day cycle, and 4- or irregular sector defined as 13-day and all other cycles occurring (Power spectrum of the two distinct sectors for the IMF  $B_y$  can be seen in Fig. 8). Previous research has highlighted the 2-sector structure as important for the manifestation of the Mansurov effect, with the argument mainly based on the occurrence rate in the regularly studied period of 1999–2002 (Tinsley, 2022). It is hypothesized that a continuous period of 2-sector structure oscillations with large amplitude jumps in the  $B_y$  ( $>6$  nT) is needed to nudge the internal atmospheric waves into partial phase coherence (from now called the  $B_y$  Nudge hypothesis). However, Tinsley (2022) also states that the period 2007–2010 does not yield a correct Mansurov manifestation due to the low occurrence of 2-sector structures (40%). As we see in Figure 4, our results show that the period 2007–2010 has as high as a 65% occurrence rate of the 2-sector structure. Nevertheless, as the 2-sector structures in the 2007–2010 period do not reach as high peak amplitudes as the 1999–2002 period, this might still be applied in favor of the  $B_y$  Nudge hypothesis. Figure 4 reveals that if this is the condition necessary for the manifestation of the Mansurov effect, there exists no other sub-period in the interval 1968–2020 having as high amplitudes and long duration of 2-sector structures as the period 1999–2002. Hence, in case the hypothesized pathway does exist, it is likely to excerpt a negligible role with respect to climate variability on decadal scales. This is supported by our analysis of the correlation between the  $B_y$  and pressure after the sector division, as seen in Figure 10. As our results show, the sector division does not enhance any response associated with the current Mansurov theory. It does, however, enhance the day  $-5$  anomaly in the SH. Compared to Figure 4, which is the full-time period, the sector structure division lowers the  $p$ -value for the day  $-5$  anomaly substantially in support of favorable 2-sector structures in the IMF.

The final step in this study includes both seasonal and sector structure divisions. The results are shown in Figure 11. None of the combinations show a response in either hemisphere that is in line with the current Mansurov theory. However, for the day  $-5$  anomaly pattern, both MAM and JJA show phase coherence in both hemispheres for the 2-sector structures. In the NH, MAM and 4- or irregular sector structures also show phase coherence, but with less significance than the 2-sector. As stated early, none



of the combinations show a signal that is significant at the 95% level after considering MC-simulation and FDR-method for the interval  $-13$  to  $+13$  lead-lags.

This study aims to unravel any seasonal or solar wind sector structure dependence on the Mansurov effect, as this was an open end in our earlier study (Edvartsen et al., 2022). For the main known arguments about specific dependencies, mainly seasonal and IMF structural effect, no results obtained show the existence of a significant correlation between the pressure in either hemisphere and the IMF  $B_y$ , acting according to the hypothesized mechanism. The study is not able to conclude that such a pathway does not exist, only that the data used in our study does not support it. However, in this process, the analyses have unraveled a rather strange but persistent occurrence, namely the day  $-5$  positive peak anomaly occurring in both hemispheres mostly in the MAM period and the 2-sector solar wind structure. The anomaly is persistent and also renders significant values for some of the analyses after FDR. Figure 12 shows the zonal mean pressure with respect to days for which  $B_y > 3nT$  subtracted days with  $B_y < -3nT$  for all latitudes at day  $-5$  in the combined MAM and 2-sector structure period. As the behavior of the anomaly does not fit any existing theory, the MC simulations were run 1 million times, just as a test of robustness. As the figure shows, for latitudes  $75-80^\circ$ , the response obtained is outside the probability distribution. This is equivalent to  $p < 0.000001$ . We conclude that the signal is extremely robust and very unlikely to be produced by chance. To clarify this rather strange anomaly, Figure 13 shows the MAM period for HCSC, where these events are treated to produce differing signed anomalies depending on if it's an "A T" or "T A" event. Since the peak  $B_y$  values usually occurs some days after a crossing of the 0-line, the HCSC was considered a potential driver. The crossing events do produce statistically significant positive anomalies in the NH. However, the anomaly still occurs 2 days before the key date, which now represents the day of the HCSC. Another problem with the HCSC is the fact that the 4-sector structures in MAM produce more significance than the 2-sector, while the opposite is true for the correlation between  $B_y$  and the pressure. As explained earlier, this could be due to the effect having a non-linear relationship between the strength of the  $B_y$  and the surface impact, which could influence how the response in the correlation analysis appears.

Edvartsen et al. (2022) showed how periodic forcing and an autocorrelated response variable will induce an artificial periodicity in the response obtained, even if completely random numbers are used (Fig. 9 in Edvartsen et al., 2022). The results obtained in this study further build on this by showing how two structurally different forcing data series (from 2- and 4-sector structures) exhibit very different degrees of this artificial bias (Fig. 7). This highlights the importance of MC simulation, which is able to take the full autocorrelation function of both forcing and response variables into account. As seen in Figure 8, this leads to the significance distributions being adjusted for the specific periods, and not a one size fits all period. To our knowledge, there exists no method taking this into account as efficiently as MC simulations.

Finally, we will discuss possible hypotheses potentially explaining the lack of significant support of the Mansurov hypothesis and the potential  $-2$  day lag for an HCSC driver.

1. External forcing on the GEC can lead to effects on the internally driven thunderstorm generator. Changes in the GEC could also manifest themselves as changes in the rate of lightning, again leading to atmospheric changes. Changes in the lightning rate at low latitudes can lead to atmospheric disturbances propagating to higher latitudes. Owens et al. (2014) find a statistically significant result for correlations between different IMF polarities and local distribution of lightning. For the toward sector, the lightning rate above the UK is enhanced with respect to the away sector. It is suggested that rather than the annual lightning rate being modulated, a redistribution of the lightning activity with respect to location occurs. However, no definite mechanism is established. Owens et al. (2015) also find results of HCSC correlating at a significant level with thunderstorm activity in the UK over the time period 2000–2007. "A T" crossings are cited to be associated with a strong rise in lightning flash rates immediately following the HCSC. On the contrary, "T A" crossings are cited to be associated with a decrease in flash rates. Both results are statistically confirmed significant by MC-simulation. These results are compelling, as the pressure response also shows asymmetric behavior at the two sector boundary crossings consistent with this study. However, a physical explanation for the  $-2$  day lag in our results is not found. A recommended pathway is a further investigation with improved and prolonged data correlating the IMF  $B_y$  and HCSC with the global or local distribution of lightning.

2. The relation is known as the Mansurov Effect is misunderstood. The data does not support the peak  $B_y$  as the maximum force, and asymmetry between the hemispheres is also not supported by our analyses. The relation could be non-linear depending on the rate of change of  $B_y$ , or both the rate of change of  $B_y$  and the maximum  $B_y$  in an intricate manner. The pressure response could also have a threshold value before the switching sign as mentioned by Burns et al. (2008). However, for the MAM period (Figs. 5, 11, and 12) the hemispheres have opposite seasons. It can therefore be argued that due to the different atmospheric conditions, this could manifest itself as the same signed responses, even though the forcing itself is asymmetric between the hemispheres.

3. The Mansurov effect exists as it is hypothesized, but the actual effect in the atmosphere is too small to stand out from the noisy background. This is supported by Zhou et al. (2018) showing how the internal thunderstorm generator produces anomalies in accord with the Mansurov effect for the period 1998–2001. However, problems with this specific analysis are the small time period of data and the limited assessment of significance. A better way of detecting the Mansurov effect would be through correlation analyses of the internally generated ionospheric vertical electrical field ( $E_z$ ) and polar surface pressure. The externally generated changes are suggested to attribute  $<10\%$  of the total change in Ionosphere-Earth current flow (Tinsley, 2022). If analyses over longer timescales can show the internally generated Ionosphere-Earth current flow ( $>90\%$  of total) significantly correlating with surface pressure according to the Mansurov hypothesis, one can also assume that external effects will play a role. The external effect might be too small to be detected in a noisy background with the data periods available today, but the existence of statistically significant internal effects would strengthen the hypothesis tremendously.

In addition, as the internal changes are larger, it should also be easier to detect significant changes. These kind of analyses are out of the scope of the article but is a highly recommended pathway for further research on this and related phenomena.

4. The HCSC, not the  $B_y$  amplitudes, are responsible for the low altitude pressure correlations. As our results show, HCSC shows up as a statistically significant anomaly in the NH for MAM. However, the significant peak anomaly occurs 2 days before the actual sector boundary crossing. Wilcox et al. (1973) found correlations between the atmospheric vorticity poleward of 20° N and HCSC during the winter months of 1963–1970. These results showed no preference for an “A T” or “T A” crossing and were confined to 500–300 hPa. Figure 13, demonstrates, however, a sector boundary preference. Nevertheless, no mechanism is established for the HCSC correlations termed the Wilcox effect. To our knowledge, there also does not exist recent research on the Wilcox effect. Recommended further research for this pathway would be to look at the correlation between HCSC and pressure for higher atmospheric levels. Before dismissing the physically unjustifiable –2 day lag of the response, it is also recommended to look for solar structures or other phenomena related to HCSC.

5. There exists no physical link between external effects originating from the IMF  $B_y$  on the global electric circuit and surface polar pressure. Our analyses show that the sorting of common non-stationary features dependent on the seasons and IMF sector structure gives no statistical evidence in favor of the Mansurov Effect, and the anomaly seen at day –5 could be purely coincidental. However, the extremely low  $p$ -values obtained in the NH at MAM are hard to discredit on a statistical basis, especially as the same levels of low  $p$ -values are also found for the HCSC. Nevertheless, the responses are also hard to justify on a physical basis with the current knowledge of possible mechanisms rendering a day –2 or –5 lag physically unlikely. An explanation for the discrepancy could therefore also be an aliasing phenomenon. Evidence of the solar rotational UV cycle influencing the Madden–Julian Oscillation (MJO) has been obtained at significant levels after MC simulations (Hood, 2018). The MJO itself is a tropical weather phenomenon, but it has still been shown to impact the Arctic (Zhou & Wang, 2021). Incorporating the MJO oscillation in studies between the IMF and atmospheric pressure is beyond the scope of this paper, but remains a pathway for future research.

## 5 Conclusion

This study has extended the analyses of the Mansurov effect to possible seasonal and solar wind sector structure-dependent responses on decadal timescales compared to Edvartsen et al. (2022). By correlating the IMF  $B_y$  and surface polar pressure, no statistical evidence for dependent behavior is found. However, a new statistically significant anomaly has appeared in multiple sub-periods in both hemispheres. The anomaly occurs approximately 5 days before the maximum  $B_y$  value, implying that the effect precedes the forcing, which is not physically justified. We, therefore, provide five different hypotheses as an attempt to explain the phenomena and open pathways for further investigation.

**Acknowledgements.** We thank the ECMWF (European Center for Medium Weather Forecast) for ERA5 data (<https://www.ecmwf.int/en/forecasts/datasets/reanalysis-datasets/era5>), NASA Goddard Space Center for OMNIWeb database (<https://omniweb.gsfc.nasa.gov/>) and Svalgaard (2020) (<https://www.leif.org/research/sblist.txt>). All codes and data required to reproduce the results of this study are openly available and can be downloaded from Zenodo (<https://doi.org/10.5281/zenodo.7851658>). The research was funded by the Norwegian Research Council under contracts 223252/F50 (BCSS) and 300724 (EPIC). The editor thanks Maarten Jansen and Jaroslav Urbar for their assistance in evaluating this paper.

## References

- Benjamini Y, Hochberg Y. 1995. Controlling the false discovery rate: A practical and powerful approach to multiple testing. *J Roy Stat Soc: Ser B (Methodol)* **57**: 289–300. <https://doi.org/10.1111/j.2517-6161.1995.tb02031.x>.
- Burns G, Tinsley B, Frank-Kamenetsky A, Bering E. 2007. Interplanetary magnetic field and atmospheric electric circuit influences on ground level pressure at vostok. *J Geophys Res* **112**. <https://doi.org/10.1029/2006JD007246>.
- Burns GB, Tinsley BA, French WJR, Troshichev OA, Frank-Kamenetsky AV. 2008. Atmospheric circuit influences on ground-level pressure in the Antarctic and Arctic. *J Geophys Res* **113**: D15112. <https://doi.org/10.1029/2007JD009618>.
- Edvartsen J, Maliniemi V, Nesse Tysøy H, Asikainen T, Hatch S. 2022. The Mansurov effect: Statistical significance and the role of autocorrelation. *J Space Weather Space Clim* **12**: 11. <https://doi.org/10.1051/swsc/2022008>.
- Frederick JE, Tinsley BA, Zhou L. 2019. Relationships between the solar wind magnetic field and ground-level longwave irradiance at high northern latitudes. *J Atmos Sol-Terr Phys* **193**: 105063. <https://doi.org/10.1016/j.jastp.2019.105063>.
- Freeman MP, Lam MM. 2019. Regional, seasonal, and inter-annual variations of Antarctic and sub-Antarctic temperature anomalies related to the Mansurov effect. *Environ Res Commun* **1**: 111007. <https://iopscience.iop.org/article/10.1088/2515-7620/ab4a84>.
- Hood L. 2018. Short-term solar modulation of the Madden-Julian climate oscillation. *J Atmos Sci* **75**: 857–873. <https://doi.org/10.1175/JAS-D-17-0265.1>.
- Kan L, Wu CC. 2021. Characteristics of the heliospheric current sheet at the sector boundaries: Wind observations from 1995–2020. *Astrophys J* **920**: 39 (12 pp). <https://doi.org/10.3847/1538-4357/ac1586>.
- Lam MM, Tinsley BA. 2016. Solar wind-atmospheric electricity cloud microphysics connections to weather and climate. *J Atmos Sol-Terr Phys* **149**: 277–290. <https://doi.org/10.1016/j.jastp.2015.10.019>. ISSN: 1364-6826.
- Lam MM, Chisham G, Freeman MP. 2013. The interplanetary magnetic field influences mid-latitude surface atmospheric pressure. *Environ Res Lett* **8**: 045001. <https://doi.org/10.1088/1748-9326/8/4/045001>.
- Lam MM, Freeman M, Chisham G. 2018. IMF-driven change to the Antarctic tropospheric temperature due to the global atmospheric electric circuit. *J Atmos Sol-Terr Phys* **180**: 148–152. <https://doi.org/10.1016/j.jastp.2017.08.027>.
- Lancaster G, Iatsenko D, Pidde A, Ticcinelli V, Stefanovska A. 2018. Surrogate data for hypothesis testing of physical systems. *Phys Rep* **748**: 1–60. <https://doi.org/10.1016/j.physrep.2018.06.001>. ISSN 0370-1573.

- Mansurov SM, Mansurova LG, Mansurov GS, Mikhnevich VV, Visotsky AM. 1974. North-south asymmetry of geomagnetic and tropospheric events. *J Atmos Terr Phys* **36(11)**: 1957–1962. [https://doi.org/10.1016/0021-9169\(74\)90182-2](https://doi.org/10.1016/0021-9169(74)90182-2).
- Owens MJ, Scott CJ, Lockwood M, Barnard L, Harrison RG, Nicoll K, Watt C, Bennett AJ. 2014. Modulation of UK lightning by heliospheric magnetic field polarity. *Environ Res Lett* **9**: 115009. <https://doi.org/10.1088/1748-9326/9/11/115009>.
- Owens MJ, Scott CJ, Bennett AJ, Thomas SR, Lockwood M, Harrison RG, Lam MM. 2015. Lightning as a space-weather hazard: UK thunderstorm activity modulated by the passage of the heliospheric current sheet. *Geophys Res Lett* **42**: 9624–9632. <https://doi.org/10.1002/2015GL066802>.
- Russell CT, McPherron RL. 1973. Semiannual variation of geomagnetic activity. *J Geophys Res* **78**: 82–108. <https://doi.org/10.1029/JA078i001p00092>.
- Siingh D, Gopalakrishnan V, Singh R, Kamra A, Singh S, Pant V, Singh A. 2007. The atmospheric global electric circuit: An overview. *Atmos Res* **84(2)**: 91–110. <https://doi.org/10.1016/635>.
- Svalgaard L. 2020. *IMF sector boundaries*. Available at: <https://www.leif.org/research/sblist.txt>.
- Theiler J, Prichard D. 1996. Constrained-realization Monte-Carlo method for hypothesis testing. *Phys D* **94**: 221–235. [https://doi.org/10.1016/0167-2789\(96\)00050-4](https://doi.org/10.1016/0167-2789(96)00050-4).
- Tinsley BA. 2000. Influence of solar wind on the global electric circuit, and inferred effects on cloud microphysics, temperature, and dynamics in the Troposphere. *Space Sci Rev* **94**: 231–258. <https://doi.org/10.1023/A:1026775408875>.
- Tinsley BA. 2008. The global atmospheric electric circuit and its effect on cloud microphysics. *Rep Progr Phys* **71**: 66801–66831. <https://doi.org/10.1088/0034-4885/71/6/066801>.
- Tinsley BA. 2022. Uncertainties in evaluating global electric circuit interactions with atmospheric clouds and aerosols, and consequences for radiation and dynamics. *J Geophys Res: Atmos* **127**: e2021JD035954. <https://doi.org/10.1029/2021JD035954>.
- Tinsley BA, Deen GW. 1991. Apparent tropospheric response to MeV-GeV particle flux variations: A connection via electrofreezing of supercooled water in high-level clouds? *J Geophys Res* **96(D12)**: 22283–22296. <https://doi.org/10.1029/91JD02473>.
- Tinsley BA, Heelis RA. 1993. Correlations of atmospheric dynamics with solar activity evidence for a connection via the solar wind, atmospheric electricity, and cloud microphysics. *J Geophys Res: Atmos* **98(D6)**: 10,375–10384. <https://doi.org/10.1029/93JD00627>.
- Tinsley BA, Zhou L, Liu W. 2012. The role of volcanic aerosols and relativistic electrons in modulating winter storm vorticity. *Adv Space Res* **50**: 819–827. <https://doi.org/10.1016/j.asr.2011.12.019>.
- Tinsley BA, Zhou L, Wang L, Zhang L. 2021. Seasonal and solar wind sector duration influences on the correlation of high latitude clouds with ionospheric potential. *J Geophys Res: Atmos* **126(4)**: e2020JD034201. <https://doi.org/10.1029/2020JD034201>.
- Veretenenko S, Ogurtsov M. 2012. Regional and temporal variability of solar activity and galactic cosmic ray effects on the lower atmosphere circulation. *Adv Space Res* **49(4)**: 770–783. <https://doi.org/10.1016/j.asr.2011.11.020651>.
- Veretenenko S, Ogurtsov M, Lindholm M, Jalkanen R. 2018. Galactic cosmic rays and low clouds: Possible reasons for correlation reversal. In: *Cosmic Rays*, IntechOpen, Rijeka, pp. 79–98. <https://doi.org/10.5772/intechopen.75428>.
- Viall NM, DeForest CE, Kepko L. 2021. Mesoscale structure in the solar wind. *Front Astron Space Sci* **8**: 2296–987X. <https://doi.org/10.3389/fspas.2021.735034>.
- Wilcox JM, Scherrer PH, Svalgaard L, Roberts WO, Olson RH. 1973. Solar magnetic structure: Relation to circulation of the Earth's atmosphere. *Science* **180**: 185–186. <https://doi.org/10.1126/science.180.4082.185>.
- Wilks DS. 2016. “The stippling shows statistically significant grid points”: How research results are routinely overstated and over interpreted, and what to do about it. *Bull Am Meteorol Soc* **97**: 2263–2273. <https://doi.org/10.1175/BAMS-D-15-00267.1>.
- Williams ER. 2005. Lightning and climate: A review. *Atmos Res* **76(1–4)**: 272–287. <https://doi.org/10.1016/j.atmosres.2004.11.014>.
- Zhou Y, Wang Y. 2021. Influence of the Madden-Julian oscillation on the Arctic oscillation prediction in S2S operational models. *Front Earth Sci* **9**: 2296–6463. <https://doi.org/10.3389/feart.2021.787680>.
- Zhou L, Tinsley BA, Huang J. 2014. Effects on winter circulation of short and long term solar wind changes. *Adv Space Res* **54**: 2478–2490. <https://doi.org/10.1016/j.asr.2013.09.017>.
- Zhou L, Tinsley BA, Wang L, Burns GB. 2018. The zonal mean and regional tropospheric pressure responses to changes in ionospheric potential. *J Atmos Sol-Terr Phys* **171**: 111–118. <https://doi.org/10.1016/j.jastp.2017.07.010>.

Seasons; 1999-2002: 20000 MC-iterations + FDR[-13,13]

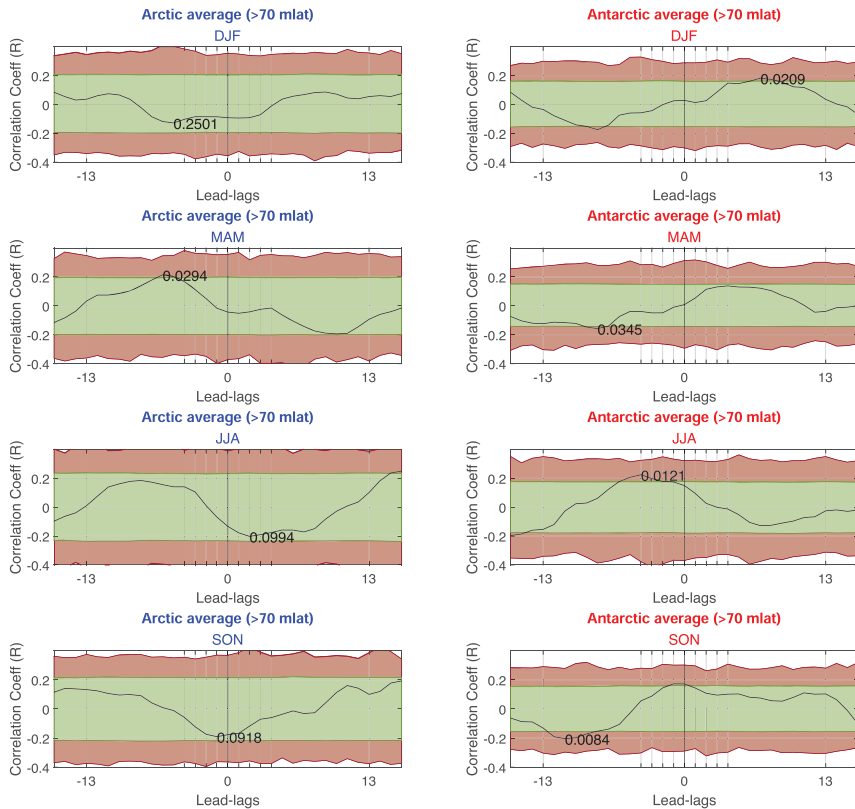


**Fig. A.1.** Left panels: The significance level for the time-lagged cross-correlation after 10,000 MC-iterations for the period 1999–2002 in the NH for the months DJF (top panel), MAM (middle top panel), JJA (middle bottom panel) and SON (bottom panel). FDR interval is set between lead and lag  $-13$  to  $+13$ . Right panels: Same procedure, only for the SH. No significance is observed after the FDR method.

## Appendix

A similar analysis as done in Section 3.2 (seasonality) is performed for the most cited period of 1999–2002 and shown in Figure A.1. It is noted that due to the small time period (implying cheaper computations for the MC simulation), we perform 20,000 MC iterations for increased accuracy. Tinsley (2022) discuss how the mixing of the seasons might affect the significance assessment, due to favorable conditions for the Mansurov effect in the local wintertime. However, as the figure shows, no specific season has a statistically significant response when the FDR is applied over the interval  $-13$  to  $+13$  lead-lags.

A similar analysis as done in Section 3.5 (sector structure) is performed for the most cited period of 1999–2002 and shown in Figure A.2. No specific sector structure shows a statistically significant response when the FDR is applied over the interval  $-13$  to  $+13$  lead-lags.

A similar analysis as done in Section 3.6 (seasons and sector structure) is also performed for the most cited period of 1999–2002 and shown in Figure A.3. No specific combination of season and sector structure shows a statistically significant response when the FDR is applied over the interval  $-13$  to  $+13$  lead-lags. The most notable anomaly occurs in the Arctic for the JJA period in 4- or irregular sector structures. Here, the negative anomaly on day 1 obtains a  $p$ -value equal to 0.0061. It is noted that if the FDR method is only performed over the interval  $-2$  to  $+2$  lead-lags the anomaly at day 1 would be rendered statistically significant. However, this result is not in line with the hypothesized mechanism being favored in local winter and 2-sector structures (Tinsley, 2022), as the result would be significant in the opposite combination (local summer and 4- or irregular sector structures). A reasonable explanation for this result might very well be appointed to chance. For the FDR interval set to  $-2$  to  $+2$  lead-lags, this particular response

All months; 1999–2002: 20000 MC-iterations + FDR[-13,13]

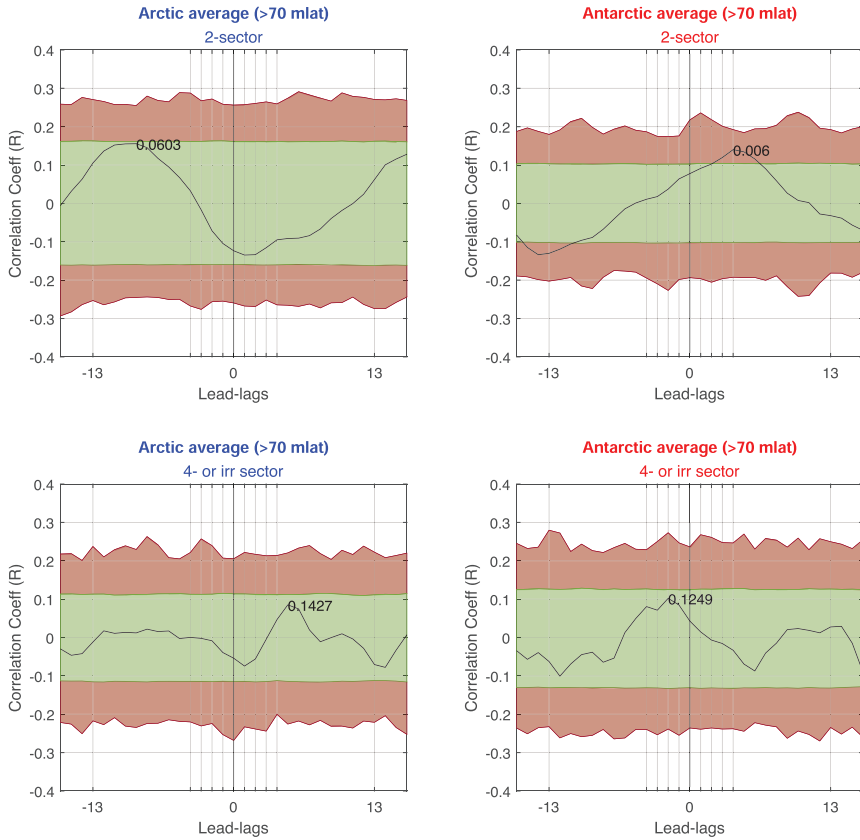


**Fig. A.2.** *Left panels:* The significance level for the time-lagged cross-correlation after 10,000 MC-iterations for the period 1999–2002 in the NH for 2-sector structures (top panel)/4- or irregular sector structures (bottom panel). FDR interval is set between lead and lag  $-13$  to  $+13$ . *Right panels:* Same procedure, only for the SH. No significance is obtained in either hemisphere.

is per definition statistically significant as only 5% of rendered responses will have equally low  $p$ -values within this interval. However, as the figure display a total of 16 subplots, this means that the expected value of getting 1 signal that passes the FDR limit is  $16/20 = 0.8$ . Based on the premise that this particular period does not fit the hypothesized mechanism, it is therefore

reasonable to assume that this might occur by chance. Nevertheless, as discussed in [Section 3.8](#) (Heliospheric Current Sheet Crossings), the most significant responses are seen under the 4-sector structures. A mechanism including crossing events might then give an explanation for this occurrence.

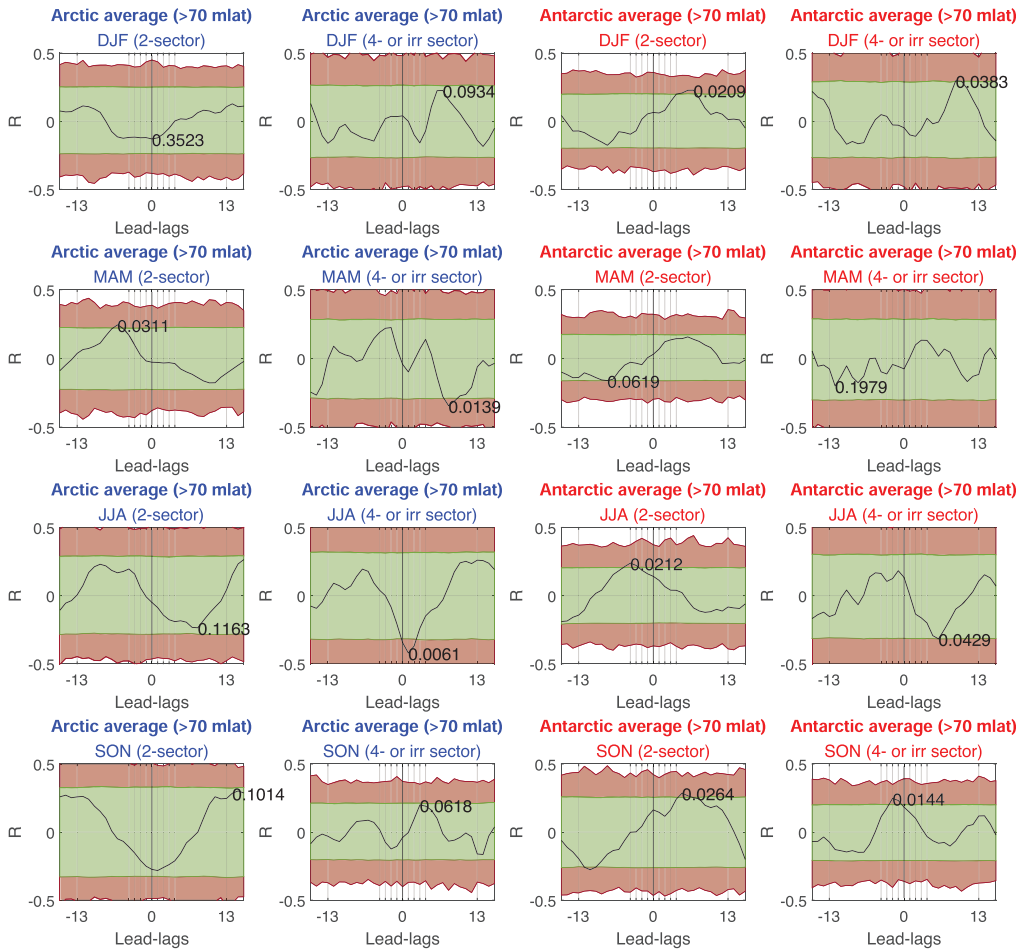


**Fig. A.3.** *Left panels:* The significance level for the time-lagged cross-correlation after 10,000 MC-iterations for 2-sector structures in the period 1968–2020 in the NH for the months DJF (top panel), MAM (middle top panel), JJA (middle bottom panel), and SON (bottom panel). FDR interval is set between lead and lag  $-13$  to  $+13$ . *Left middle panels:* Same procedure for the 4- or irregular sector structures in the NH. *Right middle panels:* Same procedure for the 2-sector structures in the SH. *Right middle panels:* Same procedure for the 4- or irregular sector structures in the SH. No significance is observed in either hemisphere.

**Cite this article as:** Edvartsen JØ, Maliniemi V, Nesse H & Hatch S 2023. The Mansurov effect: Seasonal and solar wind sector structure dependence. *J. Space Weather Space Clim.* 13, 17. <https://doi.org/10.1051/swsc/2023013>.



# Paper III

## **Effects of Energetic Particle Precipitation on stratospheric temperature during disturbed Stratospheric Polar Vortex conditions**

J.Ø. Edvartsen, V. Maliniemi and H. Nesse. *Journal of Geophysical Research: Atmospheres*, **128**, 10. doi:10.1029/2022JD038010 (2023)





**Special Section:**

Monitoring the Earth radiation budget and its implication to climate simulations: Recent Advances and Discussions

**Key Points:**

- We investigate links between Energetic Particle Precipitation and atmospheric dynamics during times of disturbed stratospheric polar vortex
- By usage of model data, significant temperature anomalies are observed in the middle stratosphere, consistent with observational studies
- A disturbed polar vortex (enhanced planetary wave activity), favor stratospheric temperature impact by Energetic Particle Precipitation

**Correspondence to:**

J.Ø. Edvartsen,  
[jone.edvartsen@uib.no](mailto:jone.edvartsen@uib.no)

**Citation:**

Edvartsen, J. Ø., Maliniemi, V., & Nesse, H. (2023). Effects of energetic particle precipitation on stratospheric temperature during disturbed stratospheric polar vortex conditions. *Journal of Geophysical Research: Atmospheres*, 128, e2022JD038010. <https://doi.org/10.1029/2022JD038010>

Received 19 OCT 2022

Accepted 13 APR 2023

**Author Contributions:**

**Conceptualization:** J. Ø. Edvartsen

**Data curation:** V. Maliniemi

**Investigation:** J. Ø. Edvartsen

**Methodology:** J. Ø. Edvartsen, V. Maliniemi

**Software:** J. Ø. Edvartsen

**Supervision:** V. Maliniemi

**Validation:** V. Maliniemi

**Visualization:** J. Ø. Edvartsen

**Writing – original draft:** J. Ø. Edvartsen

**Writing – review & editing:** V. Maliniemi

© 2023. American Geophysical Union.  
 All Rights Reserved.

## Effects of Energetic Particle Precipitation on Stratospheric Temperature During Disturbed Stratospheric Polar Vortex Conditions

J. Ø. Edvartsen<sup>1</sup> , V. Maliniemi<sup>1</sup> , and H. Nesse<sup>1</sup>

<sup>1</sup>Birkeland Center for Space Science, Department of Physics and Technology, University of Bergen, Bergen, Norway

**Abstract** Recently, observational and re-analysis studies have outlined potentially enhanced influence of Energetic Particle Precipitation (EPP) either at times preceding Sudden Stratospheric Warmings (SSW) or when the distribution of planetary wave activity is suitable. In addition, significant correlations have been found between EPP and the occurrence rate of SSWs when the phases of the Quasi-Biennial Oscillation (QBO) are taken into account. Here we study the influence of EPP during disturbed stratospheric polar vortex conditions using chemistry-climate model SOCOL-MPIOM3 over the 20th century. When classifying disturbed conditions, the definition of minor SSWs are utilized along with a temperature gradient (day-to-day variations) criteria at 90°N and 10 hPa acting as a measure of the strength of the events. We find no influence of EPP on the occurrence rate of disturbed conditions over the last 100 year period. However, conditions preceding and during the disturbances are significantly different when EPP forcing is included into the model. This is especially true for stratospheric disturbances occurring in February. Furthermore, there is a clear tendency that the EPP effect becomes more notable after the 1950s. Our results imply that EPP forcing could be important for the stratospheric conditions during winter and that pre-conditioning forced by atmospheric disturbances are an important factor when considering how the mechanism operates.

**Plain Language Summary** Energetic particles precipitating into the atmosphere is known to produce nitric (NO<sub>x</sub>) and hydrogen (HO<sub>x</sub>) oxides. These molecules are known to be associated with ozone (O<sub>3</sub>) loss, which is further shown to impact the temperature and weather patterns of the middle atmosphere. Recently, studies have shown that this impact could potentially be largest during winter time when the polar vortex experiences disturbed and unstable conditions. To study the impact of energetic particle precipitation (EPP) during these conditions, we use model data from the chemistry-climate model SOCOL-MPIOM3 over the period 1900–2008. In the model runs, we have 10 experiment ensembles which include ionization rates from historical records of EPP, and eight reference ensembles excluding these ionization rates. Our results show no relationship between EPP and the rate of occurrence of disturbed polar vortex conditions. However, conditions preceding and during disturbed times are significantly different when EPP ionization rates are included. Also, the results show that this effect only becomes noticeable after the 1950s, indicating that this mechanism might become even more important in the future.

### 1. Introduction

In the Northern Hemisphere (NH), the polar vortex is a large scale stratospheric circulatory wind system, predominately in the westerly direction. It is a winter phenomenon, occurring due to the temperature difference between the pole and lower latitudes (D. G. Andrews, 2010). The strength of the vortex varies over the winter, with considerable variations also found from one year to the next. A strong polar vortex manifests itself as strong westerly winds, creating low pressure zones and cooler temperatures in polar latitudes relative to lower latitudes, with the opposite pattern being indicative of a weak or even reversed polar vortex. These variations are strongly linked to planetary wave propagation (Salby & Callaghan, 2002). Converging planetary waves and the dissipation of energy from gravity waves can act as drag on the westerly flow. This allows for enhanced air mixing between the pole and lower latitudes, as well as strengthening of downwelling of air in the polar stratosphere (Holton, 1980). However, the planetary wave activity itself is also affected by changes in atmospheric temperature and wind patterns (Matsumo, 1970), as these patterns influence the propagation and refraction of planetary waves. The system therefore creates a back and forth feedback loop known as wave-mean-flow interaction (D. Andrews, 1987).

If the convergence of planetary and gravity waves becomes sufficiently strong, the increased drag can result in either a splitting or displacement of the polar vortex. This leads to increased temperatures in the polar stratosphere. These events are known as Sudden Stratospheric Warmings (SSW). If the increased drag is able to completely reverse the meridional wind direction, the event is termed as a major SSW. These happen roughly every other year and it typically takes several days to weeks after the SSW for the polar stratosphere to cool and reform the polar vortex (Baldwin et al., 2021; Schoeberl, 1978).

Multiple studies have shown how EPP can affect the NH polar atmospheric temperatures during winter time (Baumgaertner et al., 2011; Maliniemi et al., 2013, 2016; Rozanov et al., 2012; Seppälä et al., 2009, 2013). Ionization of the mesosphere due to EPP creates  $\text{NO}_x$  (N, NO,  $\text{NO}_2$ ) and  $\text{HO}_x$  (H, OH,  $\text{HO}_2$ ) chemical species, which are known to be catalysts of ozone loss (Callis et al., 1991; Randall et al., 2005; Rozanov et al., 2005; Turunen et al., 2009). This process happens either directly in the mesosphere, or indirectly by downward transport of  $\text{NO}_x$  into the stratosphere (Funke et al., 2014; Smith-Johnsen et al., 2017). Ozone absorbs UV-radiation and emits thermal long wave radiation. Lack of UV in the winter polar stratosphere leads to a dominating radiative cooling effect (Graf et al., 1998; Langematz et al., 2003). When destroyed, the radiative balance of the stratosphere changes, leading to variations in the temperatures. The polar vortex is further influenced by wave-mean-flow interactions as temperature variations affect the refraction and propagation of planetary waves, potentially leading to larger scale winter time weather variations (Scaife et al., 2005).

In relation to disturbed conditions associated with SSWs, early studies mainly excluded these events when analyzing the relation between EPP and atmospheric dynamics (Lu et al., 2008; Seppälä et al., 2009, 2013). More focus has been given to the Quasi-Biennial-Oscillation (QBO) as this atmospheric wind mode is known to influence variations in the polar vortex (Holton & Tan, 1980; Yamazaki et al., 2020). Studies have shown how the EPP influence on the polar atmosphere is larger during QBO easterly phase (Maliniemi et al., 2013, 2016; Salminen et al., 2019). The easterly phase is associated with a larger drag and more downwelling of air masses in the stratospheric polar vortex due to stronger planetary wave activity. It is therefore also hypothesized that the QBO easterly phase primes the stratospheric polar vortex to be more susceptible to wave-mean-flow interactions like the ones induced by EPP. However, the increased drag and downwelling of air masses due to stronger planetary wave activity are also associated with SSWs themselves. A recent study, focusing exclusively on these events, has found strong correlations in re-analysis data between EPP and temperature in times preceding SSWs which was interpreted to be caused by enhanced planetary wave activity (Asikainen et al., 2020). The same study showed that winters without any SSWs exhibit weaker responses in general. A study by Salminen et al. (2020) also found a significant relationship between the occurrence rate of SSWs and  $A_p$  index during the QBO easterly phase. Here, less SSWs were observed during high  $A_p$  winters when the QBO at the 30 hPa level in August, September and October was in the easterly phase. As SSWs are driven by planetary wave activity, Salminen et al. (2022) have further investigated the EPP influence for different latitudinal planetary wave propagation patterns. The study found that EPP induced wave-mean-flow interactions have a stronger influence when more planetary waves propagate at mid latitudes ( $50^\circ$ – $52.5^\circ$ ) than at polar latitudes ( $70^\circ$ – $72.5^\circ$ ). Planetary waves propagating at mid latitudes can either be refracted away or toward the polar vortex, which can be controlled by small initial EPP-induced radiative changes. On the other hand, planetary waves propagating at polar latitudes are more likely to be trapped inside the polar vortex, and therefore more likely to only dissipate and contribute to weakening of the vortex (Dickinson, 1968; Matsuno, 1970).

This study aims to investigate whether conditions associated with SSWs are important for the EPP influence on the polar stratospheric temperatures. This will be accomplished by using the EPP forcing in the SOCOL3-MPIOM chemistry-climate model, in addition to rigorous statistical significance testing. These data and methods will be discussed in detail in Section 2. To our knowledge, this is the first study using atmospheric model data to comprehensively investigate the relation between EPP and atmospheric temperature during disturbed conditions associated with SSWs. It is noted that a study by Zúñiga López et al. (2022) used the Whole Atmosphere Community Climate Model (WACCM) version 6 and found that even small levels of Medium Energy Electron (MEE) ionization rates modulated the mesospheric signal of a SSW event in 2010. However, our study provides multiple ensemble members for the time period of 1900–2008 which allows for a comprehensive statistical analysis. The overall goal is to extend the knowledge on the conditions necessary for enhanced EPP effects on the NH winter atmosphere, as well as to investigate if there is a connection between EPP and the occurrence of disturbed conditions associated with SSWs in the data. Finally, the study also aims at confirming to what extent the SOCOL3-MPIOM chemistry-climate model is able to reproduce observations.

## 2. Data and Methods

This study applies the SOCOL3-MPIOM chemistry-climate model (Muthers et al., 2014; Stenke et al., 2013) which has three coupled components. The general atmospheric circulation model ECHAM5.4 (Roeckner, 2003) represents the atmospheric part, which in our study has horizontal latitude-longitude resolution of  $3.75^\circ \times 3.75^\circ$  and vertically 30 levels from the surface to the upper mesosphere (0.01 hPa,  $\sim 80$  km). In this study, the analysis is limited to pressure levels up to 1 hPa only. ECHAM5.4 operates in a free-running mode but with a nudged QBO (according to the reconstruction by Brönnimann et al. (2007a)), since the model is not able to generate the QBO with the applied vertical resolution. The MEZON chemistry component (Egorova et al., 2003) calculates the tendencies of 41 gas species, which has a total of 200 gas-phase, 16 heterogeneous, and 35 photolytic reactions. Finally, MPIOM is the oceanic component (Marsland et al., 2003), with horizontal resolution of  $3^\circ \times 3^\circ$  and 40 vertical levels from the bottom of the ocean to the surface.

The tropospheric aerosols are taken from NCAR Community Atmospheric Model (CAM3.5) simulations with a bulk aerosol model forced with the Community Climate System Model 3 sea surface temperatures. Greenhouse gas concentration, ozone precursors and depleting substances follow historic values (Meinshausen et al., 2011). The solar radiation forcing is taken from Shapiro et al. (2011). The EPP forcing input is the Coupled Model Inter-comparison Project Phase 6 (CMIP6) recommendation (Matthes et al., 2017). This includes medium-energy electrons ( $>30$  keV) forced as daily ionisation rates, while auroral electrons ( $<30$  keV) use a semi-empirical model of NO influx through the model top (Funke et al., 2016). Finally, SPEs and GCR are forced as daily ionisation rates.

In our study, the experiment simulation (EXP) includes the EPP forcing together with all other elements, while the reference simulation (REF) has all elements except the EPP forcing. The simulation is 109 years long (1900–2008). An eleven-member ensemble was generated by varying initial  $\text{CO}_2$  concentrations with 0.1% among the different members of EXP and REF. However, a few ensembles were corrupted during the simulation process and thus we have 10 EXP ensemble members and eight REF ensemble members available.

For the atmospheric temperature we compute zonal averages and daily latitude-height profiles corrected for seasonality and long term trends. The EPP response is analyzed as a composite difference between EXP and REF simulations. We estimate the significance in each lat-height bin by computing a Monte Carlo (MC) simulation. In the original analysis, there will be one data series with a given length which represents the EXP runs, and one data series with a given length representing the REF runs. In the simulation, for each iteration (we perform 20,000), data points are chosen at random from either the EXP or REF data series to make up two data collections with similar length as the original EXP and REF data series. The same data points can also be chosen multiple times. These two random ensemble collections are subtracted similarly as the original data in each lat-height grid. The composite difference from the original analysis is then compared to the distribution of composite differences from the 20,000 repetitions to obtain the fraction of more extreme differences (both tails of the distribution). The fraction represents the  $p$ -value in each lat-height bin with the individual null hypothesis that there is no difference between EXP and REF. The technique is formally known as bootstrapping with replacement.

Atmospheric data given in a latitude-height grid contains multiple null hypotheses, which represents a multiple hypothesis testing situation (Wilks, 2016). Estimates of significance using only individual hypotheses tests will lead to an overestimation of the true number of rejected null-hypotheses. This occurs as the expected value of false positives is equal to  $n \times p$ , where  $n$  is the number of hypothesis tests and  $p$  is the used  $p$ -value. The overestimation arises from the definition of  $p$ -value itself. This problem can be avoided using a simple method called false discovery rate (FDR) (Wilks, 2016). In general terms, the false discovery rate method reduces the probability of false positives (false rejections of the null hypothesis.) More specifically, a new  $p$ -value limit is calculated which is both dependent on the amount of null hypotheses, and the autocorrelation between the grid points populated by the multiple null hypotheses. This new  $p$ -value amounts to the creation of a global null hypothesis, where a failure to reject this global null hypothesis means that one cannot conclude that any of the individual tests constitute a valid rejection of the null hypothesis either. The process involves computing the  $p$ -values for each data point (or grid point), and then arranging them in ascending order, forming the set  $i = 1, \dots, N$ , where  $N$  represents the total number of individual tests performed. The new global  $p$ -value,  $p_{FDR}$ , is then calculated by iterating through all individual  $p$ -values and looking for the one fulfilling the equation:

$$p_{FDR} = \max\{p(i) : p(i) \leq (i/N)\alpha_{FDR}\}, i = 1, \dots, N \quad (1)$$

If a  $p$ -value fulfills the equation, this  $p$ -value then becomes the global limit. Here,  $\alpha_{FDR} = 0.05$  for obtaining a test level of 95% when the data points are independent. However, as Wilks (2016) emphasizes, when autocorrelation exists between the data points incorporated in the procedure, the effective number of independent data points (or grid points),  $N$ , are reduced. An e-folding distance of about  $1.54 \cdot 10^3$  km is considered moderate to strong temporal autocorrelation, and is frequently occurring in atmospheric pressure and temperature (Wilks, 2016). This reduction of independent data points are combated by setting  $\alpha_{FDR} = 2\alpha_{FDR}$ , amounting to  $\alpha_{FDR} = 0.1$  in our case.

### 2.1. “Disturbed Events”

The World Meteorological Organization (WMO) criteria for Sudden Stratospheric Warming (SSW) events states that SSWs are identified when the zonal-mean zonal wind at 10 hPa and 60°N and the zonal-mean temperature difference between 60°N and the pole at the same level are simultaneously reversed. Two events must be separated by at least 20 consecutive days of westerly winds, and only events from November to March are considered. Also, stratospheric final warmings are excluded by imposing at least 10 days with westerly winds after the occurrence of an SSW and before 30 April. This is to ensure the recovery of the polar vortex before its final breakup (Ayarzagüena et al., 2018; Butler et al., 2015).

In our study, we have only access to temperature data. We will therefore define “disturbed events,” which by definition will be similar to minor SSW events. Our criteria for an SSW takes into account the WMO criteria of a minor SSW where the zonal-mean temperature at the pole (90°N) have to be greater than the zonal-mean temperature at 60°N at the 10 hPa level. This will ensure a subset of minor SSWs that may or may not contain major SSWs. Simultaneously, to select the stronger events in the subset, a criteria for rapid warming at the pole are included: The daily  $\Delta T$  (day-to-day variations) at 90°N at 10 hPa have to exceed a specific threshold. By stepwise changing the temperature gradient, we find that only events with  $\Delta T$  above 10.5 K produces statistically significant responses. Therefore, the remaining sections will focus on the events exceeding this threshold. The subset of strong minor SSWs is here called “disturbed event.” They will be associated with increased planetary wave activity, and hence suitable to test the hypothesis that increased wave-mean flow activity is favorable for the EPP impact on stratospheric temperatures. Detected “disturbed events” also have to happen between December and March with at least 20 consecutive days between each. Here, we do not include events occurring in November, as the time frame for the EPP mechanism to operate in November is deemed too short. We also note that by using temperature data alone, one cannot assess if a warming potentially constitutes the last breakup of the polar vortex, as the final warming is defined in relation to zonal winds (e.g., Butler et al., 2017). A conservative approach is therefore applied to guarantee the exclusion of final warmings. For every winter (December–April), the last detected “disturbed event” is marked as a potential final warming candidate and subsequently removed from the “disturbed event” list. To minimize the risk of false exclusion, we extend the search through April, as many abrupt final warmings occur in this month. However, for winters with gradual final warmings, the method risks excluding actual mid-winter events, as gradual final warmings not associated with a day-to-day  $\Delta T$  above 10.5 K will go undetected. Hence, while this conservative method might reduce the statistics, it guarantees that no final warmings are included in our “disturbed events”.

The top panels of Figure 1 show the normalized amount (with respect to the number of ensembles) of “disturbed events” for the different winter months for experiment (left) and reference (right) runs when  $\Delta T = 10.5$  K over the full data period. The bottom panels show the normalized amount of “disturbed events” occurring in different months when only winters containing a single event are chosen. Due to our large sample of data (10 experiment ensembles and 8 reference ensembles), these are the events that will be used in this study, and referred to as standalone events. This is done to minimize potential aliasing of conditions before or after the “disturbed events.”

## 3. Analysis and Results

### 3.1. Occurrence Rate of “Disturbed Events”

The threshold of  $\Delta T > 10.5$  K (day-to-day), to ensure a selection of strong minor SSWs, is acquired by performing all analyses in the coming section for two groups, “disturbed events” with  $\Delta T$  threshold between 1 and 10.5 K, and “disturbed events” with  $\Delta T$  threshold above 10.5 K. As only the subgroup of events with  $\Delta T$  threshold above 10.5 K produced statistically significant anomalies, the following analyses will show the results from this subgroup only. However, as a first test, we check if there is a statistically significant difference in the occurrence rate of “disturbed events” between the experiment and reference runs for all possible  $\Delta T$  thresholds. This investigation is conducted to reveal if there is a tendency of more or less “disturbed events” irrespective of

1900-2008: For  $\Delta T = 10.5$

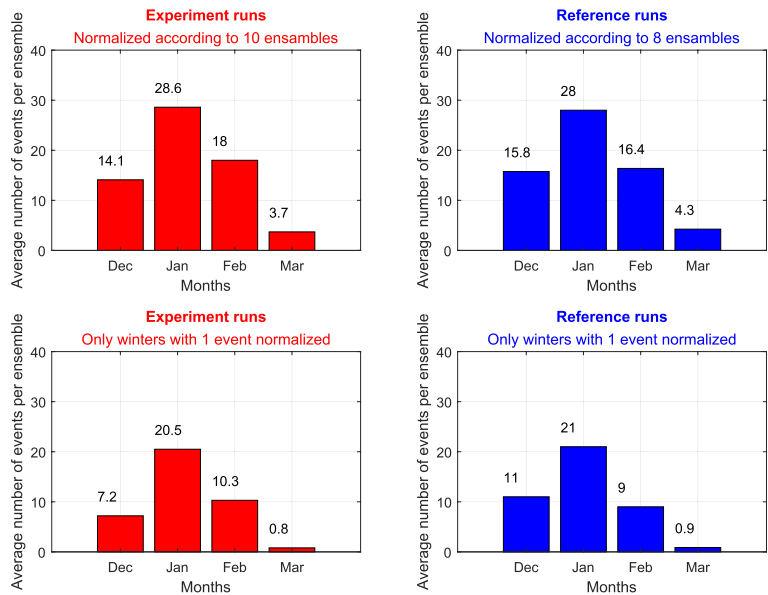


**Figure 1.** Top panels: The distribution of all “disturbed events” in respect to month for the experiment (left) and reference (right) runs. Bottom panels: The distribution of “disturbed events” in respect to month when only standalone events are chosen (standalone events defined as those that are the only one occurring in a whole winter for a specific year). The numbers are normalized according to the number of available ensemble members they are collected from. As mentioned, 10 ensembles are available for the experiment runs, while 8 ensembles are available for the reference runs.

the  $\Delta T$  threshold. Furthermore, the years are divided into QBO-easterly (QBOE) and QBO-westerly (QBOW) depending on the QBO value at 30 hPa averaged over the months August, September, and October. This QBO division is done according to the results of Salminen et al. (2020), which shows a significant difference in the fraction of major SSWs between QBOE and QBOW when sorted in this manner.

Figure 2 shows the occurrence rates of “disturbed events,” with top panels displaying both QBO phases, middle panels QBOE and bottom panels QBOW. The left panels show the average number of stand-alone “disturbed events” per ensemble for the experiment (red) and reference (blue) runs for different  $\Delta T$  thresholds in the range 1–25 K. Both experiment and reference exhibit very similar curves for the combined QBO, and for both respective QBO sorting. A sharp decline in number of events happens with an increase of  $\Delta T$ . From the QBO panels, one can also observe the Holton-Tan effect, with generally more “disturbed events” occurring in QBOE. The middle panels show the difference between EXP and REF for different  $\Delta T$  together with significance limits. Details of the significance estimation can be found in Section 2. The results after the MC-simulation concludes that there is no  $\Delta T$  threshold where the average number of “disturbed events” between the EXP and REF differ significantly. However, even though not significant, there seems to be a slight inclination of QBOE having more “disturbed event” in the reference (particles excluded), while slightly inclination of more “disturbed events” in the experiment (particles included). In the right panels the integral of the EXP-REF lines from the middle panels are calculated, and compared to the distribution of all 10,000 integrals obtained from the MC-simulation in the middle panels. As seen, the integral of the difference line (EXP-REF) is close to zero for the composite of both QBO phases (top panel), slightly skewed to the negative for QBOE and skewed to the positive for QBOW.

Furthermore, we investigate if the occurrence rate of “disturbed event” changes over time. Figure 3 shows the “disturbed event” occurrence rate in a 10-year running window over the whole simulation period using the  $\Delta T > 10.5$  K threshold for all data (top panel), QBOE (middle panel) and QBOW (bottom panel). A 10-year

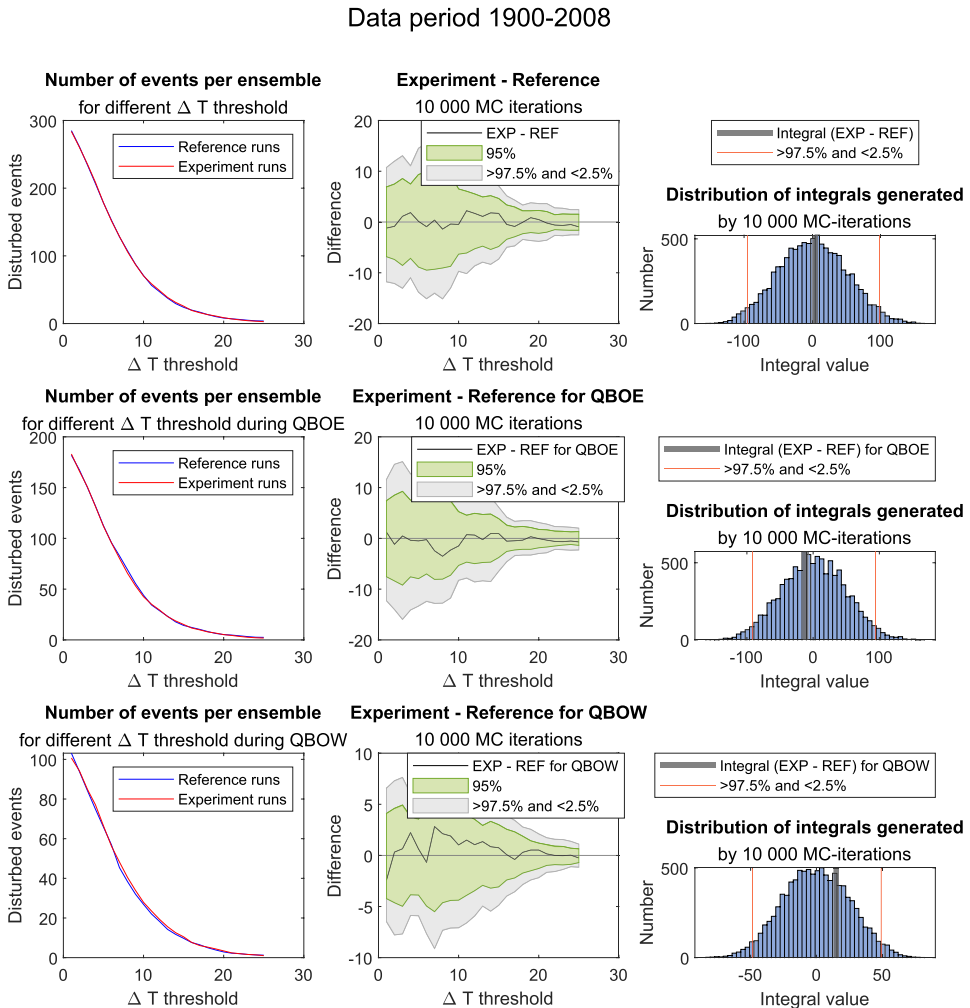


**Figure 2.** Left panels: The average number of events per ensemble member in both experiment (red) and reference (blue) runs plotted against different  $\Delta T$  thresholds (1–25 K) for all data (top panel), QBO-E (middle panel), and QBO-W (bottom panel). Middle panels: EXP-REF (lines from the left panels subtracted from each other) for all  $\Delta T$  thresholds and limits of statistical significance. Right panels: Integral of the EXP-REF curve (value shown as gray line) in the middle panels. This value is then compared against 10,000 integrals of EXP-REF obtained through a MC-simulation where the data bins EXP and REF are chosen at random from all available ensemble members. This is done to investigate whether there is tendency of more or less “disturbed events” irrespective of  $\Delta T$  threshold. However, no significant results are obtained.

window is chosen to ensure approximately equal amounts of QBOE and QBOW phases in each step. By choosing a narrower time window, one risks having one of the QBO phases dominating, leading to an artificial periodic pattern in the middle and bottom panel induced by the QBO phases. The experiment (red) and reference (blue) shows no clear deviations in form of a long term trend. However, at shorter time scales, larger variations are seen between the experiment and reference. In the composite of both QBO phases, there seem to be a 25-year cycle of fluctuations between the experiment and reference obtaining the highest number of events. When looking at QBO division, this 25-year fluctuating pattern clearly emerges mostly from the QBOE phase.

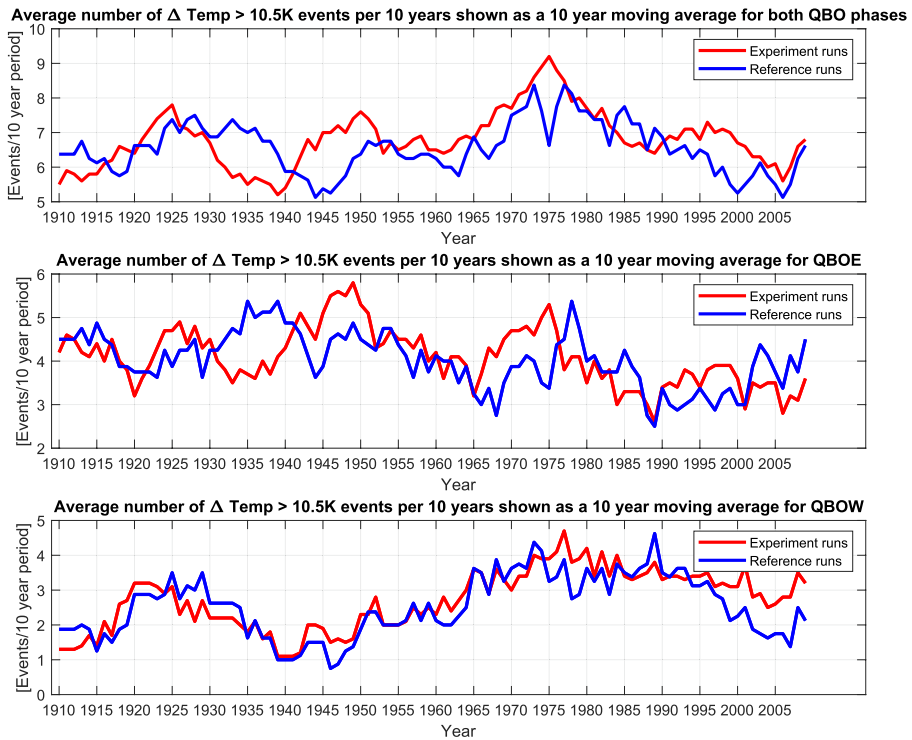


**Figure 3.** The average number of “disturbed events” for the EXP (red) and REF (blue) calculated as a 10-year running average starting from 1900 to 1909 and running to 1999–2008 with 95 increments.

### 3.2. EPP Effect Preceding and During “Disturbed Event”

Asikainen et al. (2020) shows how atmospheric conditions preceding SSWs are susceptible to the influence of EPP. The study performs a regression analysis between  $A_p$  and temperature on the individual months Dec–Mar. All Decembers are chosen where an SSW occurs in either December or January, and all January–March months where an SSW occurs in either February or March.

We apply the same sorting of the winter months as Asikainen et al. (2020). However, we utilize the advantage of being able to compare the ideal model runs with and without EPP forcing, examining the composite difference for EXP–REF. It allows for the inclusion of more data points, as a regression analysis would be limited to the experiment runs scaled by  $A_p$ .

Figure 4 shows the result when all months selected are averaged and the EXP–REF composite difference is calculated. The left panel shows the period 1900–1954, and the right panel shows the period 1955–2008. Investigating different time periods, revealed that by splitting the data set in half, only the latter period showed a significant response correlated with EPP. In the right panel there is a large significant negative anomaly from about 250 hPa to 63 hPa and extending all the way from 60 to 90°N in the 1955–2008 period. For the 1900–1954 period, no significance is obtained, and the temperature response for the northernmost latitudes is reversed with respect to the response seen in the 1955–2008 period. The results from the latter period are also in line with the results obtained by Asikainen et al. (2020).

Figure 5 shows the same sorting as above, but now for each individual winter month from December to March. After MC and FDR method, only February shows a statistically significant response (thick magenta lines).



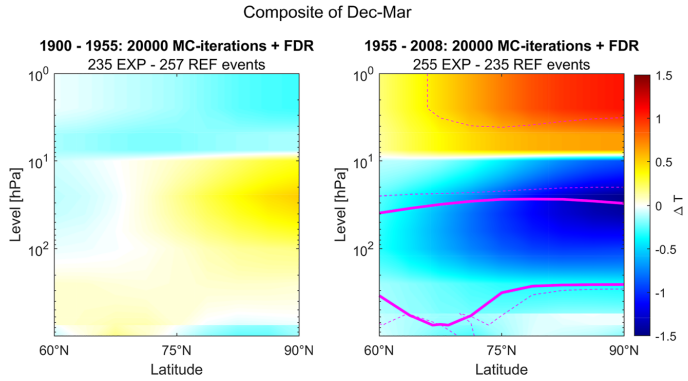


**Figure 4.** Left panel: The composite difference of EXP-REF from winter months (December to March) preceding a “disturbed event” during 1900–1955. Before calculating the composite, the response in December was calculated by choosing all Decembers where a “disturbed event” occurred in either December or January, while for the response in Jan-Mar those months were chosen where a “disturbed event” occurred in either February or March. Right panel: Same as left panel but during 1955–2008. Thick magenta line represents the area significant at the 95% level after MC and FDR method, while dotted magenta lines represent significance at the 95% level after only MC method.

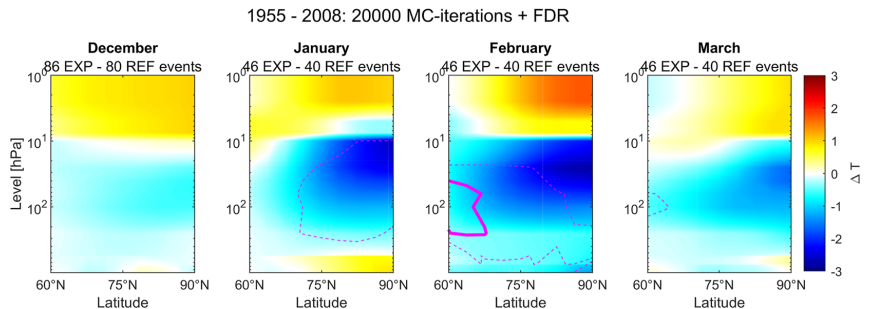
However, January also exhibit statistical significance after MC only (dotted magenta lines). A pattern emerges exhibiting warming around 75°–90°N at 1 hPa, and cooling of the middle stratosphere from 60° to 90°N. For the months December–March, the signatures of the anomalies are coherent with the results of Asikainen et al. (2020).

Figure 6 shows the EXP-REF in different time intervals before and after the “disturbed events” when all standalone “disturbed events” occurring in all months are considered for the period 1955–2008. No statistical significance is observed after MC and FDR method is applied. However, the largest negative anomaly in the middle atmosphere is seen for the windows preceding and during the onset of the “disturbed event.” There is also a subsequent warming from 5 to 25 days after the event.

Figure 7 shows the same analysis, only for February. A statistically significant negative anomaly is seen around 60°–75°N extending from 250 hPa to the 63 hPa level. The anomaly starts in the –15 to –5 days window, with the most significant response obtained in the –5 to 5 days window. The significant anomalies are consistent with the ones found in Figure 5. Both Figures 6 and 7 indicate that the strongest negative anomaly occurs close to, or exactly at the onset of the “disturbed event.”

#### 4. Discussion

The aim of this paper is to examine the hypothesis that conditions set up before and during SSWs playing a key role in the link between the polar vortex and EPP. This is accomplished by the use of a large statistical sample



**Figure 5.** Same as Figure 4 but with individual winter months during 1955–2008.

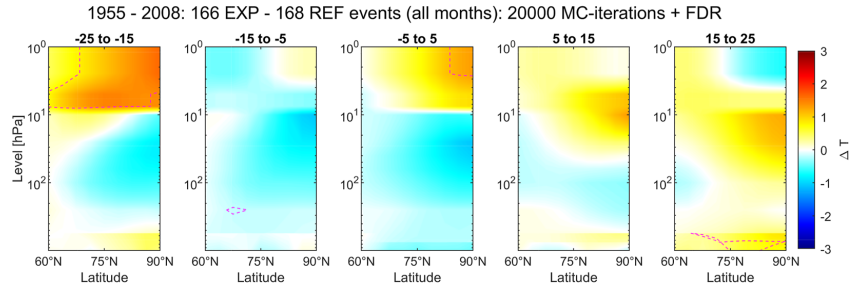


**Figure 6.** EXP-REF before and after the onset of the “disturbed event” in 10 days intervals. The figure is a composite of all months (December to March). No significance is obtained when applying MC and FDR method.

(8 reference and 10 experiment runs spanning the time interval 1900–2008) combined with rigorous statistical testing. With only temperature data available, events are chosen based on the criterion of minor SSWs (positive meridional temperature gradient (60°–90°N at 10 hPa)), with an additional criterion ensuring sufficiently strong events (day-to-day temperature gradient at 90°N at 10 hPa exceeding 10.5 K). The combination of these criteria ensures that we are investigating a subset of minor SSWs that may or may not contain major SSWs which are associated with considerable polar stratospheric heating which again is associated with increased planetary wave activity (Butler et al., 2015; Kozubek et al., 2020). As these events do not strictly fall into the category of either minor or major SSWs, but rather a subset that may contain both, they are termed “disturbed events.” When investigating the relationship between EPP and the conditions associated with “disturbed events,” the possibility of EPP modulating the occurrence rate of the events is first examined. Here, the full data set is used, as well as the data set split into the two distinct QBO phases. However, no statistically significant relationships are found. Second, the atmospheric temperature during “disturbed events” are investigated by comparing EXP containing EPP forcing with REF which excludes EPP. In agreement with an observational study by Asikainen et al. (2020), we find a statistically significant difference in temperatures mostly during the build up of the events.

As the EPP effect is hypothesized to affect stratospheric temperatures, we investigate if the presence of EPP could modulate the occurrence rate of our defined “disturbed events.” Salminen et al. (2020) found a statistically significant difference in the number of major SSWs in observational data between low and high  $A_p$  periods during QBOE. Figure 2 shows the normalized number of events in EXP and REF, as well as the difference between the two. Figure 3 shows the result of occurrence rate over time for “disturbed events.” Both figures show the full data set, as well as the data set split into the two QBO phases according to the average QBO 30 hPa value occurring in August, September and October, which was the QBO sorting found by Salminen et al. (2020) leading to the strongest impact on the frequency of major SSWs. However, when investigating the occurrence rate, both results conclude that no significant difference is seen between the experiment and reference runs. Nevertheless, our results still show a small tendency of QBOE having less disturbances when EPP is present, while QBOW shows slightly more disturbances when EPP is present. Also, from Figure 3, the QBOW phase seem to induce larger variations between the experiment and reference

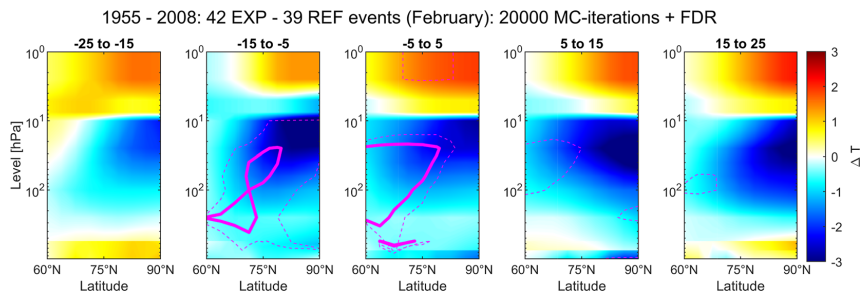


**Figure 7.** Same as Figure 6 but only for February. Thick magenta line encircles the significance of 95% after MC and FDR, while dotted magenta line encircles the significance of 95% after MC only.

runs in respect to occurrence rate of “disturbed events” compared to the QBOE phase, where experiment and reference follows each other more closely. These variations seen for QBOE are clear on short time scales, but averages out on longer timescales. As such, our analysis does not support that the frequency of disturbed events are modulated by EPP events. However, we cannot rule out the possibility that this link exist for EPP and major SSWs. Our study defines minor SSWs which may or may not contain major SSWs. Major SSWs where the zonal wind completely reverses may respond more strongly to EPP induced changes than the events detected in our study. However, there is also the possibility that the results obtained from observation and reanalysis data occurs by chance, where the usage of models with large ensemble sizes reduces the chances of random anomalies dominating the results. Therefore, to confirm these findings, more model studies including the definition of major SSWs have to be conducted.

Previous theories suggest planetary wave activity as the main driver behind SSWs (Matsuno, 1971). However, recent studies have suggested that gravity waves may play a larger role in these events than previously thought (Shpynev et al., 2015; Song et al., 2020; Yasyukevich et al., 2022). A detailed explanation of a physical mechanism using the analogy of a whirlpool for the polar vortex is given by Shpynev et al. (2015). In the winter polar vortex, with little sunlight or thermal heating, a significant source of kinetic energy in the polar vortex can be due to the down welling of cooling stratospheric air masses. Then, it is proposed that baroclinical instabilities occurring inside the polar vortex at the boundary between flows of different velocities can produce GWs. In the framework of this mechanism, the polar vortex itself can be a source of GWs, which ultimately also can make additional contributions to the evolution of an SSW event. In addition to GWs playing a role in the evolution of SSWs, there has been a long standing problem of precise parameterization of GWs in general circulation models (Alexander et al., 2010; Fritts et al., 2006; Geller et al., 2013; Hindley et al., 2020; Plougonven et al., 2020). On this basis, if EPP influences mostly the refraction rate of planetary waves, this may not be the decisive factor of SSWs happening or not. Also, in climate models the accuracy of GW parameterizations are questionable. It could therefore be that SOCOL model does not capture the full mechanism responsible for the prevention of SSWs, which might be an additional explanation to why observations show a relationship of less SSWs during high  $A_p$  winters during QBOE (Salminen et al., 2020), while our results in respect to the “disturbed events” do not.

However, even though the occurrence rate is unaffected by the inclusion of EPP, the general signature of the “disturbed events” are significantly different and in agreement with the observational study by Asikainen et al. (2020) on major SSWs. In February (Figure 5 4th panel and Figure 7), large statistically significant negative anomalies are observed around 10–100 hPa. By closer inspection, the differences in manifestation occurs before (–15 to 5 days), and during the onset of the “disturbed events” (–5 to 5 days). Figures 4, 5 and 7 all show statistically significant anomalies mostly southwards of 75°N. However, the  $\Delta T$  condition is calculated at 90°N. Therefore, another viable explanation of why the occurrence rate of SSWs are not affected, while the signature of the events are, is that the atmospheric dynamics are more influenced at the outer edges of the vortex, than in the center. Such southwardly localized responses could occur if the EPP induced wave-mean-flow interactions affect the refraction rate of planetary waves at the outer zonal edges of the polar vortex. Southward refracted planetary waves affecting less variable conditions outside the polar vortex could be more readily distinguishable from the background noise than poleward refracted planetary waves dissipating in the polar vortex. In this framework, the disturbed conditions could be a necessity for the rather small EPP induced wave-mean-flow interactions to influence the refraction of planetary waves.

Asikainen et al. (2020) uses re-analysis data for the time period 1957–2017. In our study, we first split the data set into two equally long periods, 1900–1954 and 1955–2008. Interestingly, we find that only the latter period shows a significant temperature response correlated with EPP. In this period, the signature of the responses closely resembles the responses obtained by Asikainen et al. (2020). As the significant responses are only obtained in the latter half of the data set, our study highlights a general trend of EPP induced atmospheric responses becoming significant only in the last half of the 20 century. This trend of stronger EPP impact under climate change era is also found by Maliniemi et al. (2020, 2021), which shows how downwelling of  $\text{NO}_x$  increases due to an increased Brewer-Dobson circulation. Additionally, stratospheric chlorine species (which destroy  $\text{NO}_x$ ) are also shown to follow a decreasing trend. Combining the two can therefore lead to enhanced ozone depletion from EPP, regardless of the level of EPP activity. Thus, the EPP mechanism might become more important in the future.

## 5. Conclusion

By using SOCOL-MPIOM3 chemistry-climate model we have conducted a statistical study involving in total 18 ensemble members on the relationship between EPP and disturbed conditions associated with minor SSWs in

the northern polar atmosphere. Our results show no clear significant relationship between the occurrence rate of disturbed conditions and particle forcing. However, we find statistically significant differences in the signature right before and during the onset of our subset of minor SSWs when particle forcing is included (EXP) compared to when it is excluded (REF). These anomalies match results seen in analyses of re-analysis data on the same phenomenon (Asikainen et al., 2020). There is also a general trend where the particle forcing becomes significant only in the late part of the 20th century.

The study further discusses possible explanations of why the occurrence rate of our subset of minor SSWs is unaffected, while the signature of the events are significantly different. However, as this study is merely a statistical assessment, no definite conclusion can be offered for viable mechanisms. To confirm if the link between EPP and middle atmospheric dynamics is controlled by conditions associated with SSWs, more research is needed. A first step would be to see if other general circulation models can reproduce these results when also applying wind measurements for the detection of major SSWs. Future research would also have to incorporate the potential new paradigm of gravity waves being an important driving force behind SSWs.

### Data Availability Statement

Temperature data from all model runs used in this study is uploaded to Zenodo by the authors (Edvartsen et al., 2023) and can be accessed directly at: <https://doi.org/10.5281/zenodo.7599218>. The long QBO reconstruction by Brönnimann et al. (2007a, 2007b) can be accessed at: [https://climexp.knmi.nl/getindices.cgi?WMO=BernData/qbo\\_30&STATION=QBO\\_30&TYPE=i&id=someone@somewhere](https://climexp.knmi.nl/getindices.cgi?WMO=BernData/qbo_30&STATION=QBO_30&TYPE=i&id=someone@somewhere).

### References

- Alexander, M. J., Geller, M., McLandress, C., Polavarapu, S., Preusse, P., Sassi, F., et al. (2010). Recent developments in gravity-wave effects in climate models and the global distribution of gravity-wave momentum flux from observations and models. *Quarterly Journal of the Royal Meteorological Society*, 136(650), 1103–1124. <https://doi.org/10.1002/qj.637>
- Andrews, D. (1987). Chapter 5 - Extratropical planetary-scale circulations. In D. G. Andrews, J. R. Holton, & C. B. Leovy (Eds.), *Middle atmosphere dynamics* (Vol. 40, pp. 220–258). Academic Press. <https://doi.org/10.1016/B978-0-12-058575-5.50010-4>
- Andrews, D. G. (2010). Atmospheric thermodynamics. In *An introduction to atmospheric physics* (2nd ed., pp. 19–51). Cambridge University Press. <https://doi.org/10.1017/CBO9780511800788.003>
- Asikainen, T., Salminen, A., Maliniemi, V., & Mursula, K. (2020). Influence of enhanced planetary wave activity on the polar vortex enhancement related to energetic electron precipitation. *Journal of Geophysical Research: Atmospheres*, 125(9), e2019JD032137. <https://doi.org/10.1029/2019JD032137>
- Ayarzagüena, B., Polvani, L. M., Langematz, U., Akiyoshi, H., Bekki, S., Butchart, N., et al. (2018). No robust evidence of future changes in major stratospheric sudden warmings: A multi-model assessment from CCM1. *Atmospheric Chemistry and Physics*, 18(15), 11277–11287. <https://doi.org/10.5194/acp-18-11277-2018>
- Baldwin, M. P., Ayarzagüena, B., Birner, T., Butchart, N., Butler, A. H., Charlton-Perez, A. J., et al. (2021). Sudden stratospheric warmings. *Reviews of Geophysics*, 59(1), e2020RG000708. <https://doi.org/10.1029/2020RG000708>
- Baumgaertner, A. J. G., Seppälä, A., Jöckel, P., & Clilverd, M. A. (2011). Geomagnetic activity related NO<sub>x</sub> enhancements and polar surface air temperature variability in a chemistry climate model: Modulation of the NAM index. *Atmospheric Chemistry and Physics*, 11(9), 4521–4531. <https://doi.org/10.5194/acp-11-4521-2011>
- Brönnimann, S., Annis, J. L., Vogler, C., & Jones, P. D. (2007a). Reconstructing the quasi-biennial oscillation back to the early 1900s. *Geophysical Research Letters*, 34(22), L22805. <https://doi.org/10.1029/2007GL031354>
- Brönnimann, S., Annis, J. L., Vogler, C., & Jones, P. D. (2007b). Reconstructing the Quasi-Biennial oscillation back to the early 1900s. Retrieved from [https://climexp.knmi.nl/getindices.cgi?WMO=BernData/qbo\\_30&STATION=QBO\\_30&TYPE=i&id=someone@somewhere](https://climexp.knmi.nl/getindices.cgi?WMO=BernData/qbo_30&STATION=QBO_30&TYPE=i&id=someone@somewhere)
- Butler, A. H., Seidel, D. J., Hardiman, S. C., Butchart, N., Birner, T., & Match, A. (2015). Defining sudden stratospheric warmings. *Bulletin of the American Meteorological Society*, 96(11), 1913–1928. <https://doi.org/10.1175/BAMS-D-13-00173.1>
- Butler, A. H., Sjöberg, J. P., Seidel, D. J., & Rosenlof, K. H. (2017). A sudden stratospheric warming compendium. *Earth System Science Data*, 9(1), 63–76. <https://doi.org/10.5194/essd-9-63-2017>
- Callis, L. B., Baker, D. N., Blake, J. B., Lambeth, J. D., Boughner, R. E., Natarajan, M., et al. (1991). Precipitating relativistic electrons: Their long-term effect on stratospheric odd nitrogen levels. *Journal of Geophysical Research*, 96(D2), 2939–2976. <https://doi.org/10.1029/90JD02184>
- Dickinson, R. E. (1968). Planetary Rossby waves propagating vertically through weak westerly wind wave guides. *Journal of the Atmospheric Sciences*, 25(6), 984–1002. [https://doi.org/10.1175/1520-0469\(1968\)025<0984:PRWPVT>2.0.CO;2](https://doi.org/10.1175/1520-0469(1968)025<0984:PRWPVT>2.0.CO;2)
- Edvartsen, J., Maliniemi, V., & Nesse, H. (2023). Effects of energetic particle precipitation on stratospheric temperature during disturbed stratospheric polar. [Dataset], Zenodo. <https://doi.org/10.5281/zenodo.7599218>
- Egorova, T., Rozanov, E., Zubov, V., & Karol, I. (2003). Model for investigating ozone trends (MEZON). *Izvestiya - Atmospheric and Oceanic Physics*, 39, 277–292.
- Fritts, D. C., Vadas, S. L., Wan, K., & Werne, J. A. (2006). Mean and variable forcing of the middle atmosphere by gravity waves. *Journal of Atmospheric and Solar-Terrestrial Physics*, 68(3), 247–265. <https://doi.org/10.1016/j.jastp.2005.04.010>
- Funke, B., López-Puertas, M., Stiller, G. P., Versick, S., & von Clarmann, T. (2016). A semi-empirical model for mesospheric and stratospheric NO<sub>x</sub> produced by energetic particle precipitation. *Atmospheric Chemistry and Physics*, 16(13), 8667–8693. <https://doi.org/10.5194/acp-16-8667-2016>
- Funke, B., López-Puertas, M., Stiller, G. P., & von Clarmann, T. (2014). Mesospheric and stratospheric NO<sub>x</sub> produced by energetic particle precipitation during 2002–2012. *Journal of Geophysical Research: Atmospheres*, 119(7), 4429–4446. <https://doi.org/10.1002/2013JD021404>

- Geller, M. A., Alexander, M. J., Love, P. T., Bacmeister, J., Ern, M., Hertzog, A., et al. (2013). A comparison between gravity wave momentum fluxes in observations and climate models. *Journal of Climate*, *26*(17), 6383–6405. <https://doi.org/10.1175/JCLI-D-12-00545.1>
- Graf, H.-F., Kirchner, I., & Perlwitz, J. (1998). Changing lower stratospheric circulation: The role of ozone and greenhouse gases. *Journal of Geophysical Research*, *103*(D10), 11251–11261. <https://doi.org/10.1029/98JD00341>
- Hindley, N. P., Wright, C. J., Hoffmann, L., Moffat-Griffin, T., & Mitchell, N. J. (2020). An 18-year climatology of directional stratospheric gravity wave momentum flux from 3-D satellite observations. *Geophysical Research Letters*, *47*(22), e2020GL089557. <https://doi.org/10.1029/2020GL089557>
- Holton, J. R. (1980). The dynamics of sudden stratospheric warmings. *Annual Review of Earth and Planetary Sciences*, *8*(1), 169–190. <https://doi.org/10.1146/annurev.ea.08.050180.001125>
- Holton, J. R., & Tan, H.-C. (1980). The influence of the equatorial quasi-biennial oscillation on the global circulation at 50 mb. *Journal of the Atmospheric Sciences*, *37*(10), 2200–2208. [https://doi.org/10.1175/1520-0469\(1980\)037<2200:TIOTEQ>2.0.CO;2](https://doi.org/10.1175/1520-0469(1980)037<2200:TIOTEQ>2.0.CO;2)
- Kozubek, M., Lastovicka, J., & Krizan, P. (2020). Comparison of key characteristics of remarkable SSW events in the southern and northern hemisphere. *Atmosphere*, *11*(10), 1063. <https://doi.org/10.3390/atmos11101063>
- Langematz, U., Kunze, M., Krüger, K., Labitzke, K., & Roff, G. L. (2003). Thermal and dynamical changes of the stratosphere since 1979 and their link to ozone and CO<sub>2</sub> changes. *Journal of Geophysical Research*, *108*(D1), ACL9-1–ACL9-13. <https://doi.org/10.1029/2002JD002069>
- Lu, H., Clilverd, M. A., Seppälä, A., & Hood, L. L. (2008). Geomagnetic perturbations on stratospheric circulation in late winter and spring. *Journal of Geophysical Research*, *113*(D16), D16106. <https://doi.org/10.1029/2007JD008915>
- Maliniemi, V., Asikainen, T., Mursula, K., & Seppälä, A. (2013). QBO-dependent relation between electron precipitation and wintertime surface temperature. *Journal of Geophysical Research*, *118*(12), 6302–6310. <https://doi.org/10.1002/jgrd.50518>
- Maliniemi, V., Asikainen, T., & Mursula, K. (2016). Effect of geomagnetic activity on the northern annular mode: QBO dependence and the Holton-Tan relationship. *Journal of Geophysical Research: Atmospheres*, *121*(17), 10043–10055. <https://doi.org/10.1002/2015JD024460>
- Maliniemi, V., Marsh, R., Daniel-Tysøy, H. N., & Smith-Johnsen, C. (2020). Will climate change impact polar NO<sub>x</sub> produced by energetic particle precipitation? *Geophysical Research Letters*, *47*(9), e2020GL087041. <https://doi.org/10.1029/2020GL087041>
- Maliniemi, V., Nesse Tysøy, H., Smith-Johnsen, C., Arsenovic, P., & Marsh, D. R. (2021). Effects of enhanced downwelling of NO<sub>x</sub> on Antarctic upper-stratospheric ozone in the 21st century. *Atmospheric Chemistry and Physics*, *21*(14), 11041–11052. <https://doi.org/10.5194/acp-21-11041-2021>
- Marsland, S., Haak, H., Jungclaus, J., Latif, M., & Röske, F. (2003). The Max-Planck-Institute global ocean/sea ice model with orthogonal curvilinear coordinates. *Ocean Modelling*, *5*(2), 91–127. [https://doi.org/10.1016/S1463-5003\(02\)00015-X](https://doi.org/10.1016/S1463-5003(02)00015-X)
- Matsuno, T. (1970). Vertical propagation of stationary planetary waves in the winter northern hemisphere. *Journal of the Atmospheric Sciences*, *27*(6), 871–883. [https://doi.org/10.1175/1520-0469\(1970\)027<0871:VPOSPW>2.0.CO;2](https://doi.org/10.1175/1520-0469(1970)027<0871:VPOSPW>2.0.CO;2)
- Matsuno, T. (1971). A dynamical model of the stratospheric sudden warming. *Journal of the Atmospheric Sciences*, *28*(8), 1479–1494. [https://doi.org/10.1175/1520-0469\(1971\)028<1479:ADMOTS>2.0.CO;2](https://doi.org/10.1175/1520-0469(1971)028<1479:ADMOTS>2.0.CO;2)
- Matthes, K., Funke, B., Andersson, M. E., Barnard, L., Beer, J., Charbonneau, P., et al. (2017). Solar forcing for CMIP6 (v3.2). *Geoscientific Model Development*, *10*(6), 2247–2302. <https://doi.org/10.5194/gmd-10-2247-2017>
- Meinshausen, M., Smith, S. J., Calvin, K., Daniel, J. S., Kainuma, M. L. T., Lamarque, J., et al. (2011). The RCP greenhouse gas concentrations and their extensions from 1765 to 2300. *Climate Change*, *109*(1–2), 213–241. <https://doi.org/10.1007/s10584-011-0156-z>
- Muthers, S., Anet, J. G., Stenke, A., Raible, C. C., Rozanov, E., Brönnimann, S., et al. (2014). The coupled atmosphere–chemistry–ocean model SOCOL-MPIOM. *Geoscientific Model Development*, *7*(5), 2157–2179. <https://doi.org/10.5194/gmd-7-2157-2014>
- Plougonven, R., de la Cámara, A., Hertzog, A., & Lott, F. (2020). How does knowledge of atmospheric gravity waves guide their parameterization? *Quarterly Journal of the Royal Meteorological Society*, *146*(728), 1529–1543. <https://doi.org/10.1002/qj.3732>
- Randall, C. E., Harvey, V. L., Manney, G. L., Orsolini, Y., Codrescu, M., Stioris, C., & Russell, J. M., III. (2005). Stratospheric effects of energetic particle precipitation in 2003–2004. *Geophysical Research Letters*, *32*(5), L05802. <https://doi.org/10.1029/2004GL022003>
- Roeckner, E. (2003). The atmospheric general circulation model ECHAM5: Model description.
- Rozanov, E., Calisto, M., Egorova, T., Peter, T., & Schmutz, W. (2012). Influence of the precipitating energetic particles on atmospheric chemistry and climate. *Surveys in Geophysics*, *33*(3–4), 483–501. <https://doi.org/10.1007/s10712-012-9192-0>
- Rozanov, E., Callis, L., Schlesinger, M., Yang, F., Andronova, N., & Zubov, V. (2005). Atmospheric response to NO<sub>x</sub> source due to energetic electron precipitation. *Geophysical Research Letters*, *32*(14). <https://doi.org/10.1029/2005GL023041>
- Salby, M. L., & Callaghan, P. F. (2002). Interannual changes of the stratospheric circulation: Relationship to ozone and tropospheric structure. *Journal of Climate*, *15*(24), 3673–3685. [https://doi.org/10.1175/1520-0442\(2003\)015<3673:ICOTSC>2.0.CO;2](https://doi.org/10.1175/1520-0442(2003)015<3673:ICOTSC>2.0.CO;2)
- Salminen, A., Asikainen, T., Maliniemi, V., & Mursula, K. (2019). Effect of energetic electron precipitation on the northern polar vortex: Explaining the QBO modulation via control of meridional circulation. *Journal of Geophysical Research: Atmospheres*, *124*(11), 5807–5821. <https://doi.org/10.1029/2018JD029296>
- Salminen, A., Asikainen, T., Maliniemi, V., & Mursula, K. (2020). Dependence of sudden stratospheric warmings on internal and external drivers. *Geophysical Research Letters*, *47*(5), e2019GL086444. <https://doi.org/10.1029/2019GL086444>
- Salminen, A., Asikainen, T., & Mursula, K. (2022). Planetary waves controlling the effect of energetic electron precipitation on the northern polar vortex. *Geophysical Research Letters*, *49*(6), e2021GL097076. <https://doi.org/10.1029/2021GL097076>
- Scaife, A. A., Knight, J. R., Vallis, G. K., & Folland, C. K. (2005). A stratospheric influence on the winter NAO and North Atlantic surface climate. *Geophysical Research Letters*, *32*(18), L18715. <https://doi.org/10.1029/2005GL023226>
- Schoeberl, M. R. (1978). Stratospheric warmings: Observations and theory. *Reviews of Geophysics*, *16*(4), 521–538. <https://doi.org/10.1029/RG016i004p00521>
- Seppälä, A., Lu, H., Clilverd, M. A., & Rodger, C. J. (2013). Geomagnetic activity signatures in wintertime stratosphere wind, temperature, and wave response. *Journal of Geophysical Research: Atmospheres*, *118*(5), 2169–2183. <https://doi.org/10.1002/jgrd.50236>
- Seppälä, A., Randall, C., Clilverd, M., Rozanov, E., & Rodger, C. (2009). Geomagnetic activity and polar surface air temperature variability. *Journal of Geophysical Research*, *114*(A10), A10312. <https://doi.org/10.1029/2008JA014029>
- Shapiro, A. I., Schmutz, W., Rozanov, E., Schoell, M., Haberleiter, M., Shapiro, A. V., & Nyeki, S. (2011). A new approach to the long-term reconstruction of the solar irradiance leads to large historical solar forcing. *A&A*, *529*, A67. <https://doi.org/10.1051/0004-6361/201016173>
- Shpynev, B., Churilov, S., & Chernigovskaya, M. (2015). Generation of waves by jet-stream instabilities in winter polar stratosphere/mesosphere. *Journal of Atmospheric and Solar-Terrestrial Physics*, *136*, 201–215. <https://doi.org/10.1016/j.jastp.2015.07.005>
- Smith-Johnsen, C., Nesse Tysøy, H., Hendrickx, K., Orsolini, Y., Kishore Kumar, G., Ødegaard, L.-K. G., et al. (2017). Direct and indirect electron precipitation effect on nitric oxide in the polar middle atmosphere, using a full-range energy spectrum. *Journal of Geophysical Research: Space Physics*, *122*(8), 8679–8693. <https://doi.org/10.1002/2017JA024364>

- Song, B.-G., Chun, H.-Y., & Song, I.-S. (2020). Role of gravity waves in a vortex-split sudden stratospheric warming in January 2009. *Journal of the Atmospheric Sciences*, *77*(10), 3321–3342. <https://doi.org/10.1175/JAS-D-20-0039.1>
- Stenke, A., Schraner, M., Rozanov, E., Egorova, T., Luo, B., & Peter, T. (2013). The SOCOL version 3.0 chemistry–climate model: Description, evaluation, and implications from an advanced transport algorithm. *Geoscientific Model Development*, *6*(5), 1407–1427. <https://doi.org/10.5194/gmd-6-1407-2013>
- Turunen, E., Verronen, P. T., Seppälä, A., Rodger, C. J., Clilverd, M. A., Tamminen, J., et al. (2009). Impact of different energies of precipitating particles on NO<sub>x</sub> generation in the middle and upper atmosphere during geomagnetic storms. *Journal of Atmospheric and Solar-Terrestrial Physics*, *71*(10), 1176–1189. (High Speed Solar Wind Streams and Geospace Interactions). <https://doi.org/10.1016/j.jastp.2008.07.005>
- Wilks, D. S. (2016). “The stippling shows statistically significant grid points”: How research results are routinely overstated and overinterpreted, and what to do about it. *Bulletin of the American Meteorological Society*, *97*(12), 2263–2273. <https://doi.org/10.1175/BAMS-D-15-00267.1>
- Yamazaki, K., Nakamura, T., Ukita, J., & Hoshi, K. (2020). A tropospheric pathway of the stratospheric quasi-biennial oscillation (QBO) impact on the boreal winter polar vortex. *Atmospheric Chemistry and Physics*, *20*(8), 5111–5127. <https://doi.org/10.5194/acp-20-5111-2020>
- Yasyukevich, A. S., Chernigovskaya, M. A., Shpynev, B. G., Khabituev, D. S., & Yasyukevich, Y. V. (2022). Features of winter stratosphere small-scale disturbance during sudden stratospheric warmings. *Remote Sensing*, *14*(12), 2798. <https://doi.org/10.3390/rs14122798>
- Zúñiga López, H. D., Tysøy, H. N., Smith-Johnsen, C., & Maliniemi, V. (2022). The direct effect of medium energy electron precipitation on mesospheric dynamics during a sudden stratospheric warming event in 2010. *Geophysical Research Letters*, *49*(13), e2022GL097812. <https://doi.org/10.1029/2022GL097812>



# Appendix A

## Appendix

### A.1 Additional theory

#### A.1.1 Three types of particle motion

Figure 2.3 illustrates three types of particle motions of particles trapped in Earth's magnetic field. This section will derive some of the fundamental forces driving these motions.

A charged particle moving in a homogeneous electromagnetic field will experience a force perpendicular to both the magnetic field direction and the velocity direction. This is known as the Lorentz force, and is given by

$$m \frac{d\mathbf{v}}{dt} = q(\mathbf{E} + \mathbf{v} \times \mathbf{B}) . \quad (\text{A.1})$$

In an inertial frame of reference where the electrical field is zero, as the force is always perpendicular to the direction of motion, the charged particle will move in a circular gyromotion. By equating the acceleration in the Lorentz force with formula for the centripetal acceleration, the radius and angular velocity of the gyromotion can be calculated as follows:

$$\frac{mv_{\perp}^2}{r_g} = qv_{\perp}B; \quad (\text{A.2})$$

$$r_g = \frac{mv_{\perp}}{qB}; \quad (\text{A.3})$$

$$\omega_g = \frac{qB}{m}. \quad (\text{A.4})$$

Secondly, particles bounce between geomagnetic conjugate mirror points, i.e., where the pitch angle  $\alpha = 90^\circ$ . When particles move along the geomagnetic field lines towards the poles, the magnetic field converges. Such converging field with decomposed components are illustrated in Figure A.1. The convergence equates to the magnetic field having a component  $B_2$ , pointing towards the center of the circular path traced out by the gyromotion. The cross product between the perpendicular velocity  $v_{\perp}$  and the  $B_1$ -component trace out the regular gyromotion, while the parallel velocity  $v_{\parallel}$  does not interact with  $B_1$  as they point in the same direction. However, the additional magnetic field component  $B_2$  is perpendicular to both  $v_{\perp}$  and  $v_{\parallel}$ . This gives rise to a force in the opposite direction of the parallel velocity component ( $\mathbf{v}_{\perp} \times \mathbf{B}_2$ ), as well as a force accelerating the perpendicular velocity component ( $\mathbf{v}_{\parallel} \times \mathbf{B}_2$ ). The former is known



as the mirror force, as it acts to decelerate the parallel speed of the gyrating particle. Given a strong enough  $B_2$ -component (large convergence), the mirror force would be strong enough to reverse the  $v_{\parallel}$  direction. Further, the geometry allows us to express the velocity vectors as

$$v_{\perp} = v \sin \alpha; \tag{A.5}$$

$$v_{\parallel} = v \cos \alpha. \tag{A.6}$$

If  $\alpha = 90^\circ$ , then  $v_{\parallel} = 0$ , and the charged particle reaches the point of reversal, also known as the mirror point. From the same equations it is also evident that  $v_{\perp}$  maximises at the same point, thereby conserving the velocity (momentum). The magnetic field cannot change the total velocity of the particle, only the direction, as the magnetic force is always perpendicular to the velocity. This fact, in addition to assuming slowly changing magnetic fields with respect to the period of gyration, leads to the magnetic dipole moment of the charged particle being conserved. This is also often referred to as the first adiabatic invariant of particle motion in plasma physics. The magnetic dipole moment can be expressed by considering the charged gyrating particle as a current ring with radius  $r_g$ . The magnetic dipole moment  $\mu$ , is then proportional to the current  $I$  multiplied by the size of the enclosed area  $A$ :

$$IA = \left(\frac{q\omega_g}{2\pi}\right)(\pi r_g^2) = \mu. \tag{A.7}$$

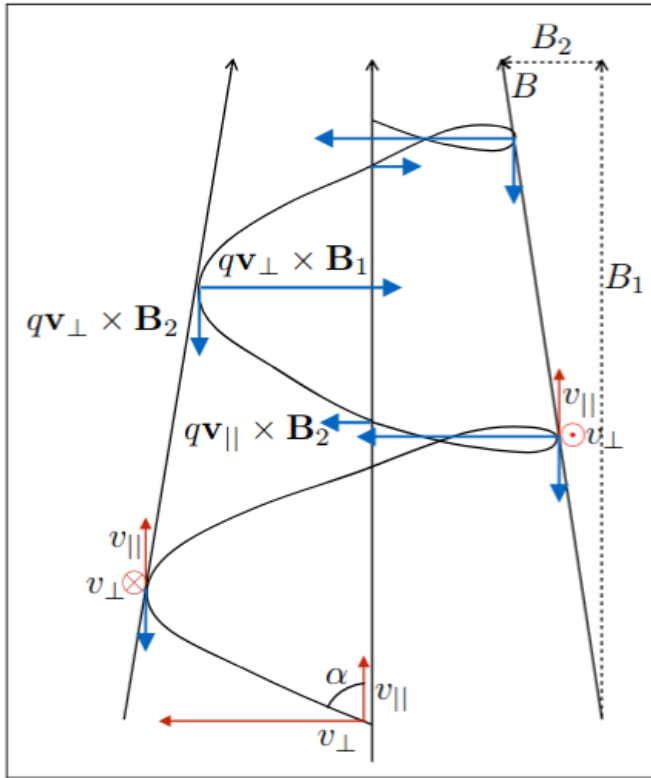


Figure A.1: Motion of charged particles in a converging magnetic field. The Lorentz force have been decomposed into a parallel and perpendicular component, derived from the parallel and perpendicular velocity and magnetic field [Obtained from PHYS 251 compendium].

By inserting for the gyroradius and angular velocity (Eq. A.3-A.4) the equation yields

$$IA = \frac{q^2 B}{2\pi m} \pi \left( \frac{mv_{\perp}}{qB} \right)^2 = \frac{mv_{\perp}^2}{2B} = \mu. \quad (\text{A.8})$$

Finally, by inserting Eq. A.5 and assuming the quantity is conserved under a slowly changing magnetic field in respect to a gyration, one obtains

$$\mu = \frac{mv^2 \sin^2 \alpha}{2B} = \text{constant}. \quad (\text{A.9})$$

As the mass and the total speed of the charged particle remains constant, only the magnetic field and pitch angle are left to vary, such that

$$\frac{\sin^2 \alpha}{B} = \text{constant}. \quad (\text{A.10})$$

For  $\alpha = 90^\circ$ , which is the mirror point (as  $v_{\parallel} = 0$ ), the relationship yields:

$$\frac{\sin^2(\alpha = 90^\circ)}{B} = \frac{1}{B_{\text{Strength at } \alpha=90^\circ}} \quad (\text{A.11})$$

where the pitch angle can be defined as:

$$\sin \alpha_0 = \sqrt{\frac{B_0}{B_1}} \quad (\text{A.12})$$

Here,  $B_0$  denotes the field strength at the location of the particle, while  $B_1$  denotes the field strength at the "mirror point". By setting  $B_1$  equal to the magnetic field near Earth's atmosphere (<100 km from surface), the pitch angle range for particles at different locations that will penetrate the atmosphere before the mirror point can be calculated. These angles trace out a cone around the magnetic field line and are often referred to as the "loss cone", as particles reaching the atmosphere before the mirror point have a high possibility of colliding and ending up as particle precipitation. Particles with pitch angles outside the loss cone will keep oscillating between magnetic conjugate mirror points.

Thirdly, trapped charged particles also exhibit drift motion, with electrons drifting eastward and protons drifting westward. This leads to the ring current. An increased ring current decreases the strength of the horizontal component of the terrestrial field. Although the perturbation is small, it is still measurable in the equatorial region. The geomagnetic disturbance index Dst is a measure of the strength of the ring current. Whereas the gyromotion and bouncing between magnetic conjugate points can be easily derived, the drift motion arises due to higher order corrections resulting from a combination of three factors: the  $E \times B$  drift, the gradient  $B$  drift, and the curvature drift. Detailed derivation of these drift motions can be found, for example, at <https://farside.ph.utexas.edu/teaching/plasma/lectures1/node23.html>.

## A.1.2 Adiabatic invariants

Adiabatic invariants are physical quantities within a system that changes slowly enough to be considered constants of motion. In plasma physics, all three charged particle motions described in Appendix A1 have their respective adiabatic invariants, which are conserved for

slowly changing fields.

As already described in Appendix A1, the first invariant

$$\mu = \frac{mv_{\perp}^2}{2B} = \text{constant} . \quad (\text{A.13})$$

is the magnetic dipole moment of a gyrating charged particle. This shows, for example, that for a magnetic field whose temporal evolution occurs on time scales less than a gyroperiod, the perpendicular velocity of a particle varies as the square root of the magnetic field.

The second invariant is the longitudinal invariant of a trapped particles parallel momentum which bounces off mirror points. The trajectory of the guiding center can be regarded as approximately closed, even though a small azimuthal drift component exists. It is expressed as

$$J = \oint p_{\parallel} ds = \text{constant} . \quad (\text{A.14})$$

The path of integration is along a field line and back, with  $ds$  representing the arch length along the field line. Provided that the magnetic field varies on time scales much longer than the bounce time between mirror points, the invariant assures that charged particles mirroring always return to the same line of force.

The third invariant is associated with the azimuthal drift motion, and is defined by the conservation of the magnetic flux, denoted as  $\phi$ , which is enclosed by a drift surface. In simpler terms, this ensures that the magnetic flux through a particle's drift orbit is conserved. The conservation is subject to the condition that variations in the magnetic field occur over time scales that are longer than the drift period, which is often on the order of an hour. This means that the invariant is only primarily under relatively quiet geomagnetic conditions.

## A.2 Errata

Given the steep learning curve associated with the statistical methods, as well as new insights gained towards the end of the thesis, minor statistical errors have been identified in the published Paper I and III. This section is best understood after reading the mentioned papers.

### A.2.1 Paper I

In this study,  $\alpha_{\text{FDR}}$  was set equal to 0.05, and only 3000 MC-iterations were conducted for the significance assessment. The autocorrelation of the data were therefore not taken into account when choosing  $\alpha_{\text{FDR}}$ , Equation 3.10 (with 55 data points for FDR correctly assessed between lead-lags -27 and 27) yields only a 93% accurate representation of the significance limits. The correct approach would be to estimate  $\alpha_{\text{FDR}}$  (Section 3.3.2), and accordingly estimate the number of iterations for sufficient accuracy. However, since the conclusion of the paper is that no significant response is found, setting  $\alpha_{\text{FDR}}$  equal to the least conservative value of 0.1 is appropriate. In addition to 55 lead-lags ( $N$ ), Equation 3.12 gives us a lower limit of 11 387 iterations performed for an error in accuracy of  $10^{-9}$ . This should ensure the distribution at the given resolution to be fulfilled with a 99.9999999% accuracy.

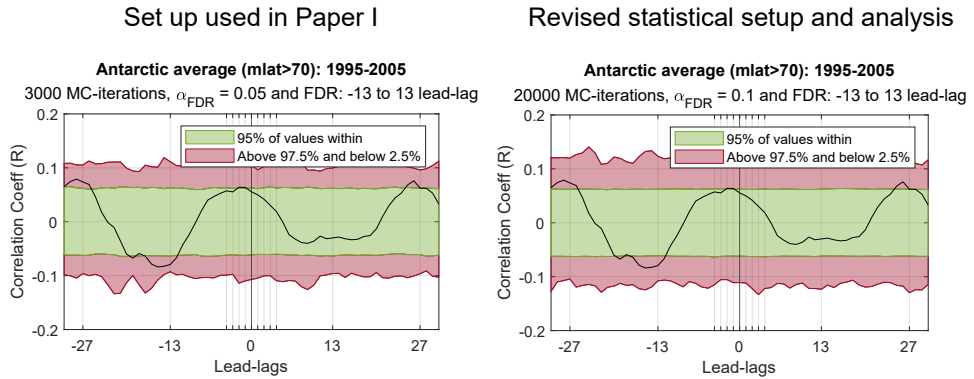


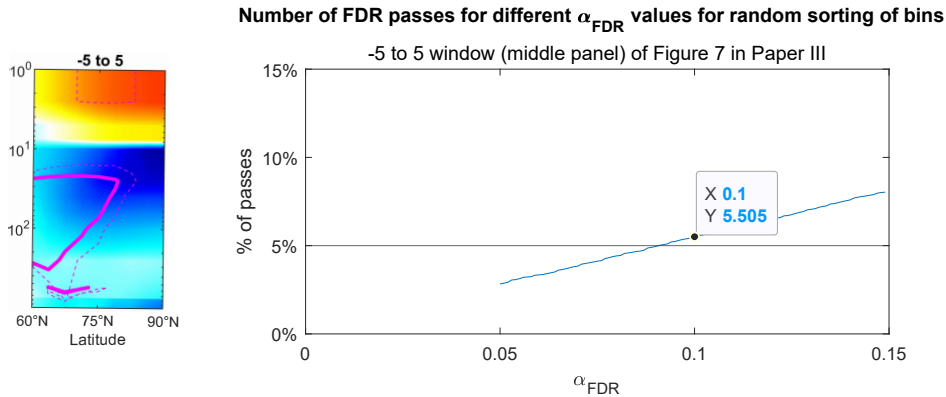
Figure A.2: **Left panel:** Set up used in Paper I. **Right panel:** Revised setup. As shown, only negligible chances are seen for the

Figure A.2 shows a side by side comparison between the set up used in Paper I (3000 iterations,  $\alpha_{FDR} = 0.05$ ) and the revised set up (20 000 iterations,  $\alpha_{FDR} = 0.05$ ). The applied changes do not result in any observable differences in significance, meaning that the conclusions drawn in the paper remain unaffected. Additionally, it is worth noting that the applied changes also do not result in any observed differences for the period 1999–2002 (Figure 6 in Paper I, not shown).

## A.2.2 Paper III

Section 3.3.1 describes how the FDR method assumes identical distribution of observations, which means that the data characteristics, such as mean, median, variance, and standard deviation, are the same for every data point being compared. However, in Paper III, none of the temperature response versus altitude plots (Figure 4, 5, 6 and 7) have identical distribution of data between all data points where FDR is performed, as different altitude levels have temperature data with different data characteristics. A natural conclusion could therefore be that the FDR method is not an appropriate tool to assess the global significance limits in these cases.

We perform an additional MC experiment on an arbitrary plot in Paper III (Fig 4-7), with the goal of calculating the percentage of global null hypotheses passing the FDR-method (should ideally be 5%) with the set up used in paper III. The choice of plot is arbitrary, as all plots have similar deviations in the data characteristics between data points compared by the FDR method. The left panel of Figure A.3 represents the middle panel of Figure 7. It displays 42 experiment events averaged, with 38 reference events averaged and subtracted from the experiments (42 EXP - 38 REF). The solid magenta lines show the calculated statistical significance after MC bootstrapping (Section 3.2.2) and the FDR (Section 3.3.1) with  $\alpha_{FDR} = 0.1$ . Ideally, and also suggested in the paper, is that these solid significance lines indicate global significance at the 95% confidence level. The right panel of Figure A.3 shows the additional MC experiment, similarly performed applying the optimization technique for  $\alpha_{FDR}$  discussed in Section 3.3.2. Firstly, significance limits are calculated exactly how they are calculated in the paper yielding a "reference" distribution (20 000 random selections with replacement of the EXP (length 42) and REF (length 38) bins from the 80 available choices). Then, 20 000 additional random selections with replacement are performed in the same manner, resulting in



**Figure A.3: Left panel:** The plot shows the temperature response for all Februaries in the period 1955–2008 in a -5 to 5 day window with respect to minor SSW events (42 EXP - 38 REF). The stippled magenta lines show statistical significance after the MC approach, while solid magenta lines show statistical significance after MC and the FDR approach. The temperature scale is not of importance. Obtained from the middle panel of Figure 7 in Paper III. **Right panel:** The FDR method with different  $\alpha_{\text{FDR}}$  values performed for 20 000 randomly sampled EXP-REF result when using the exact set up from the left panel. For  $\alpha_{\text{FDR}} = 0.1$  as set in the paper, 5.5% of the 20 000 random iterations pass the FDR.

another set of 20 000 temperature anomaly plots of the form  $\Delta T_{\text{rand}} = \text{EXP}_{\text{rand}} - \text{REF}_{\text{rand}}$ . The temperature anomalies from the second step are then compared to the "reference" distribution. This yields 20 000 sets of p-values for all data points (lat-alt) where the null hypotheses are assumed to hold, as the bins are chosen randomly. Applying the FDR method (with different  $\alpha_{\text{FDR}}$  values) iteratively to each of the 20 000 sets of p-values, the percentage of the 20 000 sets of p-values passing the FDR method is calculated. This equals the global FDR pass rate when the null hypothesis is assumed correct. When  $\alpha_{\text{FDR}} = 0.1$ , 5.5% of the 20 000  $\text{EXP}_{\text{rand}} - \text{REF}_{\text{rand}}$  results pass the FDR criteria. This proves that for the exact set up used in Paper III, the solid significance lines given in Figure A.3 indicate global significance at the 94.5% level, nearly equal to the proposed 95% level. Ideally, Paper III should have included an  $\alpha_{\text{FDR}}$  optimization routine, and used  $\alpha_{\text{FDR}} = 0.091$ , as this renders global significance at exactly 5%. However, by using 0.091 instead of 0.1, only negligible differences are seen, and the conclusion of the paper still stands. Furthermore, this also suggest that the FDR approach is valid even if the data points compared only have approximately identical distribution of observations.

# Appendix B

## Dictionary

Definitions according to *Wikipedia*:

- **Adiabatic cooling:** The process of reducing heat through a change in air pressure caused by volume expansion.
- **Angular momentum:** The rotational analog of linear momentum. It is an important physical quantity because it is a conserved quantity the total angular momentum of a closed system remains constant.
- **Anomaly:** In the natural sciences, especially in atmospheric and Earth sciences involving applied statistics, an anomaly is a persisting deviation in a physical quantity from its expected value, e.g., the systematic difference between a measurement and a trend or a model prediction.
- **Anthropogenic:** Environmental pollution and pollutants originating from human activity.
- **Artefact:** In natural science and signal processing, an artifact or artefact is any error in the perception or representation of any information introduced by the involved equipment or technique(s).
- **Assimilation:** Data assimilation is a mathematical discipline that seeks to optimally combine theory (usually in the form of a numerical model) with observations.
- **Atmospheric dynamics:** The study of motion systems of meteorological importance, integrating observations at multiple locations and times and theories. Common topics studied include diverse phenomena such as thunderstorms, tornadoes, gravity waves, tropical cyclones, extratropical cyclones, jet streams, and global-scale circulations.
- **Autoconversion rate:** The rate at which water mass in the form of cloud droplets forms raindrops.
- **Autocorrelation:** The correlation of a signal with a delayed copy of itself as a function of delay. Sometimes known as serial correlation in the discrete time case.

- **Baroclinic:** A mechanism by which vorticity is generated. Baroclinic vorticity generation occurs whenever there is a density gradient along surfaces of constant pressure. Baroclinic flows can be contrasted with barotropic flows in which density and pressure surfaces coincide and there is no baroclinic generation of vorticity.
- **Barotropic:** A barotropic fluid is a fluid whose density is a function of pressure only.
- **Bias:** In science and engineering, a bias is a systematic error. Statistical bias results from an unfair sampling of a population, or from an estimation process that does not give accurate results on average.
- **Cascading effect:** An inevitable and sometimes unforeseen chain of events due to an act affecting a system.
- **Catalytic:** Increasing the speed at which reactions happen.
- **Climatology:** Weather conditions averaged over a period of time.
- **Coalescence:** In the context of the thesis, it is the process by which two or more droplets fuse to form a bigger droplet.
- **Conjugate geomagnetic points:** Two points on Earth are geomagnetically conjugate if they are on opposite ends of the same field line.
- **Convection:** The movement caused within a fluid by the tendency of hotter and therefore less dense material to rise, and colder, denser material to sink under the influence of gravity, which consequently results in transfer of heat.
- **Coriolis force:** An inertial or fictitious force that acts on objects in motion within a frame of reference that rotates with respect to an inertial frame. In a reference frame with clockwise rotation, the force acts to the left of the motion of the object. In one with anticlockwise (or counterclockwise) rotation, the force acts to the right. In popular (non-technical) usage of the term "Coriolis effect", the rotating reference frame implied is almost always the Earth.
- **Curvilinear coordinates:** In geometry, curvilinear coordinates are a coordinate system for Euclidean space in which the coordinate lines may be curved.
- **Data assimilation:** A mathematical discipline that seeks to optimally combine theory (usually in the form of a numerical model) with observations.
- **Degrees of freedom:** The number of parameters of a system that may vary independently. In statistics, the number of degrees of freedom is the number of values in the final calculation of a statistic that are free to vary.
- **Dissociate:** In chemistry, it is the general process in which molecules separate or split into other things such as atoms, ions, or radicals.
- **Easterly wind:** Wind coming from east.
- **Ecliptic:** The ecliptic or ecliptic plane is the orbital plane of Earth around the Sun. The ecliptic is an important reference plane and is the basis of the ecliptic coordinate system.

- 
- **Eddy:** The swirling of a fluid and the reverse current created when the fluid is in a turbulent flow regime.
  - **Endothermic:** A chemical reaction that absorbs heat.
  - **Ensembles:** A climate ensemble involves slightly different models of the climate system. Due to the non-linear nature of fluid mechanics, small changes in initial conditions when running a climate model (e.g. 1% differing CO<sub>2</sub> concentration) lead to independent model runs known as ensemble members. The ensemble average is expected to perform better than individual ensemble runs.
  - **Equilibrium:** The condition of a system in which all competing influences are balanced.
  - **Equipotential:** Refers to a region in space where every point in it is at the same potential (e.g. in terms of field strength).
  - **Exothermic:** A chemical reaction that releases heat.
  - **Fair weather:** Calm and stable weather, often characterized by clear skies, sunshine, and mild temperatures. Fair weather usually occurs when high-pressure systems dominate an area, causing sinking air and inhibiting cloud formation and precipitation.
  - **Fourier transform:** A mathematical technique used to transform a signal from the time domain to the frequency domain.
  - **Geocentric orbit:** A geocentric orbit or Earth is simply an orbital path encircling the Earth. The Moon and artificial satellites have geocentric orbits.
  - **Geoeffective:** Capable of causing a geomagnetic disturbance
  - **Geomagnetic conjugate:** Two points on Earth are "geomagnetically conjugate" if they are on opposite ends of the same field line.
  - **Geopotential height:** A measure of the height of a pressure surface in the atmosphere above mean sea level, which is determined by the distribution of mass and gravity in the Earth's atmosphere. It is defined as the height that a hypothetical, constant-pressure surface would have above sea level if the Earth's gravity field were uniform and the atmosphere was at rest. It is typically measured in meters and can be thought of as an indicator of atmospheric pressure at a given altitude.
  - **Heliosphere:** The vast, bubble-like region of space which surrounds and is created by the Sun. In plasma physics terms, this is the cavity formed by the Sun in the surrounding interstellar medium.
  - **In situ:** A Latin phrase that translates literally to "on site" or "in position". In the atmospheric sciences, in situ refers to obtained through direct contact with the respective subject, such as a radiosonde measuring a parcel of air.
  - **Interannual:** Occurring between years, or from one year to the next.
  - **Interstellar medium:** The matter and radiation that exists in the space between the star systems in a galaxy.



- **Lagrange point:** Lagrange points are positions in space where objects sent there tend to stay put. At Lagrange points, the gravitational pull of two large masses precisely equals the centripetal force required for a small object to move with them.
- **Longwave Radiation:** Electromagnetic radiation of wavelengths from 3100  $\mu\text{m}$  emitted from Earth and its atmosphere out to space in the form of thermal radiation.
- **Magnetometer:** A device that measures magnetic field or magnetic dipole moment.
- **Meridional:** In the north-south direction. Expression used to illustrate directions when on a globe.
- **Mirror point:** A magnetic mirror point is a point where the motion of a charged particle trapped in a magnetic field (such as the (approximately) dipole field of the Earth) reverses its direction. More precisely, it is the point where the projection of the particle's velocity vector in the direction of the field vector is equal to zero.
- **Opacity:** Describes the absorption and scattering of radiation in a medium. Higher opacity accounts for more absorption and scattering in the medium.
- **Perturbation:** A small change in a physical system.
- **Photodissociation:** Photodissociation, photolysis, photodecomposition, or photofragmentation is a chemical reaction in which molecules of a chemical compound are broken down by photons. It is defined as the interaction of one or more photons with one target molecule.
- **Potential vorticity:** In fluid mechanics, this is a quantity which is proportional to the dot product of vorticity and stratification. This quantity, following a parcel of air or water, can only be changed by diabatic or frictional processes. It is a useful concept for understanding the generation of vorticity in cyclogenesis (the birth and development of a cyclone), especially along the polar front, and in analyzing flow in the ocean.
- **Plasma:** A state of matter happening in a gas if the temperature is so high that electrons can not be bound to the atoms nucleus. Plasma is then defined as a gas consisting of ions and electrons, contrary to a normal gas consisting of neutral atoms.
- **Proxy:** An indirect association with a physical phenomenon. The phenomenon itself is usually difficult to quantify and/or measure.
- **Radiative balance:** The relationship between the amount of energy reaching an object (or a portion of it) and the amount leaving it.
- **Radiative forcing:** The change in energy flux in the atmosphere caused by natural or anthropogenic factors of climate change as measured by  $\frac{\text{watts}}{\text{meter}^2}$ . It is a scientific concept used to quantify and compare the external drivers of change to Earth's energy balance
- **Reciprocal:** A mutual relationship/connection between two or more components. A relationship/connection going both ways, where each of the participants affects each other.
- **Stochastic:** A randomly determined process.

- **Synoptic waves:** Atmospheric waves with horizontal length in the synoptic length scale (also known as large scale or cyclonic scale). Defined as lengths on the order of 1000 kilometers or more.
- **Westerly wind:** Wind coming from west.
- **Zonal:** In the east-west direction. Expression used to illustrate directions when on a globe.





Graphic design: Communication Division, UIB / Print: Skjipes Kommunikasjon AS



[uib.no](http://uib.no)

ISBN: 9788230844960 (print)  
9788230857700 (PDF)